Numéro d'ordre : 42472

Thèse en Physique et Science des Matériaux

Soutenue le 5.12.2017

Université De Lille – 1 Sciences et Technologies

Ecole Doctorale des Sciences de la Matière, du Rayonnement et de l'Environnement

FORMATION OF EXTRUSION-INTRUSION IN A MARTENSITIC STEEL STUDIED BY ADVANCED MICROSCOPIES

La formation des extrusions et des intrusions dans un acier martensitique étudiée par les microscopies de pointe

Gulzar Seidametova
Master in Airport Technologies of National Aviation University in Kyiv (Ukraine)

Directeurs de la thèse :

Vogt Jean-Bernard – Professeur, ENSCL

Proriol Serre Ingrid – Chargée de recherche CNRS, HDR, UMET

Jury de la thèse :

Risbet Marion – Professeur, UTC

Hardouin Duparc Olivier – Chargé de recherche CNRS, HDR, LSI

Tromas Christophe – Professeur, Université de Poitiers

Crépin Jérôme – Directeur de recherche, Centre des Matériaux

Bouquerel Jérémie – Maître de conférence, ENSCL

Unité Matériaux et Transformations

UMR CNRS 8207 – Université de Lille

Abstract

The particularity of martensitic steels is their complex hierarchical microstructure consisting of prior austenite grains, packets, blocks and laths, the influence of which on the early-stage fatigue deformation at nano-scale is little studied. As a result the objective of this work is to explain the mechanism of extrusion-intrusion pair formation in a 12%Cr martensitic steel during low cycle fatigue at room temperature in regards to the different interfaces creating the material complexity.

To achieve the purpose, the fatigue slip markings were thoroughly investigated at the fatigued metal surface with a help of atomic force microscope and then the microstructural evolution was studied directly under fatigue slip markings on the transmission electron microscope thin lamellae extracted by focused ion beam.

The atomic force microscope analysis of the specimen surface after each interruption step of low cycle fatigue test revealed two different morphological types of extrusions that were named principal and secondary extrusions. For the latter there was not found any scientific equivalence in the case of martensitic steels in the reviewed literature bank. Additionally, this technique gave an idea about the localization of principal extrusions in the vicinity of different boundaries making the complex martensitic microstructure.

The transmission electron microscope investigation of microstructural evolutions under the fatigue slip markings demonstrated the localization of principal extrusions in the vicinity of different martensitic boundaries as well as of fatigue dislocation cell walls, and the localization of intrusions in the boundaries or walls themselves. As for the secondary ones, their localization inside the laths was validated too.

The ensemble of results together with the Polak's model helped to propose the mechanism of formation of fatigue slip markings in the hierarchically organized martensitic steel. Thus, the existing different boundaries and the formed dislocation cells were found to play a definitive role in the creation of intrusions. The extrusion is believed to be the direct result of slip activity of dislocations close to the boundary as well as the result of volume swelling caused by vacancy generation and migration directed by the boundary dislocations. The intrusion is rather a result of vacancy accumulation in the boundaries or walls due to the dislocation movement. As follows, the martensitic hierarchical interfaces and dislocation cell walls are considered to be a source of dislocations and at the same time a sink for vacancies.

Keywords: Low Cycle Fatigue, plastic deformation, microcrack initiation, martensitic microstructure, boundary, 12%Cr steel, Persistent Slip Markings, Atomic Force Microscope, Transmission Electron Microscope analysis

Résumé

La spécificité des aciers martensitiques est leur microstructure hiérarchisée complexe constituée d'anciens grains austénitiques, de paquets, de blocs et de lattes. L'influence de chaque élément de cette microstructure sur les premières étapes de l'amorçage des microfissures de fatigue est cependant peu étudiée. En conséquence, l'objectif de ce travail est, d'une part, d'expliquer le mécanisme de formation d'extrusion-intrusion par fatigue oligocyclique à température ambiante à la surface d'un acier martensitique à 12% de chrome et, d'autre part, de définir le rôle des différentes interfaces de la microstructure sur la formation des extrusions et des intrusions.

Pour atteindre cet objectif, les marques de glissement observées à la surface après sollicitation cyclique ont été étudiées en détail à l'aide de la microscopie à force atomique. L'évolution de la microstructure en dessous des marques de glissement a été ensuite analysée à partir d'observations en microscopie électronique en transmission des sections transverses obtenues par extraction de lames par faisceau d'ions focalisé.

L'analyse en microscope à force atomique de la surface de l'échantillon après chaque interruption de l'essai de fatigue oligocyclique a révélé deux morphologies d'extrusions qui ont été appelées extrusions principales et extrusions secondaires. Pour ces dernières, aucune équivalence scientifique dans le cas des aciers martensitiques n'a été mentionnée auparavant dans la littérature. De plus, ces analyses, ont montré que les extrusions principales étaient localisées à proximité des différents joints – des éléments constituant la microstructure martensitique.

L'étude des évolutions microstructurales sous les marques de glissement à l'aide de la microscopie électronique à transmission a confirmé la localisation des extrusions principales à proximité des différentes interfaces de la structure martensitique ou des murs des cellules de dislocations, et prouvé la localisation des intrusions dans les interfaces elles-mêmes. Quant aux extrusions secondaires, leur localisation à l'intérieur des lattes a également été validée.

L'ensemble des résultats confrontés au modèle de Polak a conduit à proposer un mécanisme de formation des extrusions et intrusions à la surface de l'acier martensitique hiérarchiquement organisé. Ainsi, les différents joints inhérents à la structure martensitique et les cellules de dislocation formées par fatigue jouent un rôle primordial dans la création des intrusions. Nous pensons que l'extrusion serait le résultat direct du glissement des dislocations au sein même de la latte et proches d'un joint, ainsi que le résultat d'un gonflement de volume causé par la génération des lacunes et leur migration vers les dislocations aux interfaces. L'intrusion résulterait plutôt de l'accumulation de lacunes dans les joints ou les parois des cellules de dislocation en raison du mouvement des dislocations. Ainsi, les interfaces de la structure martensitique hiérarchisée et les parois des cellules de dislocations sont à la fois considérées comme source de dislocations et puits de lacunes.

Mots clés : fatigue oligocyclique, déformation plastique, nucléation de microfissure, microstructure martensitique, joint microstructural, acier 12%Cr, marque de glissement, microscopie à force atomique, microscopie électronique à transmission

Abstract ... 3
Résumé ... 4
List of abbreviations ... 9
List of symbols ... 12

1. Introduction ... 15

2. Literature review ... 19

2.1 About martensitic steels ... 19
2.1.1 What is a martensitic steel? ... 19
2.1.2 Martensitic transformation ... 19
2.1.2.1 Mechanism of martensitic transformation: quenching ... 21
2.1.2.2 Mechanism of martensitic transformation: tempering ... 21
2.1.2.3 Crystallography of martensitic transformation: notion of habit plane and KS relationship ... 22
2.1.3 Martensitic microstructure ... 23
2.1.3.1 Review of microstructural unit sizes defined by some authors ... 26
2.1.3.2 Relationship between units of microstructure and their sizes ... 29
2.1.3.3 Disorientation relationships of different interfaces in PA grain ... 31
2.1.4 Conclusions ... 33
2.2 Fatigue ... 33
2.2.1 What is fatigue? ... 33
2.2.2 Fatigue stages ... 34
2.2.3 Fatigue modes ... 34
2.2.4 LCF variables ... 35
2.2.5 Data recording during LCF test ... 36
2.3 Fatigue deformation ... 39
2.3.1 Low energy dislocation structures produced by cyclic deformation in the bulk of metals ... 39
2.3.2 Fatigue behaviour of 9-12% Cr martensitic steels and resulting microstructural evolutions ... 41
2.3.3 Mechanisms of fatigue surface relief formation ... 48
2.3.3.1 Dickson model ... 50
2.3.3.2 EGM model ... 50
2.3.3.3 Polak's model ... 51
2.3.3.4 Grain boundary sliding as a deformation mechanism in monotone and cyclic loading ... 53
2.3.3.5 Deformation of ultra-fine grained steels ... 55
2.3.4 Fatigue crack nucleation ... 56
2.3.4.1 Fatigue crack initiation in different metals ... 56
2.3.4.2 Fatigue crack initiation in martensitic steels ... 59
2.4 Conclusions ... 63

3. Experiment 65

3.1 STUDIED MATERIAL 65

3.1.1 Chemical composition 65

3.1.2 Phase identification by XRD 65

3.1.3 Microstructural characterization 66

3.1.4 Mechanical properties 74

3.2 EXPERIMENTAL PROCEDURE OF FATIGUE TEST 75

3.2.1 Specimen concept and sample surface preparation 75

3.2.2 Fatigue test and fatigue behaviour 76

3.3 AFM 77

3.3.1 Force curve 79

3.3.2 Contact mode 79

3.3.3 Intermittent (tapping™) mode 80

3.3.4 Image types 82

3.3.5 AFM image resolution 82

3.3.5.1 Vertical resolution 82

3.3.5.2 Lateral resolution 82

3.3.6 AFM topography image artefacts 83

3.3.7 AFM Peak Force™ mode 85

3.3.8 AFM equipment and conditions for the imaging in the present work 87

3.3.9 AFM for studying the fatigue and tensile plasticity 88

3.3.9.1 AFM in the studies on the different metals and metallic alloys 88

3.3.9.2 AFM in the studies of martensitic steels 90

3.4 TEM 95

3.4.1 Principle of work 95

3.4.1.1 Bright field imaging 95

3.4.1.2 Imaging of a dislocation 95

3.4.2 FIB for TEM thin foils preparation 96

3.4.2.1 Principle of work 96

3.4.2.2 Extraction of thin lamella for TEM observation 98

3.4.2.3 FIB artefacts 99

3.4.2.4 FIB for studying the fatigue damage 101

3.5 CONCLUSIONS 101

4. Study of FSM at the specimen surface 103

4.1 CHARACTERIZATION OF DEFORMATION RELIEF MORPHOLOGY 103

4.1.1 Principal extrusions ... 104
4.1.2 Intrusions ... 109
4.1.3 Secondary extrusions ... 112
4.2 Evolution of FSM ... 113
4.3 Localization of FSM ... 121
4.4 Validation of localization of FSM ... 124
4.4.1 Microstructural characterization and some mechanical properties ... 124
4.4.2 Experimental procedure ... 127
4.4.3 Results of AFM observations of deformation relief ... 128
4.5 Conclusions ... 131

5. Study of microstructural evolution under FSM ... 133

5.1 Microstructural evolution in the bulk ... 133
5.2 Observations of lamellae FIB under the FSM ... 135
5.2.1 Localization of principal FSM ... 136
5.2.2 Role of precipitates in FSM localization ... 140
5.2.3 Localization of secondary extrusions ... 141
5.2.4 Morphology of FSM cross-sections ... 142
5.2.5 Some dimensions of FSM cross-sections ... 146
5.2.6 Comparison with the results obtained by AFM profiling ... 148
5.3 Coupled SEM-ECCI-EBSD-TEM study of FSM ... 149
5.3.1 SEM-ECCI ... 149
5.3.2 SEM-EBSD ... 150
5.3.2.1 Image quality ... 151
5.3.2.2 Orientation Imaging Microscopy ... 152
5.3.2.3 Inverse Pole Figure ... 153
5.3.2.4 Line Segment Method ... 154
5.3.3 Results of principal extrusion observations ... 154
5.3.4 Results of secondary extrusion observations ... 160
5.4 Conclusions ... 164

6. Formation of extrusion and intrusion ... 165

6.1 The starting point of the model ... 166
6.2 The 12%Cr martensitic steel as an easy deformable material ... 167
6.3 Vacancy production and agglomeration ... 169
6.4 Nucleation of extrusion and intrusion ... 171

6.5 SUMMARIZED MECHANISM 175

7. Conclusions and perspectives 177

List of figures 180

List of tables 192

References 194

List of abbreviations

AFM	Atomic Force Microscope
bcc	Body-Centered Cubic
BSE	BackScattered Electrons
bct	Body-Centered Tetragonal
BSSA	British Stainless Steel Association
CCT	Continuous Cooling Transformation
COM	Crystal Orientation Map
DMT	Derjaguin-Muller-Toporov model
EBSD	Electron Backscatter Diffraction
ECCI	Electron Contrast Channeling Imaging
EDX	Energy Dispersive X-ray spectrometry
EGM	Essmann-Gösele-Mughrabi model
fcc	Face-Centered Cubic
FIB	Focused Ion Beam
FSM	Fatigue Slip Marking
GBS	Grain Boundary Sliding
GND	Geometrically Necessary Dislocations
GT	Greninger-Troiano
HAB	High Angle Boundary
HAGB	High Angle Grain Boundary
HCF	High Cycle Fatigue
HV	Vickers Hardness
IF	Interstitial Free
IPF	Inverse Pole Figure
IQ	Image Quality

KS (K-S)	Kurdjumov-Sachs
LAB	Low Angle Boundary
LAGB	Low Angle Grain Boundary
LCF	Low Cycle Fatigue
LMIS	Liquid Metal Ion Source
LSM	Line Segment Method
ND	Normal Direction
NW	Nishiyama-Wassermann
OM	Optical Microscopie
OIM	Orientation Imaging Microscopy
PA grain	Prior Austenite grain
PF	Peak Force
PF-QNM	Peak Force Quantitative Nano-Mechanical
PSB	Persistent Slip Band
PSM	Persistent Slip Marking
RD	Rolling Direction
RT	Room Temperature
SE	Secondary Electrons
SEM	Scanning Electron Microscope
S-N curve	Wöhler curve
SSD	Statistically Stored Dislocations
STEM	Scanning Transmission Electron Microscope
TD	Transverse Direction
TEM	Transmission Electron Microscope
UFG	Ultra-Fine Grained

UTS	Ultimate Tensile Strength
VHCF	Very High Cycle Fatigue
XRD	X-ray Diffraction
YS	Yield Stress (Strength)
YM	Young's Modulus
2D	Two-dimensional
3D	Three-dimensional

List of symbols

a	Lattice parameter
a	Radius of circular ion beam profile on the sample
A	Total tensile elongation
A_u	Total uniform elongation
Cr_{eq}	Chromium equivalent
D	Grain size
D	Diffusivity coefficient
D_g	Grain size
D	Packet size or deformation value
d_g	Prior austenite grain size
d_b	Block width
d_{packet}	Packet size
d_{block}	Block size
$d_{Cottrell}$	Cottrell atmosphere thickness
E	Modulus of elasticity or Young's modulus
E_i	Indenter Young's modulus
E_{mig}	Migration energy
F	Force
F_{adh}	Adhesion force
f	Frequency
$H_{Vickers}$	Vickers hardness
k	Spring constant or stiffness
k	Thermal conductivity
k_B	Boltzmann's constant
l	Length of extrusion

M_f	Martensite finish temperature
M_s	Martensite start temperature
N_b	Number of blocks
N_p	Number of packets
Ni_{eq}	Nickel equivalent
P	Beam power
R	Stress (strain) ratio or tip radius
R_ε	Strain ratio
T	Temperature
t	Time
V	Variant
w	Block width
x	Vacancy path
α	Ferritic phase
α'	Martensite
γ	Austenitic phase
Δz	Cantilever deflection
$\Delta\varepsilon$	Strain range
$\Delta\varepsilon_{pl}$, $\Delta\varepsilon_p$	Plastic strain range or variation
$\Delta\varepsilon_{el}$, $\Delta\varepsilon_e$	Elastic strain range or variation
$\Delta\varepsilon_t$	Total strain range or variation
$\Delta\sigma_t$	Total stress range
ε	Strain
ε_a	Strain amplitude
ε_{el}, ε_e	Elastic strain

ε_m	Mean strain
ε_{max}	Maximum strain
ε_{min}	Minimum strain
ε_m	Mean strain
ε_{pl}, ε_p	Plastic strain
$\acute{\varepsilon}$	Strain rate
θ	Diffraction angle
ν	Poisson's ratio
ν_i	Indenter Poisson's ratio
ν_{jump}	Jump frequency
ν_{vib}	Vibrational frequency
σ	Stress

1. Introduction

Fatigue of metals and metallic alloys is often a reason of failure in aircraft, car industry, nuclear equipment etc. Fatigue of material means damage as a result of repetitive loading. The majority is aware that the crack and failure are a manifestation of the final damage, but the cracking takes its roots in the initial accommodation of damage which is present on the material surface but invisible for a naked eye. In the case of homogeneous materials the "roots" of crack are often believed to be in the extrusions and intrusions at the surface. After initiation at the free surface in the intrusions, the cracks propagate inside the bulk of material. The propagation can be intergranular or transgranular but it is often of a mixed character. The fatigue cracking is often considered in the frame of fracture mechanics, while the mechanisms of emergence of crack precursors – persistent slip bands (extrusions + intrusions), and microcrack or short crack propagation are more frequently studied form the point of view of material science. The extrusion-intrusion at the metal surface is believed to be a result of dislocation activity in the material during cycling and represents the irreversibility of plastic deformation. The development of these precursors happens during a large number of cycles of structure lifetime. Once the mechanism of their development is understood, the mechanism of crack formation can be easier revealed too. The point is that the "before cracking" stage is not negligible and needs to be studied.

The precursors of cracks were investigated by such authors as Mughrabi, Man, Polak, Vogt, Basinski, Essmann and many others [1]–[7]. Different materials were studied by them: copper single crystals and polycrystals, austenitic and ferritic steels, aluminium etc.

The most prominent result was the revealing of a ladder-like structured persistent slip bands (PSB) in high stacking fault energy face-centered cubic (fcc) metals and development of a fatigue crack at the interface between PSB and material matrix (Figure 1-1).

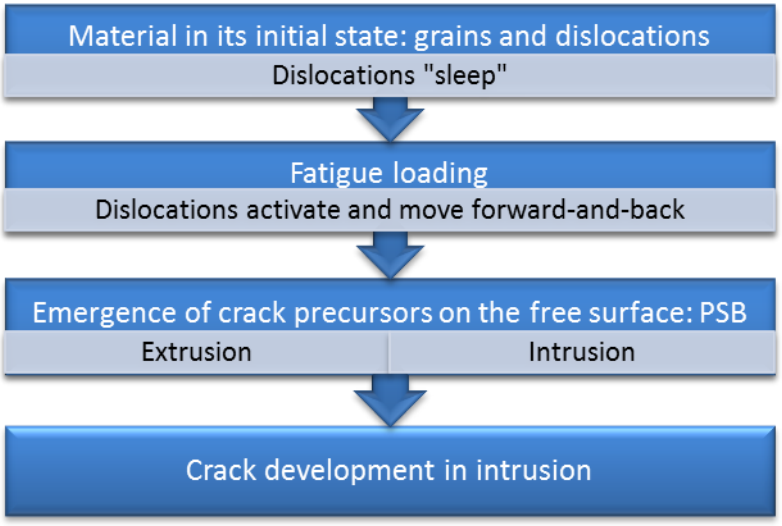

Figure 1-1 One of the scenarios of fatigue crack development in a metal

The ladder-like PSB was observed principally in the metals or metallic alloys that have fcc crystal structure and consist of rather large grains (a few tens of microns). They also have a dislocation microstructure quite well studied. As for the body-centered cubic (bcc) metals they are represented mainly by ferritic and martensitic steels in the industry subjected to the fatigue problems. The development of a deformation relief preceding the cracking is less studied for these materials especially for the martensitics. The latter have a complex and very fine microstructure comparing to ferritics which possess the equiaxed big grains. The fatigue of martensitic steels was essentially studied for temperatures higher than room temperature. The mechanical aspect of fatigue life of these steels is well studied by some authors [8]–[10]. Many authors observed the intergranular cracking of martensitic steels in the environments different than air [11]–[13]. Some scientific works report the localization of extrusions in different interfaces comprised in the steel [14], [15]. But for the moment to our knowledge nobody tried to explain the microstructural reasons of the initiation of cracks (i.e. initiation of extrusions and intrusions) in these hierarchically-structured steels at room temperature and in air.

The purpose of the present work is to explain the mechanism of extrusion-intrusion pair formation in a 12%Cr martensitic steel during Low Cycle Fatigue (LCF) at room temperature. The studied X19CrMoNbVN11-1 steel possesses a good resistance to corrosion and thermal shock, and good creep properties. It is usually used in aerospace industry for clamp rings and cooled turbine discs, and in marine and land-based machines for construction of gas turbine

rotors and blades, various steam turbine components and fasteners for high temperature environments. The mentioned above components are certainly subjected to fatigue loading in service. The results obtained in this work have a direct impact on the reliability of this material.

The second chapter of this Ph.D. thesis is devoted to the review of the existing knowledge on concerned issue, i.e. the review of martensitic steel transformation and morphology, and of the LCF damage of metallic materials.

The third chapter is designed to describe the studied material, the main steps of experimental procedure and the main techniques of material analysis before and after the mechanical tests.

In the fourth chapter the morphology of deformation relief is characterized by Atomic Force Microscope (AFM) after each interruption of LCF test.

Consequently, in the fifth chapter the microstructural evolution is studied directly under Fatigue Slip Markings (FSM) with Transmission Electron Microscope (TEM) thin lamellae extracted by Focused Ion Beam (FIB). The coupled SEM-EBSD-ECCI study of FSM on the specimen surface will reveal the slip systems of extrusions.

And finally, the model describing the origin of extrusion-intrusion in the studied martensitic steel will be proposed in the chapter 6.

2. Literature review

This chapter is designed for the reviewing of literature concerning the thesis objective. It contains 4 subchapters. In the first subchapter the notion of martensitic steel will be defined and the main aspects of martensitic transformation will be considered. The second one is dedicated to the fatigue phenomenon. Some general knowledge and the known mechanisms of fatigue deformation will be described. The third subchapter represents a summary of a few scientific works done on the monotonic and cyclic deformation of martensitic steels. The final subchapter is a conclusion of this bibliographic study.

2.1 About martensitic steels

2.1.1 What is a martensitic steel?

Martensitic steels are quenched steels with crystallographic structure close to the ferritic steels with a body-centered tetragonal (bct) crystal lattice or sometimes if the carbon content is lower than 0.02% with a body-centred cubic (bcc) crystal lattice. Another feature, defining the martensitic steel, is a particular lath or needle (plate) morphology of the alloy. Usually the martensitic steels are tempered after quenching. Due to this heat treatment the martensitic steel combines good hardness and high toughness. Untempered martensitic steel possesses low toughness which makes it brittle. According to British Stainless Steel Association (BSSA) they are classed as a "hard" ferro-magnetic group.

2.1.2 Martensitic transformation

Martensite is a metastable phase formed in steels by the rapid cooling (quenching) of austenite, where carbon is in solid solution, at such a high rate that carbon atoms do not have time to diffuse out of the fcc crystal structure in large enough quantities to form cementite Fe_3C. The

speeds of cooling can reach 450°C/s for some grades. During this cooling the diffusionless, i.e. displacive transformation takes place in the result of weak displacement or shearing of iron atoms for the tenth order of interatomic distance. This "cooperative" movement of atoms, due to the shearing of austenitic matrix because of the presence of significant supersaturation in interstitial (carbon), was called "military" by J.W. Christian [16]. As a result the fcc austenite transforms to a highly strained bct or bcc form of ferrite that is supersaturated with carbon. The crystal lattice change implies the volume and shape changes on a macroscopic level. On the microscopic level the resultant shear deformations produce large number of dislocations, which is a primary strengthening mechanism of steels. The martensitic reaction begins (Figure 2-1) during cooling when the austenite reaches the martensite start temperature (M_s) and the parent austenite becomes mechanically unstable. As the sample is quenched, an increasingly large percentage of the austenite transforms to martensite until the lower transformation temperature M_f (martensite finish) is reached, at which time the transformation is completed [17]. The M_f temperature is around the room temperature.

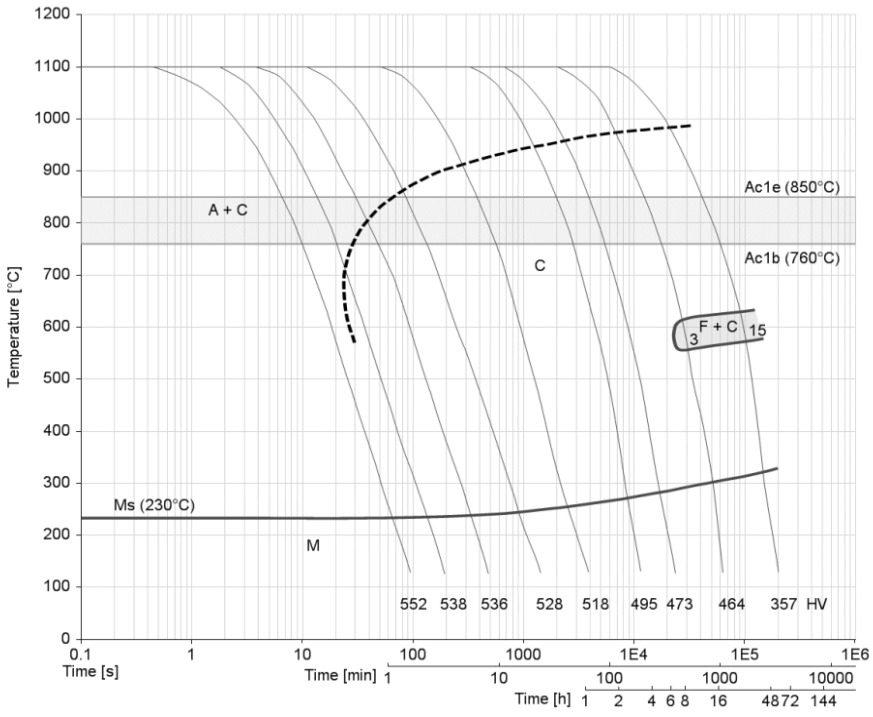

Figure 2-1 Continuous Cooling Transformation (CCT) diagram of 1.4913 X19CrMoNbVN11-1 steel [18]

The Bain model explains the transformation of austenite fcc to martensite bct during quenching, and then to martensite bcc after tempering if the steel possess less than 0.02% of carbon. The major elements of crystallographic theory for martensite formation are shown in Figure 2-2.

2.1.2.1 Mechanism of martensitic transformation: quenching

In quenching, firstly, the iron atoms in the center of base faces in austenite fcc become the martensite bct corner atoms, in which the c parameter of the unit cell is greater than the other two parameters (Figure 2-2). And as far as the cooling is very rapid and the solubility of carbon (0.02%) is greatly exceeded, the carbon atoms are trapped at the z octahedral interstitial sites and occupy a few ribs of the bct. This prevents the carbide pecipitation. With the higher carbon concentration of the martensite, more interstitial sites are filled, and the tetragonality increases.

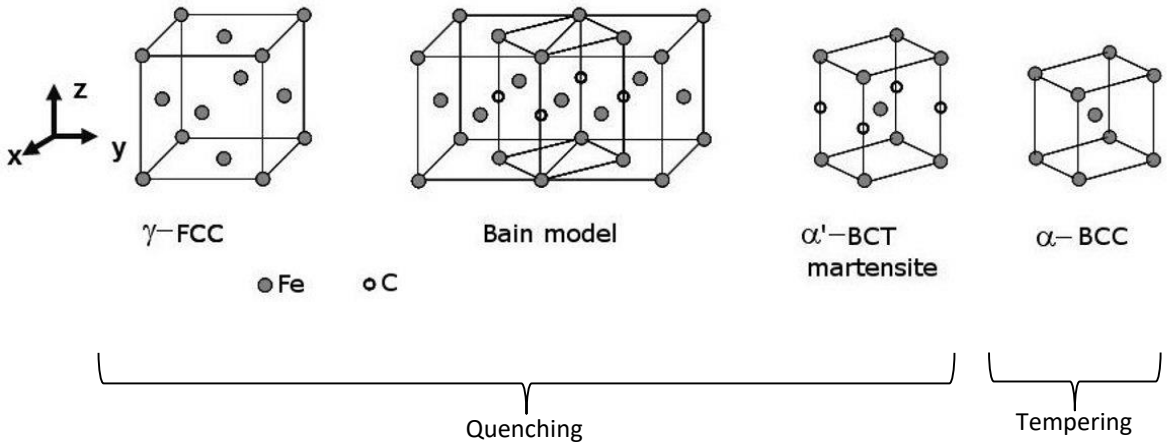

Figure 2-2 Bain model sketch of martensitic transformation [17]

2.1.2.2 Mechanism of martensitic transformation: tempering

After quenching martensitic stainless steels are usually subjected to tempering, i.e. heating of the material and isothermal holding at a temperature lower than the temperature of austenization start, usually between 700°C and 750°C. The tempering is necessary to obtain a good combination of yield strength, ductility and toughness. During tempering the martensite with a low carbon content (less than 0.02%; however some authors don't consider as a limit the solubility percentage of carbon in iron (0.02%) but rather the value 0.2% of carbon content

[19]) transforms from bct crystal structure to bcc structure. The carbon has enough time to diffuse from the octahedral interstices. As a result carbides and other precipitates form if the carbon content is high enough, and the lattice is expanded in x and y directions and contracted in z direction in order to be transformed from bct to bcc. The expansion of x and y axis is about 12% , and the contraction is of a 20% along the z-direction. The nature of the precipitation depends on the chemical composition and the tempering temperature and time. After quenching the martensitic steel may contain few fine cementite precipitates due to a slight tempering at the end of cooling. At approximately 300-350°C of tempering process the hardness reduces because the amount of cementites increased and solid solution impoverished in carbon. At 400-450°C the secondary hardening happens due to the precipitation of M_2X and M_7C_3. Starting from 500°C the $M_{23}C_6$ precipitate at the boundaries [17], [20].

2.1.2.3 Crystallography of martensitic transformation: notion of habit plane and KS relationship

The mechanism of martensitic transformation leads to a particular morphology: lath or plate (needle in cross-section) [21]. The latter is formed if the carbon content is higher than 1%. But the most frequently encountered morphology is the lath morphology [22] characteristic for the steels with less than 0.6% of carbon. A lath grows on the habit plane (Figure 2-3), so for the better comprehension of how it grows the notion of habit plane should be explained.

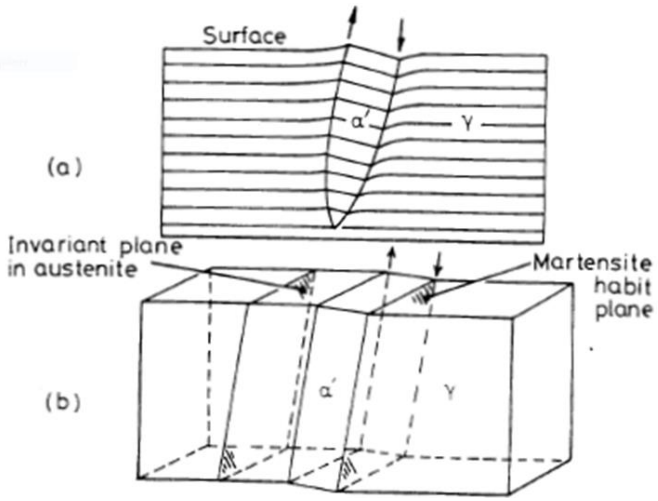

Figure 2-3 The growth of lath on the habit plane [23]

Habit plane is a plane of a parent austenite on which the product martensite grows. The habit plane is usually a close-packed plane of a structure and it is unrotated or invariant and undistorted. This plane has two conservative properties: its orientation is not affected by transformation and the relative positions of the atoms in this plane are not modified (distance and angles). The shear or displacement on planes parallel to the habit plane produces surface tilting that we observe as lath (Figure 2-3). So the shape change on the surface is a result of plane strain. The first variant of lath creates a volume incompatibility, i.e. the laths occupy some restricted volume and the rest of material volume around them cannot follow the same arrangement. As a result around this first variant other variants are created.

The martensitic transformation needs good coupling between parent and product phases. The well-known orientation relationship between parent austenite and product martensite is Kurdjumov-Sachs (KS) relationship:

$$\{111\}\gamma \,//\, \{101\}\alpha$$

$$<110>\gamma \,//\, <111>\alpha$$

In case of this relationship there are four different $\{111\}\gamma$ planes, each plane being parallel to a $\{101\}\alpha$ plane. A $\{111\}\gamma$ plane contains three different $<110>\gamma$ directions and each $<110>\gamma$ direction can be parallel to two different $<111>\alpha$ directions. Therefore there are 24 different KS variants [17], [23].

Other relationships between parent austenite and product martensite known to science are, for example, Nishiyama-Wassermann (NW) relationship [24] or Greninger-Troiano (GT) relationship [25].

2.1.3 Martensitic microstructure

As it was said in the previous subchapter the martensitic transformation leads to a particular microstructure, often called lath microstructure in steels with less than 0.6% of carbon. The speed of lath formation reaches 1100 m/s. The laths form and stop growing when they hit another lath or grain boundary. Therefore one would expect the largest laths to form first [20].

The majority of authors distinguish another 3 units of martensitic microstructure: prior austenite (PA) grain, packet, and block (Figure 2-4).

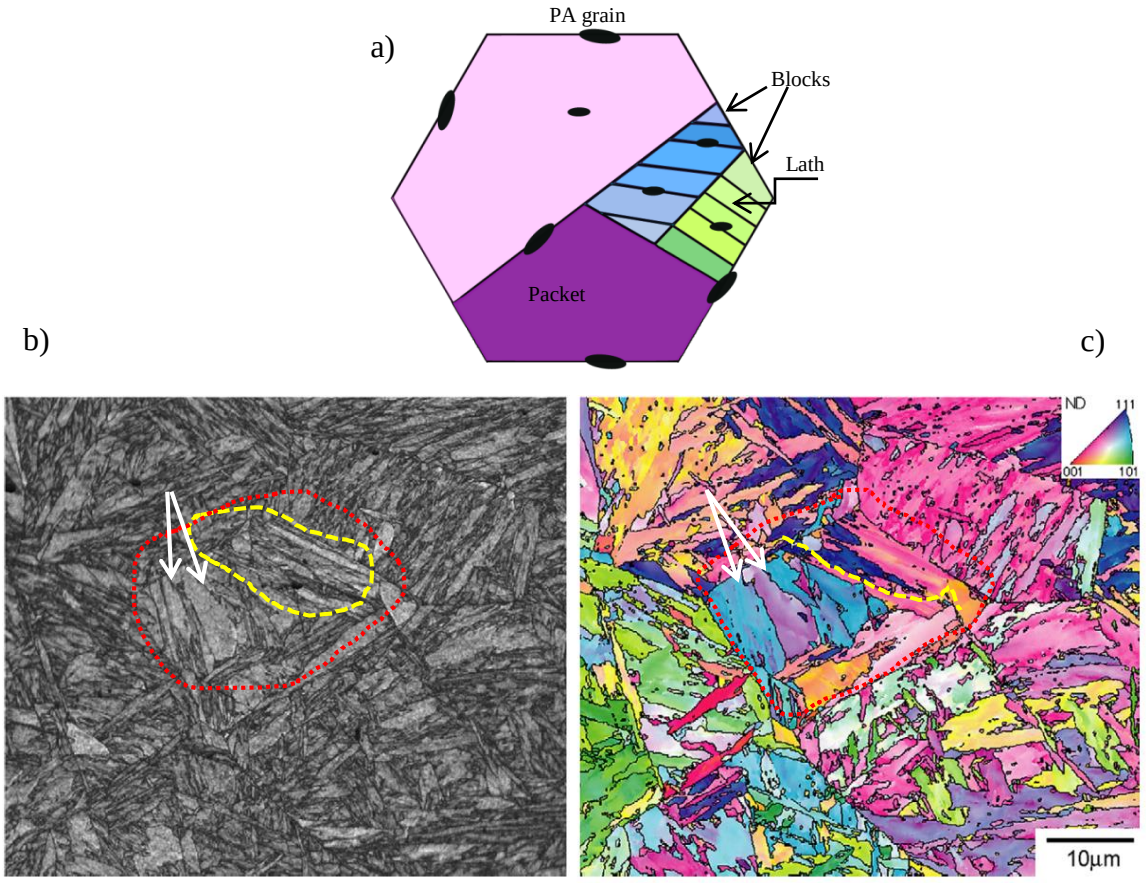

Figure 2-4 a) sketch of the martensitic microstructure; b) optical image of a 0.2%C martensitic microstructure; c) Inverse Pole Figure (IPF) color map of the martensitic microstructure; red dashed line illustrates the PA grain boundary, yellow dashed line – packet boundary; white arrows indicate the blocks [26]

Barrett has called this multiscale microstructure of 9-12 % Cr martensitic steels the *hierarchical* microstructure [27]. Krauss and Marder defined a packet as a group of laths with almost the same habit plane, and block as a group of laths with almost the same orientation [28]. Brachet points out that one block of 9-12 % Cr steels usually contains 5-10 laths weakly disoriented and almost aligned (almost parallel to each other) [22]. Some authors mention sometimes the term subgrain or micrograin [8], [29] along with the term of lath. According to Fournier a subgrain generally means a microstructural submicronic zone able to be strongly or weakly disoriented relatively each other. Also this author indicates that the laths after a tempering may be defined

as an alignment of micrograins [8]. Marmy and Kruml differ the laths from subgrains by their (laths') elongated form appearing on microscopic images [30] (Figure 2-5).

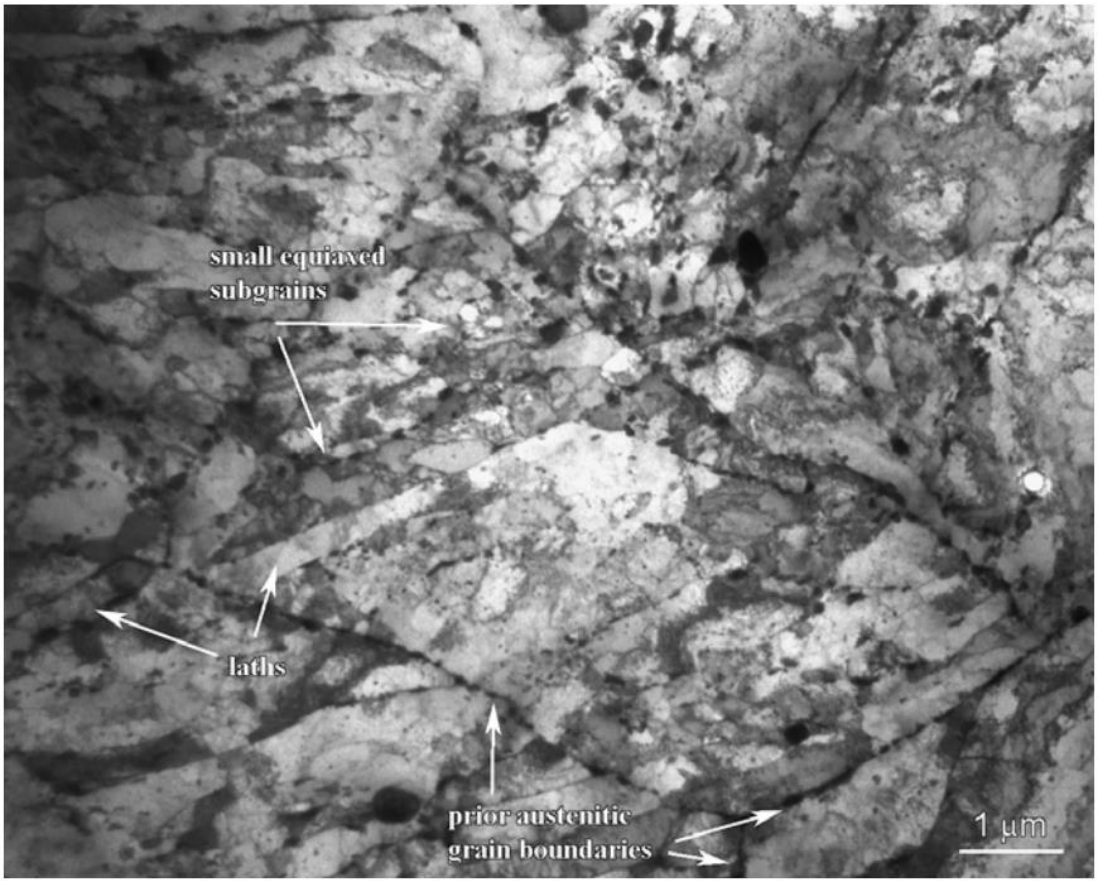

Figure 2-5 Microstructure of as received EUROFER 97 (9Cr-1W-0.47Mn-0.2V-0.12C) steel. Prior austenitic grains are decorated by lines of carbides. Elongated martensitic laths are not frequent. The structure is composed mainly of sub micrometric equiaxed subgrains [30]

At the same time some authors such as Krauss [31] suppose that probably each lath is subdivided into again smaller units, which are not visible because the etchant is not able to selectively attack the boundaries and/or because the microscope cannot resolve the closely spaced boundaries.

After reviewing the different sources discussed above, the next definitions of each microstructural unit can be deducted. A lath is the smallest unit of microstructure. It is usually very thin and long on two-dimensional microscopic images. Its length can reach 10 µm. The laths are gathered in blocks, where they share the same variant. Blocks are quasi-parallel between each other and form packets. The laths in a packet share the same habit plane.

The mechanical properties of martensitic steels are dependent on the sizes of the microstructural units of material. The finer the microstructure is, the better properties the material has. The size is dependent on the temperature and duration of austenization. The lower the temperature is, the smaller the size of packet and block is. The longer the austenization duration is, the bigger the size of PA grains, packets and blocks is. The size of lath is independent on the quenching temperature [32]. Moreover, the knowledge of size of each microstructural unit is crucial because the dimensions of each unit are integral in the recognition of each microstructural member during microscopic observations.

2.1.3.1 Review of microstructural unit sizes defined by some authors

Figure 2-6 shows the distribution of lath widths received by measurements from electron micrographs obtained from thin foils and replicas of polished and etched specimens of Fe-0.2C steel. The important result shown in this figure is that most of laths have widths smaller than 0.5 µm, which is the resolution limit of light microscope, and therefore the lath cannot possibly be revealed by light metallography. However, rarely there are some laths with widths up to almost 2 µm [17].

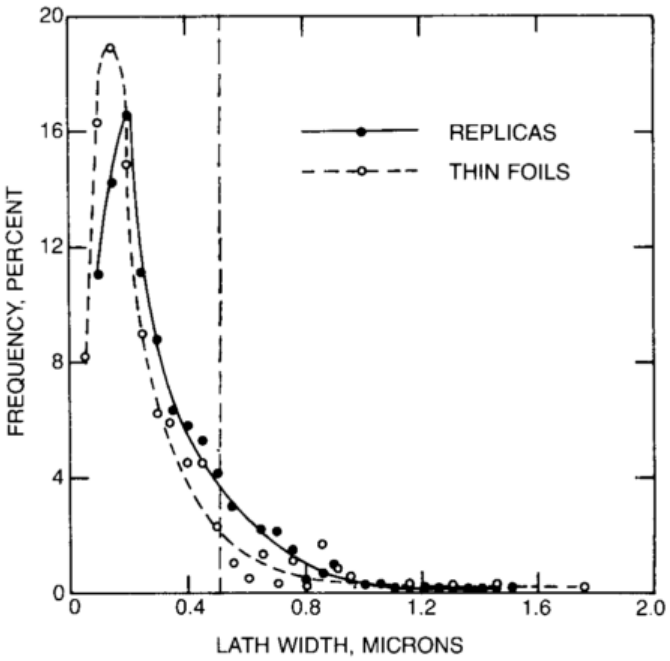

Figure 2-6 Distribution of lath widths in Fe-0.2C martensite. Vertical dashed line shows the limit of the resolution of light microscope [17]

Sauzay *et al*. [29] have defined some sizes of 9Cr1Mo steel when they studied the creep deformation. The width of block was approximately 4 µm, the thickness of lath was about 0.7 µm. The laths were elongated inside the blocks. One more microstructure unit was mentioned by them – subgrain which was equiaxed along the lath and had a diameter in general equal to 0.7 µm.

Fournier *et al.* [33] reported the average grain size ranging from 10 to 60 µm in his study of fatigue-creep of 9-12%Cr steels.

Batista *et al*. [15] describing as received microstructure of ferritic-martensitic AISI 410 containing 13% of chromium said that it consists of a tempered martensitic lath structure composed of small subgrains of about 0.5 µm diameter with an essential dislocation structure (Figure 2-7a).

Endo *et al*. [34] observing 9Cr-1Mo steel in TEM noticed a randomly oriented lath structure with average lath width 0.54 µm of as received specimen (Figure 2-7b). Besides, this value of lath width was confirmed later by authors' measurements with AFM.

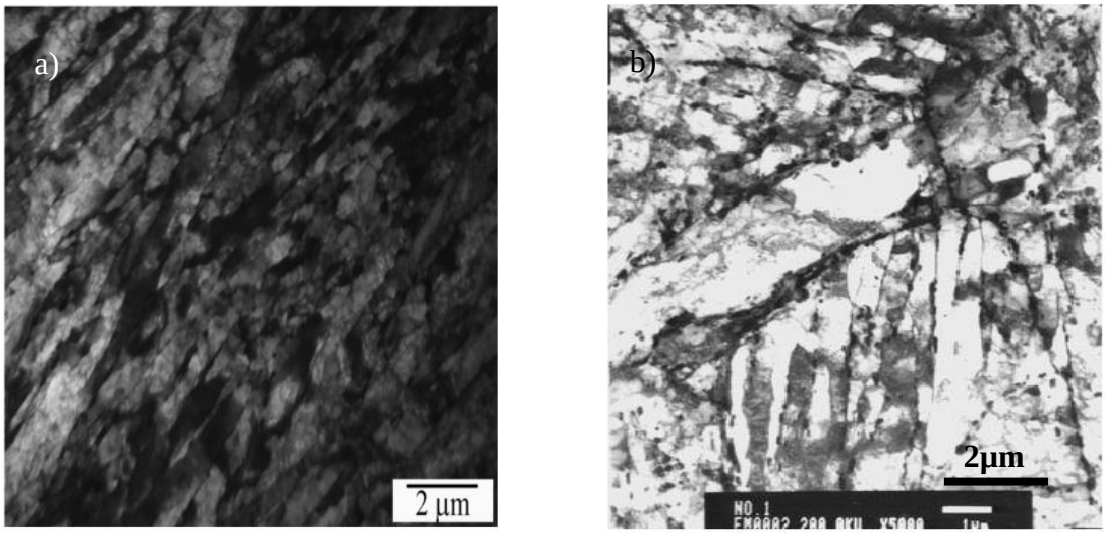

Figure 2-7 TEM images showing the microstructure of AISI 410 steel (a) [15] and of Mod.9Cr-1Mo steel (b) [34]

Another authors working a lot on the martensitic microstructures is Morito *et al.* [35], [36]. They have conducted significant experiments utilizing TEM, SEM and EBSD techniques in order to characterize the martensitic structures, their sizes, orientation relations and

distributions. In the work of Morito *et al*. [37] the crystallography, microstructure and mechanical properties of as-quenched martensite of Fe–0.2C– Mn(–V) alloys were studied. The authors reported the size of PA grain between 2 µm and 370 µm (Figure 2-8). The prior austenite grains whose size was larger than 28 µm were subdivided into several packets. When the prior austenite grain size was about 2 µm, mainly one packet appeared inside it.

Among the reviewed papers it seems that all authors observed the laths with sizes ranging from 0.2 µm to 0.7 µm in average. However, the PA grain diameters may vary from 2 µm up to 370 µm. As for the block and packet sizes, a little of authors performed direct measurements of their sizes. Nonetheless, there are a few studies that have reported theoretical relationships between PA grain size, packet and block sizes. Thus, Morito *et al.* [35], [37], [38] performed an important contribution in the development of size relationships between members of martensitic microstructure, which will be discussed in the next paragraph.

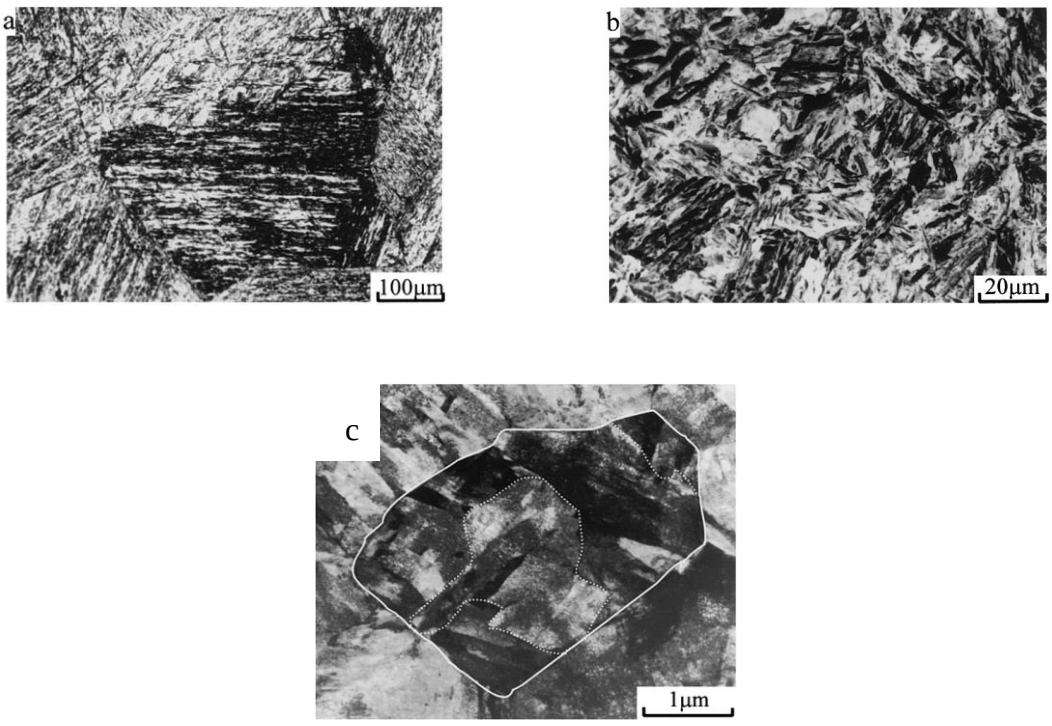

Figure 2-8 OM images of lath martensite structure in the Fe-0.2C-2Mn steel with prior austenite grain size 370 µm (a) and 28 µm (b); (c) TEM image of lath microstructure of Fe-0.2C-1.5Mn-0.15V with prior austenite grain size 2.3 µm; white solid line and dashed line indicate the prior austenite grain boundary and packet boundary respectively [37]

2.1.3.2 Relationship between units of microstructure and their sizes

Maki *et al*. affirmed in their work [39] that both the block width and the packet size are proportional to the PA grain size. Later, Morito together with his coauthors [37] proposed a relationship between prior austenite grain size, packet size and block width, generated from the relationships of Maki and supported by his own observations. The relationships are illustrated in Figure 2-9. The packet size d (µm) decreases proportionally to the PA grain size D (µm) decrease according to the formula d=0.34D+5.34 for the grains larger than 10µm (see the solid line in Figure 2-9). However the width of blocks is seemed to be independent on the PA grain size (see the open marks in Figure 2-9) [37].

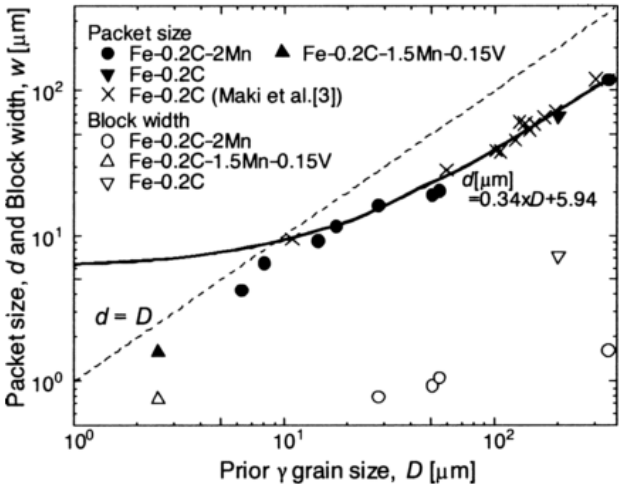

Figure 2-9 Relationship between prior austenite grain size and packet size in some low carbon steels [37]

Nonetheless, a year later, Morito *et al*. published a work where they reported a linear relationship with a larger slope between block width d_b and prior austenite grain size d_g for grains with d_g<200 µm in the case of Fe-0.2C; and continuous linear dependence between PA grain size and block width for Fe-0.2C-2Mn (Figure 2-10) [38].

Hatem and Zikry have published in [40] the schematic representation of the multiscale lath martensite microstructure and its dimensions (Figure 2-11) that they used for the simulation, built on the multiple-slip dislocation-density based crystal plasticity formulation, to investigate the large strain inelastic behaviour of martensitic steel under dynamic loadings. They developed their sketch, based on the works of Morito *et al.* [35], [37], [38], [41], [42]. The authors

mentioned again in the article the statement of Morito *et al.* [37] that the packet sizes can be approximated as a linear function of PA grain size, and can vary between 0.7 and 150 µm. Their drawing concludes well the diversity and dispersion of dimensions of each unit of the hierarchical martensitic structure as well as the linear dependence between PA grains, packets and blocks.

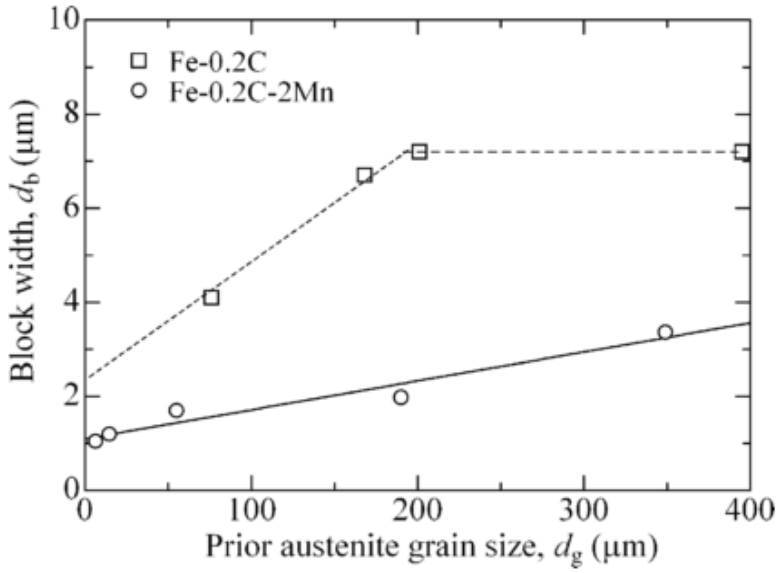

Figure 2-10 Relationship between the prior austenite grain size and the block width in the quenched martensite of Fe-0.2C and Fe-0.2C-2Mn alloys [38]

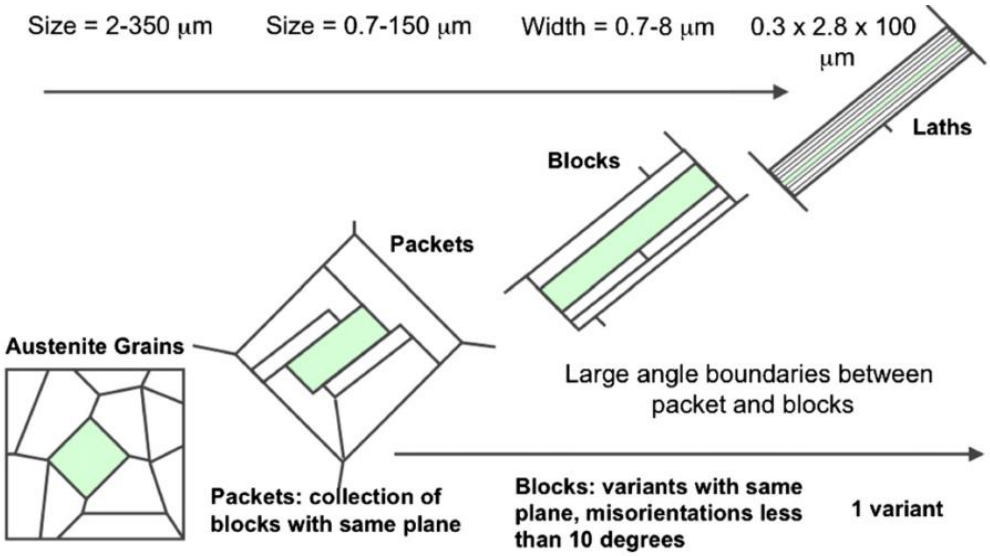

Figure 2-11 Martensite microstructure members and its sizes for some grades of steels [40]

2.1.3.3 Disorientation relationships of different interfaces in PA grain

The majority of authors, working on the martensitic steels, state in their articles that the PA grains, packets and blocks have High Angle Boundaries (HAB), while laths possess Low Angle Boundaries (LAB) [8], [9], [16], [22], [26], [35], [43]–[45]. In the next paragraph some of those authors who performed the measurements of disorientation angles will be reviewed.

The morphology and crystallography of two lath-structured Mn-containing steels and one 18Ni-8Co-5Mo maraging steel were studied in [41] using Electron BackScatter Diffraction (EBSD) analysis. For all three steels the misorientation angles between laths inside the blocks are typically less than 3°, although larger misorientations up to 4° can be observed. Based on this general observation, the misorientation angles across lath boundaries were determined in steel #2 (3 % Mn) by Kikuchi diffraction analysis in a TEM. The frequency plot in Figure 2-12 shows that most of the lath boundaries have the misorientation angles less than 3°. It has also been observed that boundaries with relatively large misorientation angles (>2°) often correspond to lath boundaries that separate laths or groups of laths with alternating contrast. These experimental observations corresponded to the previous results obtained for four different low carbon steels [35]. Therefore it indicates that the observed morphological and crystallographic features are universal for low carbon lath martensitic steels and that the effect of substitutional alloying elements on the morphology and crystallography is negligible [41].

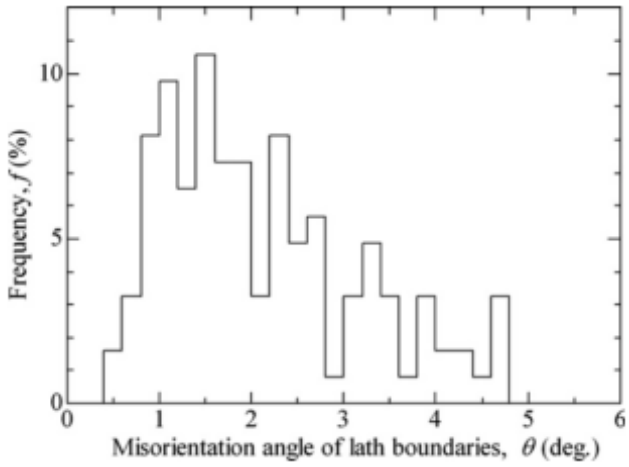

Figure 2-12 Disorientation angle distribution of lath boundaries measured by TEM Kikuchi pattern analysis in steel #2 [36]

Kitahara *et al*. [26] published a rich work on the disorientation angles in martensitic microstructure of low carbon 0.2%C steel in 2006. They showed that the laths can be grouped in sub-blocks – two particular K-S variant groups. There is a specific rule for combining two variants, which is a rotation axis <011> and an angle 10.53°. In the Figure 2-13 a PA grain can be seen marked by white boundary. Inside the grain different packet boundaries are marked by red. And in each packet the specific combinations of two variants are indicated by capital letter V and correspondent number of variant. Moreover, the figure shows that there are no HAB boundaries within each sub-block of two specific variants.

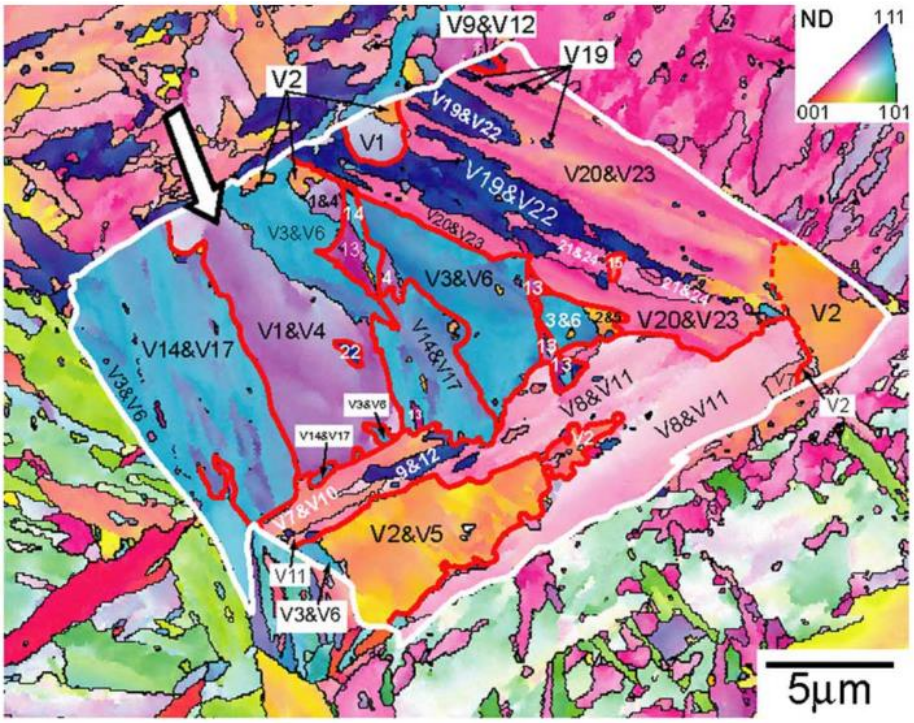

Figure 2-13 IPF color map of the lath martensite structure of 0.2%C steel. The red and white lines indicate the packet and PA grain boundaries respectively. The black boundaries are drawn when the disorientation angle is greater than 10°. The symbols and numbers indicate the variant numbers [26]

Fournier [8] performed EBSD measurements of disorientation angles in his Ph.D. thesis on fatigue-creep of 9%Cr martensitic steel as well. He showed that the disorientation angles inside the blocks, i.e. between laths and subgrains are LAB and they are smaller than 5°. However, the disorientation angles between blocks are HAB.

Batista *et al*. [46] reported the average misorientation angle of 0.8° between neighboring laths in EUROFER 97.

An interesting fact about the boundary character in martensitic steels was mentioned by Morsdorf *et al.* [44]: the PA boundary plane is curved because they are not determined by the austenite-martensite orientation relationship, while the martensite boundaries are rather straight because they are submitted to the strict orientation relationship and due to the minimization of accommodation strain energy during the martensitic transformation.

To sum up, most of authors agree that PA grains, packets and blocks have HAB, while laths have LAB usually less than 3°.

2.1.4 Conclusions

The principles of martensitic transformation leading to a particular lath structure were considered in this section. The laths are always grouped in blocks according to their variant, and into packets according to their habit plane. Some studies on the definition of sizes and disorientations of PA grains, packets, blocks and laths were reviewed in the last part of section. And it appears that the lath widths are less than 1 μm; while packet and block sizes are linearly dependent on the PA grain size. As for the angle disorientations, the PA grain, packet and block have HAB, and lath has LAB.

2.2 Fatigue

2.2.1 What is fatigue?

Fatigue is a modification of material microstructure as a result of repetitive (cyclic) mechanical loading which can lead to the deterioration of material. It is one of the primary reasons for the failure of structural components. The life in fatigue is measured by number of cycles to failure and it depends on many factors such as applied stress and deformation, environment and temperature and metallurgical microstructure.

2.2.2 Fatigue stages

The damage process under repeated loading can be divided into three stages:

1. Fatigue crack initiation: during a large number of cycles, the deformation relief develops at the external surface on the microscopic level and develops until microscopic cracks or short cracks are formed.
2. Fatigue crack propagation: the coalescence of short cracks leads to the formation of long crack or macroscopic crack, which grows for each cycle until it reaches a critical length.
3. Failure: the cracked component breaks because it can no longer sustain the peak load.

The last stages of fatigue process are usually studied within the fracture mechanics discipline, while the first stage is more considered within the material science. The main purpose of fatigue engineers is to be able to detect the crack before it reaches its critical size, and also to estimate the damage in the first stage, i.e. to control the quantity of accommodated damage before the crack forms.

2.2.3 Fatigue modes

Based on the number of load cycles needed to produce a crack, it is usual to make a distinction between low cycle fatigue (LCF), high cycle fatigue (HCF) and very high cycle fatigue (VHCF). The Wöhler curve (Figure 2-14), representing the stress change as a function of number of cycles to failure, allows determining the three domains of fatigue. This type of curve is sometimes called S-N curve and it is a result of experiments on flat specimens without geometrical defects. The limit between the first two domains LCF and HCF is generally admitted to be 10^5 cycles, while between HCF and VHCF domains is of the order 10^8 cycles. In the case of HCF, the stresses are low enough (usually under yield limit) and the stress-strain relation can be considered elastic. For LCF, meanwhile, the applied stresses usually exceed the yield limit of material, and the macroscopic deformation is plastic. In HCF tests the constant stress is usually imposed, while in LCF the engineers are more interested in the stress amplitude evolution under strain control as well as in the hysteresis loops (σ-ε) and number of cycles to failure (lifetime).

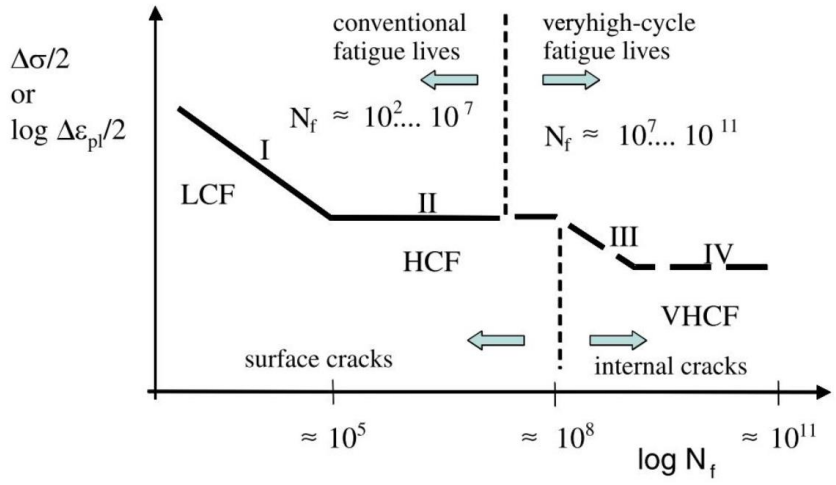

Figure 2-14 Schematic representation of stress amplitude and plastic deformation evolution as a function of number of cycles to failure, determining the different fatigue domains [47]

In the present work only LCF loading is considered.

2.2.4 LCF variables

In the real-life conditions, a component is subjected to load cycles which do not have necessarily the same amplitude. Since in general a component has a complex shape with variable dimensions, the stress and strain vary from one spot to another one. Laboratory tests aiming at understanding fatigue mechanism or at assessing reference fatigue curves as in Figure 2-14 are controlled by specific variables such as stress or strain. In the case of LCF the control variable is a strain, generally total strain and sometimes plastic strain. A triangular waveform is employed in order to have a constant strain rate. A loading cycle is defined as the duration from one peak in the studied variable to the next peak (Figure 2-15). The strain varies between a maximum strain ε_{max}, and a minimum strain ε_{min} during a loading cycle (Figure 2-15). In the field of fatigue the variation in strain is often defined using the strain amplitude ε_a, which is a half difference of maximum and minimum strains, and the mean strain ε_m, which is the arithmetic average between maximum and minimum strains. The strain range $\Delta\varepsilon$ represents difference between maximum and minimum strain. R-value is frequently used to describe a loading cycle too and is a ratio of minimum strain to maximum one. R=-1 means a maximum strain is equal to a minimum strain, and customary this mode of loading is called fully-reversed fatigue loading. When R=0 (minimum strain is equal to 0), then the mode of loading is pulsating

tension. Finally, more important than the frequency is the strain rate which is kept constant for tests campaign. This means that for a given tests campaign where the strain range is changed, the frequency also changes.

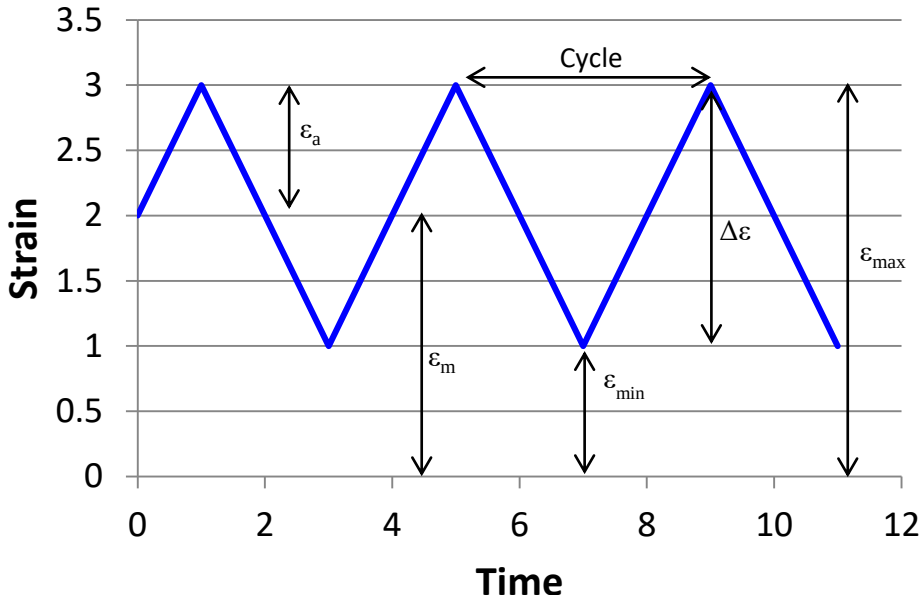

Figure 2-15 The basic loading signal in LCF revealing the commonly used variables in the science of LCF

2.2.5 Data recording during LCF test

In LCF the applied stresses exceed the elastic limit of material. Since LCF test is performed under strain control, then the hysteresis loops and the number of cycles to failure are recorded.

Hysteresis loop represents the stress evolution as a function of strain in each cycle. The stress amplitude $\Delta\sigma/2$, the total strain variation $\Delta\varepsilon_t$, plastic strain variation $\Delta\varepsilon_p$ and elastic strain variation $\Delta\varepsilon_e$ are obtained from the loop as shown in Figure 2-16. To show the different phases of loading or to compare the different tests, the stress amplitude is usually plotted as a function of number of cycles (Figure 2-17).The stress evolution is normally characterized by 3 steps:

1. Cyclic accommodation. At the beginning of strain-controlled LCF tests the stresses usually vary a lot. If the stress decreases then the phenomenon of cyclic softening takes place, which means that a lower stress should be applied in order to reach the imposed

strain (Figure 2-17, see the red arrow). Otherwise, the phenomenon of cyclic hardening happens.

2. Stabilization (Figure 2-17, green arrow). In this period the hysteresis loop does not evolve anymore, or its evolution is very slight. This phase represents generally the major part of the life, and often the hysteresis loop derived from the period of stabilization is considered as illustrative of the fatigue behaviour of material.
3. At the end of life the crack propagation in the material implies the important change of the hysteresis loop geometry and the drastic decrease of stress amplitude (Figure 2-17, black arrow). The lifetime or number of cycles to failure is usually defined as the number of cycles at which 25% of maximum tension stress relatively to the stabilized stress is reduced.

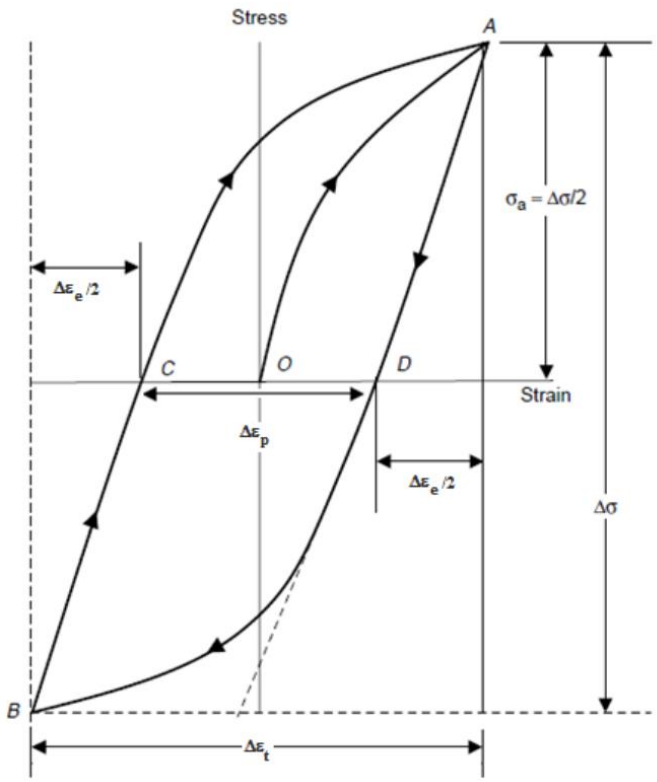

Figure 2-16 Hysteresis loop of stress versus strain

It must be mentioned here that some materials exhibit a more complex response such as cyclic hardening followed by softening and then by second hardening [48].

The resistance curve is further obtained from a set of fatigue tests performed at different strains. In LCF, it is usually called “Manson-Coffin curve” and it represents the change of plastic strain amplitude as a function of number of cycles to failure (Figure 2-18).

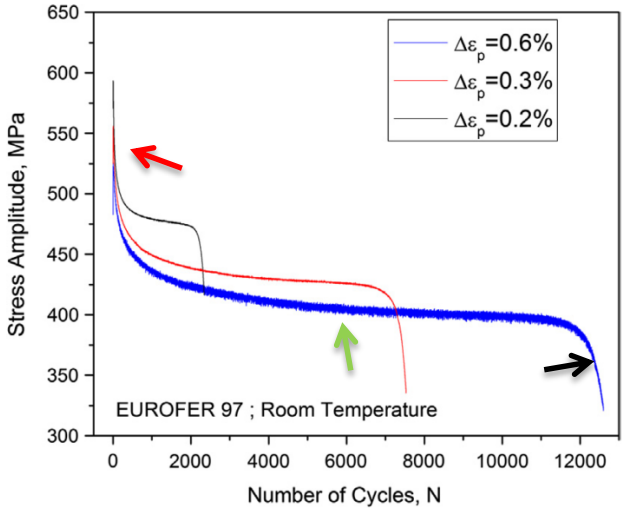

Figure 2-17 Evolution of stress amplitude as a function of number of cycles for 9%Cr steel EUROFER 97: red arrow points out the softening phase, green arrow – stabilization phase, black arrow - failure [46]

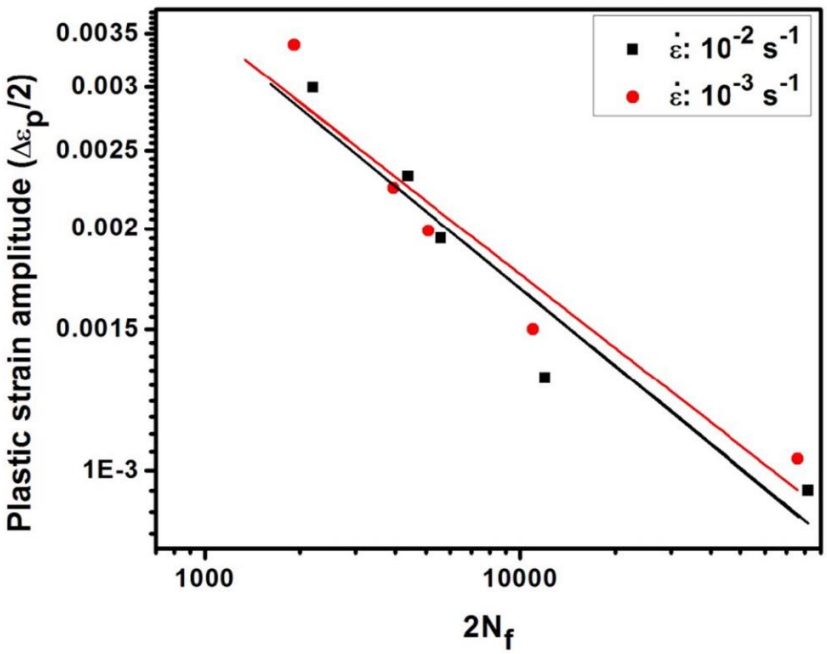

Figure 2-18 Manson-Coffin curve of modified 9Cr-1Mo steel at 600°C [49]

2.3 Fatigue deformation

The very first paper paying attention to the crack initiation in fatigue loading is the article of Sir James Alfred Ewing demonstrating the origin of fatigue failure in microscopic cracks in 1903 [50]. In the fifties such scientists as Forsyth and Stubbington studied the fatigue crack initiation in aluminium [51], [52]. They supposed that the "slip-band extrusions" may be related to the material cracking. Hull, in its turn, believed that the cracks nucleated in intrusions in fatigued copper [53]. Later King [54] reported some cracks occurring in the persistent slip bands in polycrystalline aluminium. The mentioned above terms (extrusion, intrusion and persistent slip band) leading finally to the metal cracking are believed to be the consequence of dislocation activity and resultant particular dislocation reorganization in the bulk of material. Eventually the scientists developed the models trying to link the surface deformation to the bulk activity. The next section is devoted to the review of existent theory and observations on the issue.

2.3.1 Low energy dislocation structures produced by cyclic deformation in the bulk of metals

In fatigue the dislocations move inside the material and interact. The interactions create an energy excess which will be reduced once the dislocations will have arranged in low energy configurations. Some of them will be defined below and are typical of easy cross slip materials.

At low strain level, a dipolar structure or matrix (Figure 2-19a) is formed when a single slip system enables the accommodation of the deformation. The dipolar structure consists of channels with low density of mobile screw dislocations and veins of high density of edge dislocations. The deformation occurs by the quasi-reversible movement of screw dislocations in the channels.

At medium strains, even if one slip system is activated, the matrix structure becomes unstable, and the veins transform into the wall structure (Figure 2-19b). When a second glide system is activated the labyrinth structure may be formed (Figure 2-19c).

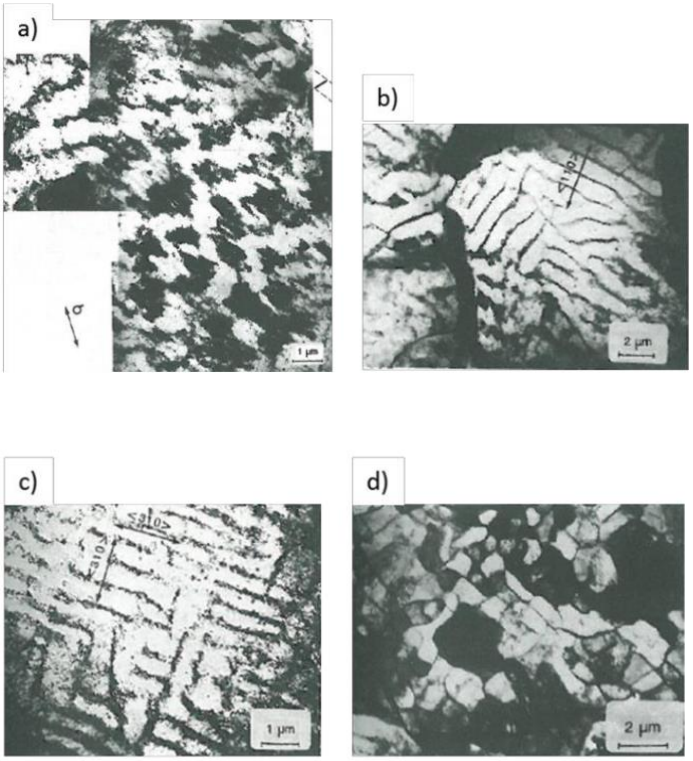

Figure 2-19 Some low energy dislocation configurations observed in a ferritic steel: a) matrix structure; b) walls; c) labyrinth; d) cells [55]

Locally the irreversible slip processes become confined into the so called persistent slip band (PSB) that exhibits the ladder-like structure (Figure 2-20). As a result the composite structure "matrix+PSB" is obtained. The adjective persistent is used because the slip bands emerge at specimen surface and reappear in the same location after the test was interrupted, the surface was polished and the test was repeated. The ladder-like structure consists of walls and channels. In the channels the dislocations are mainly of screw character, while in the walls they are of edge character. The conditions of steady state require that the dislocation densities in channels and walls are maintained constant. It is achieved by an equilibrium between the multiplication and annihilation of both edge and screw dislocations. After annihilation the edge-dislocation segments bowing out of the walls produce the screw dislocations, and those screw dislocations generate the edge dislocations by gliding. In this way the continuous flux of both types of dislocations is maintained. Without annihilation of dislocations the irreversibility and randomness of glide could not be possible. Moreover, the annihilation processes bring to the creation of point defects [56].

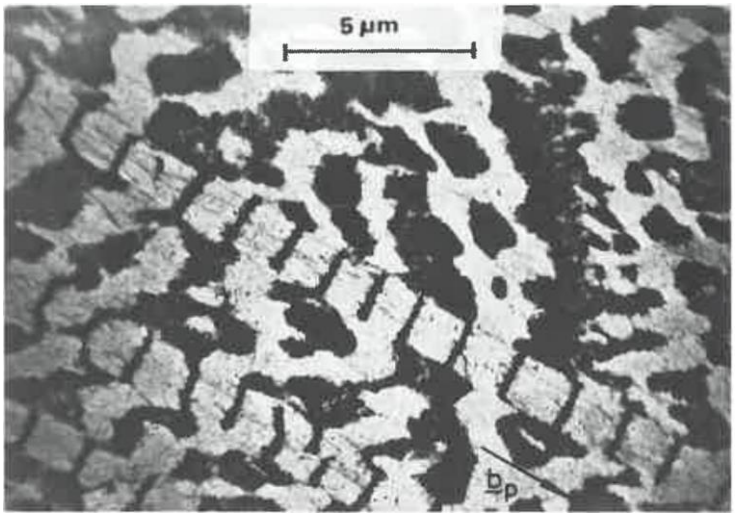

Figure 2-20 The ladder-like structure of PSB in copper crystal [57]

At high strain levels, several glide systems are activated. Dislocation cells are formed due to this multiple gliding (Figure 2-19d). Cells may accommodate plasticity by the dislocation glide from one cell wall to another. The dislocation cell configuration is known to possess the lowest energy. This type of dislocation arrangement is the most frequently observed in martensitic steels.

The dislocation cells represent a two-dimensional honeycomb-like structure with regions of high dislocation density (dislocation walls) and low dislocation density (cell interior or region in between the walls) [58]. Laird considered that the walls of cells observed in copper are constructed of the edge dislocation dipoles [59]. The formation of cells suggests that the migration and/or annihilation of boundaries occur during cycling. As far as the interior of cells is softer than the wall and with cycling the volume fraction of cells grows up, the volume fraction of soft regions grows up too and this leads to softening effect [60].

2.3.2 Fatigue behaviour of 9-12% Cr martensitic steels and resulting microstructural evolutions

One of the features of 9-12% Cr steels and more generally of many martensitic steels lies in the fact that under cyclic loading these materials soften (Figure 2-17). For fatigue tests controlled by deformation it results in a continuous decrease of maximum stress reached at each cycle. In general, regardless of the alloy or temperature, or level of deformation, the cyclic behaviour is

characterized by the first rapid softening phase (for 10 to 30% of the life fraction) followed by longer phase in which the softening kinetics is slower and almost constant. Finally when macroscopic cracks propagate, the stress drops sharply. A notable point is that, as slow as it is, softening is continuous, which means that a cycle called "stabilized" is never reached [8], [46].

As far as the 9-12%Cr martensitic steels are usually used in the conditions of high temperature, the majority of studies are performed at elevated temperatures in order to approach the real conditions. Thus, Golanski and Mrozinski [61], for example, studying the cyclic deformation of GP91 (GX12CrMoVNbN9-1, where G designates that the steel is cast) cast steel at 600°C reported the continuous softening of material too. The scientists explained the phenomenon by disappearance of lath microstructure (Figure 2-21) and formation of dislocation cells which coalesced together and formed the large subgrains. The changes in dislocation structure were intensified by the elevated temperature that caused a decrease in the stress of lattice and generated the growth of concentration of vacancies, which helped the dislocations to pass round the obstacles by the dislocation climb mechanism.

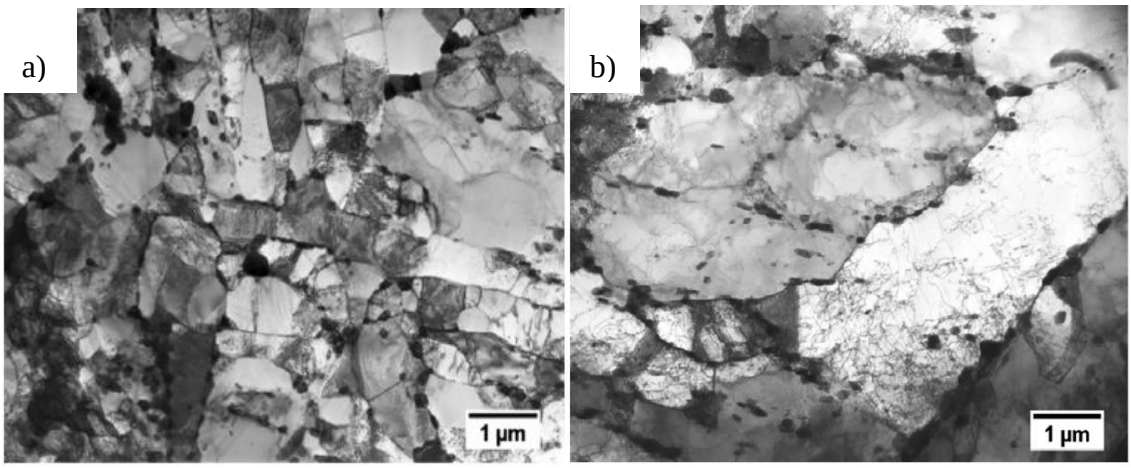

Figure 2-21 Microstructure of GP91 cast steel in the as received condition (a) and after LCF at strain amplitude ε_{ac}=0.25% and at 600°C (b) [61]

Fournier [62] studied the LCF deformation of P91 (X10CrMoVNb9-1) steel at 550°C and in air. After test he noticed the partial recovery of lath microstructure from the observations in TEM (Figure 2-22).

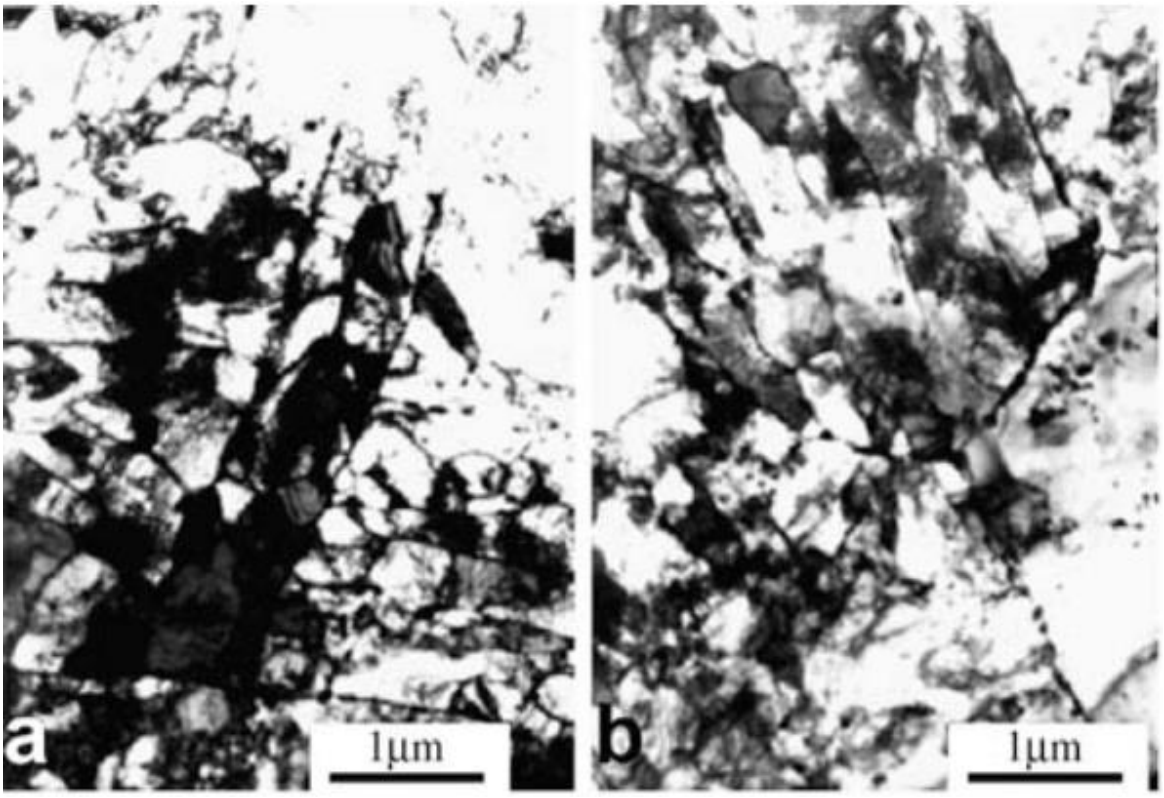

Figure 2-22 Microstructure of P91 steel in the as received condition (a) and after LCF loading at $\Delta\varepsilon_t$=0.3% and at 550°C (b) [62]

However, it turns up that the lath microstructure disappears gradually not only in the conditions of elevated temperature. Golanski and Mrozinski [61] observed the cyclic deformation of GP91 steel at high temperatures as well as at room temperature. For all five levels of controlled total strain amplitude ε_{ac} = 0.25%; 0.3%; 0.35%; 0.5% and 0.6% the authors have also observed the cyclic softening without a stabilization period. In comparison with the as-received condition (Figure 2-21a), a low cycle fatigue at room temperature (Figure 2-23) contributed to the disappearance of lath microstructure of tempered martensite and the formation of elongated dislocation cells. It also led to the decrease of dislocation density as a result of dislocation rearrangement and annihilation in the boundaries of grains and subgrains and shaping of the dislocation cell microstructure. Moreover, in the microstructure of the examined GP91 cast steel after LCF at room temperature, some dense dislocation tangles were observed, which had a wall shape and surrounded the microareas (dislocation cells) with almost no dislocations inside them. This process influenced also the slight increase in the mean diameter of $M_{23}C_6$ carbides and the extent of this increase depended on the strain amplitude [63]. The intensity of

changes in the dislocation microstructure was higher for the strain amplitude ε_{ac} = 0.6%. Thus, according to the authors the lath structure manifests the recovery even in the conditions of RT.

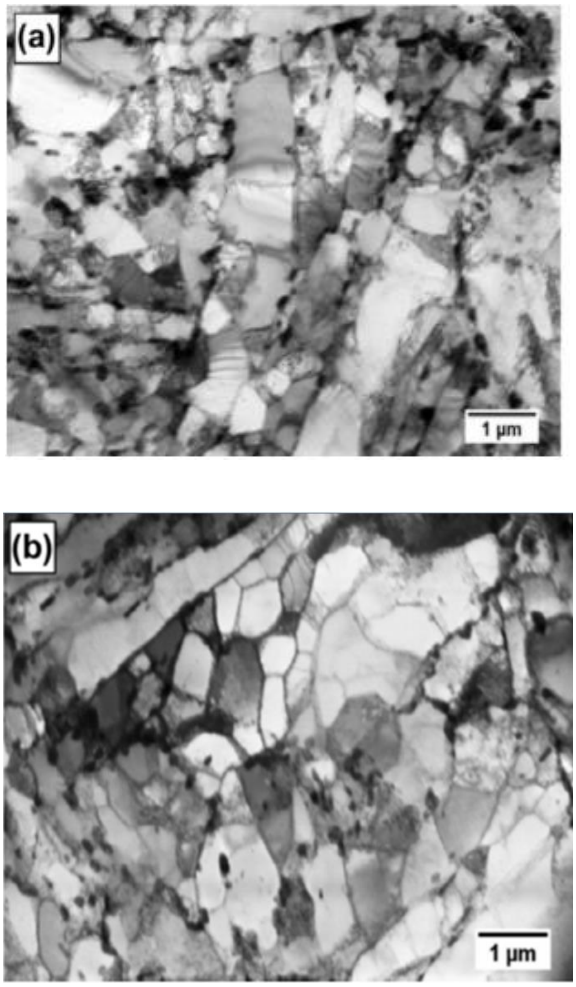

Figure 2-23 Microstructure of GP91 cast steel after LCF at room temperature (RT) at various levels of strain amplitude: a) ε_{ac} = 0.25%; b) ε_{ac} = 0.6%. The initial microstructure of steel is in Figure 2-21a [63]

Contrary to Fournier and Batista *et al*. observations [8], [46], Giordana and his coauthors [64] performed low cycle fatigue tests using three different plastic strain ranges $\Delta\varepsilon_p$ = 0.2%, 0.3% and 0.6% at room temperature on EUROFER 97 (9%Cr) steel and found out that the material hardens a little bit at the beginning of loading and only after that it softens. A pronounced cyclic softening (Figure 2-24) was accompanied by microstructural changes, such as the decrease of dislocation density inside blocks and the disappearance of low-angle boundaries. The major effect produced by cycling at room temperature was a "*cleaning out*" of dislocations inside subgrains (Figure 2-25).

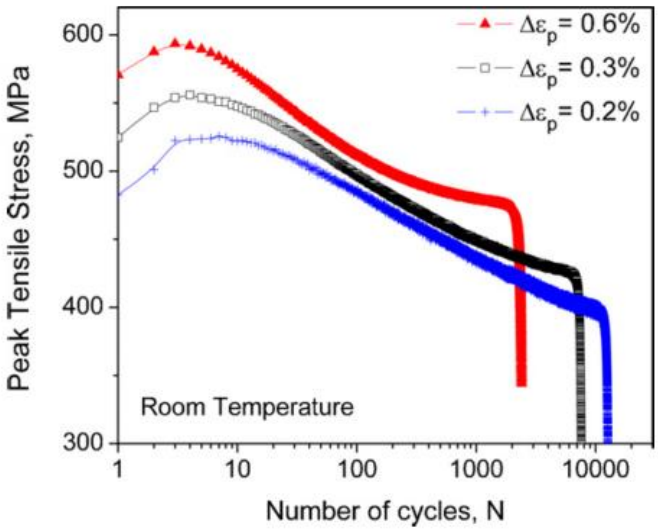

Figure 2-24 Cyclic behaviour curves of EUROFER 97 steel obtained at room temperature and at three different plastic strain ranges [64]

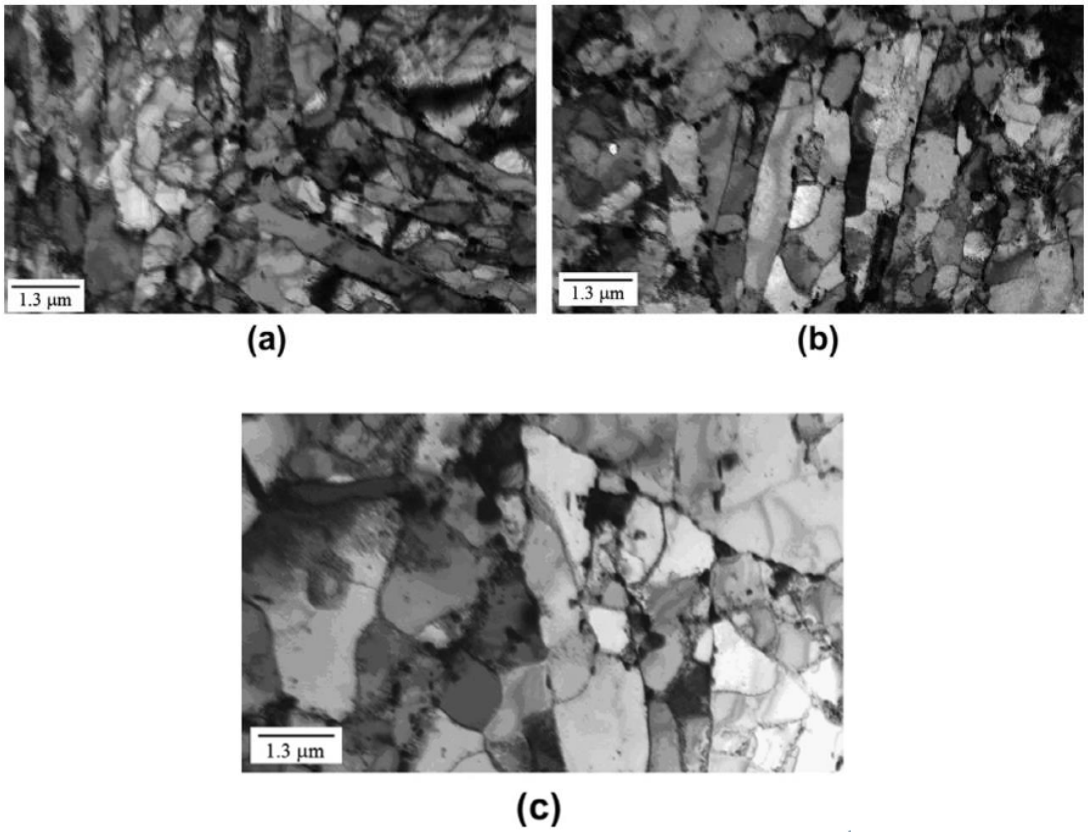

Figure 2-25 Characteristic microstructure of EUROFER 97 samples fatigued at $\Delta\varepsilon_{pl}$=0.2%, at RT: a) 10 cycles, b) 500 cycles, c) 11000 cycles [9]

Batista *et al*. [15] analyzed the fatigue behaviour of AISI 410 steel containing 13 % of chromium at a plastic strain range $\Delta\varepsilon_p$ = 0.2 % and strain rate $\dot{\varepsilon}$=0.003 s^{-1} at room temperature. The steel showed the softening after the first few cycles continuing up to failure. Figure 2-26 illustrates this behaviour in comparison with the modified EUROFER97.

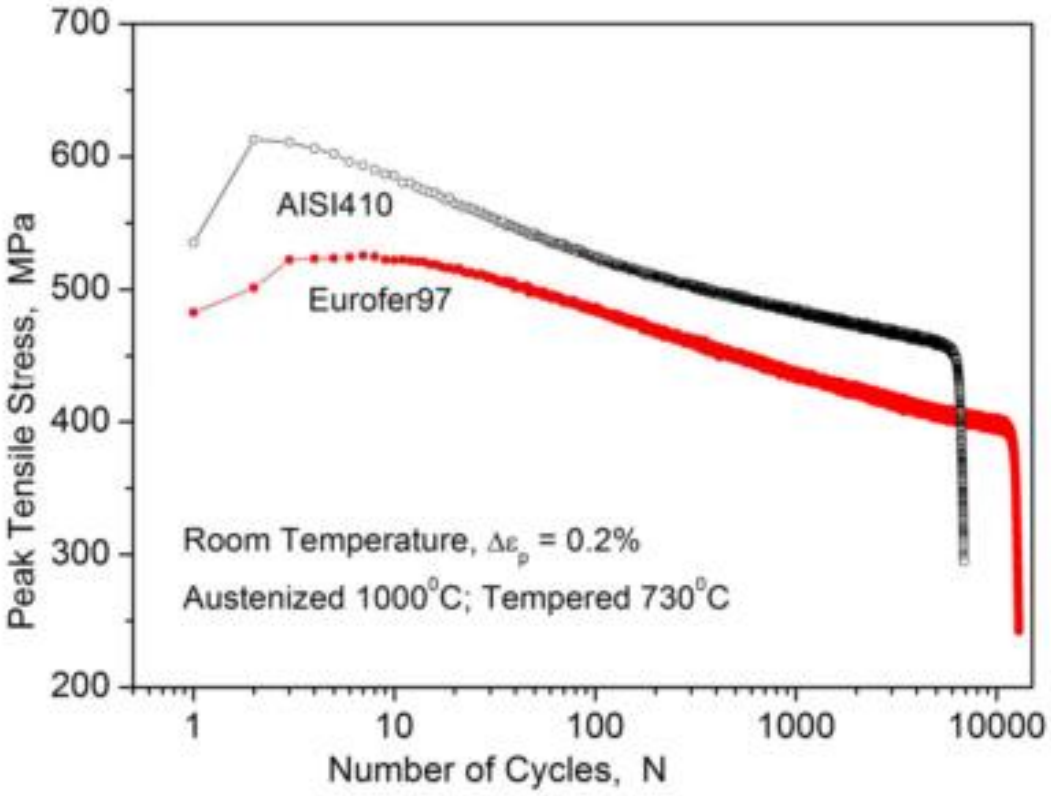

Figure 2-26 Cyclic behaviour of AISI 410 steel in comparison with EUROFER 97 steel at RT and at $\Delta\varepsilon_p$=0.2% [15]

Their performances were found to be close not only in cyclic softening but also in microstructural development. The quite stable lath martensite structure was strongly unstable under cyclic conditions. The cell structure was developed as a result of cycling. As it is seen in Figure 2-27 the original almost parallel martensitic laths were transformed into the equiaxed subgrains of larger diameter than the lath width with cleaned interior. In certain zones the dissolution of the subgrain walls was observed leaving the former precipitates enclosed (Figure 2-27c).

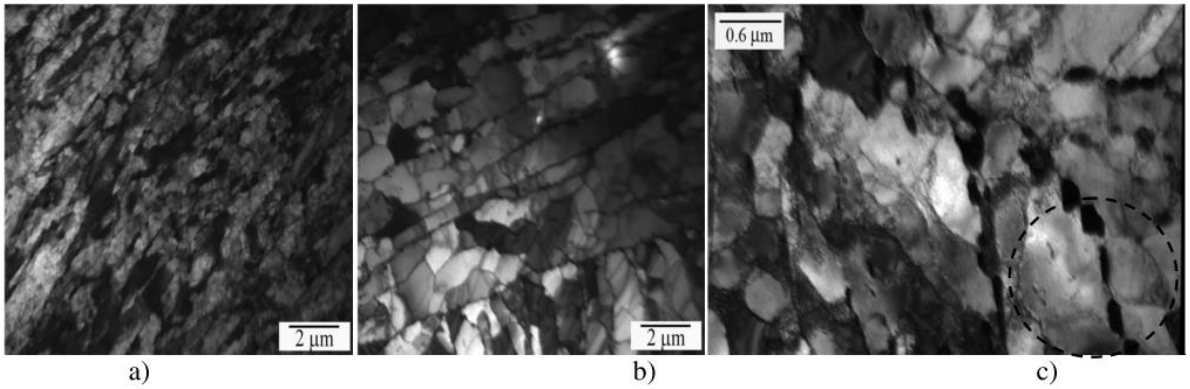

Figure 2-27 a) initial tempered microstructure of AISI 410 steel; b) fatigued lath structure turned into equiaxed subgrain microstructure; c) fatigued lath structure with disappeared subgrain wall and saved precipitates shown in circle [15]

In Figure 2-28 another TEM image of martensite, observed in a specimen fatigued at room temperature at total strain range $\Delta\varepsilon_t$=0.8 %, and witnessing the microstructural modifications in material, is shown. In comparison with the as received material, the authors concluded three major microstructural changes: 1) the martensitic laths decomposition into cells; 2) the overall dislocation density decrease; 3) and the disappearance of large grains, i.e. their decomposition into the fatigue cells with a diameter of 1 µm. The dislocations seem to be swept out to the grain/subgrain boundaries by the cyclic plastic deformation. Therefore the grains/subgrains are cleaner and well defined. Dislocations may be observed mainly in small grains, suspected not to be deformed plastically, or inside some grains attached and pinned by precipitates [30].

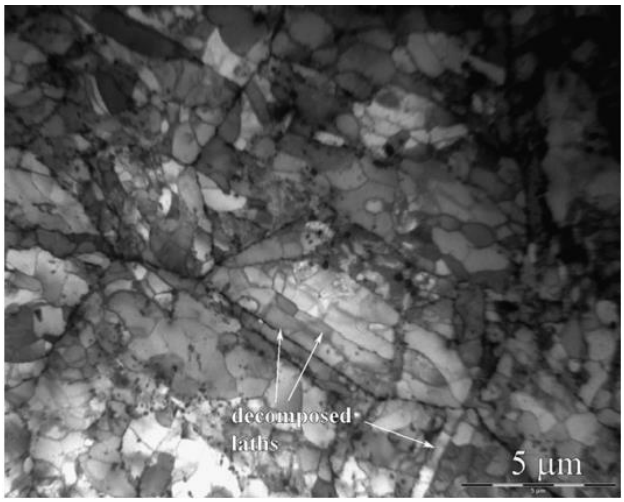

Figure 2-28 Cell structure induced by the cyclic deformation in Eurofer 97 steel, tested at room temperature, at $\Delta\varepsilon_t$=0.8 %, N=7261 cycles [30]

Besides, the authors clarified the term subgrain and fatigue cell. Subgrains are the grains with the misorientation angles smaller than 5° and formed during the thermal treatment of material and fatigue cells are the cells created by the dislocation activity on several crystallographic planes during the cyclic plastic deformation, resulting into small almost equiaxed volumes separated by dislocation walls having a small angle of disorientation. "*These are essentially the same objects, it is not possible to track their origin and therefore the designation of these objects is only a question of terminology*" [30].

In the same way Fournier concluded in his thesis that the restoration of subgrains (or microstructure growth) formed during the martensitic transformation and tempering was observed and quantified both for pure fatigue tests and for creep fatigue tests. At low levels of pure fatigue deformation the obtained microstructure was highly heterogeneous: some big, completely restored blocks free from dislocations neighbored with subgrains as fine as those of initial microstructure. This microstructural growth was accompanied by a drop of the dislocation density. The study also highlighted the fact that the restoration only affects the boundaries between sub-grains and laths, and it does not touch the block boundaries. Therefore it seems possible to connect the restoration to the mobility of dislocations and annihilation events. More mobile dislocations within a block cause the more rapid and pronounced restoration. However, only the subgrain size and the dislocation density changes were observed and not the change of precipitation state, as can be the case for long-term creep [8].

2.3.3 Mechanisms of fatigue surface relief formation

Besides the microstructural evolution in the bulk of materials, in the conditions of cyclic plasticity a certain deformation relief forms at the external surface on the loaded specimens. This relief appears as a set of "lines" called differently by different authors: slip bands, fatigue deformation markings, fatigue bands, "hills and valleys", slip striations or markings, extrusions, etc. Todays these sharp surface relief features are mainly called persistent slip bands (PSB) or persistent slip markings (PSM). The adjective persistent is used because the markings reappear in the same location after the test was interrupted, the surface was polished and the test was repeated. However, many scientists associate the term PSB with a ladder-like structure observed often in the bulk of high stacking fault energy fcc metals and alloys (Figure 2-20) [56], [65]. To avoid any confusion and misunderstanding, the vocabulary that will be employed for the

surface relief features in the following chapters, will be defined in this paragraph. In this work the term step is used to name the features observed after the first half-cycle of loading equivalent to the interrupted tension test. The term extrusion (Figure 2-29) is used to name the deformation lines resembling a “hill” on the fatigued surfaces, while intrusion means a “valley” or a crack-like defect on the deformed surface. The term fatigue slip markings (FSM) or PSM or just slip marking will be used as generic name putting in together the steps, extrusions and intrusions. PSB may be employed both as a synonym for FSM term and as a term designating the ladder-like structure observed in the bulk of metals.

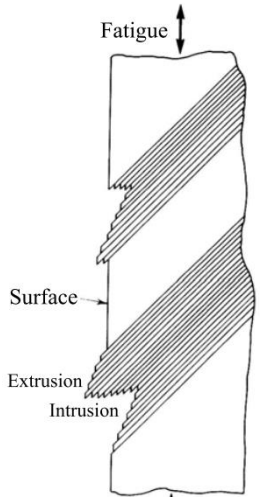

Figure 2-29 Schematic image of extrusion-intrusion

From the theory of dislocation movement it is known that the plastic deformation represented by PSMs on the metallic surface happens due to the glide of many dislocations which result in slip – successive displacement of one plane of atoms over another on slip planes. Unfortunately, this *was not* and *is not* enough to explain the complex morphologies of observed extrusions and intrusions. As a result many different models were developed to explain the formation of PSM. Man *et al*. in their work [3] divided all of them into three groups: 1) surface-stress-assisted crack nucleation models which considers the real dislocation structure of PSBs and fatigue crack initiation is ascribed to the presence of internal stresses within a PSB; 2) “vacancy” models – a decisive role in this models is attributed to point defects; 3) micromechanical models. All these models are found to be in conflict with experimental observations.

Some of these models will be described below. It should be noted that all of them were developed due to the experimental observations of ladder-like structured PSB in pure copper.

2.3.3.1 Dickson model

Dickson *et al*. [66] believed that the intrusion formed first and tended to give rise to the extrusions bordering the intrusions. According to these authors a small shallow microcrack initiated along a narrow portion of a persistent slip band in copper. This microcrack favored a non-random irreversible glide of screw dislocations in the crack tip region tending to deepen the crack. This irreversible glide resulting from the tensile stresses in the crack tip transformed the shallow microcrack into an intrusion. To accommodate the volume change resulting from this intrusion, an irreversible slip of screw dislocations produced a volume change of opposite sign in the vicinity of intrusion, and in this way the extrusion was created. Todays, this model of extrusion-intrusion formation, where the intrusion forms first and before extrusion, is not anymore considered as the true one.

2.3.3.2 EGM model

The fundamental microscopic mechanism developed by Essmann, Gösele and Mughrabi (EGM) is presented in Figure 2-30 [56].

Dislocations represented by full symbols are those moving in the tensile phase, in which the slip is transmitted across the specimen by the sequence of microscopic slip processes denoted A-A'. At the sites of edge dislocation annihilation (in copper in the walls of PSB), the combined slip process changes the atomic plane because of the disintegration of the edge-dislocation dipoles. As far as the macroscopically effective slip plane is inclined relative to the crystallographic slip plane, the surface steps are formed at A-A'. In the compressive phase the steps in B-B' are obtained in the same way. These steps make an extrusion (Figure 2-30a).

The production of interstitial-type defects by annihilation of edge dislocations brings to an intrusion (Figure 2-30b).

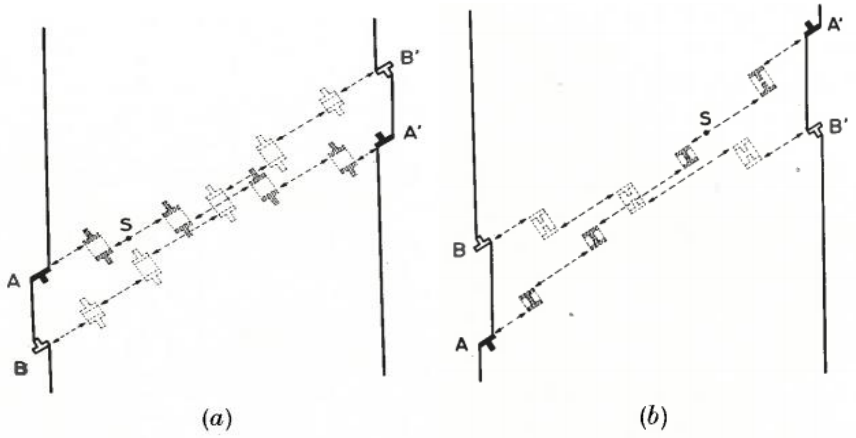

Figure 2-30 Fundamental microscopic EGM mechanism of the formation of a) extrusion formed by the annihilation of vacancy-type dipoles; b) intrusion formed by the annihilation of interstitial-type dipoles. All dislocations drawn in dipole configuration would annihilate and only the individual dislocations in A, B, A', B' would survive the annihilation [56]

The extrusion stops growing once the density of vacancies saturates in the PSB. In saturation the vacancies are produced at the same rate at which they are swept up by the moving dislocations. "*The associated climbing of the dislocations cancels the effect edge-dislocation annihilation has on the combined slip process shown in* (Figure 2-30a), *i.e. the macroscopic effective slip planes do no longer deviate from the active slip plane and the extrusion stops*.".

2.3.3.3 Polak's model

Polak developed its own "vacancy" model based on EGM model of emergence of ladder-like structure in PSB and extrusions and intrusions on the surface. Polak's model of PSM emergence is based on the redistribution of matter in the PSB and between PSB and the matrix. This redistribution happens due to the point defects production (mainly vacancies). Resistance measurements on fatigued single crystals suggest a pronounced increase in point defect concentration during fatigue. Lepistö's positron lifetime measurements confirmed the existence of small three-dimensional vacancy agglomerates in fatigued copper single crystals [67]. The vacancies are mobile at room temperature and constantly migrate and annihilate when approach the sinks. The vacancy production rate is homogeneous in the PSB, while the annihilation rate is a function of sink density. Edge dislocations are perfect sinks for vacancies and their presence is denser in the walls. It results in that the vacancy concentration is maximum in the middle of channels and decreases towards the walls and the matrix. It brings to a motion of atoms in the

opposite direction, i.e. mass redistribution. There is a mass in the channels and reduction of the mass in the walls. Consequently compressive and tensile stresses build up and can be relaxed only in the x-direction (Figure 2-31). It leads to the emergence of extrusions at the sites where the channels intersect the surface and intrusions where the walls intersect the surface [4], [68].

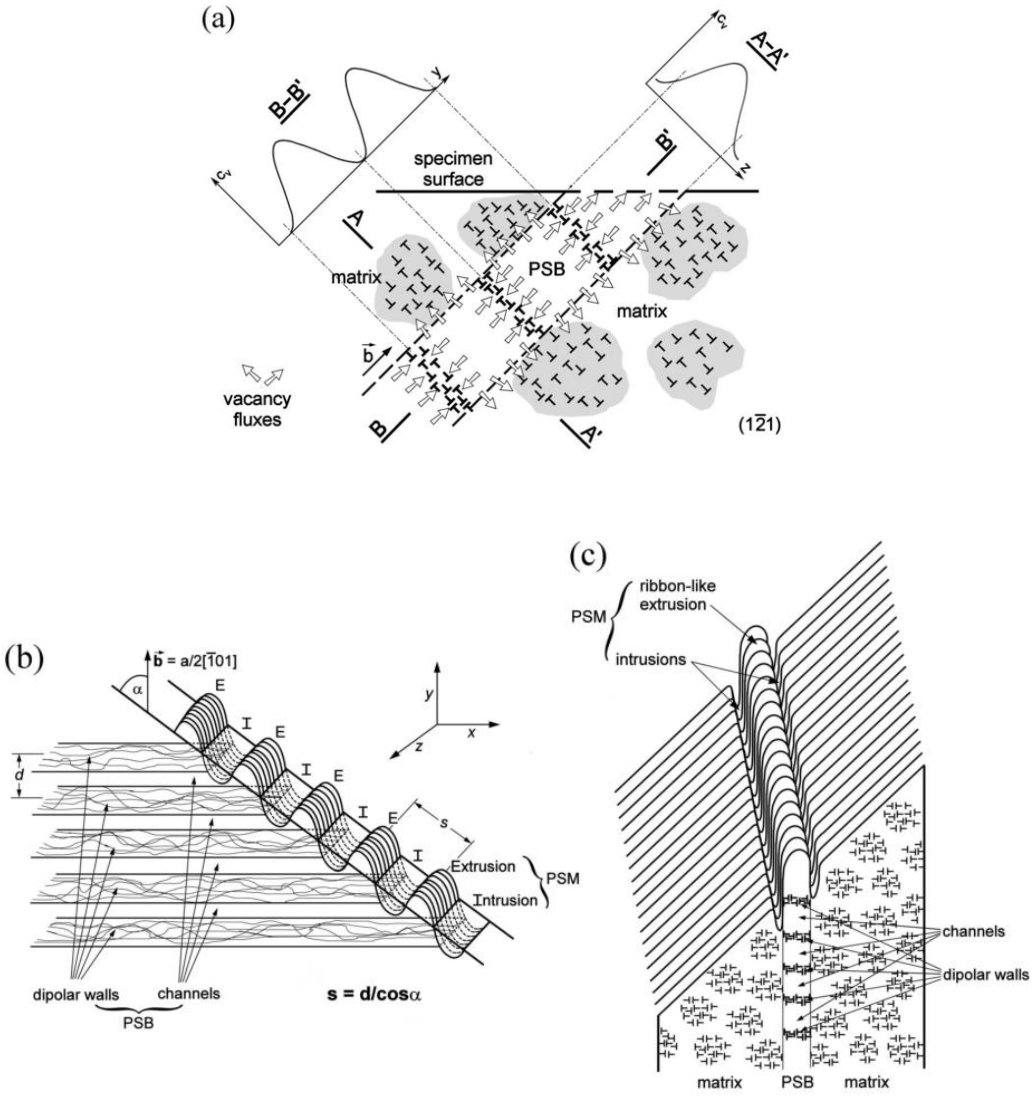

Figure 2-31 Polak's model of surface relief formation for an individual PSB. a) section through a crystal comprising PSB and matrix in a plane and quasi-stable vacancy concentration profiles within PSB and in a plane perpendicular to PSB. Arrows indicate the vacancy fluxes within PSB and out of the PSB. b) relationship of the dislocation structure of PSB with a neighbor PSM during the point defects migration within the band. c) surface profile of a PSM when points defects move forward-and-back from the band to the matrix [3]

2.3.3.4 Grain boundary sliding as a deformation mechanism in monotone and cyclic loading

In 2016 the scientists of Eindhoven University of Technology [45] reported another deformation mechanism in monotonic loading of a lath martensitic steel. They performed in-situ uniaxial micro-tensile tests on the water quenched martensitic steel (0.092C-1.68Mn-0.24Si-0.57Cr). It should be outlined here that the abundant content of carbon and manganese in the steel studied by them and the water quenching favored the retaining of austenite. Thanks to EBSD observations they saw that in a lath with a slip system with the highest Schmid factor the dislocation slip did not occur, but instead clear steps appeared exactly at the boundaries. Thus, in Figure 2-32$a_{1–6}$ a single-packet sample, of predominantly one block, with block boundaries and sub-block boundaries that are tilted to the loading direction, aligned with one (110) martensite plane corresponding to a (111) prior-austenite plane, and roughly perpendicular to the specimen surface (indicated by a red circle at the peripheral of the {011} pole figure) is shown. The slip system with the highest Schmid factor, indicated by the red circles in Figure 2-32a_5 and a_6, is parallel to the boundaries. As this favorable slip system needs not to cross the boundaries, one would expect all plastic slip to occur inside the laths. However, no slip seems to occur between the boundaries. Instead, clear steps occur exactly at the boundaries, as observed from the zoom of the edge of the deformed specimen in Figure 2-32a_4. The scientists concluded that as far as the boundaries in this specimen were favorably tilted to the loading axis (45° between loading axis and boundary) the boundary sliding happened. But in the cases where the boundary sliding was prohibited by a low resolved shear stress due to boundary orientation parallel to the loading axis, the plastic deformation occurred inside the laths and was carried out by crystallographic slip (in this case the boundaries obstructed the slipping and rather strengthened the material). They supposed that the interlath retained austenite films caused the boundary sliding. The martensite is harder than austenite so the austenite was like a “greasy” plane on which the laths could slip. Besides this, the authors confirmed that the block size is an effective grain size in the plasticity of martensitic steels.

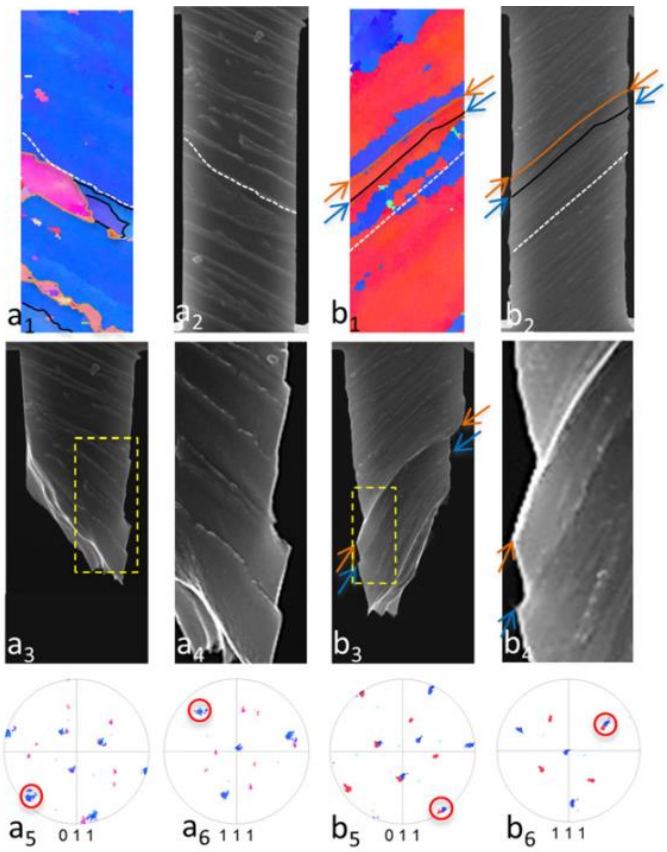

Figure 2-32 Two 9 µm-long specimens with tilted boundaries to the loading direction shown with inverse pole figure orientation map (a_1,b_1), SEM pictures before loading (a_2,b_2) and after fracture (a_3,b_3) together with a zoom (yellow frame) of the fractured specimens (a_4,b_4). The red circles in the {110} (a_5,b_5) and {111} (a_6,b_6) pole figures indicate the favored slip system. Block and sub-block boundaries are marked with orange and black lines respectively; the fracture surface with a white dotted line. The many lath boundaries are not marked. The arrows in b_1–b_4 indicate sliding boundaries

Other authors reporting the grain boundary sliding in fatigue loading are Okayasu *et al*. [69]. They performed a high cycle fatigue test on the ultra-fine grained ferrite/martensite two phase low carbon steel (0.15C-0.25Si-1.1Mn). As a result they observed the intergranular cracking. The authors supposed that the grain boundary sliding (GBS) (Figure 2-33a) led to it because the grain size (2.5 µm) of martensite in their steel was close to that of superplastic steels, and the GBS is common fracture reason in the superplastic steels as it is shown schematically in Figure 2-33b. The scientists assumed that the GBS could be related to the dislocation movement or pile-up of dislocations along the grain boundary [70]. "*The slip on the primary glide plane leads to a build-up of stress at its intersection with the grain boundary (…) and secondary grain sliding occurs at the absence of relaxation of this stress concentration. Although there is no*

clear evidence in this study, such GBS may be taking place during the deformation process" [69].

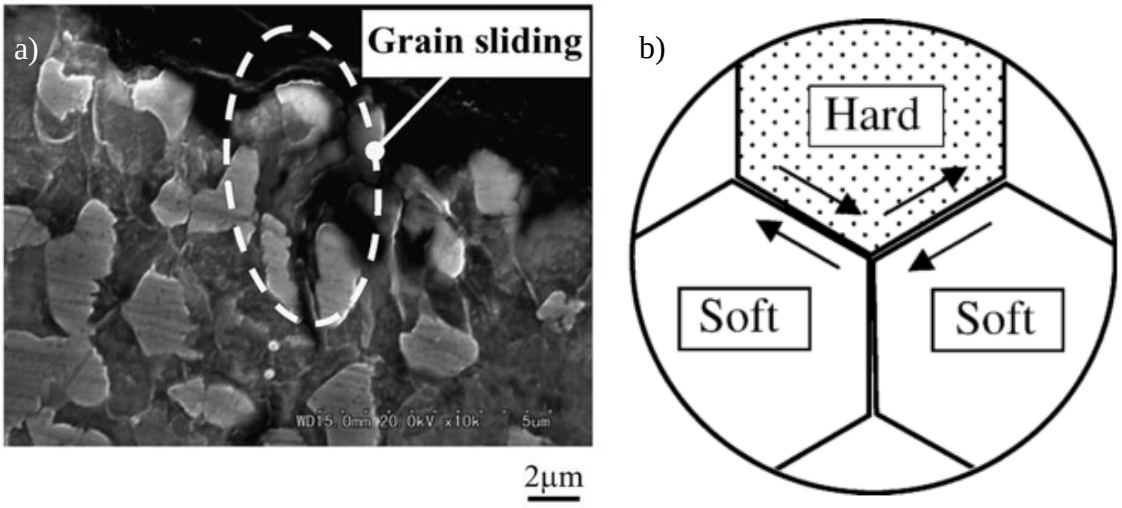

Figure 2-33 Grain sliding as a result of HCF test of UFG ferrite/martensite steel: (a) SEM evidence of GBS, (b) schematic representation of GBS [69]

2.3.3.5 Deformation of ultra-fine grained steels

The ultra-fine grained (UFG) steels have very fine microstructure with grain sizes from 100 nm to 1μm and possess the different types of boundaries: HAGB and LAGB. Their microstructure seems to be close to the one of martensitic steels, still the UFG do not have any hierarchical relationships between their grains. Some aspects of the deformation of these steels will be considered shortly in the next paragraph.

Interesting behaviour of Ti-stabilized interstitial free (IF) UFG steel under low cycle fatigue was reported by Niendorf *et al*. [71]. The studied steel contained HAGBs and LAGBs. The moving dislocations came into the interaction with grain boundaries. In case of dominance of HAGBs the dislocations were pinned. While in case of dominance of LAGBs the moving dislocations rearranged this type of boundaries eventually leading to cyclic softening of material. The additional AFM measurements found the extrusions of 1 μm and 100 nm height (depending on the sample machining method) (Figure 2-34). "*The topography plot of … steel shows that the blocks of about 20 μm were pressed out of the surface, which in fact corresponds to the average size of areas dominated by LAGBs with similar orientation … It is obvious that*

this length scale very well exceeds the average grain size of UFG material. Accordingly, there are sections of boundaries in the sample that can easily be sheared out of the samples' surface."

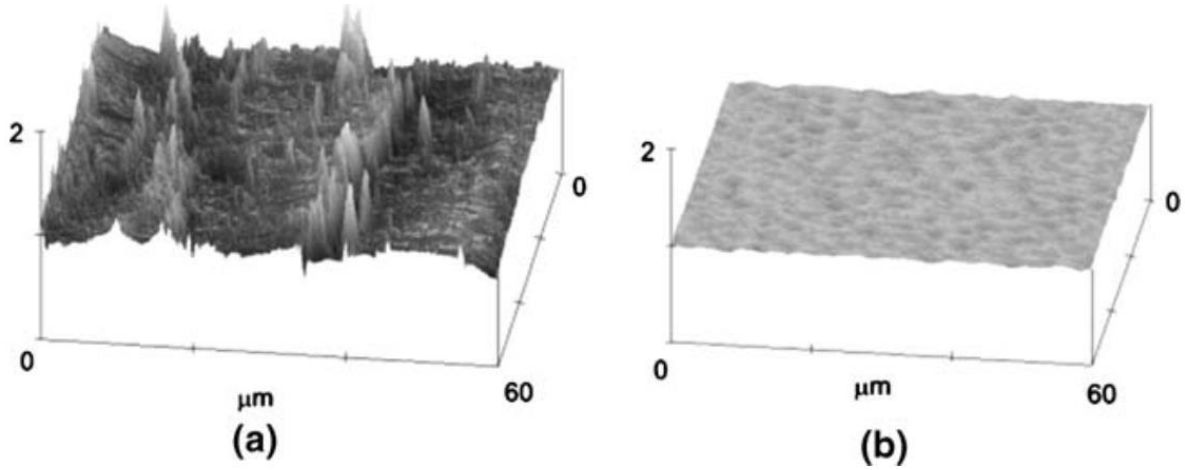

Figure 2-34 AFM images of extrusions on the surface of Ti-stabilized IF UFG steel after LCF test at $\dot{\varepsilon}=6\cdot10^{-3}$ s^{-1} and $\Delta\varepsilon_t=4\cdot10^{-3}$: a) extrusions with 1µm height; b) extrusions with 100 nm height [71]

2.3.4 Fatigue crack nucleation

Different models leading to the formation of extrusion-intrusion were considered above. In many cases the cracking occurs in those extrusion-intrusion pairs, which is why in the next section some studies on the crack nucleation are considered.

2.3.4.1 Fatigue crack initiation in different metals

In the seventies Grosskreutz and then Laird agreed that the metal cracking is a two-stage phenomenon, and the most important one is the crack initiation stage; they insisted that this stage is the priority item for studying [72], [73]. The number of scientists devoted to the crack initiation in extrusion-intrusion precursors has increased rapidly. The most known amongst them are Laird, Brown, Essmann and Mughrabi, Finney, Basinski, Hunsche and Neumann, Polak, Dickson and Vogt [5]–[7], [66], [68], [73]–[76]. The majority of these authors worked on copper.

Basinski & Basinski studied a lot the extrusion cross-sections obtained due to the sharp corner polishing of copper single crystals in SEM [77] (Figure 2-35). In the eighties Basinski &

Basinski reported the cracks started in narrow PSB in single crystals of copper. They also defined the critical depth for catastrophic propagation of crack: 100 µm. It should be noted that already at his time it was noticed that the intrusions normally do not exceed the dimensions of extrusions [6], [77]–[79].

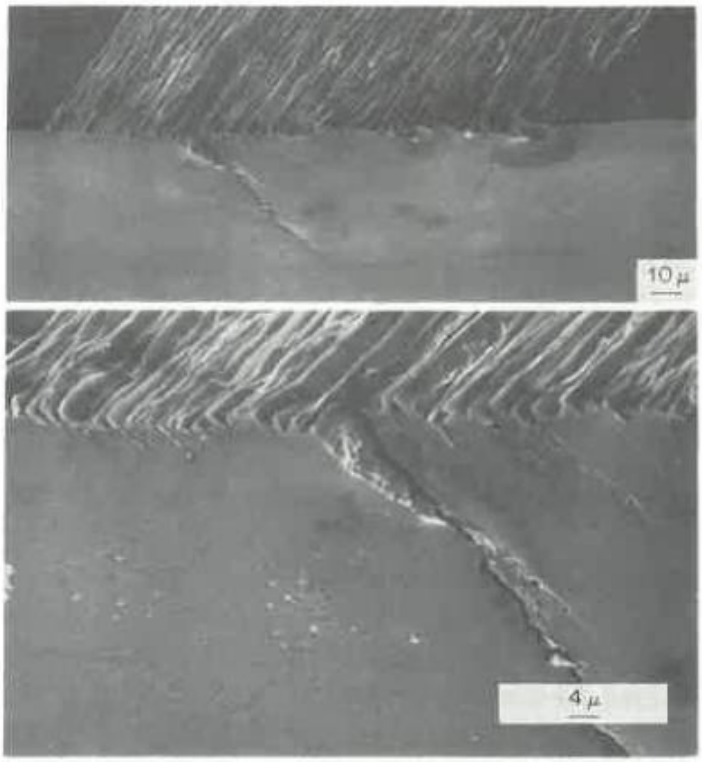

Figure 2-35 Cross-sections of extrusions, intrusions and cracks observed in copper single crystals after approximately 300 kilocycles of loading [80]

Neumann and Tonnessen [81] studied the deformation relief in copper and the correspondent dislocation structure on the extrusion cross-sections too by SEM and Electron Channeling Contrast Imaging (ECCI). They believed that the abundant interstitial dipoles pushed out the extrusions on the surface. They reported the crack initiation in the interface between PSB and the matrix in copper single crystals. However, in copper polycrystals the cracking happened at twin boundaries surprisingly for them because the twin boundaries possessed the lowest energy.

Cheng and Laird [82] studied the crack nucleation in PSB in copper single crystals by interferometric microscope and proposed their model for the crack nucleation based on the random slip of the dislocations within the PSB; while Figueroa and Laird [83] reported the crack nucleation at grain boundaries in polycrystalline pure copper (Figure 2-36). In 1989 Ma

and Laird [84] published a SEM image of fatigue crack making an acute angle with the surface plane. The crack initiated at PSB-matrix interface (Figure 2-37).

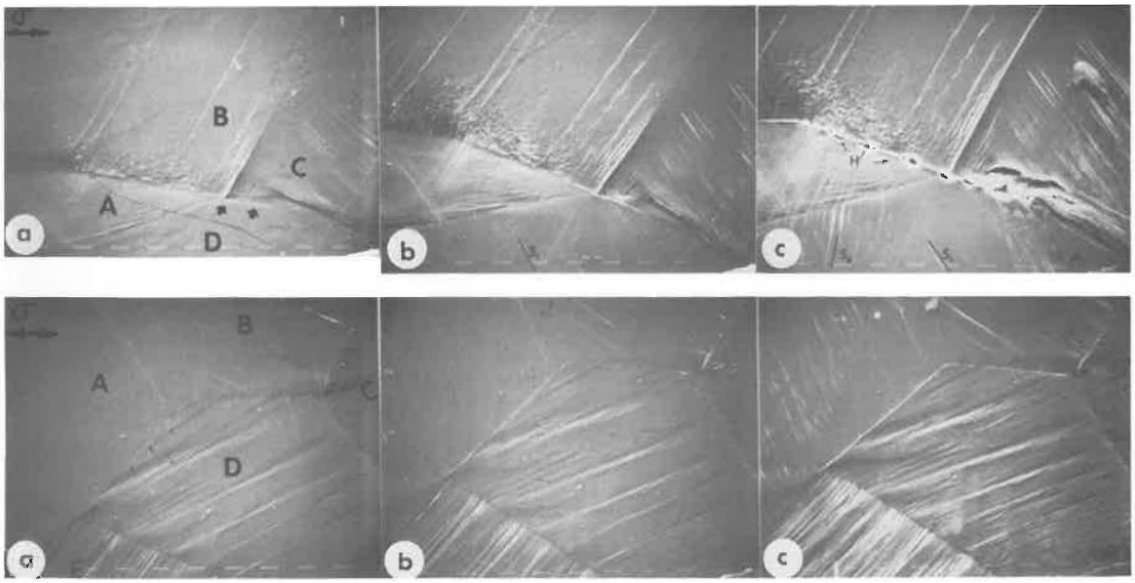

Figure 2-36 SEM images showing the intergranular crack initiation in copper polycrystalline: a) $\sum\Delta\varepsilon_p$=2, arrowed regions at boundaries AD and BC indicate the presence of crack embryo; b) $\sum\Delta\varepsilon_p$=4, new crack embryos developed and others have already begun to link up; c) $\sum\Delta\varepsilon_p$=8, crack nuclei formed along boundaries AD and BC. Since the replica is of the negative type, the crack embryos show up in light contrast [83]

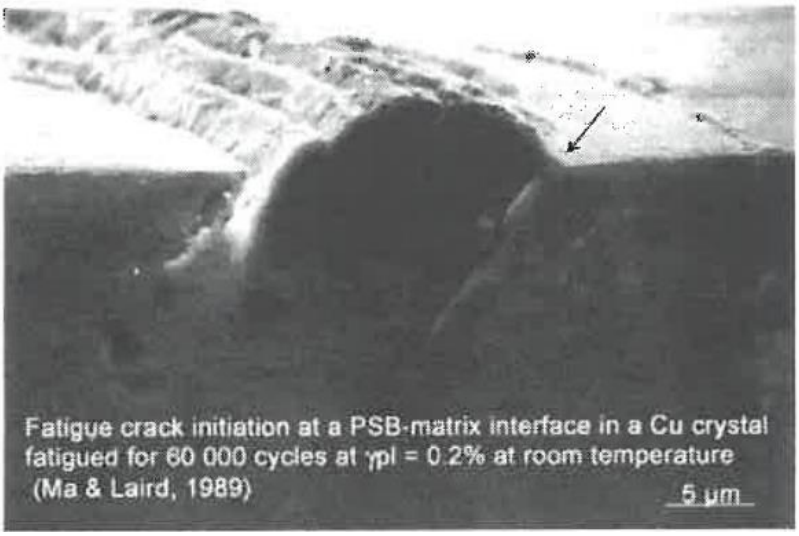

Figure 2-37 Extrusion, intrusion and crack cross-sections. The arrow points out the crack [84]

Dickson and Vogt worked on polycrystalline copper too and reported the intercrystalline cracking as well [66].

However, a few articles on the crack nucleation in PSB in pure iron and some steels were published by Guiu *et al*. and Pohl *et al*. in the early eighties [85], [86]. These authors reported the cracks at the intrusions and extrusions at low frequencies of loading (less than 0.01Hz); and at intersections of grain boundaries at frequencies higher than 0.01Hz.

Essmann, Gösele and Mughrabi, and Polak and Man are probably the most known authors working a lot on copper single crystals and polycrystals and later on the austenitic and ferritic steels. Essmann *et al*. [56] developed a model explaining the formation of static extrusion in fcc metals with ladder-like dislocation structure. Later Polak [4] developed its own model based on the EGM model explaining the formation of both extrusion and intrusion. These models were described previously in this chapter. Both authors report that in the case of austenitic and ferritic steels or single copper crystals the crack nucleates in the intrusion.

2.3.4.2 Fatigue crack initiation in martensitic steels

As the previous section has shown the majority of works on the crack initiation in LCF were performed on different than martensitic steel materials. The most of works on the LCF of martensitic steels were directed on the explaining the softening phenomenon. And only a few authors tried to explain the fatigue crack initiation in martensitic steels at RT and in air.

Vogt *et al*. described the nature of fatigue extrusions in 12%Cr steel with ferrite islands inserted in martensite in the late eighties [87]. They noticed that the plastic deformation in form of extrusions was accommodated by ferrite in the first place. Then the microcracks developed along the most favorably oriented extrusions and the PA grain boundaries provided the favorable path for microcracks coalescence. Finally, they concluded that contrary to copper polycrystals, the grain boundaries are not the sites of crack nucleation, but a way of crack joining [5]. Later in 2006 Verleene together with Vogt observed the initiation of crack at extrusion-intrusion in the specimens of T91 (X10CrMoVNb9-1) martensitic steel fatigued in air (Figure 2-38) [12].

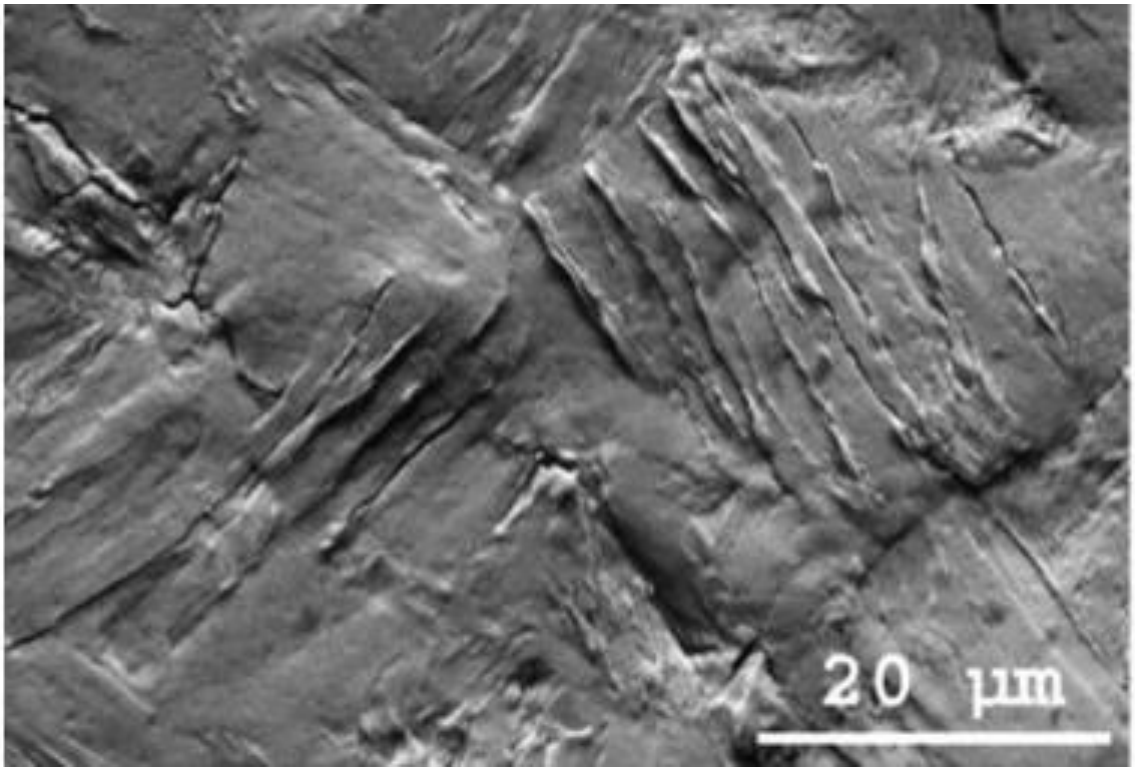

Figure 2-38 SEM image showing crack initiation in extrusion-intrusion pairs in T91 martensitic steel after LCF loading at room temperature and in air [12]

The analyses of deformation relief at the specimen surface by Cretegny and Saxena [14] and Batista *et al*. [15], [46] suggested that the cyclic plasticity is localized at the different interfaces of martensitic steel.

Cretegny and Saxena investigated the LCF of PH 13-8 Mo stainless steel and found two types of slip marks: streaks which appeared at both low strain amplitude (0.4%) and high-strain amplitude (0.6%), and extrusions which were common only for high-strain amplitudes. In this alloy a thin and soft film of austenite decorated the lath boundaries and according to the authors it favored the formation of streaks. However, the extrusions were inside the packets and PA grains, and were prevented from further growth through the HAB (high-angle boundaries) due to crystal discontinuities. Finally, the authors ascribed the crack initiation in interlath to a "*highly-reverted austenite regions creating a mismatch in surface plastic strain*" [14] (Figure 2-39).

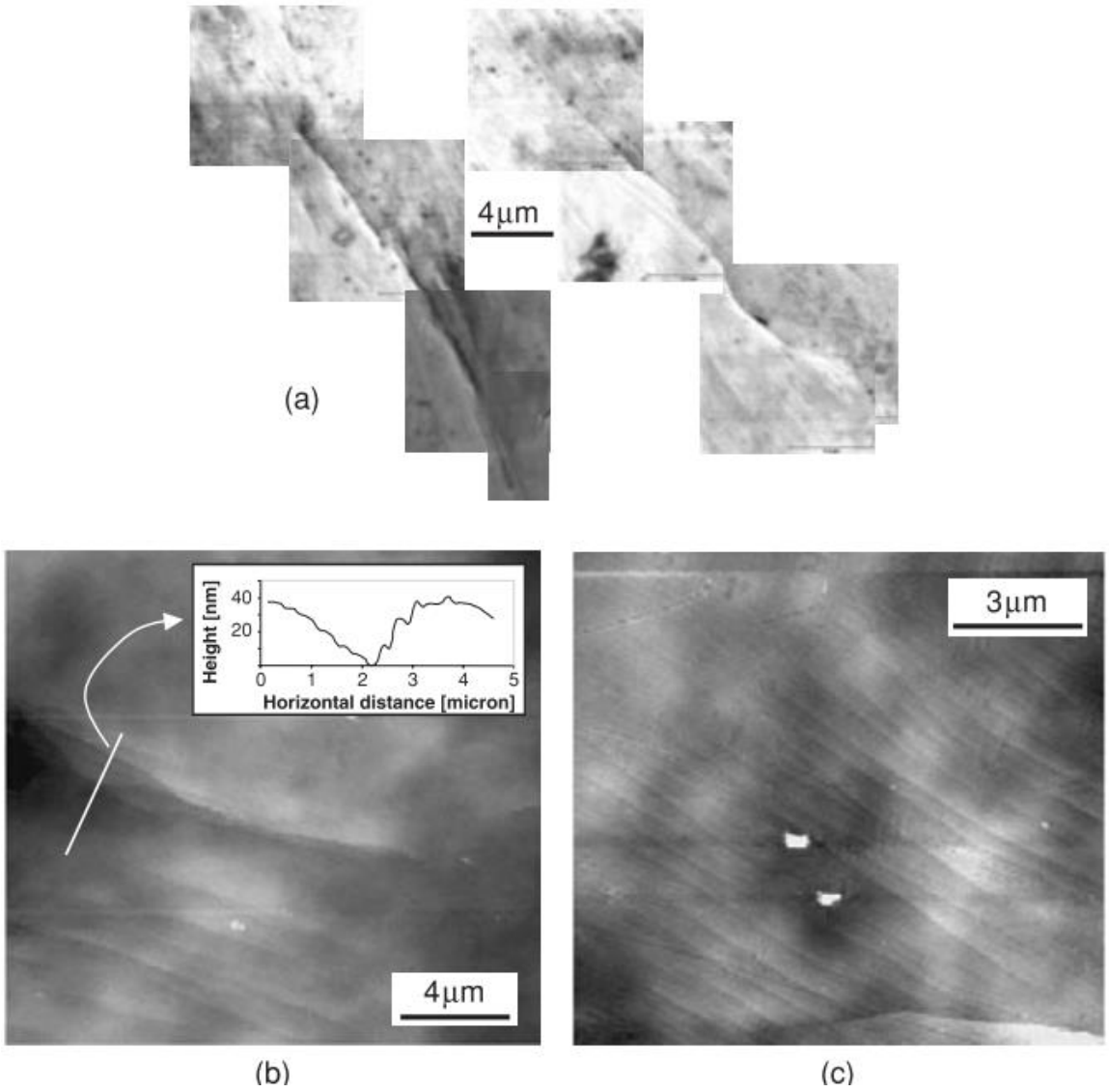

Figure 2-39 The SEM (a) and AFM images (b) of microcrack formation from the convergence of streaks in PH 13-8 Mo at Δε=0.4%; c) AFM image of a different area at slightly higher magnification than (b) illustrating a high concentration of parallel streaks, which is the precursor state before microcrack formation [14]

Batista *et al.* [15] revealed for the AISI 410 (13Cr-0.11C-0.47Si-0.7Mn-0.38Ni) steel and subjected to 0.2% of plastic strain range in fatigue that the first deformation "lines" appeared at about 50 cycles along lath boundaries oriented about 45º with respect to the tensile axis. After a certain number of cycles, the lines intensified and turned into "bands", and finally, cracks nucleated on these slip marks (Figure 2-40). The authors ascribed the interlath cracking to the stress concentration in precipitates decorating the lath interface.

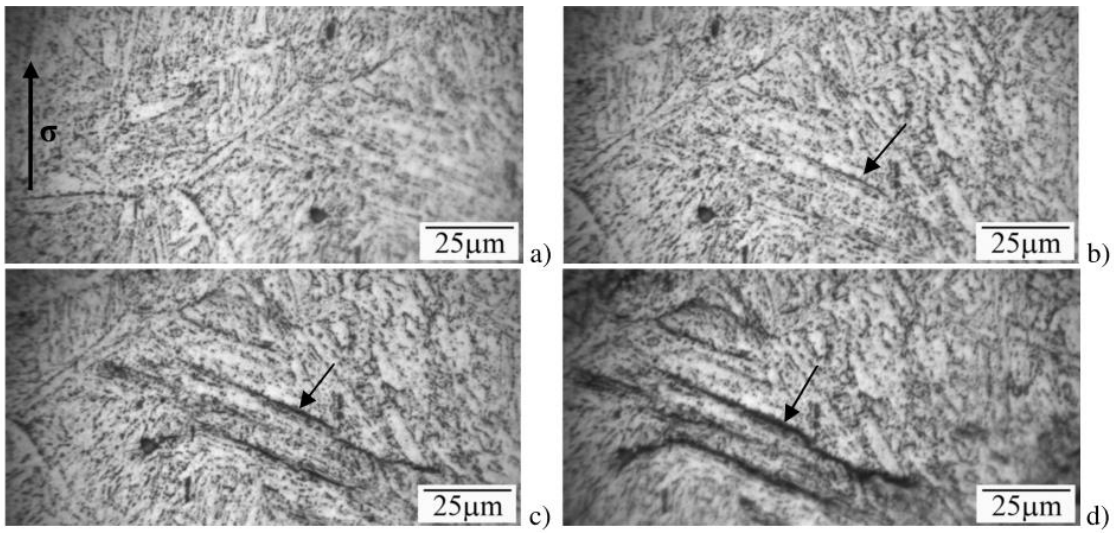

Figure 2-40 In situ optical images of AISI 410 steel taken during the fatigue test at: a) 0 cycle; b) 10 cycles; c) 60 cycles; d) 160 cycles [15]

Chai *et al*. [88] observed the formation of dislocation cells as a result of very high cycle fatigue test of a martensitic steel (0.38%C; 13.5%Cr). They supposed that the presence of dislocations in the dislocation dense areas of cell walls (Figure 2-41a) caused the local stress concentration in the material. Cyclic loading also caused the annihilation of dislocations which led to the formation of vacancies. As a result the stress concentration reduced in the annihilation area, and the dislocations in the areas with higher stress concentration moved towards the annihilation areas. In other words the "holes" (annihilation area or vacancies) absorbed the "matter" (dislocations). It brought eventually up to the emergence of "nano-pores" at the cell boundaries (Figure 2-41b). The stress concentration led to the cracking at these "nano-pores" (Figure 2-41c) [88].

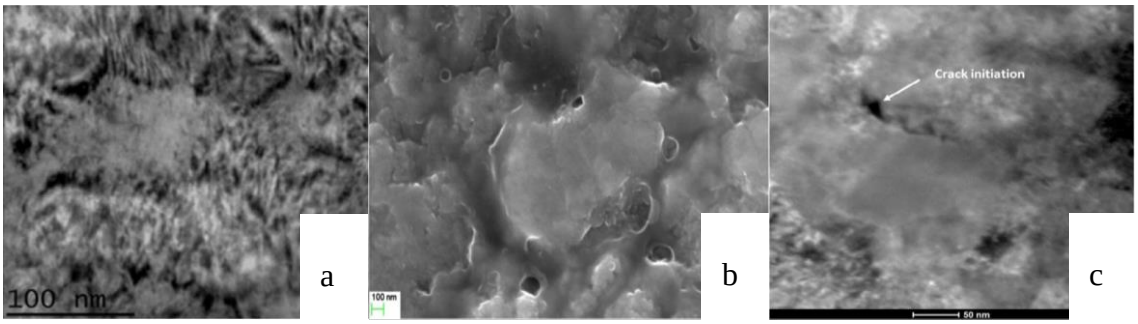

Figure 2-41 (a) dislocation cells; (b) formation of nano-pores at the boundary; (c) crack initiation in 0.38C-13.5Cr martensitic steel subjected to VHCF loading at σ = ±650 MPa and f = 20 kHz [88]

To sum up, the scientists studying the fatigue of martensitic steels report the crack initiation in slip markings appeared in the vicinity of microstructural boundaries.

2.4 Conclusions

In this chapter the complicated and hierarchical microstructure of martensitic steels was described. A PA grain contains a few packets; in a packet there are a few blocks of laths sharing the same habit plane; but each block has laths with one or two variants of lath (lath variant is a particular direction of a habit plane in which the lath lie). PA grain, packet and block have high angle grain boundaries (HAGBs), while laths have low angle grain boundaries (LAGBs).

The majority of studies on the cyclic and monotonic deformation of martensitic steels show that the martensitic steels soften during cyclic loading. This phenomenon has different origins depending on the microstructure. It can be explained by the lath boundary disappearance and dislocation density reduction, or by the appearance of tension steps due to the lath gliding on the thin retained austenite films between the laths. But still no clear mechanism explaining the formation of crack predecessors (extrusions and intrusions) at room temperature for the bcc hierarchically-organized martensitic steels exists.

However, a lot of works explaining the formation of famous ladder-like structured PSB and following cracking of fcc metals such as copper single crystals and polycrystals exist. The main of them were reviewed in the chapter. The most famous models explaining the extrusion-intrusion formation are Polak's model and EGM model. Thus, both of them rely on the fact that the point defects are produced during the fatigue of materials as a result of dislocation interactions. The vacancies and interstitials gradually generate the PSM formation according to these models.

In this work the low cycle fatigue slip marks will be studied in a multi-structured martensitic steel with an objective to understand and try to explain the mechanism of slip marks emergence and the following cracking of martensitic steel.

3. Experiment

This chapter is designed to describe the studied material, the main steps of experimental procedure and the main techniques of material analysis before and after the mechanical tests.

3.1 Studied material

3.1.1 Chemical composition

The studied material is the X19CrMoNbVN11-1 1.4913 (Z 20 CDNb 11) forged steel quenched in free air after 1 hour solution treatment at 1110°C and then tempered 4 hours at 680°C at the production plant *L'Union des Forgerons*. The steel was supplied in the form of a bar 25x25x1000 mm. The chemical composition of material analyzed in *BGH Edelstahl Siegen* is given in Table 3-1.

Table 3-1 Chemical composition of studied material

Element	C	Cr	Mn	Mo	Ni	Si	Nb	V	N	P	S	Al	B	Fe
Wt%	0.17	10.2	0.68	0.62	0.54	0.38	0.265	0.127	0.08	0.025	0.012	0.005	0.0003	Bal.

3.1.2 Phase identification by XRD

The crystallographic structure of the studied material was characterized using Philips X'Pert X-Ray Diffractometer with a cobalt emission source with 1.79Å wave length. The used scan step size was 0.02° and the scan step time was 7 seconds. In Figure 3-1 the XRD pattern is presented with three peaks, each corresponding to a particular crystallographic plane typical in the diffraction of bcc crystals. The steel has a body-centered cubic (bcc) ferritic crystal structure with a lattice parameter a = 2.86Å.

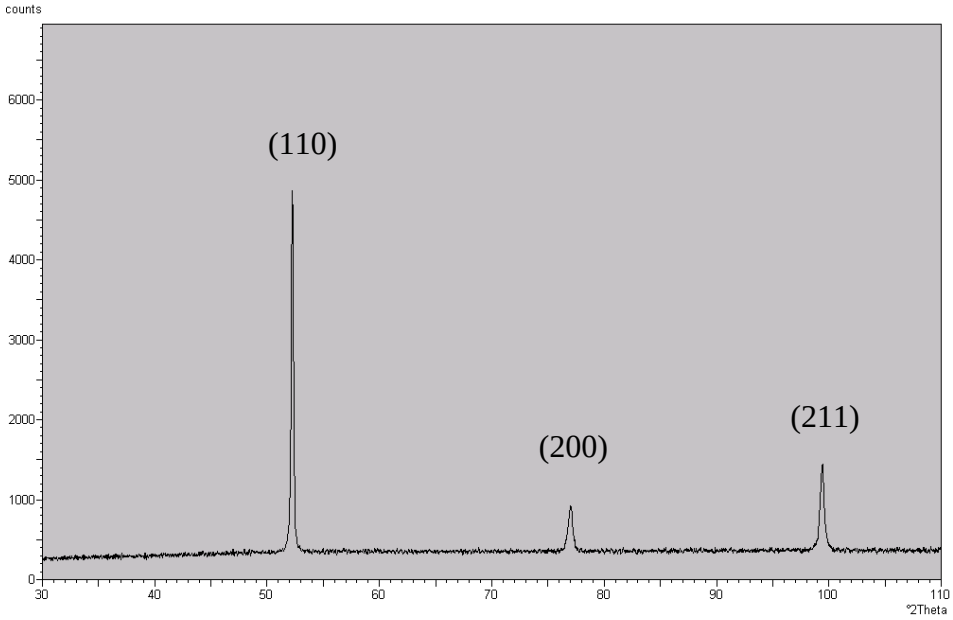

Figure 3-1 X-ray diffraction pattern of the studied steel. x-axis corresponds to the 2θ angle, where θ is the angle between diffracted X-ray and surface; y-axis indicates the diffraction intensity in counts

3.1.3 Microstructural characterization

The Schaeffler's diagram (modified by Schneider) together with equations for the calculation of Ni equivalent and Cr equivalent (Equation 2-1; Equation 2-2) can give an idea about the expected microstructure as well as about the presence or absence of delta ferrite (or residual ferrite) and retained austenite [89], [19].

$$Ni_{eq}=Ni+Co+0.5Mn+0.3Cu+25N+30C \qquad \text{Equation 3-1}$$

$$Cr_{eq}=Cr+2Si+1.5Mo+5V+5.5Al+1.75Nb+1.5Ti+0.75W \qquad \text{Equation 3-2}$$

In the case of the material under investigation, Ni_{eq}=8% and Cr_{eq}=13%. It means that the material is expected to have martensitic structure with no residual ferrite and no retained austenite according to Figure 3-2.

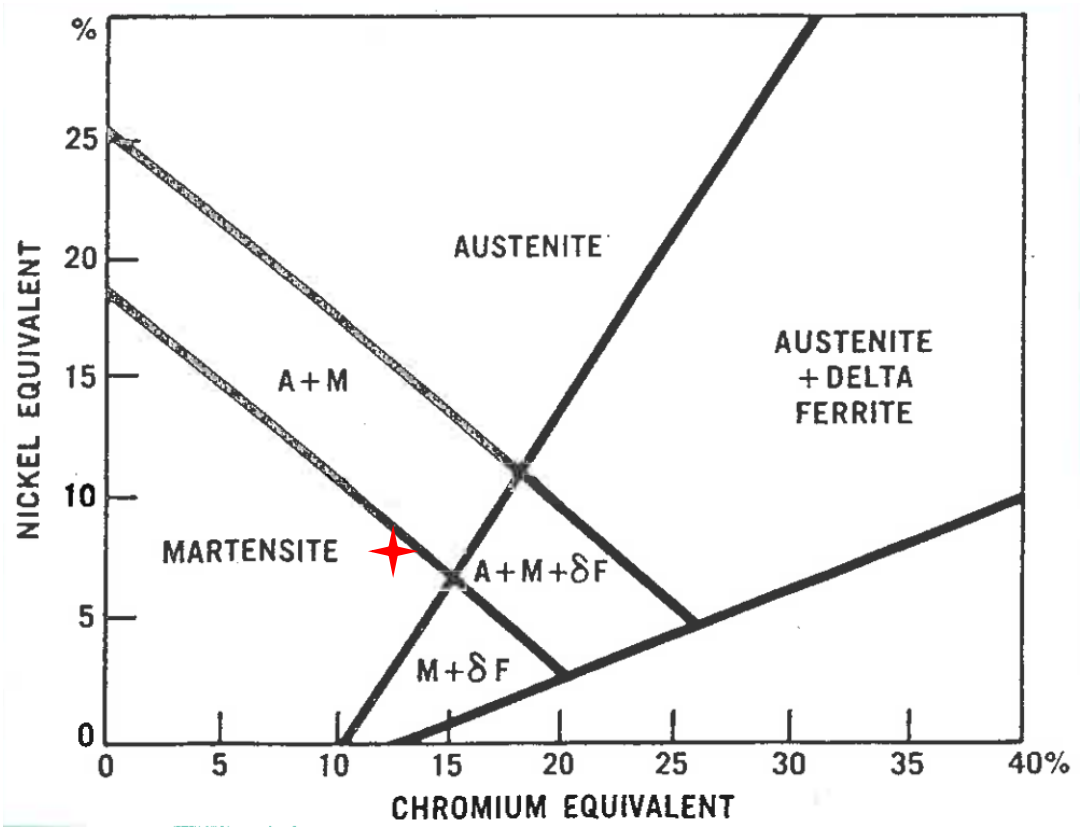

Figure 3-2 Schaeffler's diagram (modified by Schneider) revealing the effect of equivalent Cr and Ni on the microstructure of steels. The red mark indicates the position of the studied steel [89], [19]

To confirm definitely that the microstructure is fully martensitic, the as received material before fatigue was characterized by means of OM, SEM, TEM and EBSD analyses techniques. For OM and SEM investigation the microstructure was revealed after mechanical polishing and chemical etching by Vilella solution (25 g of picric acid, 50 mL of chloride acid, 925 mL of ethanol) during 15-45 seconds. For TEM observations, the metal foils cut previously from the specimens of interest were thinned up to 100 µm by mechanical polishing. Then the discs with a diameter of 3 mm were punched out from these foils. Finally the discs were electrochemically polished to perforation using the twin-jet technique in a solution of 10 vol% perchloric acid and 90 vol% ethanol. For EBSD observation, the samples were ground to 1200 grit paper, followed by mechanical polishing with 9, 3 and ¼ µm diamond pastes. The final step consisted of prolonged mechanical polishing with colloidal silica.

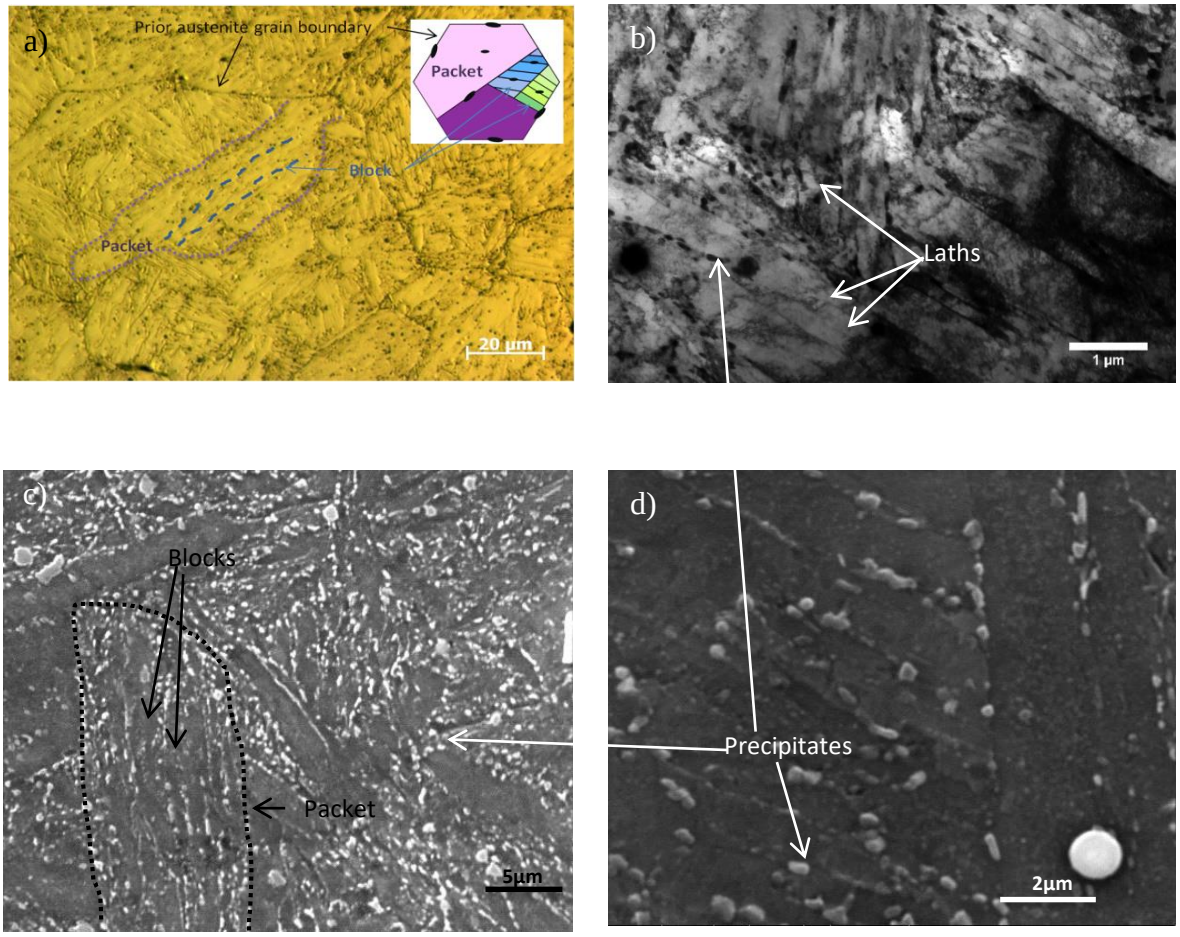

Figure 3-3 Microstructure of the studied material: a) optical image; b) TEM image; c) and d) SEM images

In Figure 3-3acd the optical micrograph and the SEM images along with the IPF map (Figure 3-4) allow identifying of the PA grains, packets and blocks. The laths are distinguishable only on the TEM image (Figure 3-3b). In addition, the EBSD IPF image permits recognizing the disorientations between different members of the microstructure. In Figure 3-4 it is seen that blocks, packets and PA grains are highly disoriented. Furthermore, the subgrains and twins were found rarely in the as received microstructure (Figure 3-5). The different interfaces are often well decorated by precipitates, formed during heat treatment (Figure 3-3bcd). The precipitates of type $M_{23}C_6$ with fcc crystal structure and lattice parameter a≈10.6Å, where M is (Cr, Mn, Mo), were identified by electron diffraction and Scanning Transmission Electron Microscope-Energy Dispersive X-ray (STEM-EDX) analysis (Figure 3-6). They are usually set up on the different boundaries. Other kinds of precipitates may exist in this material, but the

described one is the most commonly encountered in the 12%Cr martensitic steels. As for the dislocations, their occurrence is mainly a function of carbon content (Figure 3-7) and the martensitic steels are known to possess a high density of dislocations [28].

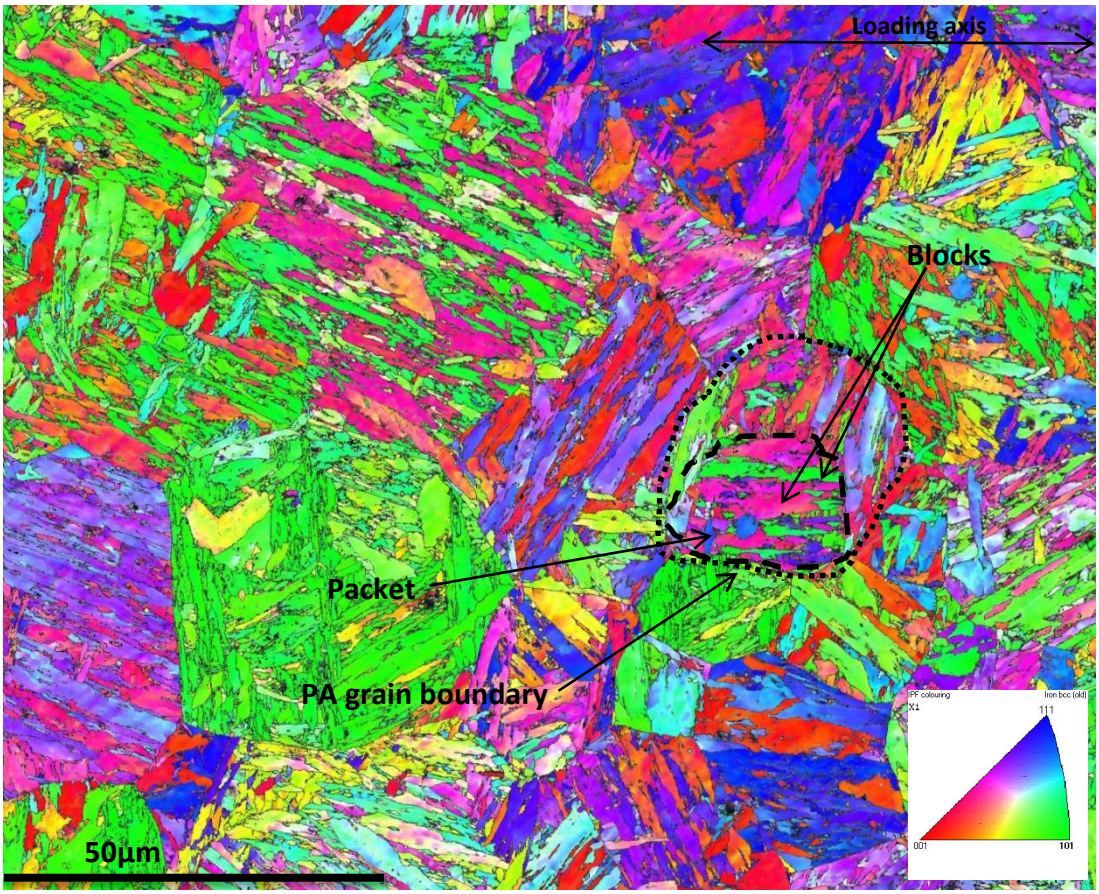

Figure 3-4 EBSD IPF color map, where disorientation angles higher than 10° (HAB) are marked by black line

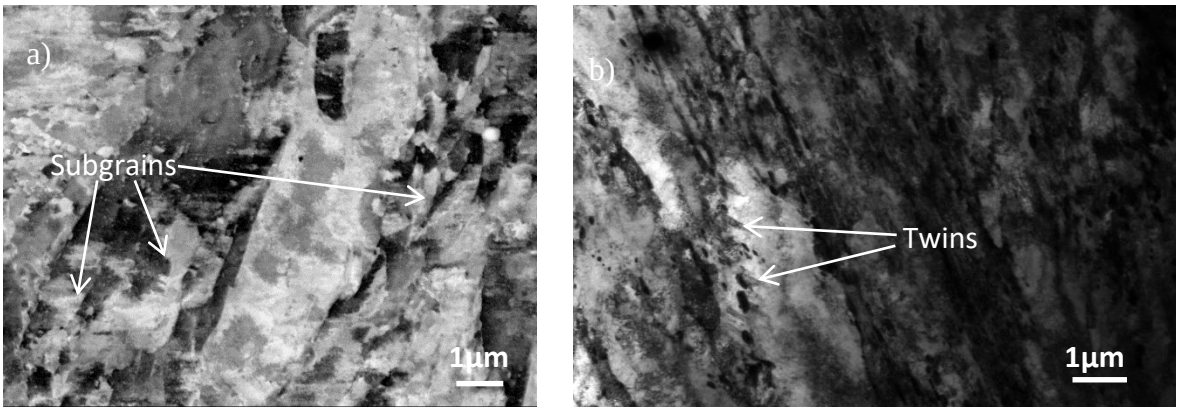

Figure 3-5 Microstructure of studied material: a) ECCI image; b) TEM image

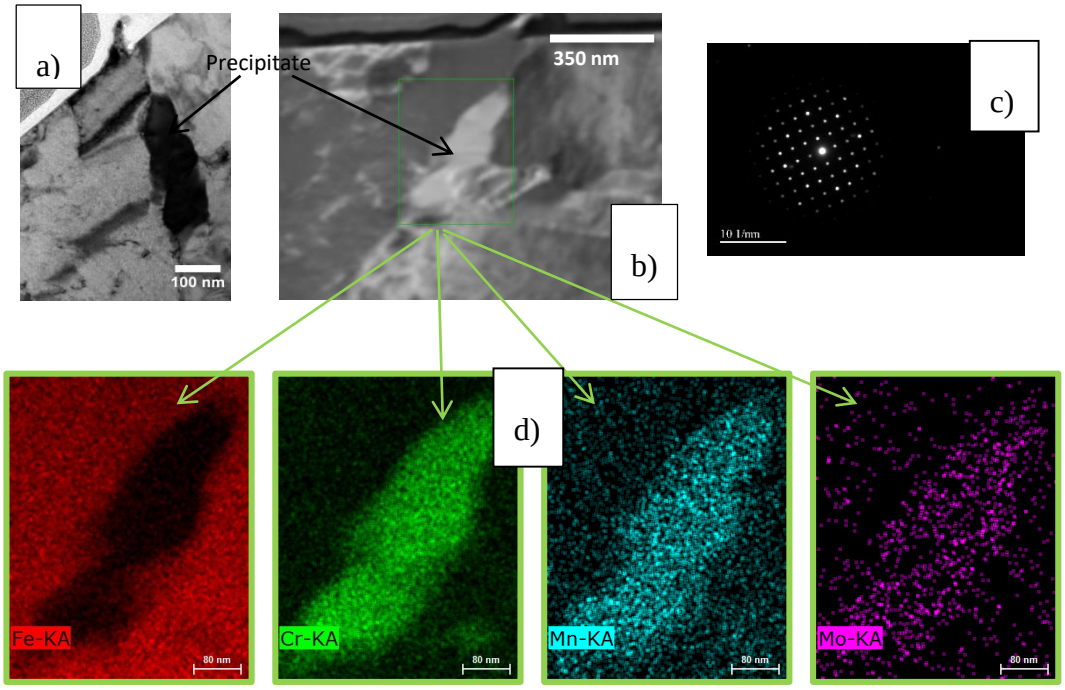

Figure 3-6 a) TEM image of a precipitate; b) STEM image of the same precipitate; c) diffraction pattern of the precipitate with the zone axis <100>; d) STEM-EDX map illustrating the chemical composition of the precipitate delimited by green rectangle in (b)

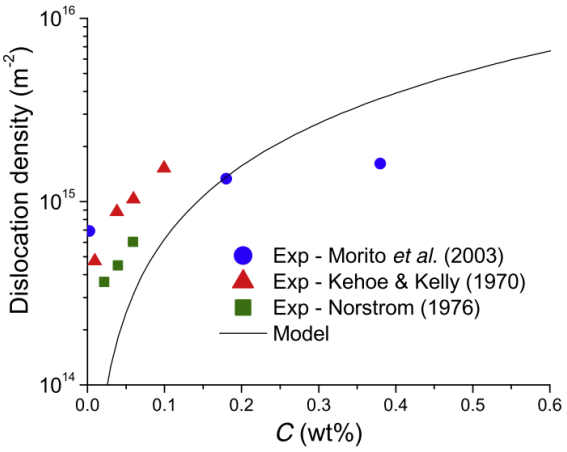

Figure 3-7 Dislocation density in different martensitic steels as a function of carbon content [43]

The predictive approach suggested that the studied material should be fully martensitic steel (Figure 3-2). This was supported by TEM observations (Figure 3-3) together with X-ray diffraction pattern (Figure 3-1), which allows us considering that the investigated material has a fully martensitic microstructure without ferritic islands and retained austenite, even if more advanced technique should be employed to confirm the latter statement.

The sizes of prior austenite grains, packets and blocks were measured by optical microscopy and SEM while the lath size, especially the width, was measured on the 2D TEM bright field images with a help of *ImageJ* image processing program. The size values of all elements are represented on the histograms in the Figure 3-8.

Most of the laths have a width between 0.2 µm and 0.4 µm and a length of about 10 µm. Blocks are between 1 and 3 µm wide and contain from 5 to 10 laths. PA grain size ranges between 10 to 60 µm while packet size was in the range of 5 to 20 µm. All the dimensions experimentally obtained are classically reported in the literature [8], [14], [27], [41].

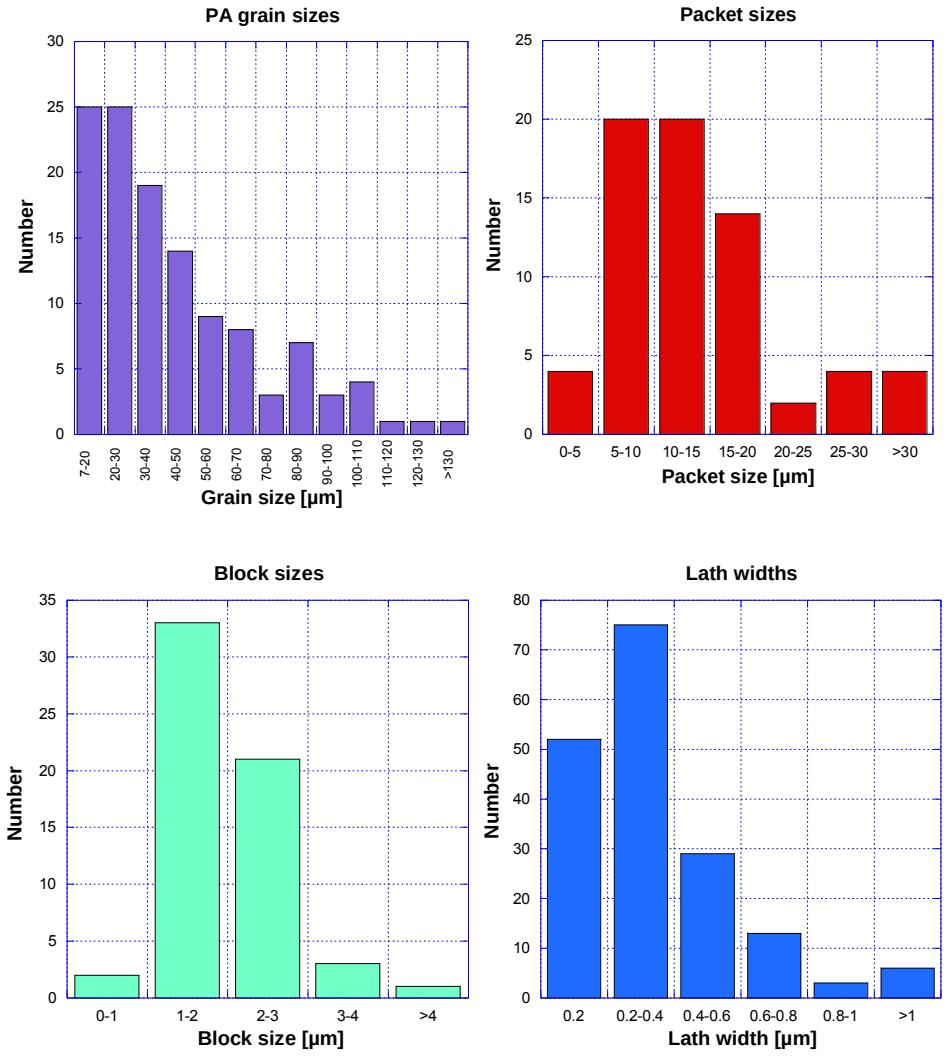

Figure 3-8 Distributions of each microstructural unit sizes for the studied martensitic steel

Galindo-Nava *et al.* [43] proposed a model for describing a complex martensitic hierarchical structure by employing as input parameters the prior austenite grain size, carbon content and

tempering conditions. These authors simplified the prior austenite grain geometry to hexagonal shape, packets to polygonal shapes, and blocks and laths to rectangular shapes. In reality all these structures have irregular shapes. They did all the sizing from 2D micrographs. Expressing the volumes of packets and blocks through their own sizes and the size of prior austenite grain, and also through the number of packets and blocks in one grain (from K-S orientation relationship between parent austenite and martensite), they deducted the formulae for determining the size of block and packet. According to them the packet size is about 40% of PA grain size, and the block size is 0.67% of PA grain size (Equation 3-3 and 3-4).

$$d_{packet} = \sqrt{\frac{3\sqrt{3}}{8N_p}} D_g = \sqrt{\frac{3\sqrt{3}}{32}} D_g = 0.40 D_g \qquad \text{Equation 3-3}$$

$$d_{block} = \frac{1}{N_b} d_{packet} = \frac{1}{6} d_{packet} = 0.67 D_g, \qquad \text{Equation 3-4}$$

where D_g is prior austenite grain size, d_{packet} is packet size, d_{block} is block size, N_p is a number of packets per PA grain, and N_b is a number of blocks per packet.

Figure 3-9 shows the relationship between prior austenite grain size D_g and packet (Figure 3-9a) and block size (Figure 3-9b) for some steels with different carbon content [38]. The solid lines represent the predictions employing the formulae in the Equation 3-3 and Equation 3-4 and the colored points in the form of different geometrical figures represent the experiments. The model illustrates considerable agreement with the measurements, indicating that the packet and block size are composition independent. Although constant block sizes are apparent for $D_g > 75$ µm, which can be due to the formation of additional sub-blocks. The model predictions are also different for $D_g < 10$ µm, since not all the crystallographic variants of K–S relation are present [37] and as a result not all blocks can form. It affects the number of packets per prior austenite grain and blocks per packet.

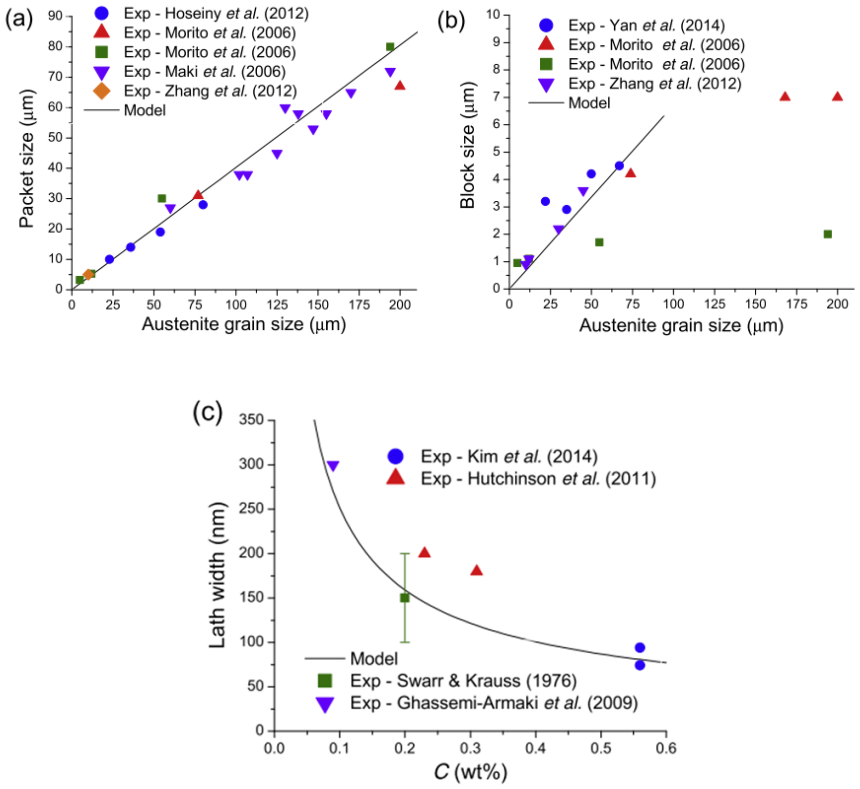

Figure 3-9 Link between the prior austenite grain size and (a) packet and (b) block size in various martensitic steels. (c) Lath width variation as a function of the carbon content in martensitic steels [43]

As for the lath sizes, they are independent of the grain size. This is due to the fact that the lattice strain at scale of lath is accommodated by the formation of interfacial dislocations at the lath boundaries [90]. This phenomenon supposes that the Cottrell atmospheres form within the boundaries, "*and the randomly distributed carbon atoms in the austenite phase (lath interiors) should relocate around these atmospheres. This implies that the lath boundary spacing (lath size) is such that it ensures complete carbon segregation within a block and the extent of carbon segregation in a lath boundary is controlled by the thickness of a Cottrell atmosphere* $d_{Cottrell}$*"*[43]. So, the lath width is rather a function of carbon content (Figure 3-9c).

Using formulae proposed by Galindo-Nava the range of sizes for blocks and packets for our material was defined. The obtained results correspond well to the measured values of sizes of PA grains, packets and blocks (Figure 3-8). In Table 3-2 the summary of the sizes of each unit of microstructure is presented.

Table 3-2 Microstructural unit sizes (packet and block size calculated using theoretical formulae) and disorientation angle types of the studied material

Element	*Size [µm]*	*Disorientation angle*
Grain	**10-60**	**HAB >10°**
Packet	**4-24**	**HAB**
Block	**0.7-4**	**HAB**
Lath	**<1**	**LAB <3°**

3.1.4 Mechanical properties

Some mechanical properties of the as received material were measured in the laboratory. The ultimate tensile strength UTS, elongation to fracture A and uniform deformation A_u were measured after a tension test on the Adamel Lhomargy-MTS DY35 Tension/Compression machine without extensometer control and at an average strain rate of $7 \cdot 10^{-5} s^{-1}$. The yield stress YS and modulus of elasticity E were determined on the stress-strain curve limited to 0.6% of total deformation (Figure 3-10) and obtained on the 63kN electromechanical computer-controlled Schenk Trebel testing machine with an extensometer directly fixed on the specimen. The test was performed at a strain rate of $4 \cdot 10^{-3} s^{-1}$ at room temperature and in air. The employed sample will be described next in the section *3.2.1Specimen concept and sample surface preparation*. As for the Vickers hardness H_V, it was measured on the polished as received samples with 5 kgf applied load. The summary of the measured values is in Table 3-3.

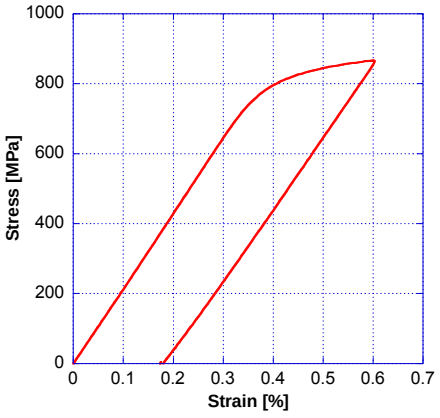

Figure 3-10 Stress-strain curve limited to 0.6% total deformation

Table 3-3 Mechanical properties of material

Property	UTS, MPa	YS, MPa	A, %	A_u, %	E, GPa	H_V (5 kgf)
Measured value	**1000**	**750**	**37**	**24**	**220**	**295±5**

3.2 Experimental procedure of fatigue test

3.2.1 Specimen concept and sample surface preparation

The flat specimens of indicated geometry in the Figure 3-11a were prepared by electrical discharge machining at *Macker Erosion company*. The samples were 72 mm long. The grip section width was 18 mm, while the thickness was 3 mm. The gage length constituted 12 mm. The specimens have flat geometry because it is more convenient for the AFM technique.

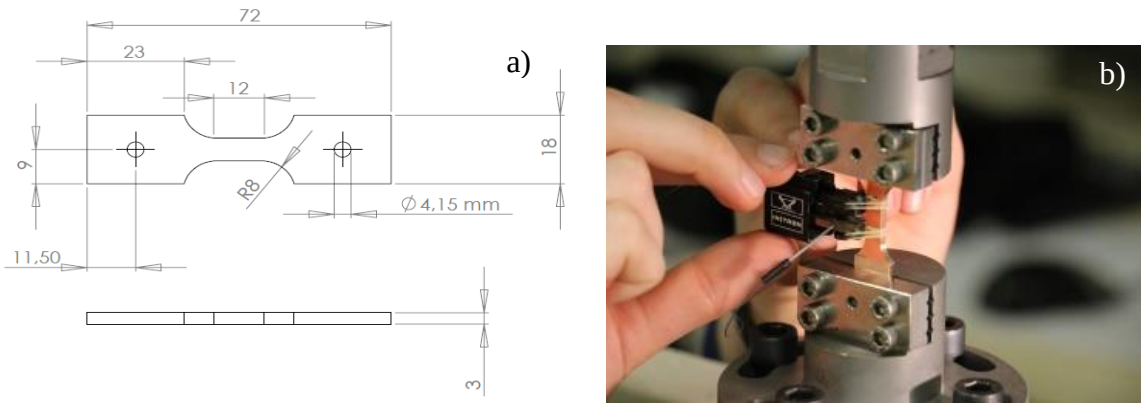

Figure 3-11 a) specimen geometry; b) extensometer mounted on the specimen installed in the fatigue machine

The AFM is highly sensitive to the specimen roughness and limited to the maximum topography of about 6 µm height for each scan. That's why the specimen surface was prepared by mechanical polishing with a help of self-controlled Buehler Phoenix 4000 Sample Preparation System. The samples were ground to 1200 grit paper, followed by polishing with 9, 3 and 1 µm water based diamond suspensions. The final step consisted of 1 minute cleaning in water on the Struers polishing disk MD Chem^{TM}. It should be noted that the surface roughness measured by AFM of freshly polished specimens made on average 2 nm.

3.2.2 Fatigue test and fatigue behaviour

Low cycle fatigue tests at a total strain range $\Delta\varepsilon_t$=1.2% were performed on mechanically polished flat specimens at room temperature and in air using the electromechanical Schenck Trebel RMC10 machine with a capacity 63 kN. The triangular signal at a strain rate $4 \cdot 10^{-3}$ s^{-1} and a strain ratio R_e=-1 was imposed. The strain was measured by means of an extensometer with 8 mm gauge length (Figure 3-11b).

At first, the stress response as a function of the number of cycles (see Figure 3-12a) was identified by cycling of two fatigue specimens. The additional experiments were performed to study the damage relief for a given fatigue life fraction. All these experiments required 10 specimens. The interrupted test was carried out on one of the specimens and the stops were executed at ¼ cycle, 100, 500, and 1130 cycles (the failure) for the surface relief analysis by AFM and SEM. By agreement, we will call the first interruption "1/4 cycle" even though the specimen is a little more deformed because of the unloading of the specimen to a load value equal to zero because of technical reasons.

In Figure 3-12a the change of stress amplitude as a function of loading cycles shows the drastic stress decrease during approximately first 100 cycles. After that the softening rate reduced, but it has never been completely stabilized. This kind of behaviour is quite usual for martensitic steels loaded in LCF [8], [15], [64], [91], [92] and the microstructural reasons of softening are detailed in *2.3.2Fatigue behaviour of 9-12% Cr martensitic steels and resulting microstructural evolutions*. The lifetime of the steel in LCF with imposed total strain range 1.2% in each cycle was 1130 cycles. The plot of plastic strain variation with a number of cycles (Figure 3-12b) illustrates that the plastic deformation increases from 0.36% to 0.43% during the lifetime. It confirms the real cyclic softening. This result is an agreement with the studies of Junak and Ciesla [91].

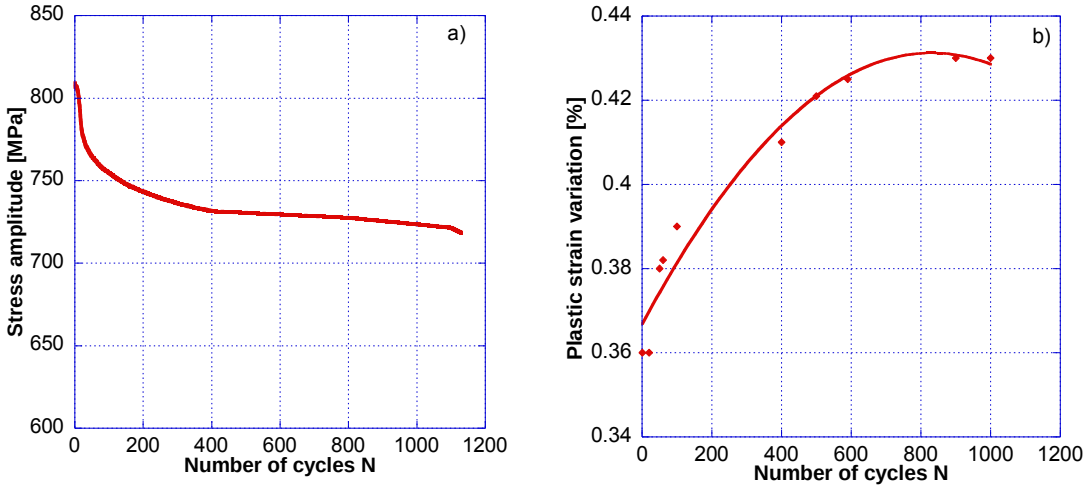

Figure 3-12 a) stress amplitude evolution as a function of number of cycles; b) plastic strain variation as a function of number of cycles

3.3 AFM

Atomic force microscope (Figure 3-13) was essentially used in this thesis to perform the evaluation of deformation relief appeared during the fatigue loading of studied steel specimens. Indeed, the main AFM advantages are 3D imaging and quantification in the z-direction of surface topography with vertical resolution which can be less than 0.1nm.

The principal components of AFM are represented in the Figure 3-14. It consists of cantilever holding the tip and driven by a piezoelectric scanner, mirrors redirecting the laser spot from the cantilever to the photodiode detector and electronic systems of control.

The main idea of AFM is that a tiny pyramidal tip with a radius of curvature of the order of a few nanometers scans a surface line by line through the x-y piezoelectric scanner. So the tip interacts with the surface and the forces of interactions are the atomic forces. They are of the order of nanonewtons. It might be the forces of attraction or repulsion. The forces and their evolutions are detected and measured by the variation in the deflection of cantilever. This deflection is quantified by the reflection of laser spot on the split photodiode detector. Depending on the type of forces the AFM works in different configurations. Thus, different information concerning the surface can be obtained. The most used result is the topography of surface.

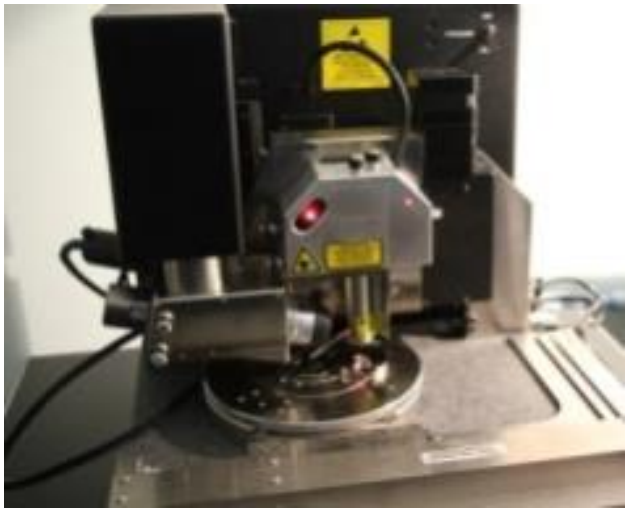

Figure 3-13 AFM

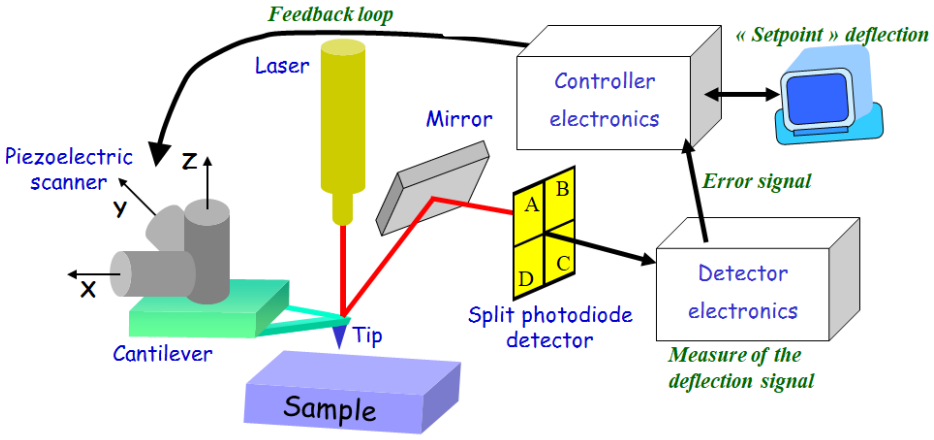

Figure 3-14 Principle parts of AFM

To obtain the topographic data of surface, the interactions between the tip and the sample are maintained generally constant. The evolutions of the surface topography induce some variations of interactions and so the evolution of the deflection or of the deflection amplitude of cantilever. The latter are minimized by a change in the vertical position of tip, and so a vertical scanner movement.

3.3.1 Force curve

Force curve is obtained in one point (no scanning in x and y directions) and represents a plot of the evolution of cantilever deflection with the z-distance between the tip and the sample surface (Figure 3-15).

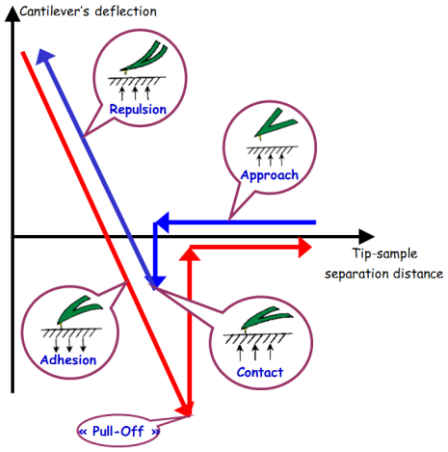

Figure 3-15 Force-distance curve: blue arrows represent an approach, red arrows - retraction

During approach, first the cantilever is moved down without touching the sample, i.e. no deflection but a declining distance is measured (Figure 3-15). At some tip-sample distance, the attractive forces (usually Van der Waals) overcome the cantilever spring constant and the tip jumps into contact with the sample. Once the tip is in contact with the sample, it remains on the surface as the separation between the base of cantilever and the sample decreases further, causing the increase of repulsive contact force and so the deflection of the cantilever.

As the cantilever is retracted from the surface, often the tip remains in contact with the surface due to some adhesion and the cantilever is deflected downwards until it suddenly loses contact and flicks up into its initial position (“pull-off”). Further retraction results no longer in a deflection.

3.3.2 Contact mode

In the contact mode the tip “touches” the surface continuously. The forces of interaction are the elastic repulsive forces F (Figure 3-16). They are responsible for the deflection Δz of cantilever according to the Hooke’s law $F=k\Delta z$, where k is the stiffness of cantilever. The topographic

images are generally obtained by keeping the cantilever deflection constant (constant force mode). Thus, the feedback loop maintains the constant deflection (the setpoint deflection for a user) of cantilever by vertically moving the tip. The z-displacement of tip corresponds to the topography of surface.

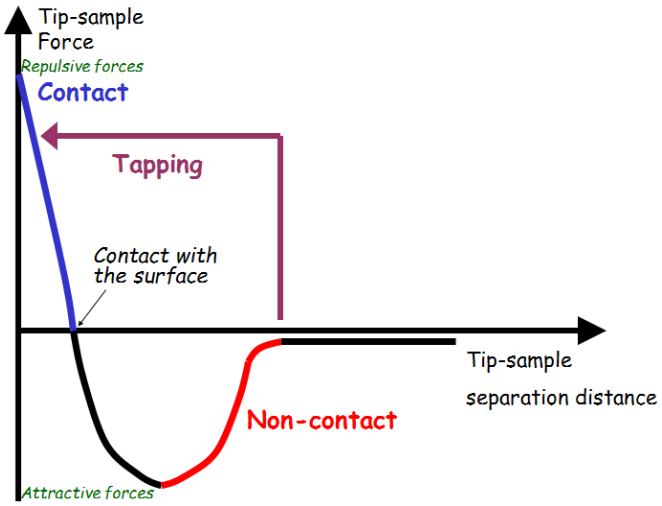

Figure 3-16 Force-distance curve of the interaction of tip with a sample surface revealing the different AFM modes

The contact mode is used for relatively "hard" materials; otherwise the tip or the sample surface can be damaged by the excessive contact forces.

3.3.3 Intermittent (tapping™) mode

The tapping™ mode was used for all the presented imaging of AFM in this work. This mode is an "average" between contact and non-contact modes. The idea of tapping mode, as of non-contact mode, is to work with non-contact forces, i.e. essentially with the Van der Waals forces, in order to limit the contact between the tip and the sample. However, contrary to non-contact mode the tip touches the surface at each oscillation to avoid the interruption of interactions between the tip and the surface and to keep better stability of the system "tip+surface". Because of the very low values of Van der Waals forces, their variations cannot be detected directly by evolutions of cantilever deflection. But their variations in amplitude are easier to measure. That is why in tapping mode, as in non-contact mode, the cantilever with the tip is oscillated. During scanning, because of the evolution of topography or other surface properties, the interactions between the tip and the surface change and induce the modifications of resonance frequency

and so a change of cantilever vibration at a given frequency. Near the cantilever's resonance frequency, this change in amplitude is large and thus easier to be detected. Hence in tapping mode the AFM works at a fixed frequency of oscillation and an operator imposes a constant oscillation amplitude, and so a constant tip-sample interaction. The vertical position of scanner, and thus of tip, is adjusted to keep the oscillation amplitude constant. The cantilever in tapping mode oscillates near the surface at a distance approximately 10 nm from the surface with fixed amplitude ranging from 20 to 100 nm according to the material. Although in every low point of oscillation track it touches the surface.

Thus, both attractive and repulsive forces of interaction are alternatively present (Figure 3-16). Before scanning the surface, the resonance frequency of cantilever is determined. Then, the cantilever is oscillated slightly below its free resonance frequency with fixed amplitude (amplitude "setpoint").

When the tip encounters the surface defects, either a "hill" or a "hole", the interaction force between tip and sample surface changes. If it is a hill the value of surface-tip interaction repulsive forces rise up changing also the cantilever vibration frequency. Consequently the cantilever oscillation amplitude changes and it does not correspond anymore to the amplitude setpoint defined by the AFM operator at the beginning of scanning. The amplitude change is measured by highly dense and thus with an excellent spatial resolution laser, reflected off the cantilever onto 4-quadranted photodiode (Figure 3-14). The mirror increases the length of reflected laser signal pathway and thus the sensitivity is increased too. The photodiode is a detector of vertical and horizontal cantilever bending and torsion. And it is also the one who sends this information to electronics. The electronics, in its turn, records the amplitude change and also it sends the command through the feedback loop to the piezoelectric scanner to compress (to move the whole probe upwards) in order to compensate this difference in the amplitude at the given point of surface and the amplitude demanded by the control operator. In such a way the feedback loop maintains constant the oscillation amplitude (setpoint amplitude) to keep constant the photodiode signal which is the measurement of cantilever oscillations. As a result, finally, the amplitude of cantilever oscillations corresponds to the setpoint and the tip continues scanning. The z-movement of cantilever due to the piezoelectric scanner vertical displacement corresponds to the surface profile.

The principle advantage of the tapping mode is that the tip is not in constant contact with the sample, which means the probability that it can damage the observed sample or the scanning tip is low. Another advantage of this mode is the capacity to scan very rough surfaces.

3.3.4 Image types

In this thesis two types of images were mainly used: height image and amplitude signal error image. The data of z-piezoelectric scanner movements create a height image (topography of surface), while the signal amplitude error image is the difference between the amplitude setpoint and the instantaneous registered amplitude of oscillations. As far as the amplitude is measured via photodiode detector, the data are expressed in volts. The latter type of imaging measures the evolution of oscillation amplitude before correction by the feedback circuit via height adjustment by the piezoelectric scanner. On the amplitude signal error image the negative values appearing in dark correspond to an upward slope ("hill") and the positive values in light to a downward slope ("hole").

3.3.5 AFM image resolution

3.3.5.1 Vertical resolution

The vertical resolution depends on the piezoelectric scanner resolution and on the dimensions of observed surface features. Due to the high sensitivity of the piezoelectric scanner the z-resolution can reach 0.1 nm if the sample is well prepared. However, in the present work it is rather 1 nm due to the relatively big dimensions of observed features.

3.3.5.2 Lateral resolution

Firstly, the spatial resolution is limited by the tip curvature radius. Secondly, it also depends on the specimen surface roughness. Apparently, less roughness favors the better lateral resolution. Thirdly, the environmental conditions of AFM scanning influence the force interaction intensity, which in its turn may change the resolution. And finally, the lateral resolution also depends on the scan size and number of scan samples per lines. For example, if the image size is 20x20 µmxµm, and during imaging the value of "samples/line" was chosen 512, the spatial

resolution for this image is believed to be about 40 nm (20 µm/512). In this work the best lateral resolution is about 8 nm.

3.3.6 AFM topography image artefacts

The artefacts in AFM can be subdivided in three major groups: 1) artefacts caused by probe; 2) by scanner; and 3) by image processing. Other sources of artefacts can be vibrations, surface contaminations, presence of water film at the surface, temperature change, etc. Most of the scanner and image artefacts can be avoided or processed. But as for the probe artefacts, they are rather the limitations than artefacts that are due to the geometry of a tip or surface under the tip. In the next paragraphs some artefacts will be shortly discussed.

Despite the high spatial AFM resolution, the particular sizes and geometry of tip can be a cause of image artifacts sometimes. So the tip size and geometry are the key factors of our image interpretation because any AFM image is a convolution of tip shape and sample feature shape.

The tip is supposed to be sharper and smaller than the scanned feature. The sharpness is defined by the tip pyramid angles and the radius of tip curvature.

AFM tip pyramid angles, namely front angle (FA) and back angle (BA) (Figure 3-17a), and also the probe inclination angle relatively to the horizontal and the scanning angle and direction have to be taken into consideration. In the Figure 3-18 the tip cannot properly scan the features with angles exceeding the angles indicated on the image. In the Figure 3-19 there is a resultant image of AFM scanning. When it is scanning the steps the tip edge rib (spatial extension) touches the step edge earlier than the tip apex, consequently tip spatial extension does not permit to scan at the upper corner of step. The tip jumps on the step once its spatial extension touched the step edge.

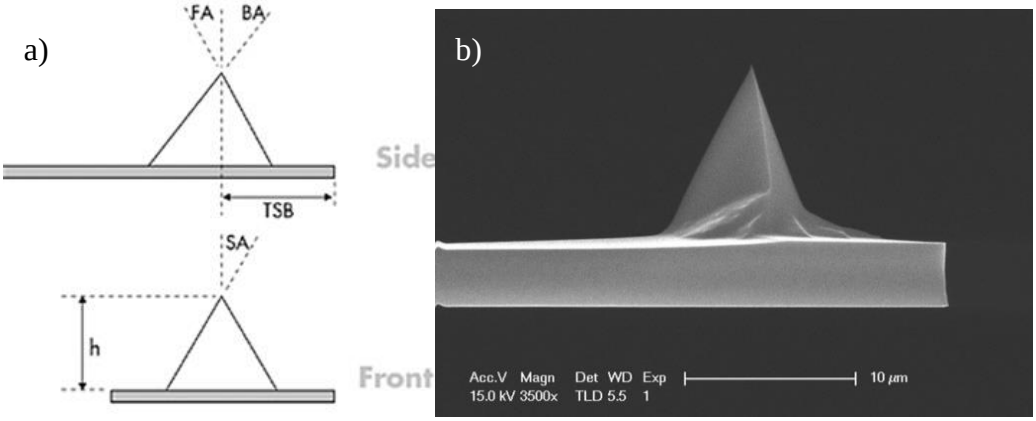

Figure 3-17 a) tip schematics with angles defining the tip: FA – front angle; BA – back angle; SA – side angle; TSB – tip setback; h - height; b) Bruker RTESPA-300 probe (Bruker company)

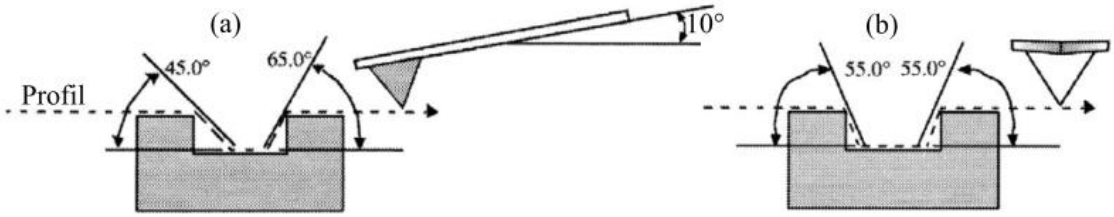

Figure 3-18 Angle limitations in contact mode: a) scanning parallel to cantilever; b) scanning perpendicular to cantilever [93]

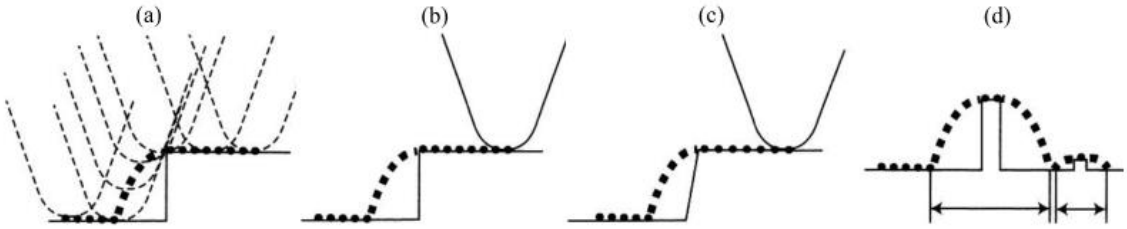

Figure 3-19 Artefact caused by the tip geometry [94]

In the present work Bruker RTESPA-300 probe is used (Figure 3-17b). Its front angle is 15°, and its back angle is 25°. It means that this tip cannot properly scan the features with angles exceeding 75° and 65° respectively if the scanning direction is parallel to the cantilever longitudinal axis.

Another problem of AFM proper scanning is orifices and cracks. When the tip is scanning a dimple, one can never be sure about the depth of the dimple because if it is too deep, the tip shape would restrict the scanning deep inside this dimple.

Polak *et al*. [95] have found the way to avoid this artifact by applying the plastic replica on the surface. This replica repeates the shape of surface features. Then the authors remove the replica from the surface and they do the AFM analysis of the inverserd replica surface. However, it should be mentioned here that if the intrusion dimensions are smaller than the replica's width, this solution is not anymore useful.

Thus, *Man et al*. [96], studying the surface relief of 316L steel after fatigue, revelaed that only the slope of the left side of extrusion (Figure 3-20) fulfilled the geometrical conditions imposed by the tip angles. As far as the slope of the right side of extrusion was not properly reflected, the width of extrusion measured by AFM could not be trusted. However, the tip geometry did not affect the height measurements. As for the intrusions, unfortunately the real depth could not be measured properly.

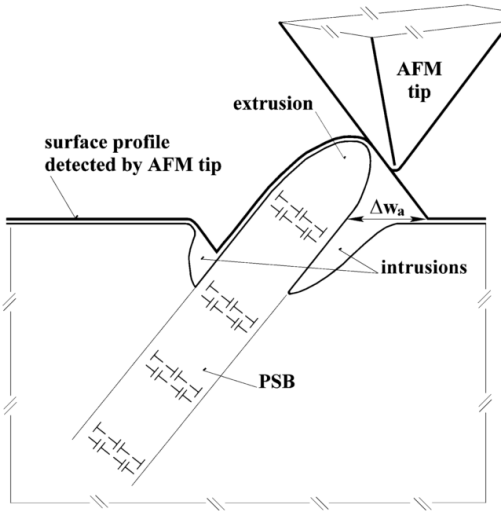

Figure 3-20 Schematic surface profile at the emerging PSB consisting of an extrusion and two intrusions. The distortion of the real surface as detected by the AFM tip is shown [96]

3.3.7 AFM Peak Force™ mode

Peak force quantitative nano-mechanical (PF-QNM) tapping™ mode developed by Bruker Company allows mapping the local elastic properties with theoretical lateral nanometer

resolution. The mode operates similarly to the tapping mode but at a non-resonant frequency. In this mode the maximum (peak) force is set to be constant for each measurement [97]. The method is based on the recording of force curves at each pixel of height image (Figure 3-21).

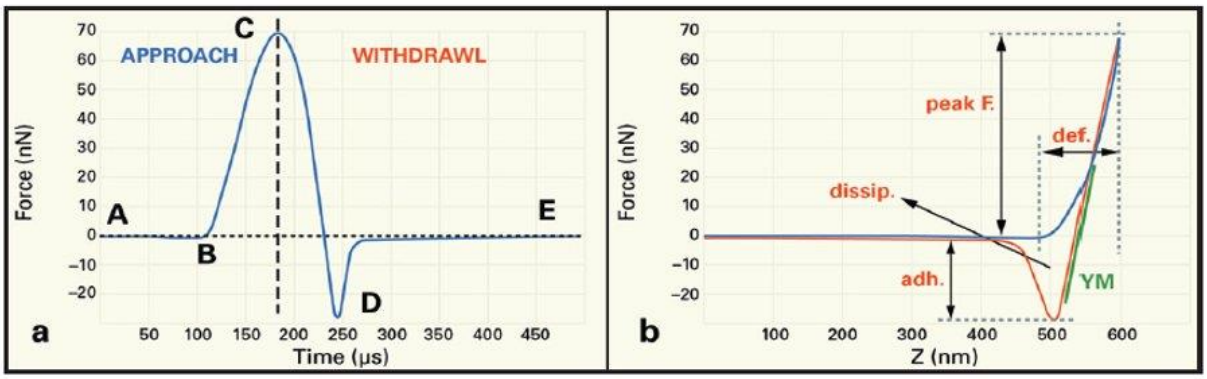

Figure 3-21 a) One cycle of the Peak Force tapping curve: A – non-contact force, B – jump into contact, C – peak force and contact with the surface, D – tip pull off, maximum adhesion forces, E – non-contact force. This process is repeated at every XY pixel in the image, at a rate of typically 2000 Hz; b) Resulting quantitative measurements

The difference with a conventional force curve is that the z-position is modulated not by a triangular signal but a sine wave signal. This helps to avoid the unwanted effects at the turnaround points of force curves. These curves are processed instantaneously. The slope of the withdrawing part of curve will indicate the local elastic modulus. In each force curve the program calculates the nano-mechanical properties taking into account the calibrated cantilever spring constant and tip radius. Usually the analysis is performed through the Derjaguin-Muller-Toporov (DMT) fit model for retracing curve and spherical indenter. The model includes the adhesion effects between the sample surface and the tip:

$$F = 4/3 \cdot E\sqrt{R} \cdot \sqrt{d^3} + F_{adh} \qquad \text{Equation 3-5,}$$

Where F is an applied force, R is a tip radius, d is a deformation value at the given force, F_{adh} is the maximum adhesion force and E is an effective elastic modulus that can be defined as:

$$1/E = (1-\nu^2)/E + (1-\nu_i^2)/E_i \qquad \text{Equation 3-6,}$$

E(ν) and $E_i(\nu_i)$ are the Young's modulus (Poisson's ratios) of the sample and indenter respectively.

The Sneddon model can be used to take into account the conical form of indenter.

Metallurgists applying the PF on the hard metallic surfaces are very rare. One of them is Morales-Rivas *et al*. [98]. They concluded that the PF allows mapping the sample elastic modulus with high lateral resolution and simultaneous conventional AFM topographical imaging. The authors evaluated the local elastic modulus of the austenite and ferrite nanophases in the nanostructured bainitic steel and concluded that the observed differences in Young's modulus between austenite and ferrite were negligible (Figure 3-22). However, they noticed that it was possible to obtain the reliable data only on the "flat" areas and not in the interfaces between two phases.

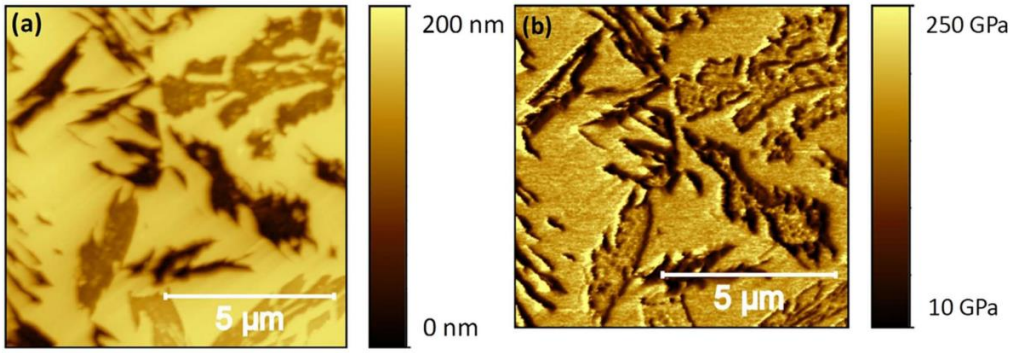

Figure 3-22 The topographical map (a) and E map (b) of etched bainitic steel sample measured by PF-QNM [98]

3.3.8 AFM equipment and conditions for the imaging in the present work

The majority of AFM analysis on the surface was performed with a help of Veeco Dimension 3100 Atomic Force Microscope in intermittent (tapping™) mode with a silicone probe Bruker RTESPA-300. Its tip curvature radius is 8-12 nm, front angle is 15°, and back angle is 25°. The maximum scan area of one image with AFM is 100µm*100µm and the maximum evolution of topography for one scan is 6µm.

As for the Young's modulus measurements, they were performed at room temperature and in air in Peak Force tapping™ mode on the Dimension Icon AFM of Bruker at Bruker Palaiseau

in France. Used AFM probe was DNISP-HS model with a diamond tip with a resonant frequency 68 kHz, average spring constant 390 N/m and nominal radius 40 nm. The loading forces were about few microns, and the probe oscillation frequency was 2 kHz with typical peak-to-peak amplitudes 300 nm in air. The tip was calibrated on sapphire sample in order to set the deflection sensitivity. It should be mentioned here that the diamond tip may eventually be contaminated during the analysis process. If it occurs the tip has to be cleaned on gold surface.

3.3.9 AFM for studying the fatigue and tensile plasticity

In order to show the capacities of AFM to investigate the tensile and fatigue damage of metallic materials in the following paragraphs some studies on the cyclic and monotonic deformation of different metals and metallic alloys will be discussed.

3.3.9.1 AFM in the studies on the different metals and metallic alloys

Early stages of surface relief evolution of persistent slip markings (PSMs) in polycrystalline austenitic stainless steels, copper, etc. cycled with constant strains at different temperatures were studied by means of AFM by Serre, Salazar, Man, Polak and others [4], [99]–[101].

Thus, for example, Salazar [100] has contributed to the comprehension of mechanisms of monotonic and cyclic plastic deformation of duplex stainless steels thanks to AFM technique. Besides describing the different morphologies of observed PSMs, he could conclude that the cyclic plasticity of the steel is a progressive contribution of the activity in two phases and their interactions (Figure 3-23).

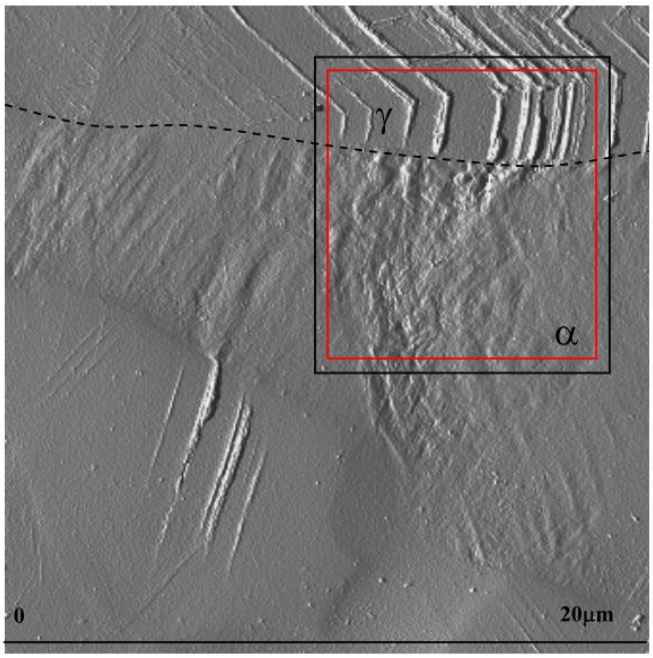

Figure 3-23 Different morphologies of deformation relief in austenitic and ferritic phases of a duplex steel imaged by AFM after LCF test at $\Delta\varepsilon_t$=1.6% [100]

Man *et al*. [102] use often the AFM in their studies of deformation relief after LCF of copper, austenitic and ferritic steels. Thus, they showed that the extrusion growth is temperature dependent in their study of LCF of different materials at different temperatures. AFM technique was used by them for monitoring the extrusion height evolution. In Figure 3-24 the growth of extrusions is displayed on the correspondent AFM images.

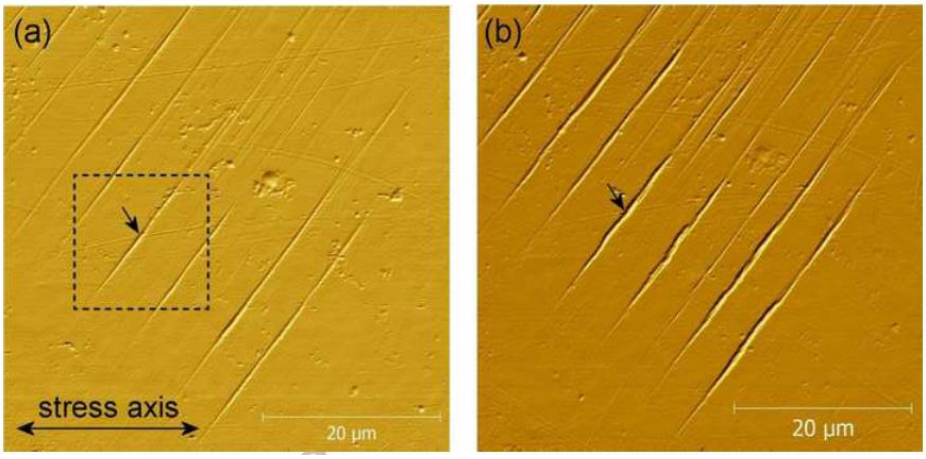

Figure 3-24 Surface relief within a grain of 316L steel fatigued at ε_{ap}=0.003 at 300 K as obtained by AFM after (a) 100 cycles and (b) 250 cycles. AFM micrographs are displayed in shadowed format [102]

Risbet *et al*. [103] studied the fatigue damage of nickel-based alloy coupling AFM and EBSD techniques. They showed that the value of 50 nm for the average extrusion height is a necessary though not sufficient condition to induce cracking in a grain. Moreover, they successfully proved that there is no correlation between the height of extrusions and corresponding Schmid factor.

Fréchard *et al*. [104] investigated the monotonic plasticity of duplex stainless steel by AFM and EBSD. As a result she witnessed the slip transmission phenomenon between two phases (Figure 3-25) and could relate the height of slip steps to the number of emerging dislocations.

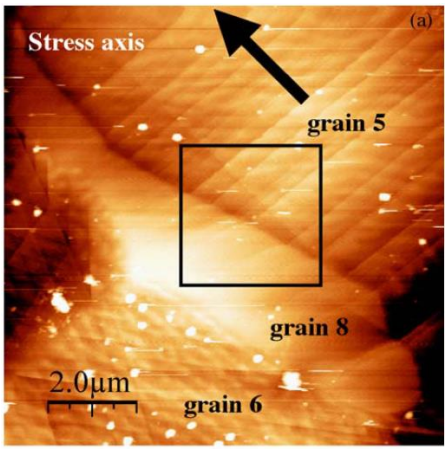

Figure 3-25 AFM height micrograph documenting slip transmission through phase boundary between grains 5 and 8 in a duplex steel [104]

3.3.9.2 AFM in the studies of martensitic steels

Fournier [8] observed plastic deformation of P91 (9Cr-1Mo) steel after the tests of fatigue. For the better understanding of the phenomenon he did the AFM measurements of extrusions but only for the samples that were fatigued in vacuum (Figure 3-26). The pictures show that the observed extrusions are very often accompanied by the intrusions. The measured extrusions can exceed the height 500 nm. The majority of extrusions were oriented 45° relatively to the loading axes, and a few of them are perpendicular. The ensemble of observations by AFM supposed that the emerged extrusions and intrusions were the origin of crack.

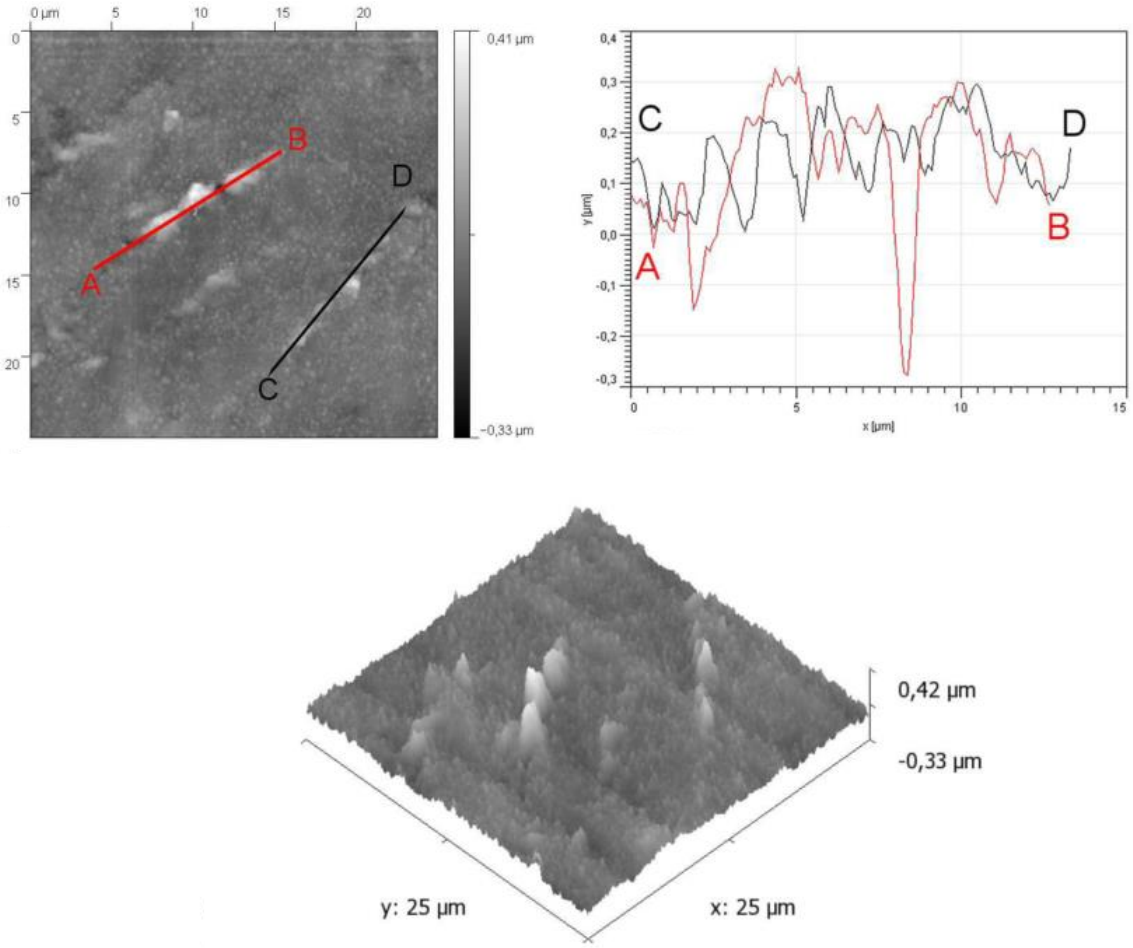

Figure 3-26 AFM observation of P91 steel surface with extrusions and intrusions after LCF test at 550 °C under vacuum at $\Delta\varepsilon$=0.7 % [8]

Hayakawa *et al*. [105] used intensively the AFM in their numerous studies on the martensitic steels, results of which are represented in many articles [105]–[107]. Due to their surface etching techniques they succeeded to recognize by AFM the blocks of 1 % Cr martensitic steel. They studied the surface evolution dependence on the various strains applied to the tensile specimen. Three different plastic strains 0.2%, 0.4% and 0.6% were applied. As a result the surface steps of 5–39 nm were observed in locally deformed blocks near prior austenite grain boundaries (Figure 3-27; Figure 3-28).

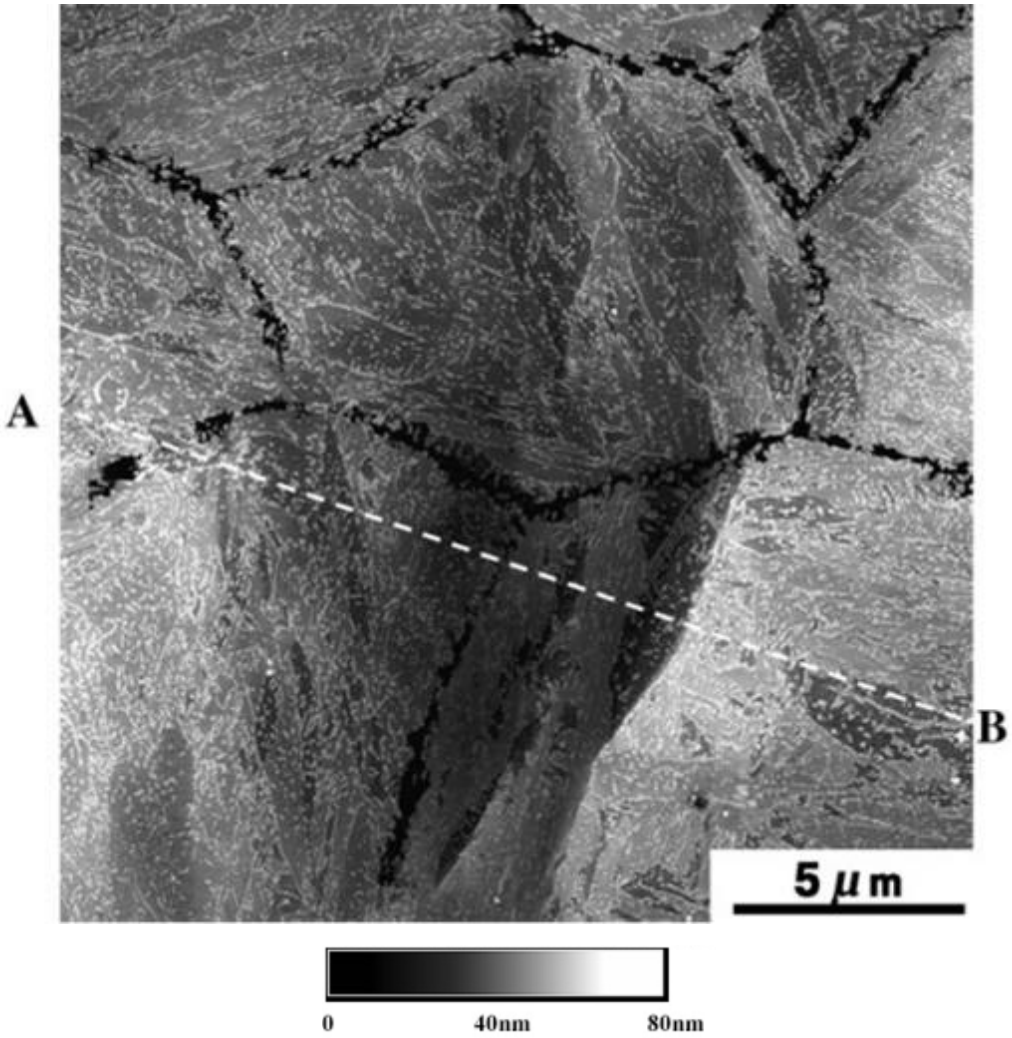

Figure 3-27 AFM image showing local plastic deformation, blocks and prior γ grain boundaries after monotonic plastic strain ε=0.6 %. This image was created by superimposing of two different AFM images: one reveals the prior austenite grain boundaries and another reveals the blocks. The loading axis is horizontal [105]

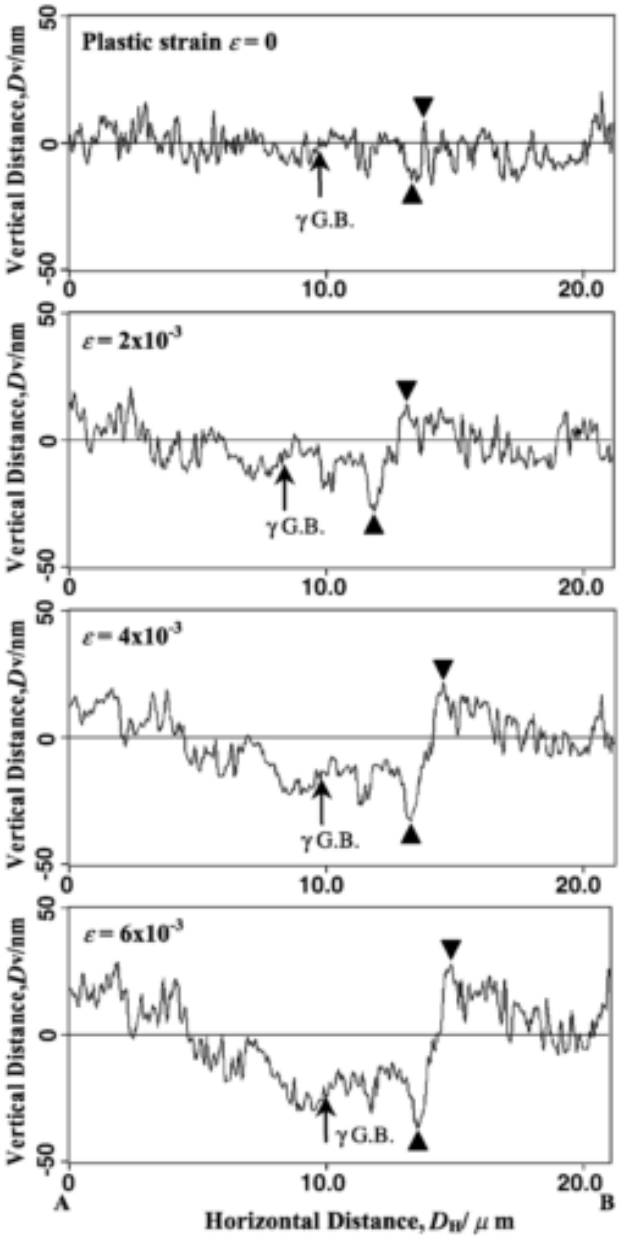

Figure 3-28 Profiles through line AB in Figure 3-27 [105]

To conclude, the summary of discussed above works and some other studies performed with AFM is presented in Table 3-4. Thanks to AFM technique, first of all, the cited authors were able to follow the evolution of height of surface features in the process of cyclic loading and to describe the observed features. But, as it appears, the AFM analyses needs to be combined with other techniques to obtain more fruitful results on the deformation mechanisms or other scientific issues.

Loading conditions	Material	Reference	AFM image	AFM contributions
LCF, vacuum 550°C ε=0.7%	Martensitic P91 (9%Cr)	Fournier 2007	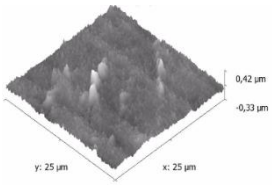	• observations of extrusions and intrusions • measurement of heights that can reach 500 nm
LCF, air RT εp=0.2%	Ferritic X10CrAl24	Man et al. 2004	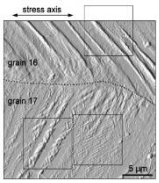	• characterization of PSMs, extrusions, and intrusions • observation of PSMs at the very beginning of cycling • measurement of the angle between PSM and loading axis • height measuring • 3D imaging and profiling
LCF, air 93, 173, 573K εp=0.01%	Austenitic 316L	Man et al.2014	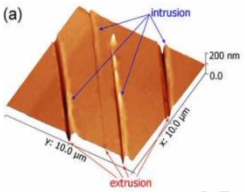	• for all three temperatures the PSMs and PSBs are observed • growth of extrusions is temperature dependent
tensile test, RT ε̇=0.005mm/min	Duplex austenic-ferrtitic steel URANUS 50	Fréchard et al. 2005	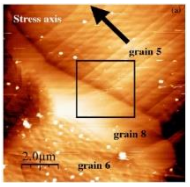	• combined AFM and EBSD in-situ investigation • the number of emerged dislocations was related to the step height: 10 nm of height correspond approximately to 50 dislocations
tensile test, RT ε=0.2; 0.4; 0.6%	Martensitic JIS-SCM440 (Cr 1,12%)	Hayakawa et al. 2003	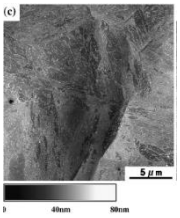	• surface steps with 2-39nm height in locally deformed blocks near prior gamma-grain boundaries were measured by AFM
LCF, air RT ε=0.4; 0.6 %	Martensitic PH 13-8 Mo (Cr 12,4%)	Cretegny et al. 2002	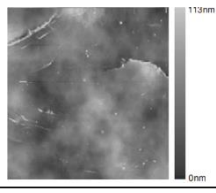	• at 0,4% small "streaks" were observed about 2µm long • at 0,6% extrusions with a length up to 25µm and heights from 10 to 200 nm
LCF, air, RT Δε=0.5%; 1.6%	DSS 25Cr-7Ni-0,25N	Vogt et al. 2009	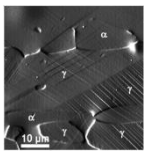	• plasticity evolution and partition in austenite and ferrite phases
LCF, air, RT εp=0.05; 0.03; 0.9 %	Nickel-base superalloy	Risbet et al. 2003	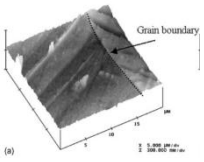	• evolution of surface relief

Table 3-4 Summary of some works on fatigue and tension of metallic alloys by AFM

3.4 TEM

Philips CM30 Transmission Electron Microscope (TEM) was used for the observations in this work. Equipped with LaB_6 filament, this microscope produces 300kV maximum accelerating voltage. It is also furnished with EDX detector for local chemical analyses. In the following paragraphs, firstly, the main principles of work of TEM will be discussed and then FIB method of thin foils preparation will be presented.

3.4.1 Principle of work

Transmission electron microscopy (TEM) is a technique in which the electron beam passes through an ultra-thin specimen. The interaction of beam with the specimen creates an image which is magnified and focused onto an imaging device (fluorescent screen).

3.4.1.1 Bright field imaging

Different modes of TEM, based on the ability to change lens strength, exist. The most known one is a bright field mode. In this mode the aperture of a single beam is centered on the main transmitted beam (Figure 3-29). In dark field mode the aperture is placed over one chosen diffracted beam. The image in the bright field mode is formed directly by absorption of electrons in the specimen. Thicker regions of the sample, or regions with a higher atomic number, will appear dark, while regions with no sample in the beam path will appear bright. The image is a simple two-dimensional projection.

3.4.1.2 Imaging of a dislocation

The contrast produced by a dislocation is due to the deformed planes of atoms near the dislocation. Because of this deformation the diffraction conditions in the dislocation are different than in the perfect non-deformed crystal. So the diffracted beam path will be deformed and will interfere the transmitted beam when entering the objective aperture. In bright field mode if the planes near dislocation are bent into a diffraction position, then the transmitted beam intensity will be reduced and the dislocation will be as a dark line on the fluorescent screen [108].

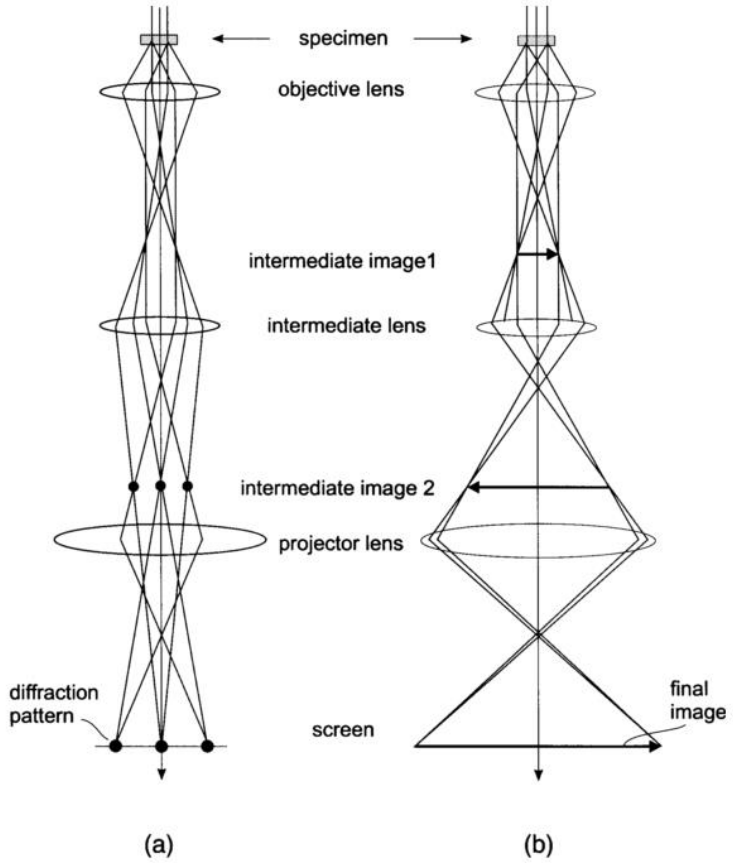

Figure 3-29 The sketch representing how a diffraction pattern (a) and contrast image (b) are created in TEM [108]

3.4.2 FIB for TEM thin foils preparation

In this work the FIB inserted in FEI Strata DB 235 dual beam microscope was used. The ion column with gallium liquid metal ion source develops the accelerated voltage from 5kV to 30kV and produces the current intensity from 1pA to 20nA.

3.4.2.1 Principle of work

In Figure 3-30 the basic elements of FIB instrument are present. They are sample stage, ion column that emits the ion beam on the sample surface, detector for the detection of secondary electrons, and gas injection needles used for the deposition of different materials on the sample surface. They are all comprised in a vacuum chamber. The FIB instrument very often comprises SEM instrument.

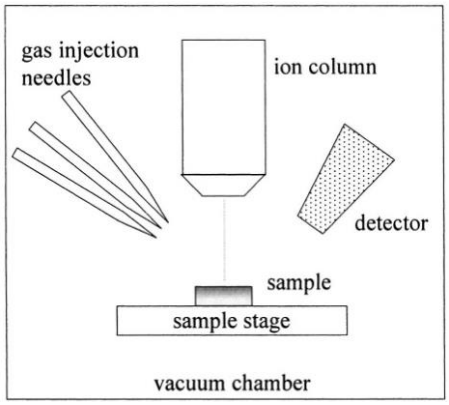

Figure 3-30. Basic FIB instrument [109]

The FIB operates in a similar manner as SEM but instead of using the electron beam it uses the ion beam, so that the low beam currents are used for imaging and high currents – for sputtering.

For the ion emission the FIB instruments use mainly the gallium (Ga) metal. The Ga^+ ions are produced by LMIS (Liquid Metal Ion Source). The heated Ga wets a W (tungsten) needle and under electrical field Ga forms a point source of ions at the end of the needle. Ga has next advantages relatively to other metals: low melting temperature (30°C) which makes it easy to achieve a liquid state for operation and minimum interdiffusion with tungsten needle substrate; low volatility for conserving of metal supply; and mass which is heavy enough to mill the heavier material and not destroy it [110], [111].

The gallium (Ga^+) primary ion beam hits the sample surface and sputters a small amount of material in form of either secondary ions or neutral atoms. The primary beam also produces secondary electrons. As the primary beam scans the sample surface, the signal from the sputtered ions or secondary electrons may be collected to form an image [109].

At low primary beam currents very little material is sputtered and modern FIB systems can easily achieve 5 nm imaging resolution. At higher primary currents a large quantity of material can be removed by sputtering allowing precision milling of the specimen down to a sub micrometer or even a nanoscale.

3.4.2.2 Extraction of thin lamella for TEM observation

There are two main applications of FIB: FIB contrast imaging and FIB sputtering and deposition. The latter was used in this work in order to extract the thin lamellae FIB for TEM observation of material microstructure directly under deformation relief. The advantage of lamella FIB is that the area of extraction may be chosen with a good precision. The production of thin lamellae FIB consists of three main steps:

1) Deposition of protective layer. Once the area of interest is defined, platinum or carbon (Figure 3-31a) is used very often for the protection of sample surface against the sputtering and implementation of Ga^+ ions in the surface layers of material under research. The thickness of platinum or carbon layer is approximately 1µm. Some FIB operators may deposit both carbon and platinum.
2) Ion machining of lamella. The production of lamella begins with the ion beam energy 20-30 keV. At approximately 10 µm on the both sides of the area of interest a trench (Figure 3-31a) is dug. The angle of incidence of ion beam on the surface is normal. The width and depth of these trenches are usually about 10 µm. Once the beam is close to the area of interest the beam energy is reduced to 3-7 keV and the milling continues with an angle of incidence 7° till the lamella is thin enough for observations but thick enough to be lifted out.
3) Lift out of thin lamella. It can be done inside or outside the FIB instrument. The lamellae observed in this work were lifted out and transferred on the support inside the instrument. Sides and base of lamella are cut by ion beam and transferred on the special support grid, which is copper M-grid in this work (Figure 3-31b). The sides of lamella are welded by platinum between two inside bars of “M” on the grid. In this work the additional thinning was performed on the lamellae mounted on the support under very low energy of beam. The purpose of this milling was to clean the lamella off the exterior amorphous layer. The thickness of final thin lamella is about 100 nm.

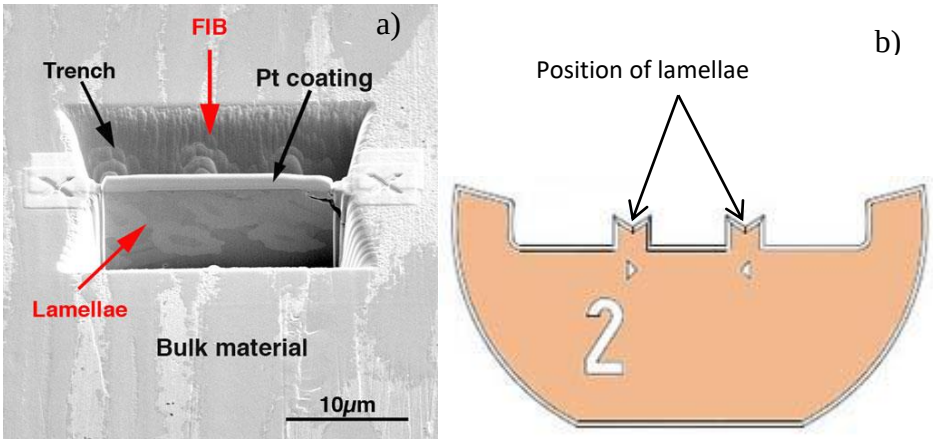

Figure 3-31 Extraction of lamella FIB (a); copper M-grid (b)

3.4.2.3 FIB artefacts

Every TEM specimen preparation method has its own procedure artefacts. Below, the most commonly encountered artefacts of FIB instrument during machining of thin lamellae are discussed and the known methods for avoiding the problem are proposed:

1) Ion beam heating

During ion milling almost all of the ion kinetic energy is finally converted to heat. Small amounts of this energy transform into defects in the sample or emitted as energetic particles. The maximum temperature reached in a sample depends on the beam power P, sample thermal conductivity k, sample geometry, and contact to a heat reservoir. Beam powers in commercial systems have maximum values of 1 mW. When the ion beam is incident on a flat surface, the temperature increase T in the sample is given by

$$T=P/(\pi ak), \qquad \text{Equation 3-7}$$

where a is the radius of circular ion beam profile on the sample surface. The values of P/a available in commercial FIBs are between 1 W/m and 1000 W/m. As a result the temperature rise according to the formula above can be both negligible for the samples with good thermal conductivity and importantly high for poor conductors. For example for stainless steels with a thermal conductivity k = 16 W/mK (The Engineering ToolBox), the maximum temperature rise is 19K.

When it is working with structured samples with high aspect ratio, the higher temperatures can be reached, because the specimen geometry blocks the heat transfer [113].

2) Ga contamination and sputtered specimen material contamination

Some Ga^+ ions could be implanted in the specimen despite the near grazing angle (angle close to 0°) between the ion beam and the specimen surface. Also the sputtered specimen material may land on another part of the specimen obstructing a clean view of the specimen. To avoid this problem the platinum coating is applied before proceed to milling. The gas assisted system incorporated in FIB instrument deposits the platinum coating with a width 1 µm in average.

3) Ion beam damage

Because of the high energy of ion beam the damaged layer on the specimen surface is one of the greatest problems for TEM observation of FIB lamellae. The damage is represented by amorphous layer in the majority of cases [114], [115]. But sometimes the dislocations or point defects can be inserted too [116]. To avoid these artefacts the final milling under very low beam energy should be performed before lift out. For example it was shown that in the case of Si the sidewall damage was reduced to 0.5-1.5 nm for the used ion energy 2 keV and at an 88° incident angle [117].

In conclusion, Andrzejczuk *et al*. [116] reported a few parallel dislocations in austenite very near the surface and ending at the free specimen surface as a result of FIB machining. Despite this, they still considered that this technique is the best solution where the precise localization of lamella is very important: "*It is well known that the best method for an austenitic stainless steel TEM specimen preparation is electropolishing. However, in case of investigating not dissolvable structural elements like non-metallic inclusions or specific areas like deformation plastic zone around the crack tip or nanoindenter impression, the FIB technique is the best substitution, despite the artefacts induction. Fortunately, by examining the samples at different angles with respect to the electron beam, true and artefact dislocations can be distinguished and the true structure of the investigated material can be obtained* [116]."

3.4.2.4 FIB for studying the fatigue damage

The FIB was reported to be suitable for extraction of thin foils which allow the observations of microstructure under PSM and at the crack tip by some authors [101], [118], [119] (Figure 3-32). New information and confirmations on the past predictions about development of PSMs could be found due to this technique.

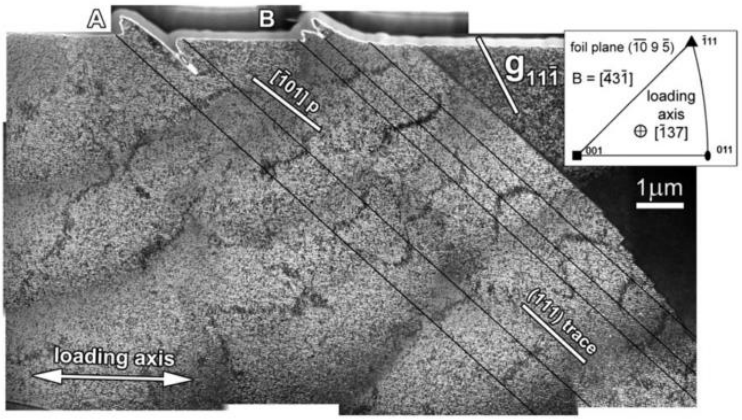

Figure 3-32 TEM image of FIB thin foil revealing the extrusions and intrusions with correspondent underlying ladder-like dislocation structures [119]

3.5 Conclusions

In this chapter the material of study, which is martensitic steel with 10.2% Cr and 0.17% C, and its properties and chemical composition were presented. The performed LCF test conditions were described. The material shows a typical behaviour for martensitic steels in fatigue, i.e. it softens during the whole lifetime. The main techniques of analysis were briefly presented too. Thus, AFM is useful and easy for topographical analysis of deformation features, while FIB was found to be an accessible technique for the preparation of TEM thin foil for the direct microstructural observations under FSM

4. Study of FSM at the specimen surface

This chapter is devoted to the deformation relief characterization by AFM and it is subdivided in 5 subchapters. In the first one the different morphological types of extrusions will be described. In the second one the localization of FSM relatively to the microstructural interfaces will be revealed. In the third subchapter the evolution of different dimensions of extrusions will be assessed as a function of number of loading cycles. The forth subchapter is designed for the validation of localization of different types of extrusions. And, finally, in the conclusion the main aspects of this chapter will be summed up.

4.1 Characterization of deformation relief morphology

The LCF interrupted test with the conditions, indicated in the previous chapter, was performed. Before test four micro indentations Vickers (100 gf) were printed in the center of specimen (Figure 4-1). The indentations played a role of reference mark for identification of each zone of investigation after each interruption. Due to them and coordinate system of AFM it was possible to find ten permanent zones on the specimen after each interruption in order to follow their evolution. The area of each zone is 80µmx80µm.

The interruptions were performed after ¼ cycle (0.04% of lifetime), at 100 cycles (9% of lifetime), then at 500 cycles (44% of lifetime) and at 1130 cycles (100% of lifetime). It should be noted that for all the following AFM images the loading axis is vertical.

During the test two important morphological groups of extrusions were revealed: principal extrusions which were observed already at the early stages of loading and secondary extrusions which were observed later than the principal ones. As a consequence, firstly the principal extrusions will be described and then the secondary ones.

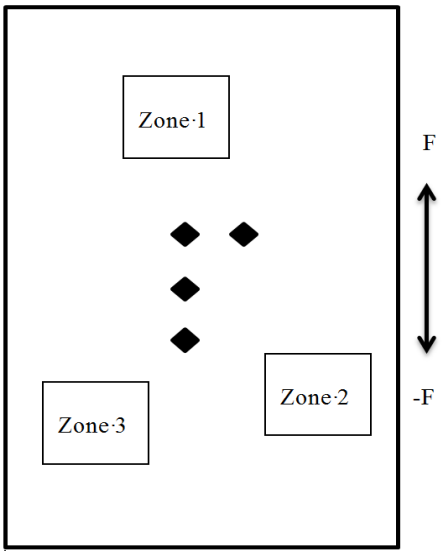

Figure 4-1 Gage section of sample with Vickers indentations and a few zones of AFM scanning

4.1.1 Principal extrusions

The surface analysis of fatigued specimens allows describing the morphology of extrusions-intrusions (plastic deformation witnesses). In the Figure 4-2 the images of the same zone with equivalent profiles of some FSM at different steps of loading are shown. The deformation relief evolves with the increase of number of cycles. However it seems that the quantity of fatigue slip markings does not increase after the second interruption of 100 cycles, while the dimensions of extrusions (especially the height) increase.

The AFM topographic analysis showed that after ¼ cycle the FSM profiles resemble a *step* (Figure 4-2a). The steps are usually believed to be the first manifestation of dislocation slip on closely spaced slip planes and they are observed in many metallic materials after ¼ cycle which is equivalent to the monotonic tension test, limited to a low value of plastic deformation [100], [104], [105]. However, some authors ascribe the steps to the gliding of laths against each other in the case of martensitic steel [45].

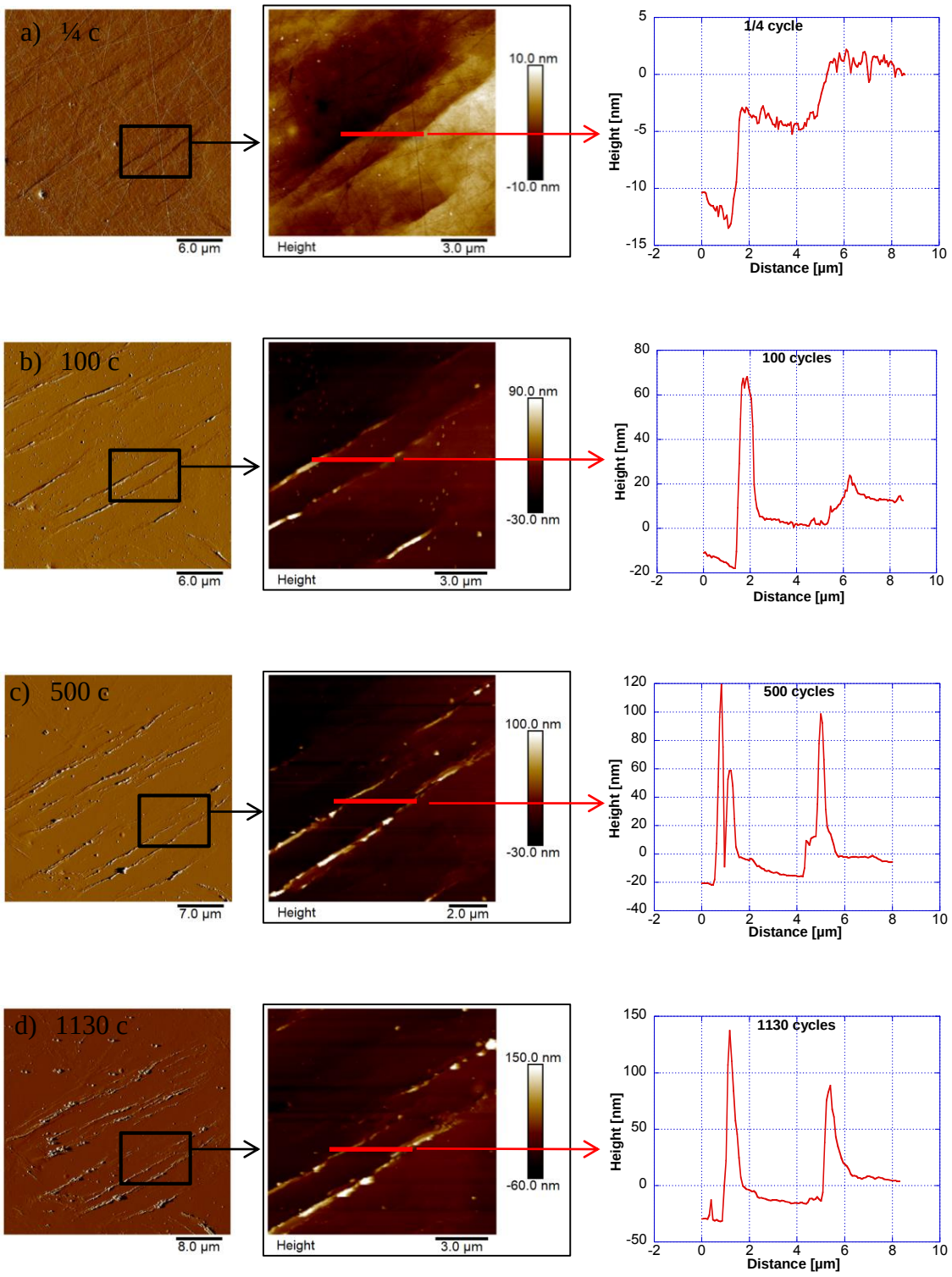

Figure 4-2 AFM images and profiles illustrating the evolution of deformation relief as a function of number of loading cycles

The heights of those steps do not exceed 10 nm. After additional cycles (100, 500, 1130) all the observed steps developed into the extrusions lately named *principal* (Figure 4-2bcd). The principal extrusions are rather long and high. The length is of the order of packet sizes (4-24 µm), and the average height is between 20 and 70 nm depending on the number of accumulated cycles.

On general large scan size AFM images (bigger than 50µmx50µm) the principal extrusions observed on the investigated material appeared very often as non-continuous "broken lines" (Figure 4-3a), consisting of a few small parts which are not necessarily collinear but parallel between each other. In the Figure 4-3b the extrusion marked by dashed red line seems to be a solid line, but in the magnified image of the extrusion (Figure 4-3c) it is seen that it is made of two parallel extrusions marked by two dashed red lines. The distance between these two parts is small enough (order of lath width) to create an illusion that it is a solid unique extrusion on the large scan size AFM images (80µm*80µm) (Figure 4-3b).

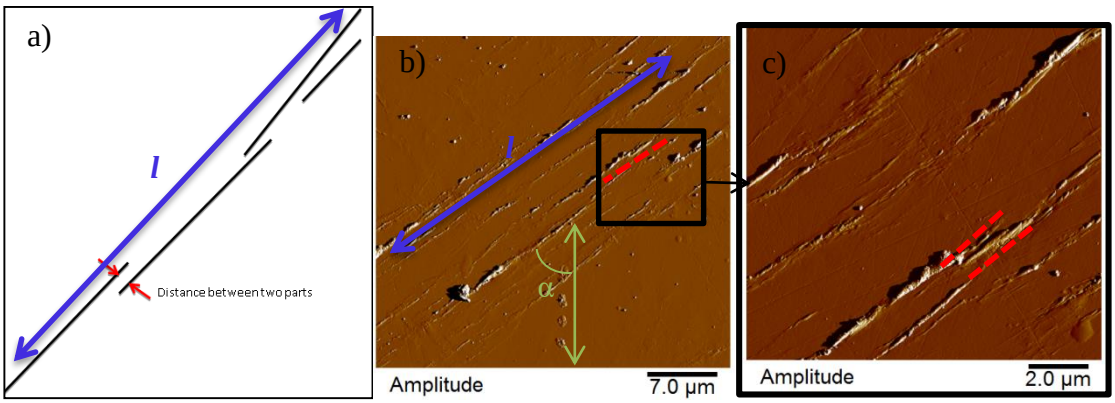

Figure 4-3: a) a sketch of principal extrusion consisting of small almost parallel parts and definition of principal extrusion length *l;* b) example of definition of principal extrusion length *l*; c) magnified image of the zone in black box in (b). The method for measuring of the angle α between principal extrusion and loading axis is in green in (b)

Moreover, at higher magnifications the different parts of extrusions were found to be quite different in their shape. Polak *et al*. [120] referred the important extrusion shape fluctuations to the simultaneous activity of many different slip systems. As far as the studied martensitic steel has bcc crystal lattice it may contain up to 48 possible slip systems, which is a high number of probable slip systems, for example, relatively to fcc metals. As a result the probability that the

closely situated planes activate at the same time grows up. In such a way the non-continuous broken extrusion could be created.

The works of Man *et al*. [3], [95] were used in order to classify the observed principal extrusions according to their form revealed by AFM images. The designation of the below described types of extrusions in the present 12%Cr martensitic steel is that employed in the literature for fcc and bcc polycrystals and monocrytals [3], [95], [120], but the mechanism of emergence is not necessarily the same (Figure 4-4). The next different types of principal extrusions were observed: band-like, cord-like, tongue-like, ribbon-like, and protrusion. *Protrusion* (Figure 4-5) represents a few parallel extrusions that are so close (order of distances 1-2 nm) that can be considered as one large extrusion. *Tongue-like extrusion* (Figure 4-6) height periodically decreases and increases along the length up to zero or up to a negative value; i.e. an extrusion turns into an intrusion on the same FSM so that tongues of extruded material appear quasi-periodically along a FSM. The surface of *cord-like extrusion* (Figure 4-7) is considerably rugged and folded and thus its height varies markedly along the FSM. *Band-like extrusions* are compact and their height is more or less uniform along the FSM (Figure 4-8). *Ribbon-like extrusion* (Figure 4-9) is often accompanied by one or two parallel intrusions running at the intersection of FSM with surface. The heights of extrusion along the FSM may fluctuate. The majority of principal extrusions on the studied material are of mixed character.

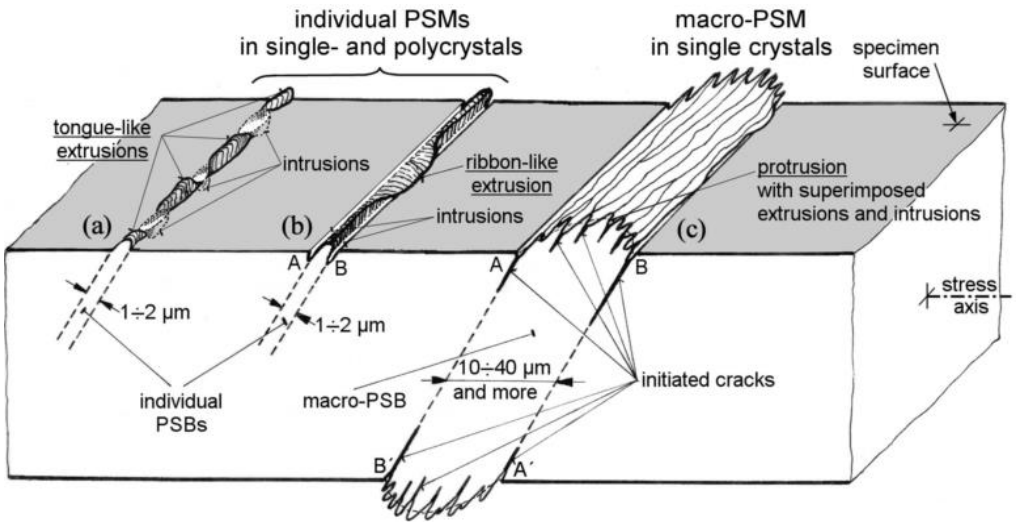

Figure 4-4 Different types of extrusions described in the work of Man *et al*. [3]

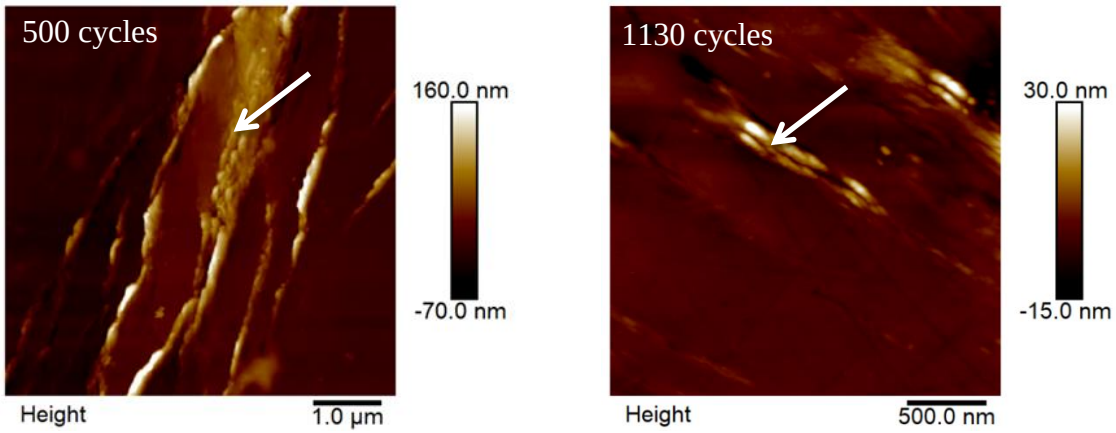

Figure 4-5 AFM height images of protrusions

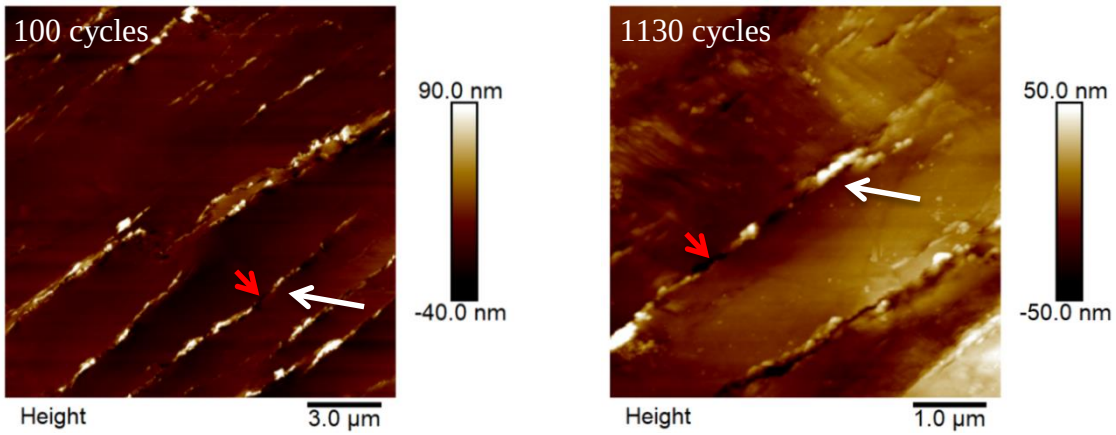

Figure 4-6 AFM height images of tongue-like extrusions (white arrows); red arrow indicates the intrusion

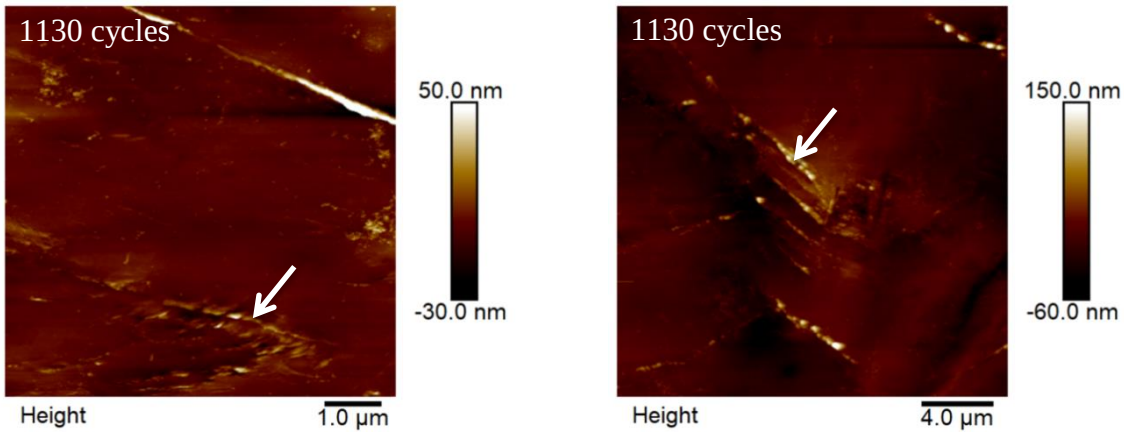

Figure 4-7 AFM height images of cord-like extrusions

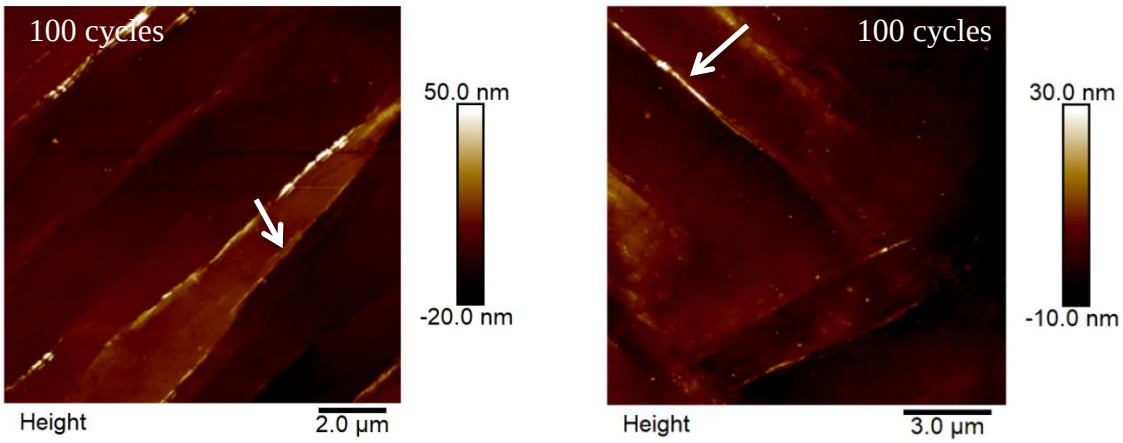

Figure 4-8 AFM height images of band-like extrusions

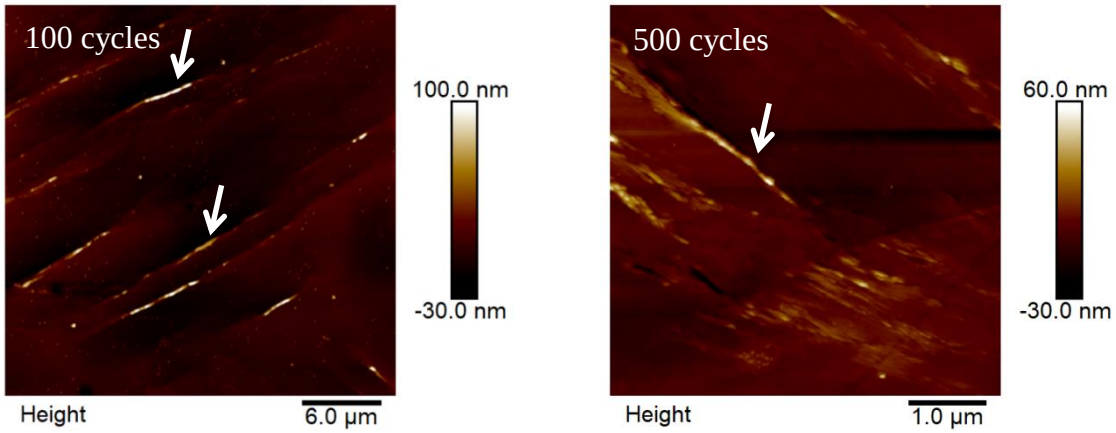

Figure 4-9 AFM height images of ribbon-like extrusions

4.1.2 Intrusions

After 100 cycles, the first few intrusions were observed. Thus, in Figure 4-6 the intrusion (red arrow) after 100 cycles is a part of tongue-like extrusion (white arrow). An intrusion has never been observed without an extrusion (Figure 4-10). It is impossible to measure the intrusion depth properly with AFM because of the tip geometry limitations and it is impossible to know their quantity because the tortuous shape of extrusions sometimes hides the intrusions. But nevertheless it was noticed by "naked eye" on the AFM images that the number of intrusions has increased between the interruption at 100 cycles and the end of life (Figure 4-11).

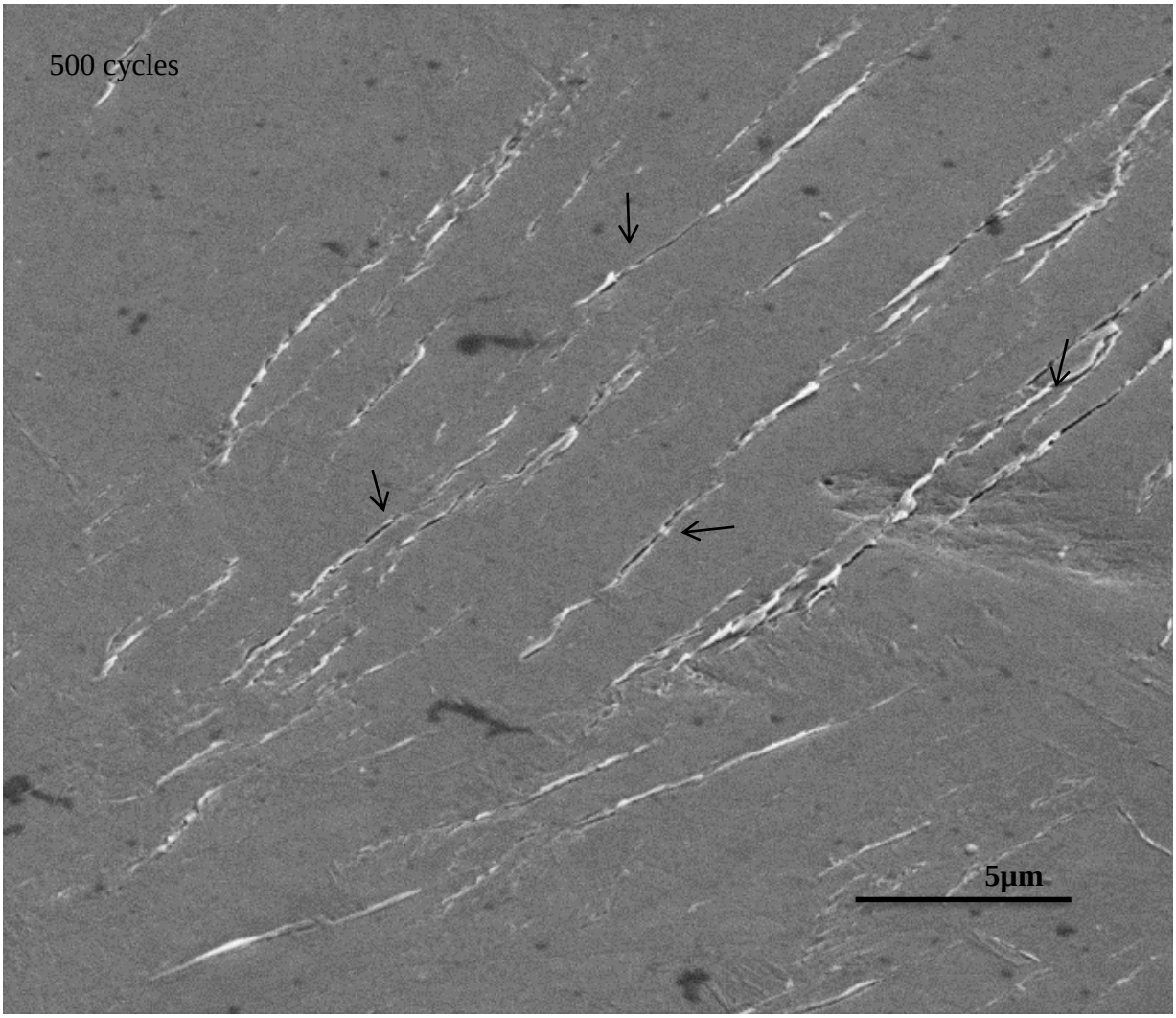

Figure 4-10 SEM image revealing the intrusions (black arrows) accompanying the extrusions after 500 cycles of loading

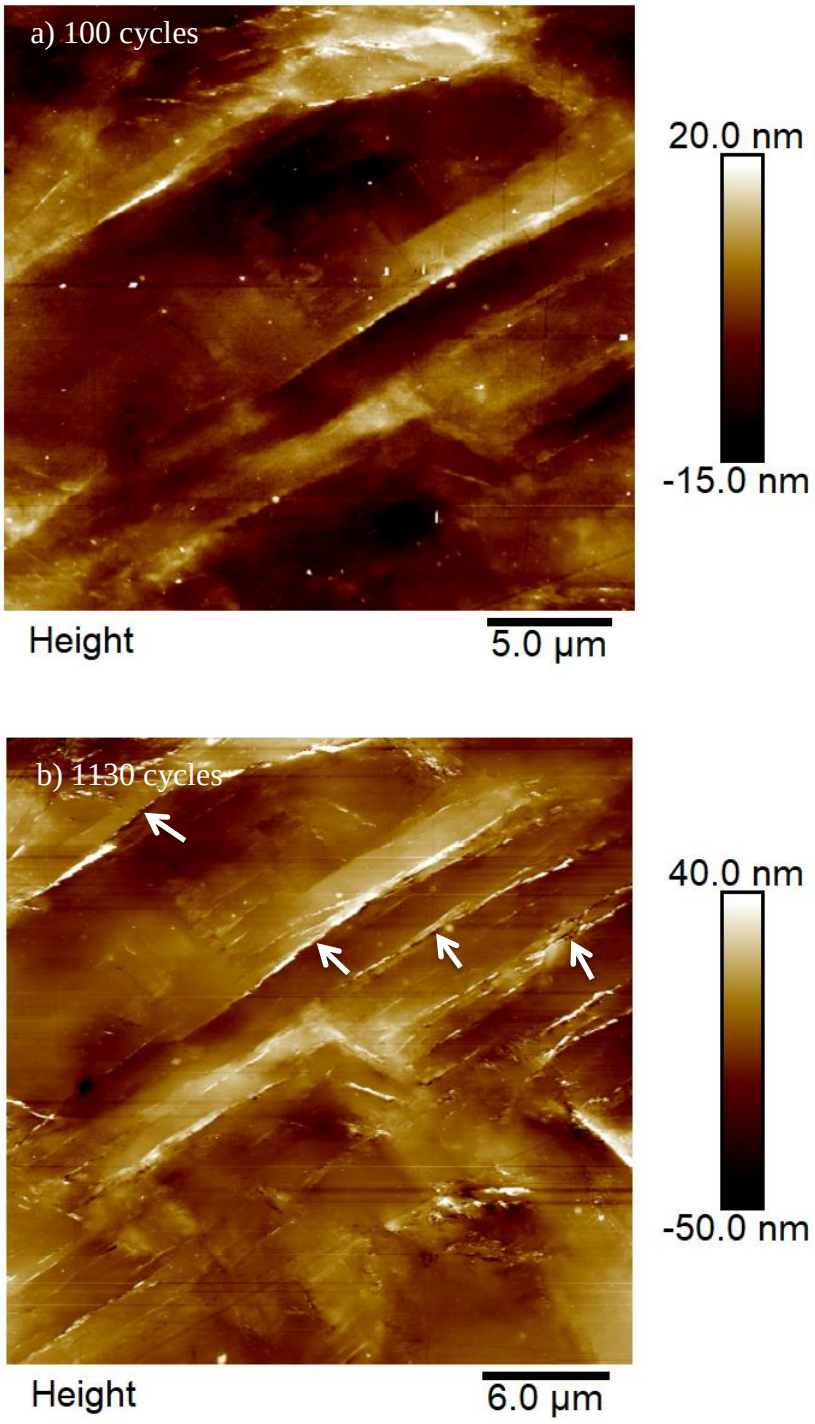

Figure 4-11 One of the zones of observation by AFM on the surface: a) 100 cycles, extrusions but no intrusions; b) 1130 cycles, extrusions and intrusions (indicated by white arrows)

4.1.3 Secondary extrusions

In addition to principal extrusions, another type of extrusions, either perpendicular or parallel to the principal ones, was observed (Figure 4-12).

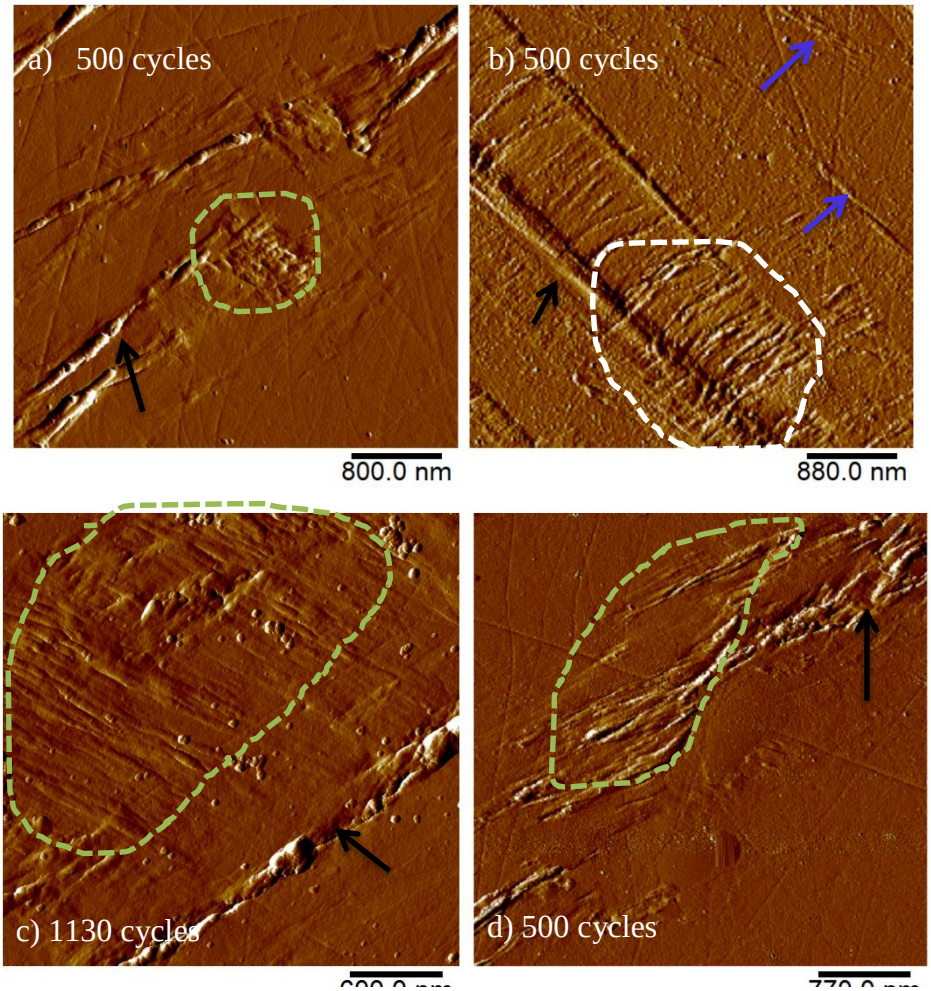

Figure 4-12 AFM amplitude signal error images. The sets of secondary extrusions are surrounded by dashed green lines and individual secondary extrusions are indicated by blue arrows. Black arrows point out the principal extrusions. Dashed white line surrounds the case when the secondary extrusions overcross the principal one

The secondary extrusions had a weak height and were short in comparison to the principal ones. The secondary extrusions formed likely between the interruptions of 100 cycles and 500 cycles, and it seems that very often they tend to accompany the principal extrusions. They may be grouped in a set of many parallel secondary extrusions (Figure 4-12), or probably many slip bands with a thickness of a few tens of nanometers (Figure 4-13). It seems that the principal

extrusions restrict the evolution of perpendicular secondary extrusions and prevent their growth by acting as an extrusion barrier (Figure 4-12acd). The individual secondary extrusions often appeared parallel to the principal ones.

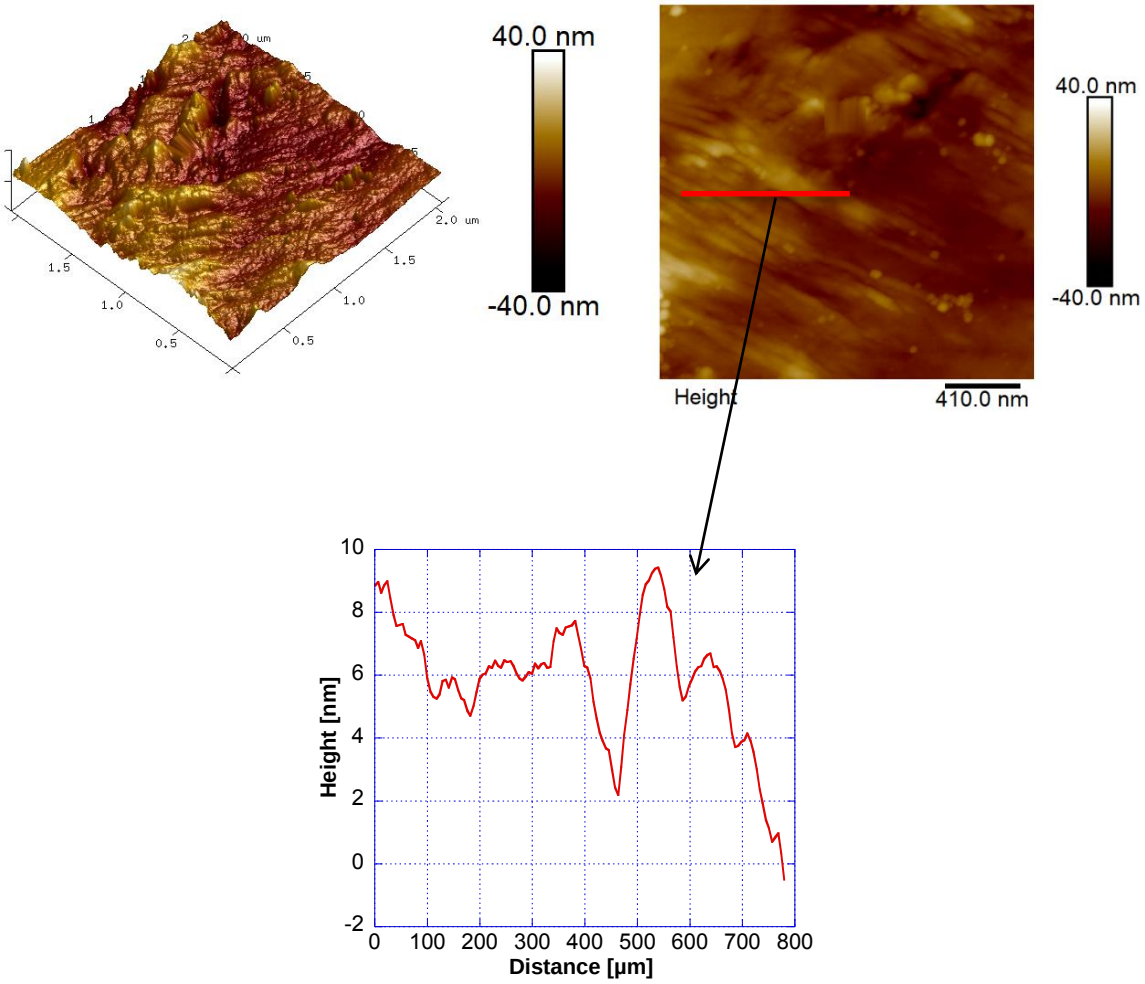

Figure 4-13 3D AFM representation of a set of secondary extrusions and correspondent AFM profile after 1130 cycles

4.2 Evolution of FSM

Different dimensions of the extrusions were measured: length, number, angle with the loading axis and height in the NanoScope Analysis program for AFM images processing.

The extrusion length was generally measured on the large scan size AFM images as it is shown in Figure 4-3ab. The lateral resolution for these images is 160 nm. The extrusion number

assessment was also realized on the large scan size AFM images. As for the measuring of the angle α between principal extrusion and loading axis, the method has been schematically shown in Figure 4-3b.

The number of principal extrusions increased mainly between the first and the second interruptions (Figure 4-2). In the Figure 4-14a it is shown that the total number of principal extrusions counted on 4 zones (each 80µm*80µm) increased from 13 extrusions at the first interruption to 25 extrusions at the interruption of 100 cycles. After 100 cycles their number changed from 25 to 26 extrusions, i.e. it did not almost change. As for the secondary extrusions, their amount increases with the increase of number of cycles of loading. But the secondary extrusions were noticed only after the interruption of 500 cycles.

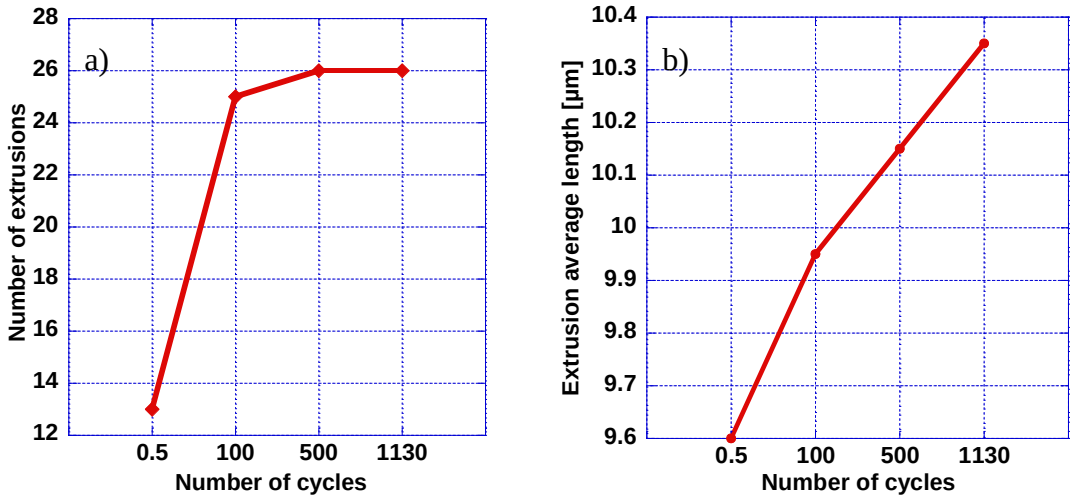

Figure 4-14: a) evolution of the number of principal extrusions as a function of number of cycles; b) evolution of the average length of principal extrusions as a function of number of cycles

Both ends of principal extrusions seem to be just little prolonged. And those prolongations of extrusions from both sides are not high. In the Figure 4-14b it is shown that the average length of principal extrusions increased from 9.6±10.5 µm to almost 10.4±10.3 µm at the end of life. The deviation of presented values is of the order of the average value of length because there are extrusions with very different lengths (Figure 4-21b). It is possible that an extrusion appeared at the boundary encounters another boundary in both ends and cannot cross it over.

Our results disagree with Cretegny and Saxena's ones [14] on the PH 13-8 Mo martensitic steel where the amount and total length per unit area of extrusions increased monotonically up to 90% of life while maintaining a constant average length. This can be attributed to their choice of strain ranges, that are lower ($\Delta\varepsilon_t$=0.4% ($\Delta\varepsilon_{pl}$/2=0.003%) during 58 000 cycles and $\Delta\varepsilon_t$=0.6% ($\Delta\varepsilon_{pl}$/2=0.025%) during 4 300 cycles) than ours ($\Delta\varepsilon_t$=1.2% ($\Delta\varepsilon_{pl}$/2=0.18%) during 1 130 cycles). It means that the low plastic strains were delivered cycle by cycle.

It was observed that the amount of extrusions on the surface increased only in the first 100 cycles of loading and the length change is almost negligible. These result in that the cyclic plasticity manifested itself mainly by the change of height of extrusions appeared after the first interruption of ¼ cycle and by the formation of secondary extrusions observed after the interruption of 500 cycles.

The height measurements were performed on ten zones (each zone area is about 80µm*80µm). The height was measured along each principal extrusion at each point of an extrusion where the height seemed to be different from the previous measurement on the same extrusions and in the same interruption (Figure 4-15). The base line was defined as the non-deformed surface level adjacent to an extrusion. In the Figure 4-16 it is seen that all the heights of steps at the first interruption are in the range between 2 and 10 nm, i.e. above the vertical resolution (1 nm) of AFM. Then with the increase of number of cycles the heights increase too. But even in the end of fatigue life there is still few principal extrusions with a height comprised in the first range, i.e. in the range of step heights. This indicates that the speed of height growth of extrusions is not constant along the whole length of an extrusion which results in the irregular shape of extrusions in the end of life.

The average height (sum of all the measurements divided by the number of performed measurements) of principal extrusions grew from 4±2 nm at the first interruption of ¼ cycle to 68±37 nm at the end of life (Figure 4-17a). The increasing of fluctuations of height values with the increase of number of cycles explains the growth of height dispersion with the increase of number of cycles.

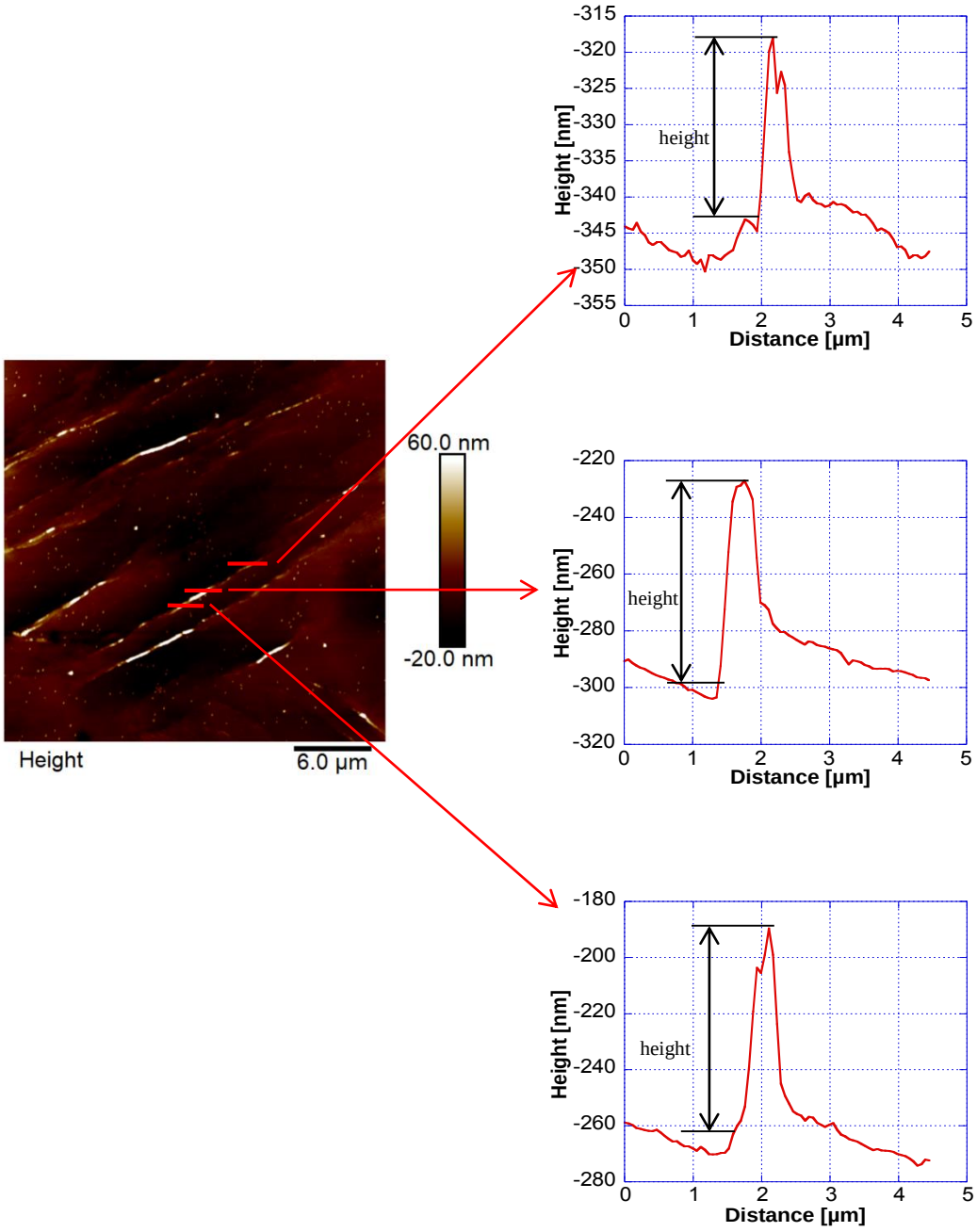

Figure 4-15 Method of extrusion height measurement

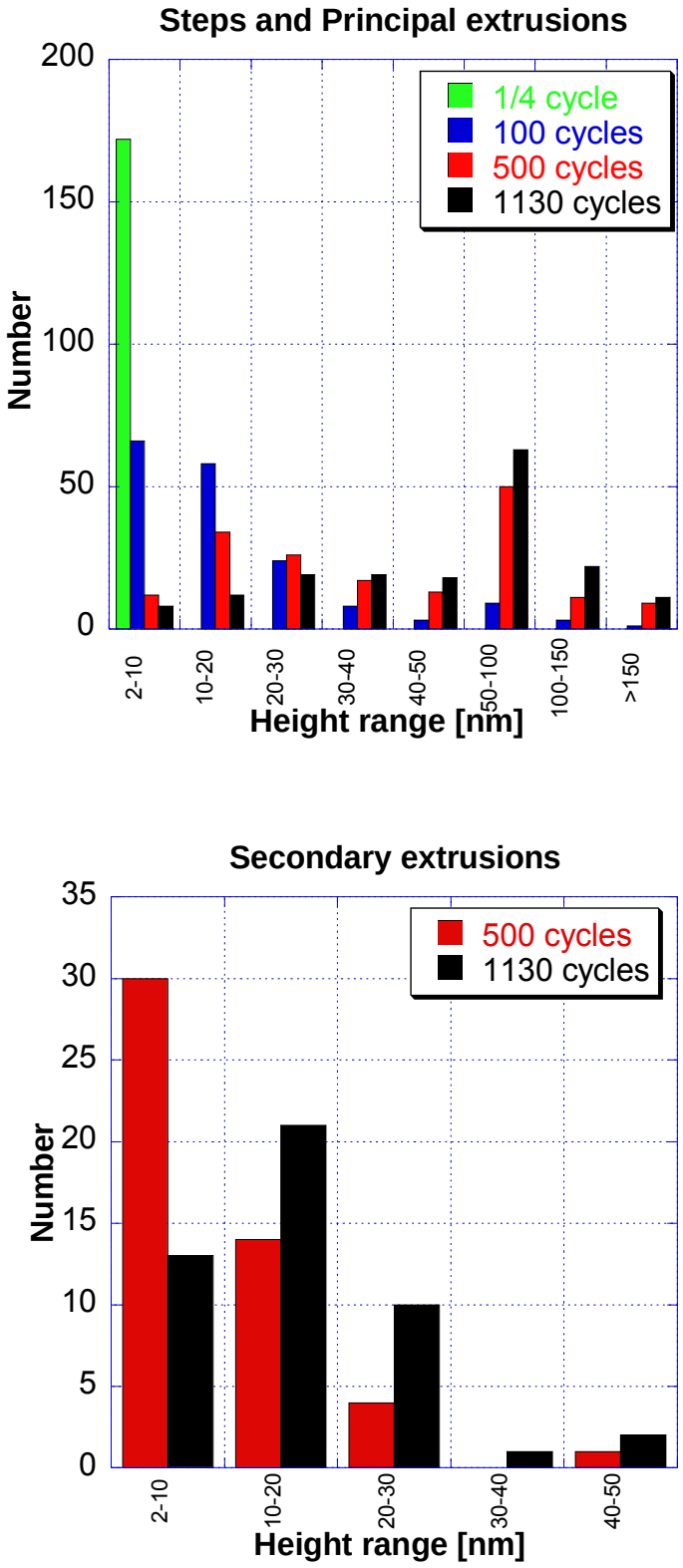

Figure 4-16 Distribution of measured heights of FSM after each interruption

The present data are in a good agreement with the next authors. Cretegny and Saxena [14] reported extrusions in martensitic steel with heights from 30 nm to 200 nm after LCF testing at $\Delta\varepsilon_{pl}$=0.05%. Man *et al.* [121] found that the average extrusion height of ferritic steel grew progressively and ranged between 75 nm and 250 nm for different extrusions after 8000 cycles (100% of life) at $\Delta\varepsilon_{pl}=2\cdot10^{-3}$. However, Vogt *et al.* [122], studying the duplex steel fatigue deformation at $\Delta\varepsilon_t$=1.6%, showed that the average height of extrusions in ferrite phase increased approximately up to 45 nm till 25% of life and then the height almost did not grow, while the extrusion height in austenite phase grew during the whole fatigue lifetime and reached approximately 90 nm at 60% of lifetime.

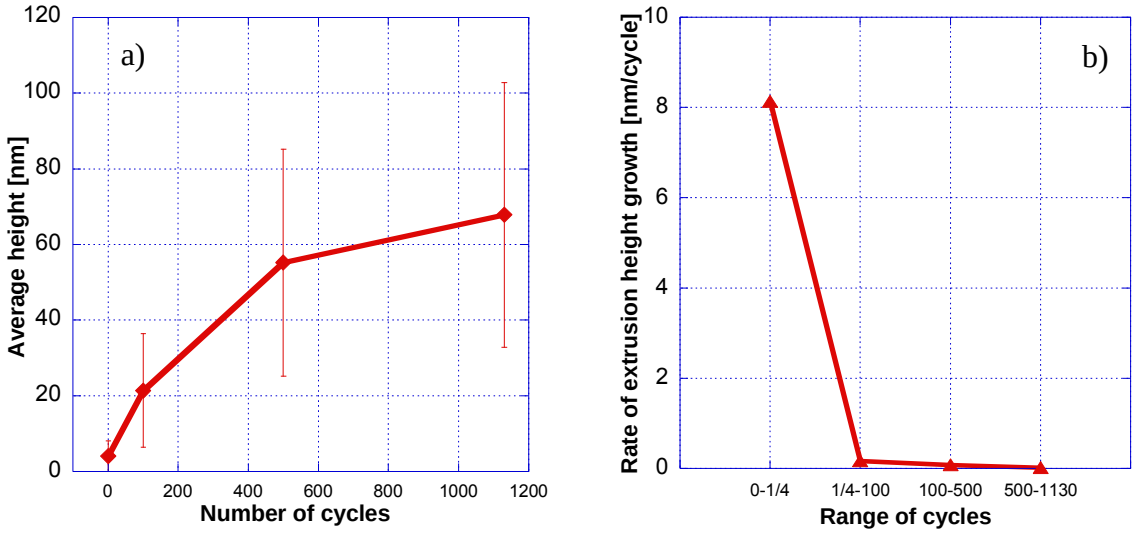

Figure 4-17: a) evolution of average height of principal extrusions with the increase of number of cycles; b) evolution of the rate of growth of principal extrusions between interruptions

The rate of height growth of principal extrusions in the studied martensitic steel decreased drastically from 8 nm/cycle at the beginning of loading to 0.02 nm/cycle at the end (Figure 4-17b). This change in growth rate can be connected with the stress response to strain cycling where the material exhibits a strong primary softening rate approximately during the first 100 cycles of life and then a more moderate one (Figure 3-12). In the work of Man *et al.* [96] the initial extrusion growth rate in 316L steel, fatigued at strain rate $\dot{\varepsilon}=3\cdot10^{-3}$ s^{-1} and plastic strain amplitude $\Delta\varepsilon_{pl}$=0.2%, was 0.081 nm/cycle. After 2.5% of life it decreased to 0.025nm/cycle, and for the rest of life the linear dependence between extrusion height and number of cycles was found. In our case the extrusion growth rate decreases constantly during the lifetime.

However, towards the end of life the speed of extrusion height growth is similar in both cases despite the different conditions of loading.

As for the secondary extrusions their heights were measured just at the interruption of 500 cycles and at the end of fatigue life, because earlier it was not possible to observe them. The secondary extrusions height develops in the same way as the height of principal ones. In the Figure 4-16 the black bars, corresponding to the secondary extrusion heights at the end of lifetime, are higher than the red bars (height at 500 cycles) at the right side of histogram. The average height of secondary extrusions has changed from 11±6 nm at 500 cycles to 18±9 nm at the end of fatigue life. Man together with his coauthors observed surface features, similar to the secondary extrusions presented in this work, after 2000 cycles (25% of fatigue lifetime) of fatigue deformation of a ferritic steel at plastic strain amplitude $\varepsilon_{pl}=2\cdot10^{-3}$ [123] (Figure 4-18). Very fine relief, observed by them, consisted of a regular system of parallel hills and valleys. This fine relief usually covered only a part of grain and it could overlap individual PSMs. The height of these features was much lower than the height of individual PSMs and typically reached 85 nm at the end of fatigue life comparatively to the typical extrusion heights around 500 nm.

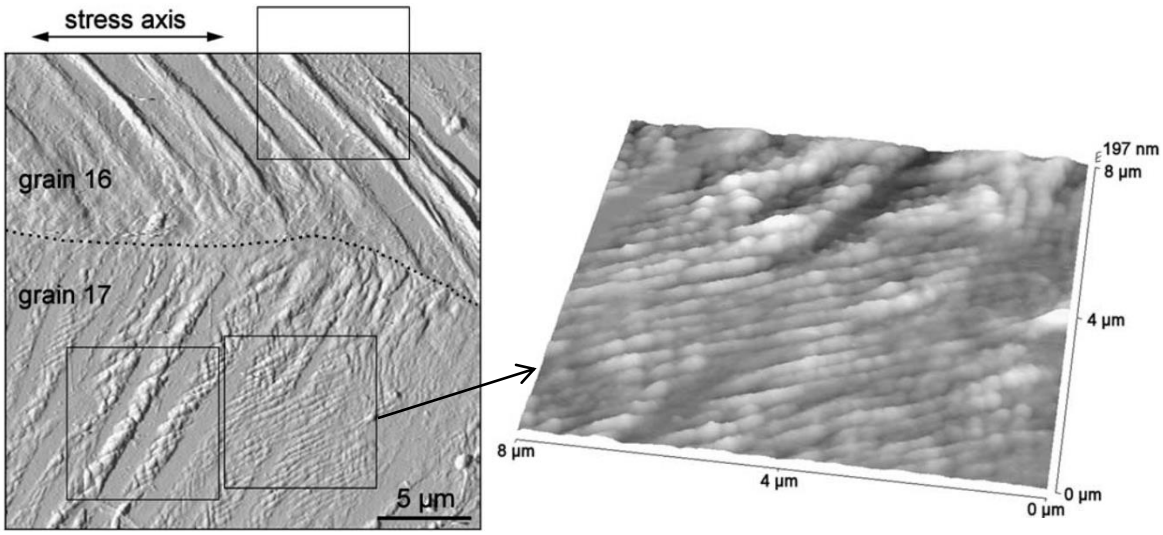

Figure 4-18 AFM 3D image of surface features observed in a ferritic steel after N=2000 cycles at $\varepsilon_{pl}=2\cdot10^{-3}$[123]

The angles between the principal extrusions on the surface and loading axis were measured on the images of AFM. The method has been shown in green in the Figure 4-3b. In the Figure 4-19

the resulting distribution of the measured angles shows that they are mainly between 30° and 60°. Thus, the measurement showed that the majority of angles on the surface between principal extrusions and the loading axis are around 45°, and there are no principal extrusions which were parallel to the loading axis. Although a few of extrusions made an angle of 90° with the loading axis: they appeared suddenly at the end of life and they were high relatively to those which developed from the first interruption and whose angle with the loading axis was between 30° and 60°.

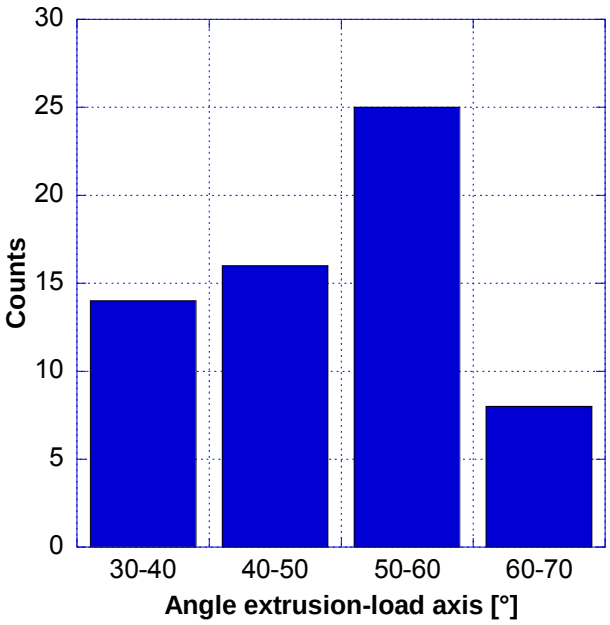

Figure 4-19 Distribution of angles between principal extrusions and load axis

The sets of secondary extrusions are often almost perpendicular to the principal extrusions. It means that they form the angle (90°-angle of principal extrusion) with the loading axis. The individual secondary extrusions, parallel to the principal ones, make the same angle with the loading axis as the principal extrusions, which usually ranges from 30° to 60° (Figure 4-19).

Cretegny and Saxena [14] observed also the majority of extrusions at approximately 45°, and Morsdorf [44] reported the "strain bands" in 45° orientation to the tensile direction of martensitic steel. He concluded that the interface plasticity is possible only if the boundary plane is at approximately 45° to the loading axis. The angle about 45° between the slip marking and the loading axis is known to be the angle at which the shearing stress τ is maximum. That is why the majority of authors agree that the fatigue slip markings usually appear at the angle

with the loading direction approaching 45° [15], [124]. This is likewise true for the extrusions observed in the present work.

To sum up, there was a radical change of the number of extrusions during the first 100 cycles and a lot of secondary extrusions were observed after 500 cycles (it means they developed in the period between 100 and 500 cycles). The number of intrusions increased importantly at the same period of lifetime as the secondary extrusions developed - between 100 cycles and 500 cycles. The evolution of the length of extrusions was not important. The height of extrusions changed during the whole lifetime although the change slowed down closer to the end of life.

4.3 Localization of FSM

Many authors did the surface analyses of deformation relief and have shown already that the cyclic plasticity is localized at the different interfaces of martensitc steel. Batista *et al*. [15] revealed for the AISI 410 steel containing 13 %Cr and subjected to 0.2% plastic strain amplitude in fatigue that the first deformation "lines" appeared at about 50 cycles *along lath boundaries* oriented about 45º with respect to the tensile axis. After a certain number of cycles, the lines intensified and turned into "bands", and finally, cracks nucleated on these slip marks. Cretegny and Saxena [14] investigated the LCF of PH 13-8 Mo stainless steel and found that the length of extrusions on the surface has the length characteristic of the packets and PA grains. As a result he suggested that the extrusions appear *at the packet and grain boundaries*. Hayakawa *et al*. [105]–[107] showed in their studies by AFM of tension of 1%Cr martensitic steel that the surface steps of 5-39 nm height appeared *in locally deformed blocks near prior austenite grain boundaries*.

The FSM appear apparently in the vicinity of different interfaces as it is seen in the Figure 4-20. The extrusions are "flexible": if they turn on its path leaving a round trace, it is because they follow a boundary (Figure 4-20a). If the path of extrusion is like a zigzag then it means the extrusion has changed the grain at the point of zigzag line broke, and consequently the growth direction has changed suddenly following another boundary inside a new microstructural element. The direction change points occur at the boundaries. Moreover after rupture the specimen surface was polished and etched by Vilella solution. The resultant surface image is

on the Figure 4-20b: the microcracks are just near the different interfaces which are well marked by carbides (in white).

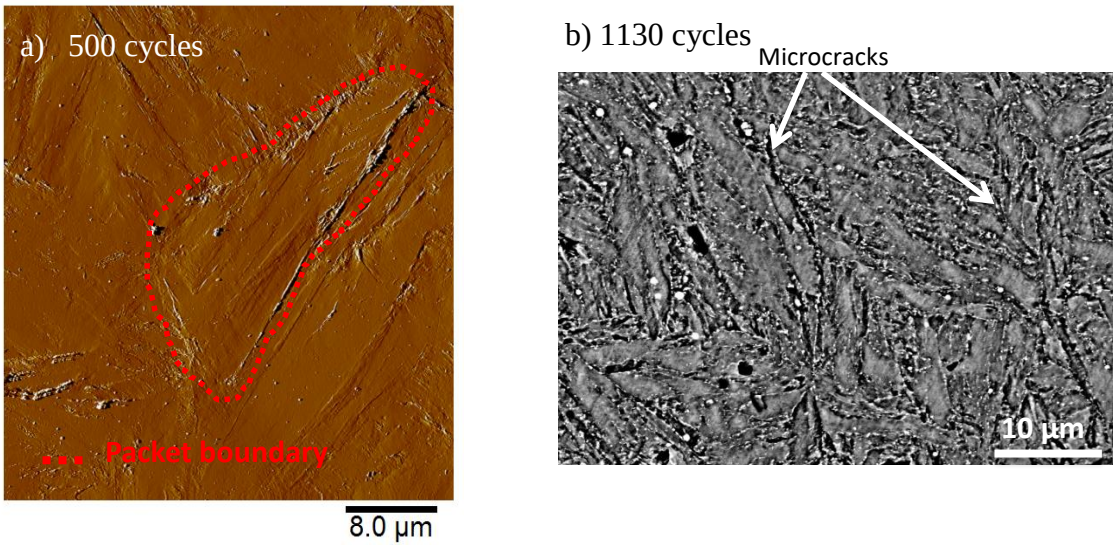

Figure 4-20 a) AFM signal error image showing the FSM following the packet boundary; b) SEM image of surface of polished and etched fatigued specimen revealing the microcracks at the interfaces marked by precipitates

At the end of life the *distances* between two parallel principal extrusions and the *lengths* of principal extrusions were measured (Figure 4-21). These measurements were compared to the known *sizes* of blocks, packets and PA grains (x-axis on the Figure 4-21). It was shown that the distances between two parallel principal extrusions correspond mainly to the packet *sizes* and to the block *widths*. When we talk about block and lath *sizes* we mean their *widths*, while packet and PA grain are equiaxed (Figure 4-21a). It means that the principal extrusions probably appear at the packet and block boundaries. Cretegny and Saxena also observed the extrusions appeared often at the packet boundaries [14] and Hayakawa *et al*. at the block interfaces [107]. On the Figure 4-21b it was shown that the measured *lengths* of principal extrusions were mainly in the range of packet *sizes*. But the *length* of blocks is also comprised in the range of packet *sizes*, and the *length* of lath is comprised between 5 and 10 µm [8]. It means that they can be easily confounded with a packet boundary and from the Figure 4-21b it can be concluded that the principal extrusions may be at the packet boundaries or at the block or lath longitudinal interfaces.

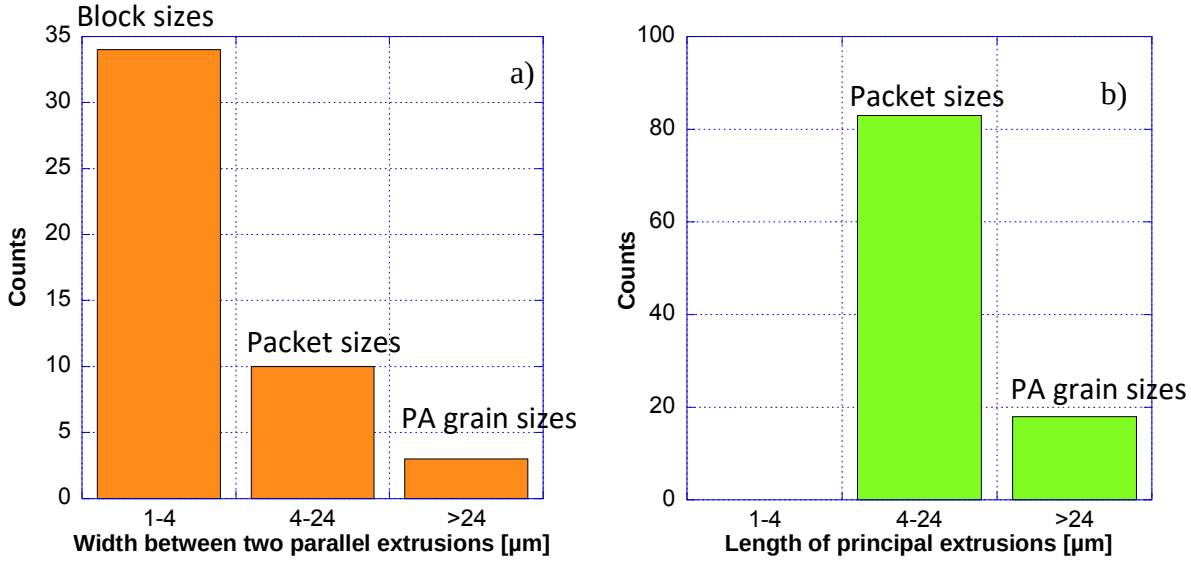

Figure 4-21: a) measured width between two parallel extrusions is compared to the known ranges of sizes of microstructure units; b) comparison of length of principal extrusions to the sizes of microstructural units

The distance between parallel parts consisting the principal extrusions (Figure 4-3) were measured for different 20 extrusions on the small scale AFM images and the results are in the Figure 4-22a. It was shown that the measured distances are in the range of average widths of laths. This was confirmed later by TEM observations of principal extrusion cross-sections made by FIB (see next chapter).

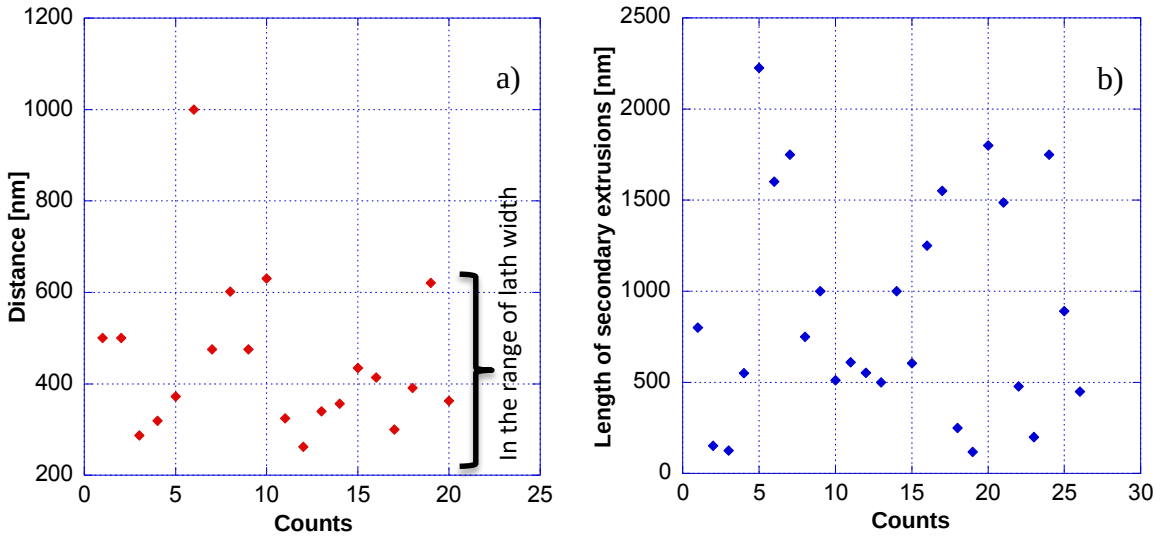

Figure 4-22: a) the scatter of the distance between two parallel parts of principal extrusions; b) the scatter of the length of secondary extrusions

As for the sets of secondary extrusions it was found that they are often perpendicular to the principal ones on the specimen surface (Figure 4-12; Figure 4-13). The length of 26 sets of secondary extrusions was measured and it was found to be lower than 2500 nm (Figure 4-22b), i.e. it was in the range of lath and block widths. The secondary extrusions rarely overlapped the principal extrusions. It means that they are rather inside the laths or blocks if the principal extrusions are at the boundaries. This was confirmed by the TEM imaging of lamellae FIB extracted perpendicular to a set of secondary extrusions (see next chapter). The observations are in excellent agreement with Du *et al*. and Morsdorf *et al*. [44], [45], who, besides the plasticity near interfaces, observed the slip activity inside the laths. If the principal extrusions appear at the vicinity of HAB, then the secondary extrusions are confined within the lath with a limited possibility to cross the boundaries. As far as the disorientation angle between two laths is of LAB type, the secondary extrusions may overcome the lath boundaries. Rarely the secondary extrusions appeared *on* the principal one (Figure 4-12).

To conclude, the principal extrusions can appear in the vicinity of different boundaries of this hierarchical microstructure, while the secondary extrusions are rather inside the laths.

4.4 Validation of localization of FSM

To validate the localization of FSM at the different boundaries of studied material as a result of LCF loading a new heat treatment was performed with a purpose to increase the sizes of each microstructural unit. For this the steel was quenched after 5 hours solution treatment at 1300°C and then tempered 4 hours at 680°C.

4.4.1 Microstructural characterization and some mechanical properties

As a result of this heat treatment the sizes of PA grain, packet and block have increased. The PA grain size was measured on optical images of the material microstructure. For microstructure revealing the Vilella solution was used as for the as-received material. The lath size was measured on the TEM images. The results are in the Figure 4-23. The PA grain sizes range from 30 to 170 µm comparing to the range 10-60 µm in as-received material. However, the lath width did not change. It is less than 1 µm in both materials (Figure 3-8; Figure 4-23). It is coherent with the studies of Zhang *et al*. [32] who showed that the lath dimensions stay

unchanged if the quenching conditions change, while all other microstructural units (PA grain, packet and block) grow if the quenching temperature and time increase.

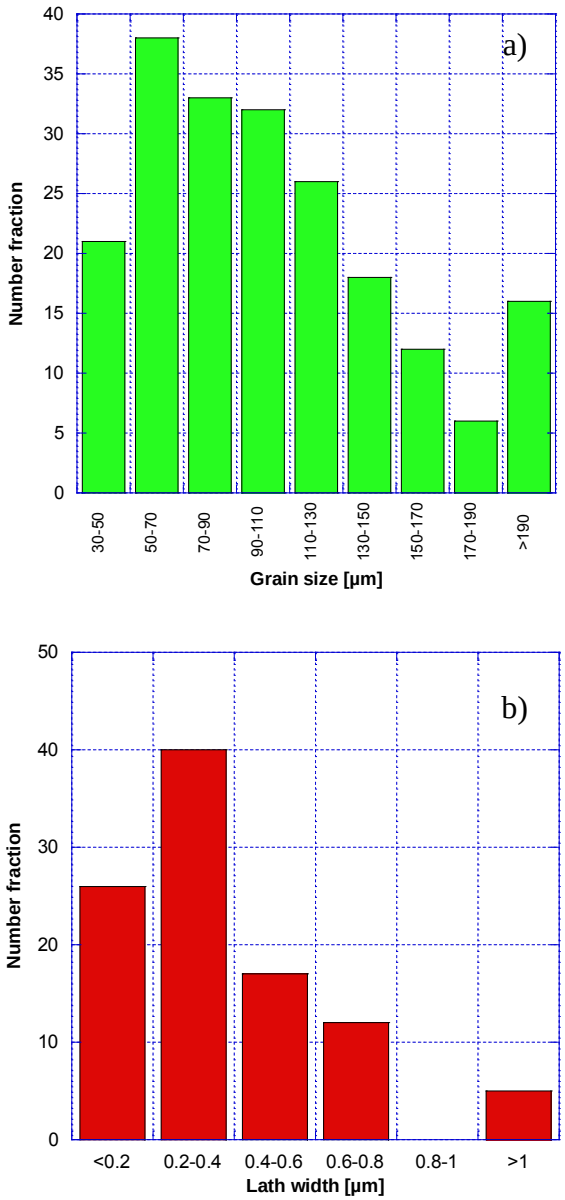

Figure 4-23 Distribution of measured grain sizes (a) and lath widths (b)

The packet and block sizes were determined using the model of Galindo-Nava described in *3.1.3Microstructural characterization*. If the grain sizes range from 30 to 170 µm, then the packet sizes range between 12 and 68 µm (40% of PA grain size) and the block size is up to 12 µm (approximately 6.7% of PA grain size).

In the Figure 4-24 the microstructure of material is shown. The material seems to be more densely populated by dislocations than the as-received material (Figure 3-3). These could be the reason for the slightly increased hardness value (HV 317) comparing to the as-received material (HV 295). However no calculations of dislocation density were performed on both materials.

a)

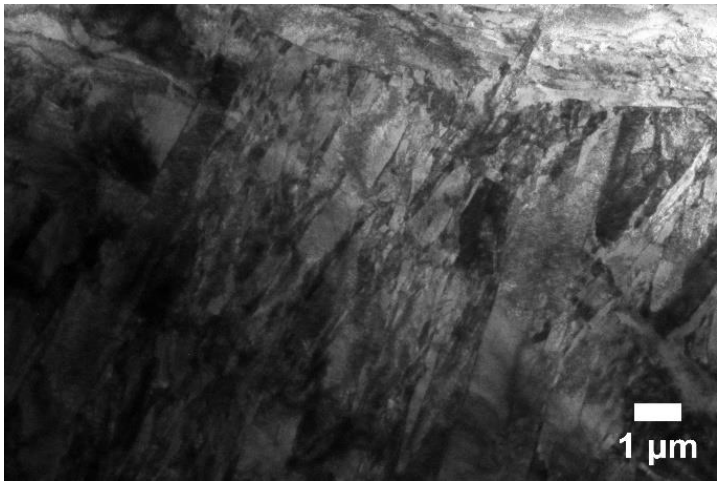

b)

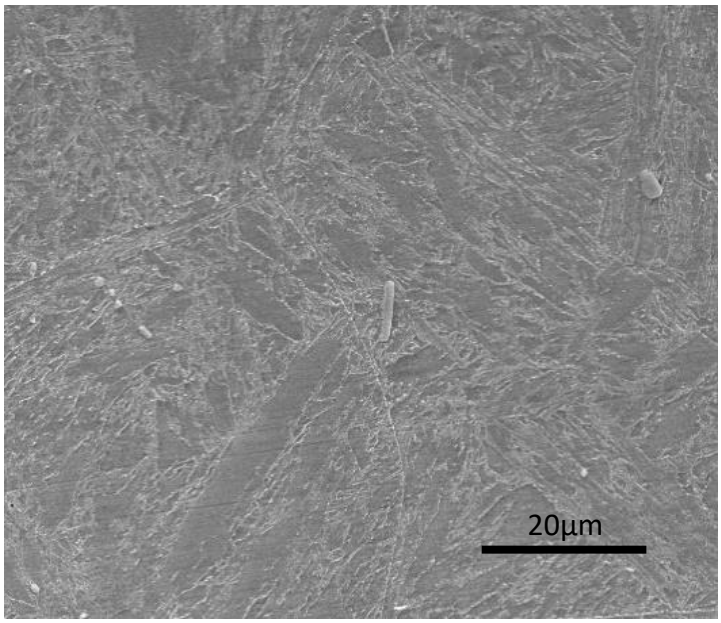

Figure 4-24 Lath microstructure of the martensitic steel austenized at 1300°C during 5 hours and imaged by TEM (a) and SEM (b)

4.4.2 Experimental procedure

The LCF test with the same conditions as for the test of as-received material was performed (see paragraph *3.2.2Fatigue test and fatigue behaviour*). It was interrupted at ¼ cycle and after 80 cycles. After each interruption the surface was analyzed again by AFM. About 6 zones were observed after each interruption; each one had area 80µm*80µm.

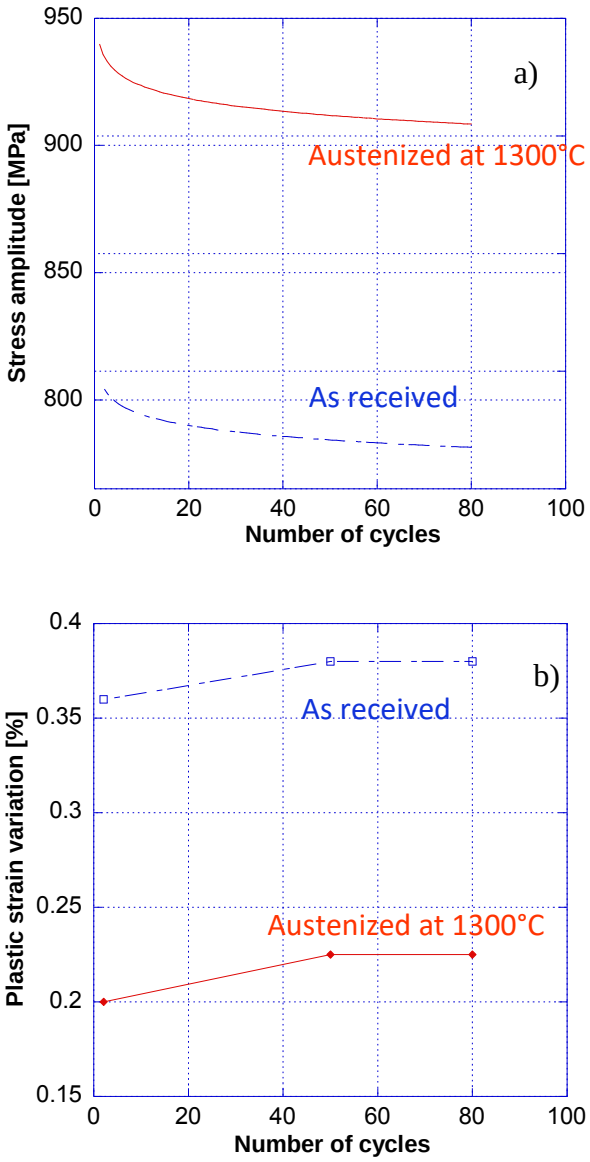

Figure 4-25 a) stress amplitude evolution as a function of the number of cycles for the as received steel and for the steel austenized at 1300°C; b) plastic strain variation as a function of the number of cycles for the as received and the austenized at 1300°C steels

In the Figure 4-25a the change of stress amplitude during 80 cycles is shown for the as received material and for the one austenized at 1300°C. The newly heat treated steel softens from 950 MPa to 910 MPa. The as-received material softened from approximately 810 MPa to 760 MPa. The higher average values of stress are measured in agreement with the higher hardness. The Figure 4-25b shows that the softening of the austenized at 1300°C steel is real as well as the softening of the as received steel.

4.4.3 Results of AFM observations of deformation relief

In the optical images of deformed surface it was already seen that the FSM are longer (of the order of packet and PA grain sizes) than on the surface of as-received steel (Figure 4-26).

By AFM the steps were observed again after the first interruption of ¼ cycle (Figure 4-27). These steps developed into principal extrusions between the interruptions of ¼ cycle and 80 cycles (Figure 4-27).

On all the zones observed by AFM the length of principal extrusions increased in comparison to the extrusions in as-received material and became of the order of "new" block, packet and PA grain sizes and lath length (Figure 4-26; Figure 4-27; Figure 4-28). Thus, in Figure 4-28 the blue arrow indicates the FSM, following the PA grain boundary. The length of the longest straight extrusions is 35 µm which is in the range of packet lengths, and the length of one of the smallest extrusions is approximately 11 µm which is equivalent to the block size. The distance between two parallel principal extrusions is often of the order of block sizes. Thus, in the Figure 4-28 the dashed line comprises a packet, in which the distance between extrusions marked by black points is between 1 µm and 8 µm which is equivalent to the block widths. The distances between two extrusions in a cluster of closely situated extrusions are of the order of lath width. Indeed, in Figure 4-28 the distances between extrusions pointed out by the green point are less than 1µm.

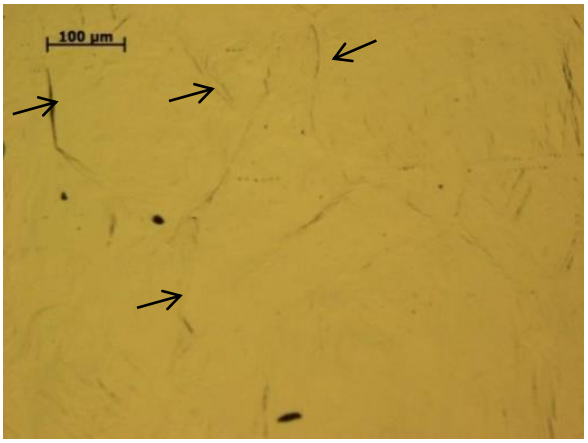

Figure 4-26 Optical image of the deformed specimen surface after 80 cycles of loading. The arrows show the extrusions and intrusions with the length of the order of PA grain and packet sizes

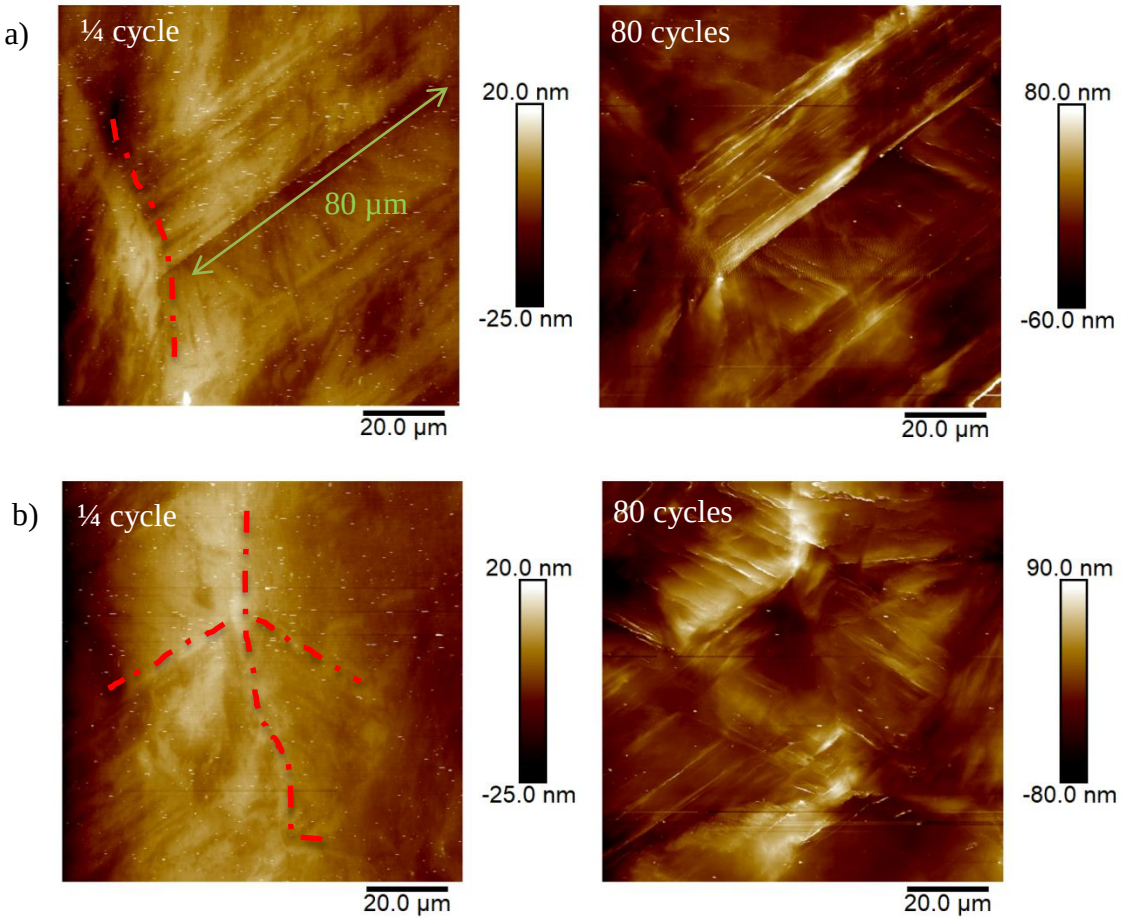

Figure 4-27 AFM height images of zones (a) and (b) after two interruptions. Dashed lines mark the boundaries

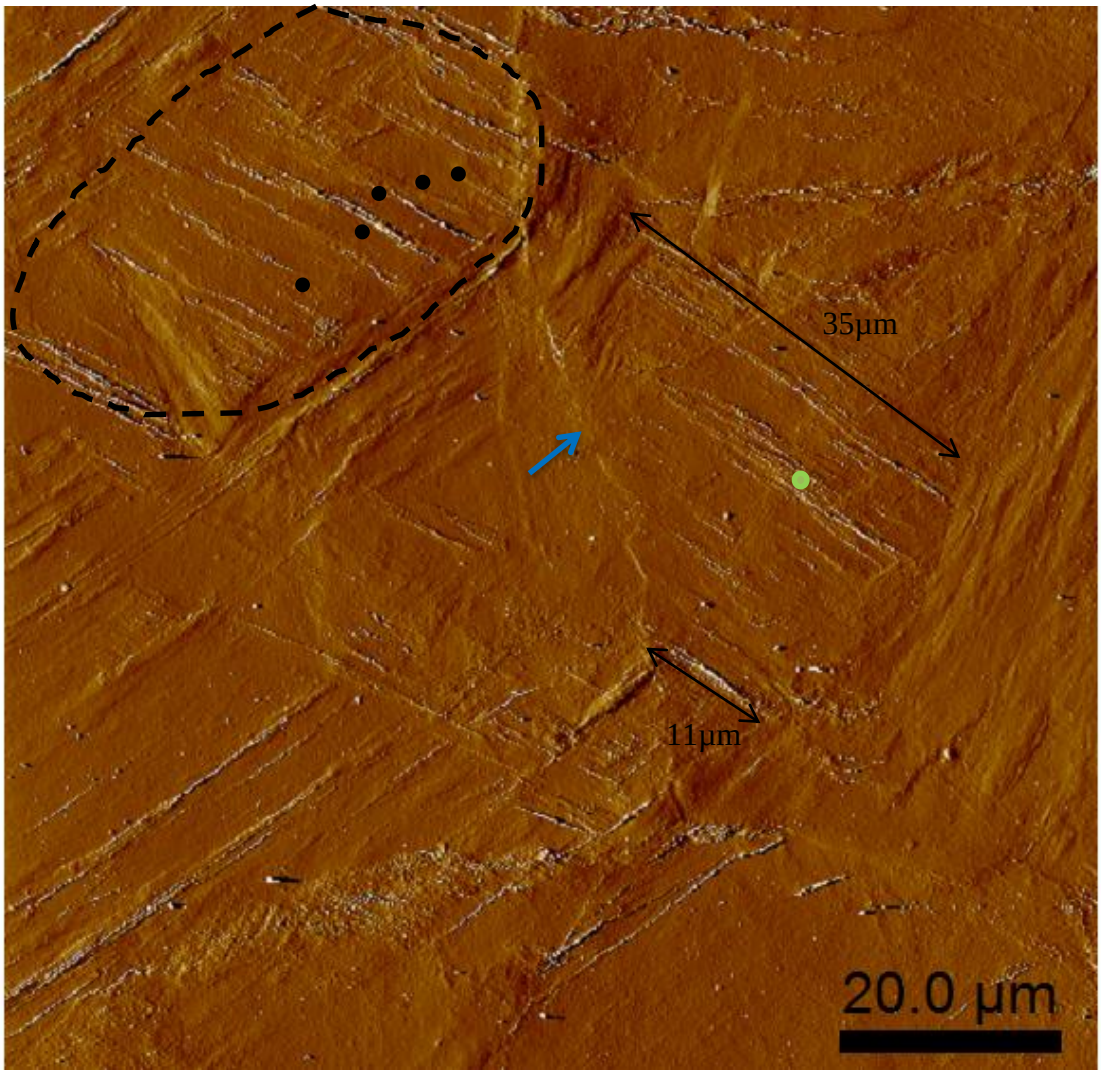

Figure 4-28 AFM signal error image of specimen surface after 80 cycles. Blue arrow indicates the FSM in the PA grain boundary. The dashed line comprises a packet. The black points indicate the extrusions, the distances between which are equivalent to the block widths. The green point shows a cluster of extrusions: the distances between each of them are less than 1µm

The heights of principal extrusions were measured after both interruptions and the resultant plot is on the Figure 4-29. The average height changed from 3 nm after ¼ cycle to approximately 23 nm at 80 cycles of life. There is no great difference of heights between two different materials (Figure 4-17).

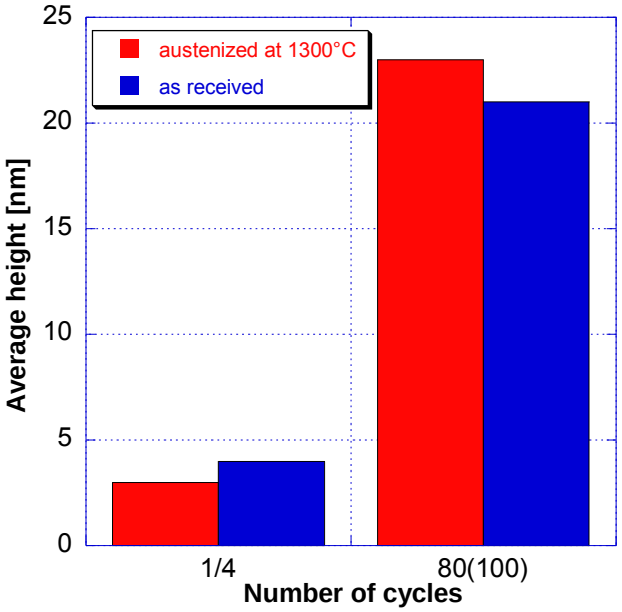

Figure 4-29 Evolution of average height of steps and principal extrusions with the increase of number of cycles

To sum up, the sizes of the first three units (PA grain, packet and block) of microstructure were increased as a result of heat treatment. The LCF test with the same conditions as for the as-received material test and interruptions at ¼ cycle and 80 cycles was performed. As a result the length of principal extrusions on this newly treated material increased following the microstructure unit sizes change and it is equivalent to the sizes of block, packet or PA grain. The distance between two parallel principal extrusions is equivalent to the sizes of blocks or packets. The average height evolution of principal extrusions with the increase of number cycles seems to be the same as in the case of as-received material.

4.5 Conclusions

As a result of LCF interrupted test on the as received martensitic steel the FSM appeared on the specimen surface. These FSM were described and classified according to their shape. Two important groups of FSM were distinguished: principal and secondary extrusions.

The FSM height, length and number were quantified. It was found that the number of principal extrusions changed only between ¼ cycle and 100 cycles. The change of their length was almost

negligible, while the height continued to grow till the end of life. The secondary extrusions were observed after 500 cycles and grew in number and height till the end of life.

The localization of FSM was defined too. The principal extrusions and intrusions seem to appear in the vicinity of different boundaries. The secondary extrusions are usually short and perpendicular to the principal one which brings up to the conclusion that they are rather within the laths or blocks.

The localization was validated on the material austenized at 1300°C during 5 hours. As a result the sizes of all the microstructural units increased, except the widths of lath. The FSM length increased too following the growth of microstructural units. It confirms the localization of FSM at the different boundaries.

The AFM analysis allowed characterizing the fatigue deformation in form of extrusion-intrusion sets on the specimen surface. In order to understand the micro-mechanism of extrusion and intrusion formation and emergence, it is necessary to characterize the microstructural deformations inside the material and directly under extrusions and intrusions. As a result, the next chapter is devoted to the observations inside the material under FSM.

5. Study of microstructural evolution under FSM

The chapter is devoted to the microstructural evolution of the alloy under the action of fatigue. Firstly, the microstructural changes in the bulk of material after 500 cycles and 1130 cycles will be discussed, and then the changes studied directly under FSM after 500 cycles will be revealed. The FSM will be definitely localized relatively to the interfaces of microstructure due to the FIB technique of lamella extraction. Also some dimensions of FSM measured on the TEM images will be estimated and compared to those found by AFM. And finally, the results of coupled SEM-EBSD-ECCI-TEM study of FSM will be discussed in the end of this chapter.

5.1 Microstructural evolution in the bulk

The cyclic loading of crystalline materials leads to an inhomogeneous distribution of cyclic strain. In materials where PSB form, the plastic strain localizes in the bands the volume fraction of which depends on the value of applied strain, while the matrix is deformed quasi-elastically. The high local plastic shear strain amplitude in the FSM associated with the specific dislocation structure involves production of dislocations and their annihilation generating point defects. Increasing the strain amplitude results in a fully wall structure and in the cell structure.

Thus, the cell structure was observed in the studied material. The TEM observations of thin electropolished disks, extracted in the bulk of fatigued specimen, were performed both after 500 cycles of loading (44% of lifetime) and after the alloy rupture at 1130 cycles (Figure 5-1). The dislocation cells were found on the TEM images after both interruptions. The observations

of lamellae FIB confirmed that the microstructure builds the cells already at 500 cycles (Figure 5-4; Figure 5-5).

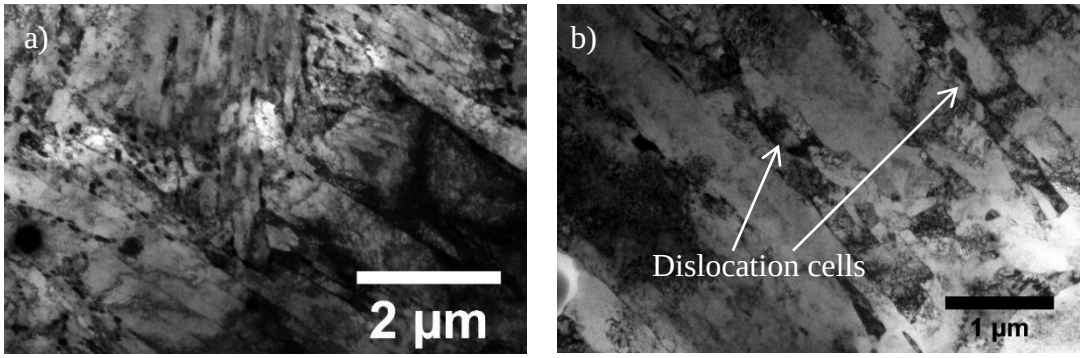

Figure 5-1 a) initial microstructure of material; b) dislocation cells after rupture at 1130 cycles

In martensitic steels the dislocation cells were observed by many authors [8], [46], [64]. These steels are known to possess a high density of dislocations. During loading these dislocations move and interact between each other. Interaction brings either to the dislocation multiplication or annihilation, although in martensitic steels the annihilation is higher than the production rate. It means that the dislocation density decreases during the loading process. This brings to the material gradual softening. Eventually the dislocations arrange into cells in order to diminish the energy of their interactions during loading. The dislocation cell structure is the cheapest configuration in terms of energy cost, i.e. the dislocations are arranged in such a way that the energy per unit length of dislocation line is minimum. Also sometimes the lath coarsening or disappearance of laths due to the migration and annihilation of the dislocations in the lath boundaries, contributes to the steel softening too, especially if the steel is loaded in high temperature.

The diameters of dislocations cells observed in this material were measured. In the Figure 5-2a the distribution of diameters is presented. It was found that the cell sizes did not exceed 500 nm and range mainly between 100 nm and 400 nm, which is in the range of average lath width.

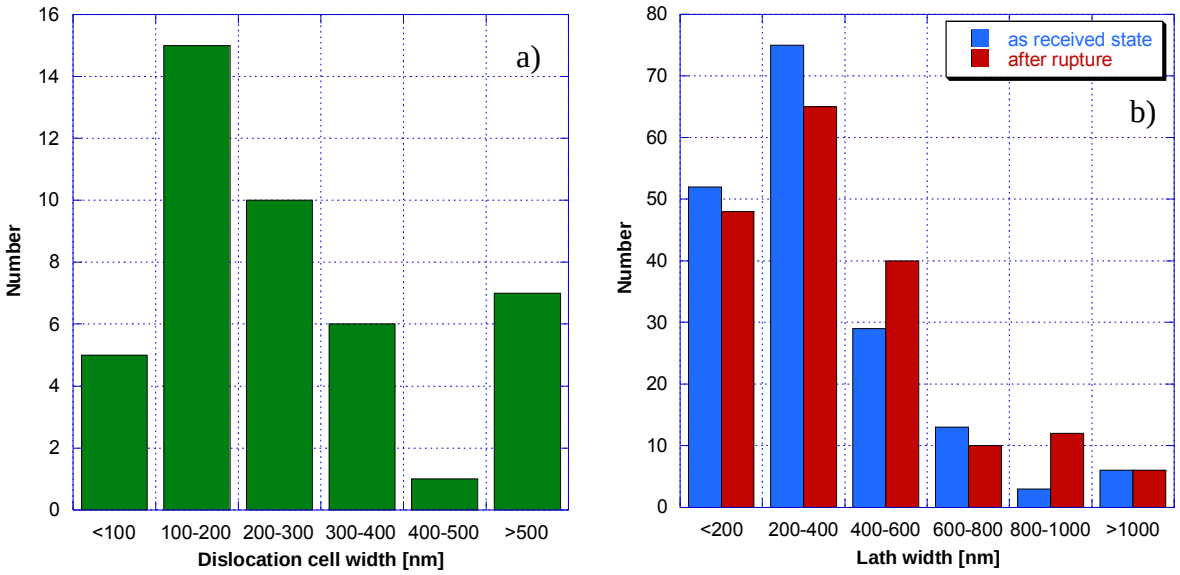

Figure 5-2 a) dislocation cells diameters measured at 500 cycles; b) comparison of lath width before deformation and after rupture at 1130 cycles

As it was mentioned in the paragraph *2.3.2 Fatigue behaviour of 9-12% Cr martensitic steels and resulting microstructural evolutions*, the laths of martensitic steel may change their widths due to the migration of dislocations from the lath boundaries inside the laths and their annihilation. In our case the laths did not change their widths (Figure 5-2b). Probably the applied strain value of $\Delta\varepsilon_t$=1.2% was not high enough for this test temperature to provoke the disappearance of lath boundaries and so the increase of lath sizes.

5.2 Observations of lamellae FIB under the FSM

The steps on the surface at tension and the extrusions and cracks in the vicinity of lath and lath boundaries were observed by many authors [14], [15], [44], [45], [64], [105], [107]. Moreover, the AFM observations of deformation relief and the observations in SEM of microcracks in the etched bulk of specimen after rupture showed that the pairs of extrusion-intrusion and cracks are rather in the vicinity of different boundaries (*4.3Localization of*). But the exact localization of extrusion-intrusion (whether it is inside the lath or inside the lath boundaries) is an issue. The observations of lamellae FIB in TEM may answer this question.

The Focused Ion Beam (FIB) is the only technique that can prepare thin lamellae with a high precision of lamellae localization. 8 lamellae were extracted after 500 cycles of loading

perpendicular to the extrusions of interest at *L'Institut d'Electronique, de Microélectronique et de Nanotechnologie (IEMN)* as it is shown in Figure 5-3. It means that 8 different zones with FSM were studied in AFM and then in TEM. 8 lamellae provided information on 40 extrusions and 40 intrusions. It should be recalled here that intrusions cannot exist separately from extrusions. Moreover, different morphological types of extrusions suppose that an extrusion such as ribbon-like, for example, can be accompanied by two intrusions: each from two sides of extrusion.

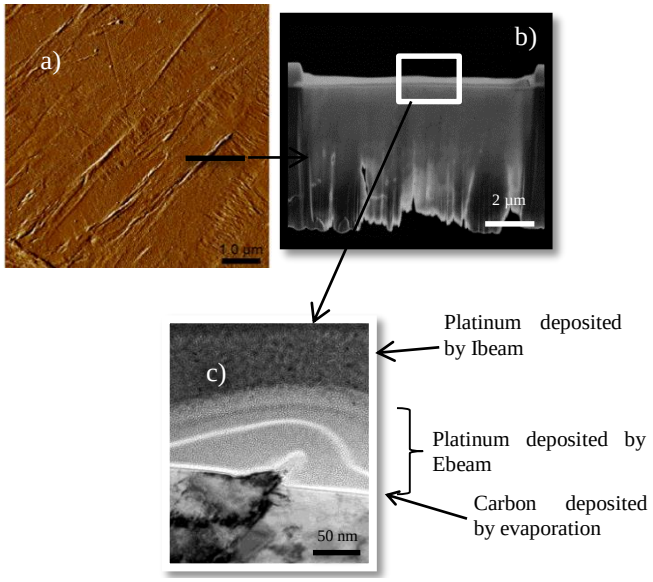

Figure 5-3 The FIB lamella extraction: a) the selection of area of interest; b) extracted lamella mounted on the copper grid; c) observation of lamella in TEM

5.2.1 Localization of principal FSM

The observations of FSM cross-sections allowed unambiguous confirming that the principal extrusions lie mainly close to lath boundaries or walls of dislocation cells, while the intrusions are just right in the boundaries. In the Figure 5-4a one of the extrusions pointed out by red arrows is right next to the boundary illustrated by a dashed green line. Another extrusion in the Figure 5-4a is delimited by the walls of dislocation cells marked by a white dashed line. Figure 5-4bc illustrates other two extrusions delimited by the walls of dislocation cells (white dashed lines), while Figure 5-4def shows the extrusions appearing right next to the lath or other boundaries.

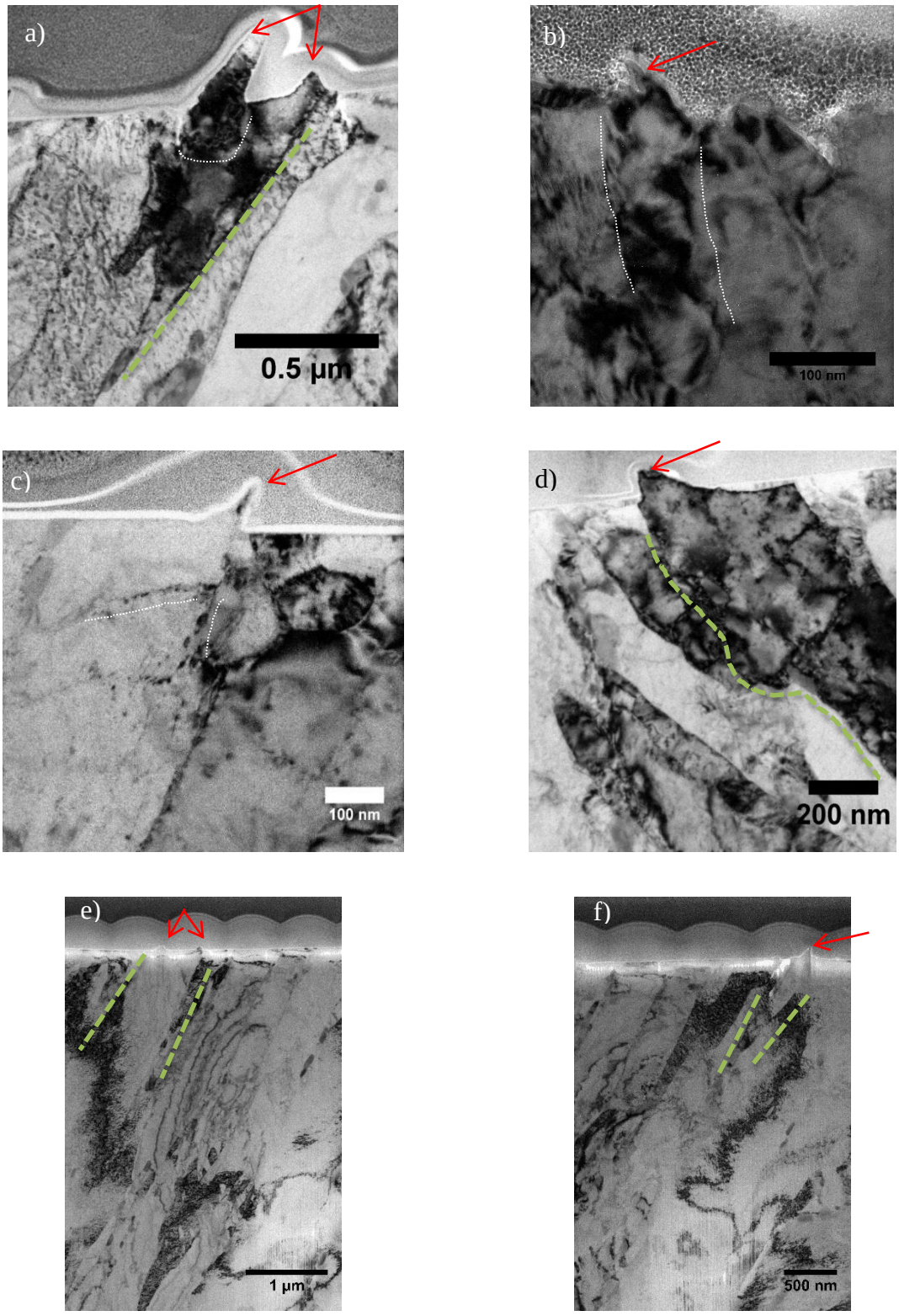

Figure 5-4 FSM cross-sections obtained by FIB and observed in TEM after 500 cycles of loading. Green dashed lines follow the lath boundaries. White dashed lines follow the walls of dislocation cells. Extrusions are pointed out by red arrows

Figure 5-5 illustrates the extrusions accompanied by the intrusions. It is clear that the extrusion in Figure 5-5a is next to the lath boundary and it is delimited by the cell wall as well; in the lath boundary the intrusion, pointed out by the blue arrow, appeared. In the Figure 5-5b the extrusion is in the narrow lath, the boundaries of which are marked by green dashed lines. The extrusion is close to the curved boundary, however from the other side the extrusion is delimited by a thin dislocation line, which is probably a future dislocation cell wall. The intrusion formed again in the lath boundary in the Figure 5-5b. Figure 5-5c shows another extrusion next to the boundary. It is accompanied by two intrusions: one of them is in the boundary, while another one is in the dislocation cell wall, which is unfortunately barely visible and which is marked by white dashed line. Finally, the Figure 5-5d illustrates two pairs of extrusion-intrusions. Both extrusions are situated next to the lath boundaries, while one of the intrusions is in the lath boundary and another intrusion is in the dislocation cell boundary marked by white dashed line.

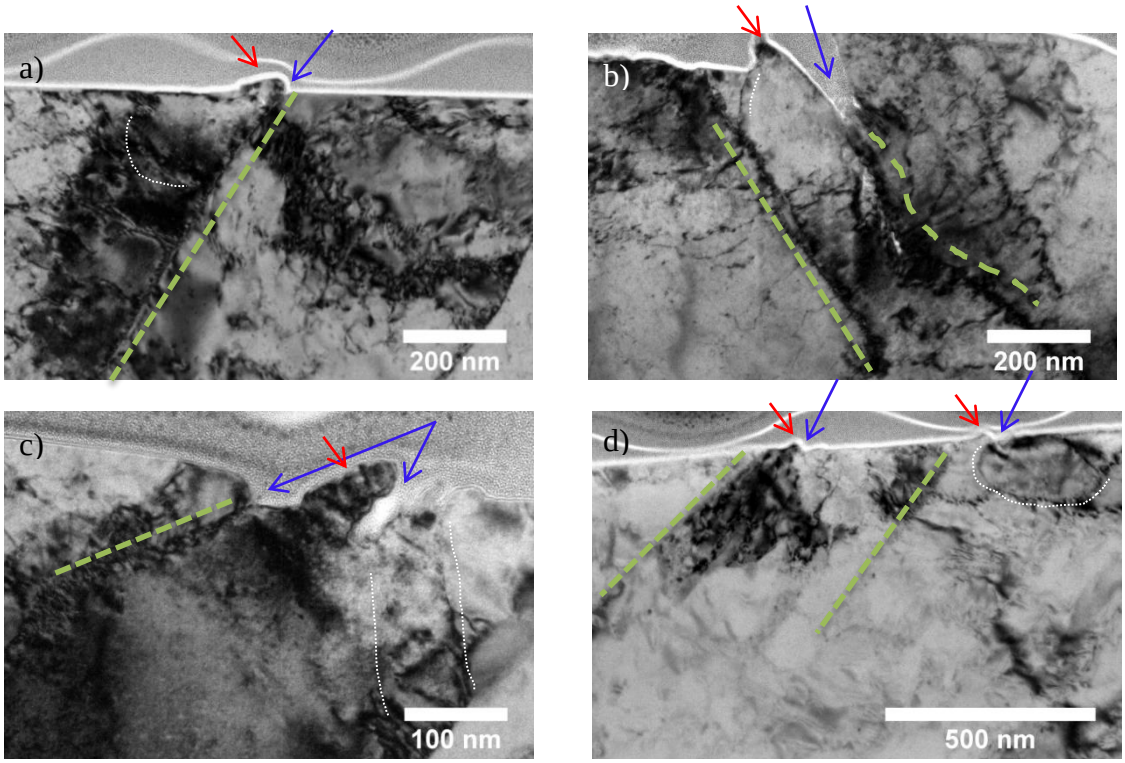

Figure 5-5 FSM cross-sections obtained by FIB and observed in TEM after 500 cycles of loading. Green dashed lines follow the lath boundaries. White dashed lines follow the walls of dislocation cells. Extrusions are pointed out by red arrows. Intrusions are pointed out by blue arrows

In the Figure 5-6 a unique image of microcrack cross-section, appeared where the extrusion made an acute angle with the surface plane, after 500 cycles is presented. The microcrack

initiated in the intrusion emerged at the dislocation cell wall (see the zoomed image of extrusion-intrusion base in the black frame). After initiation the microcrack developed inside the material following the walls of other cells, pointed out by blue arrows on the figure.

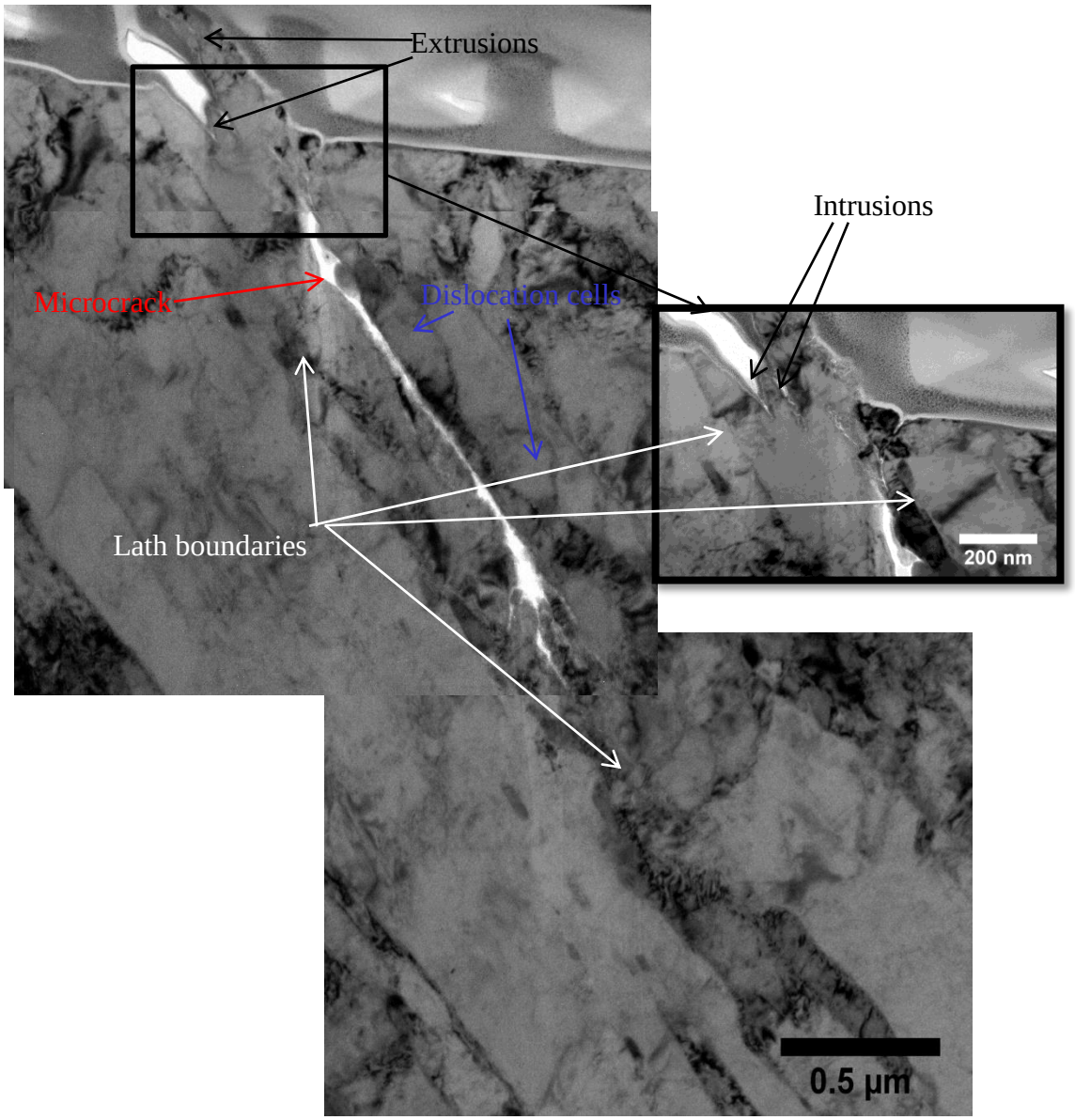

Figure 5-6 Cross-section of extrusions, intrusions and a microcrack after 500 cycles of loading

5.2.2 Role of precipitates in FSM localization

The precipitates occupy preferentially the different boundaries in the material. The FSM are closely related to the boundaries. The TEM observations of those FSM which appeared next to the boundaries decorated by a few precipitates showed that the precipitates may locally deform the boundaries in order to install themselves on those boundaries (Figure 5-7). As a consequence the boundary may locally change its path.

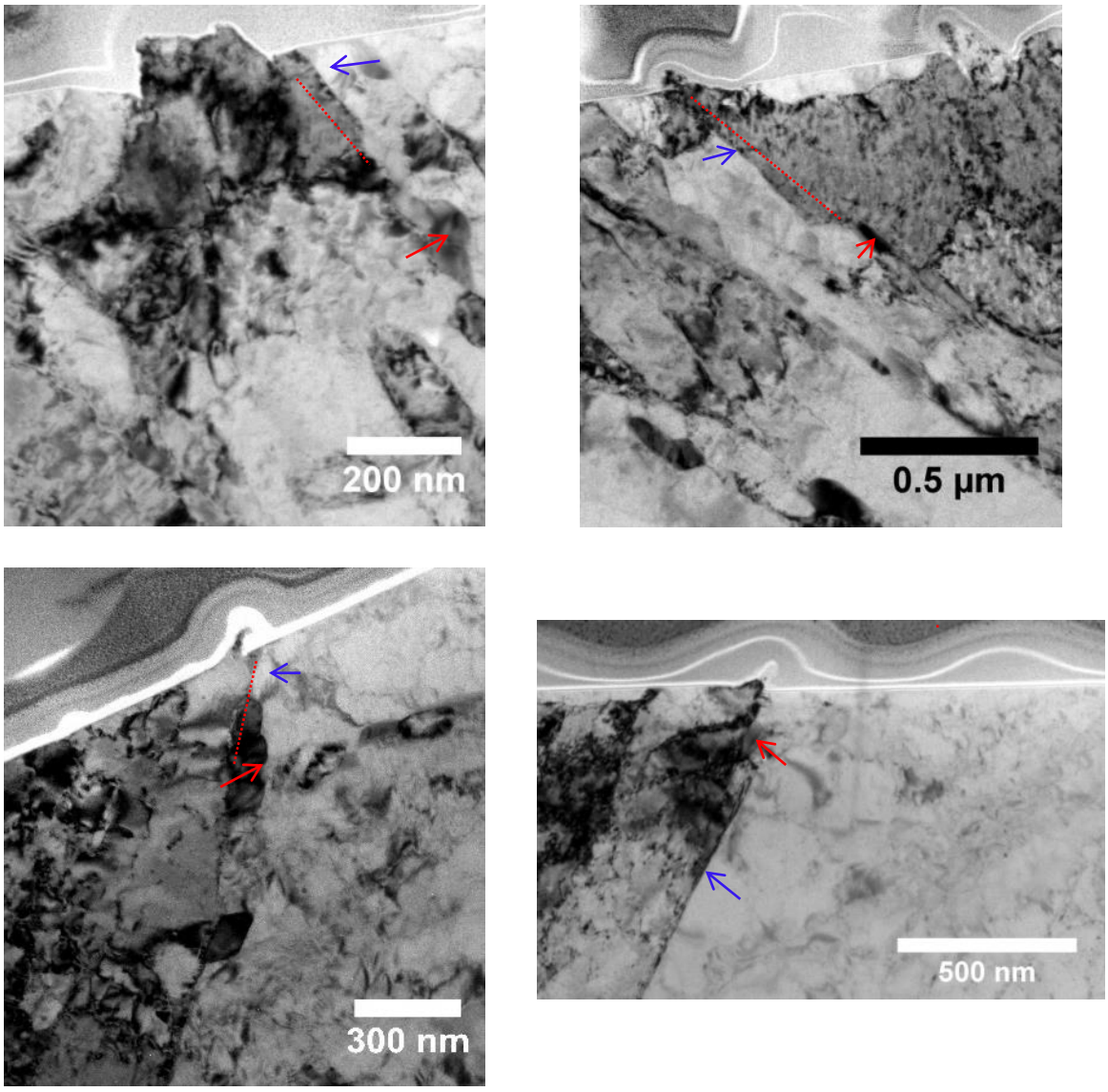

Figure 5-7 Role of precipitates in the extrusion-intrusion localization. Red arrows indicate the precipitates. Blue arrows indicate the lath boundaries. The dashed red line show the direction of intrusion growth. Images were captured after 500 cycles

As a result the extrusion with accompanying intrusion is pushed aside too. In such a way the precipitate changed the path of dislocation gliding. It means that the mobile dislocations on the whole length of the lath participate in the creation of extrusion.

5.2.3 Localization of secondary extrusions

With a help of FIB lamellae extraction and corresponding TEM observations it was also confirmed that the sets of secondary extrusions observed for the first time after 500 cycles, are inside the lath. Thus, the Figure 5-8a shows the secondary extrusions observed by AFM on the specimen surface after 500 cycles of loading. The height of these extrusions is less than 10 nm. The TEM observations of lamella extracted perpendicularly to the mentioned above secondary extrusions (as shown by the black straight line) showed that the extrusions actually are in the lath and parallel to the lath boundary marked by white dashed line in the Figure 5-8b.

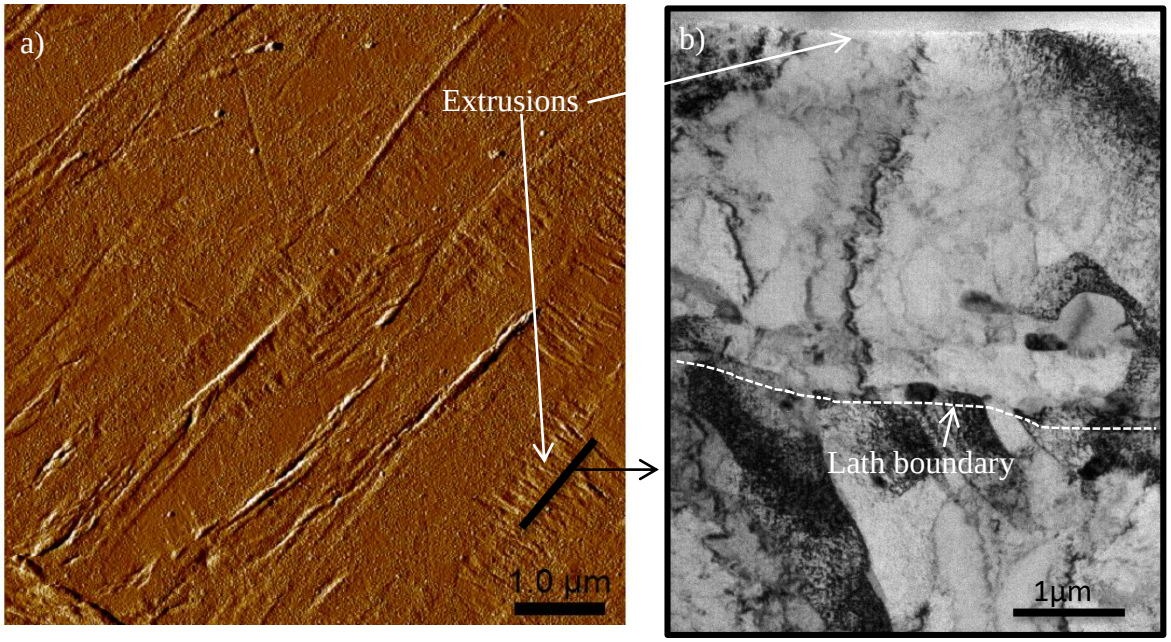

Figure 5-8 AFM amplitude signal error image showing the secondary extrusions on the surface after 500 cycles and the place of lamella extraction by FIB (a); TEM image of the lamella FIB of secondary extrusions located in the lath and parallel to the lath boundary indicated by the white dashed line (b)

5.2.4 Morphology of FSM cross-sections

The observations of FSM cross-sections revealed a number of different morphologies of extrusions. In the Figure 5-9 and Figure 5-10 the TEM and AFM images of a morphological type called “extruded lath” are illustrated. It got such name because it represents the entire lath that was pushed out on the specimen surface. The reasons for its appearance are not still well understood, but some assumptions will be discussed in the next chapter.

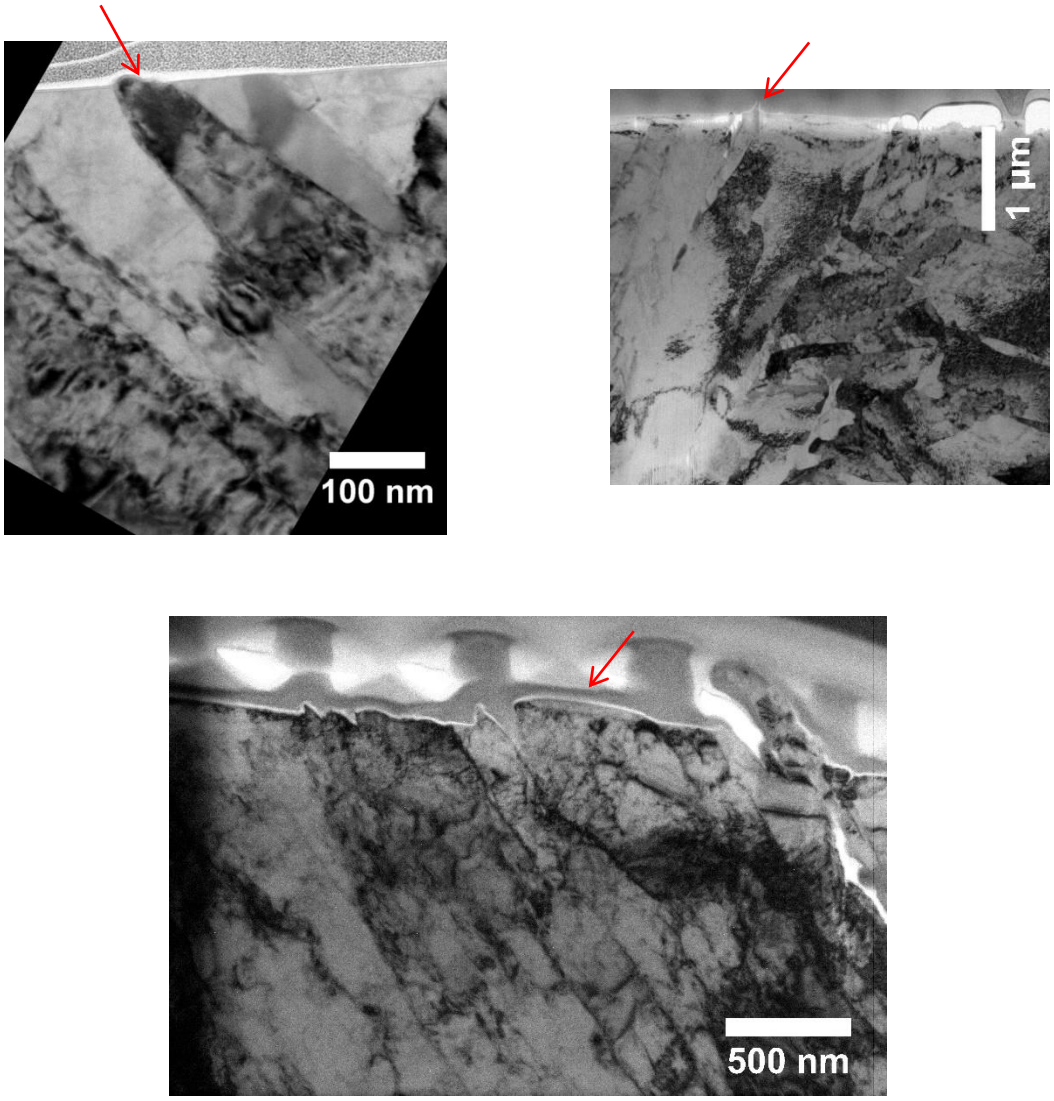

Figure 5-9 FSM cross-sections presenting the lath extruded on the specimen surface are pointed out by red arrows. Images were captured after 500 cycles

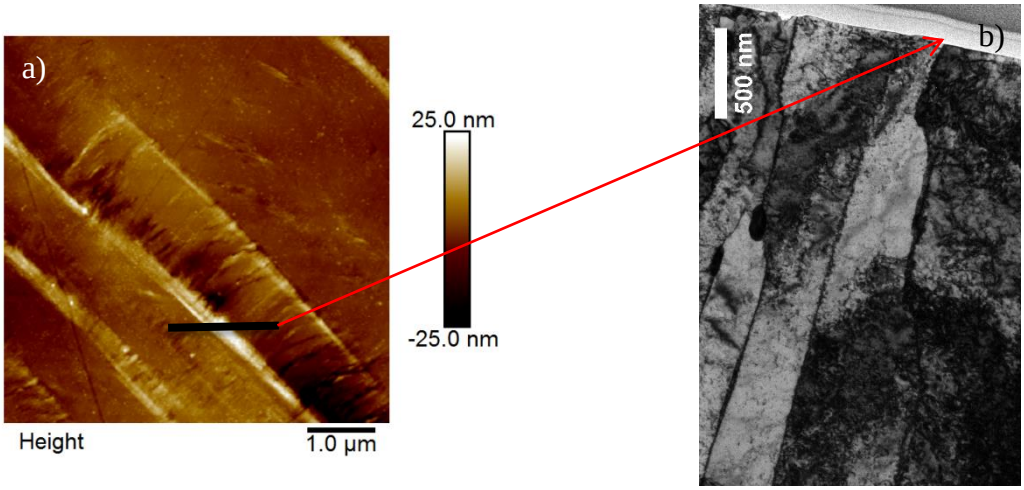

Figure 5-10 a) AFM height image showing an extruded lath on the surface after 500 cycles; b) TEM image of FSM cross-section presenting the lath extruded on the specimen surface after 500 cycles

In the Figure 5-5c the ribbon-like extrusion cross-section is presented. The extrusion surrounded by two intrusions can be well distinguished. One of the intrusions has appeared just right in the lath boundary well marked by arrays of dislocations, while the other one is in the cell wall which is, unfortunately, barely visible probably due to the partial extinguishing of the wall by FIB.

In the Figure 5-11 the protrusion cross-section and its AFM image on the specimen surface are illustrated. Different extrusions making this protrusion are delimited by the walls of dislocation cells. The intrusions are defined by the barely visible boundaries which are probably the cell walls.

In the Figure 5-12a another large protrusion is shown. The width of this one is about 400 nm and it occupies the whole width of underlying dislocation cell marked by white dashed line. At the extreme right of this protrusion an intrusion, appeared in the dislocation cell wall, is seen. Figure 5-12b illustrates a protrusion that occupies the whole lath width (approximately 400 nm).

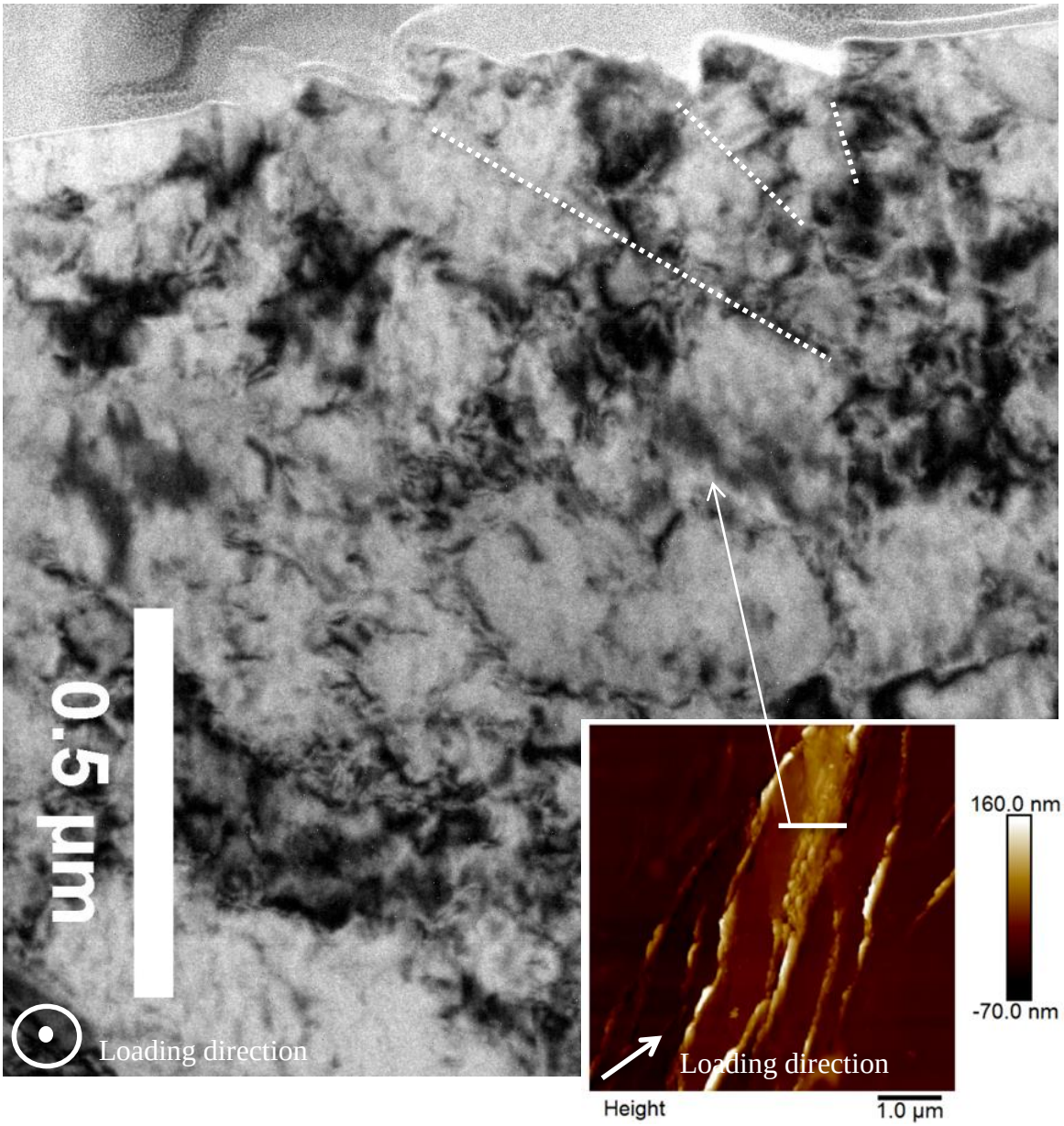

Figure 5-11 Protrusion cross-section. AFM image shows the same protrusion from the top. The dashed lines indicate the slight boundaries of cells defining the intrusions of protrusion. The images were captured after 500 cycles

Additionally, a rare shape of extrusion cross-section was found. In the Figure 5-13 a large and high extrusion, appeared in the dislocation cell, is presented. The width of extrusion is approximately 200 nm and the height is about 100 nm. Both dimensions are equivalent to the average width of lath or to the average diameter of cells. The walls of the cell are marked by white dashed lines. The red dashed lines show the slightly distinguishable interfaces; the

intrusions are located in these interfaces. The AFM image of extrusion on the specimen surface together with its profile (Figure 5-14) permits to classify the extrusion as a potential protrusion.

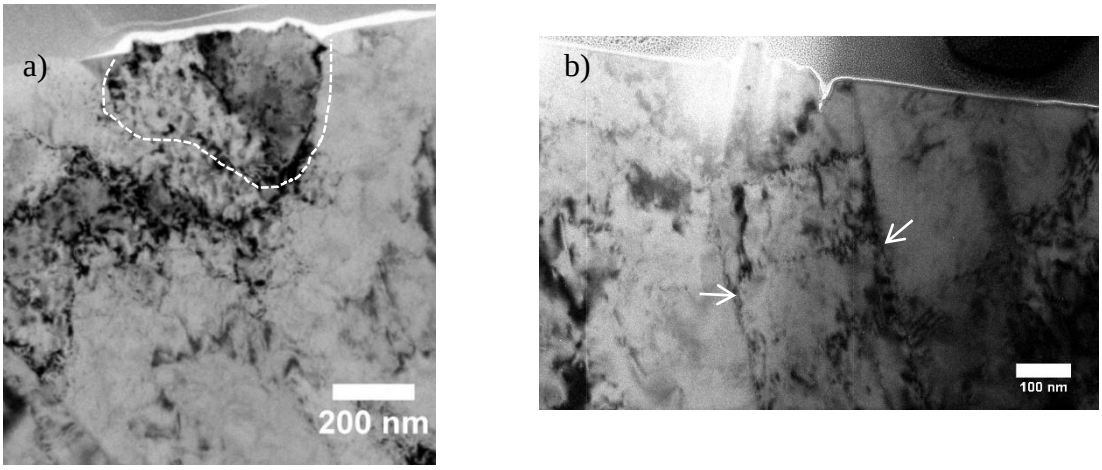

Figure 5-12 Cross-sections of protrusions after 500 cycles. The white dashed line indicates the cell wall; the arrows show the lath boundaries

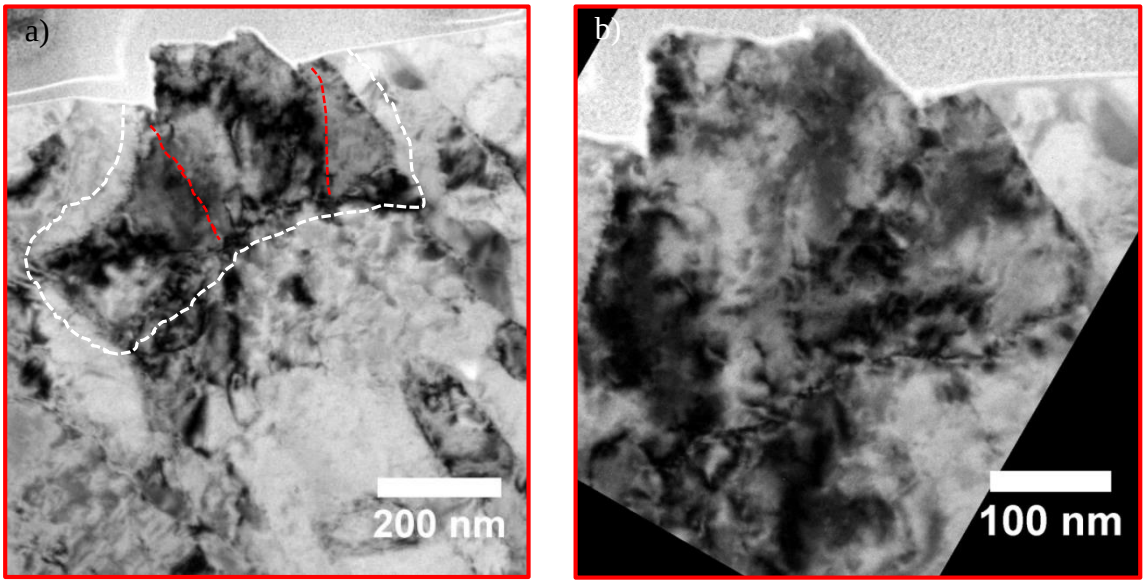

Figure 5-13 a) TEM image of protrusion cross-section after 500 cycles; the white dashed lines indicate the cell walls; the red dashed lines inside the cell indicate the slight LAB which define the route of intrusion; b) magnified TEM image of protrusion in (a)

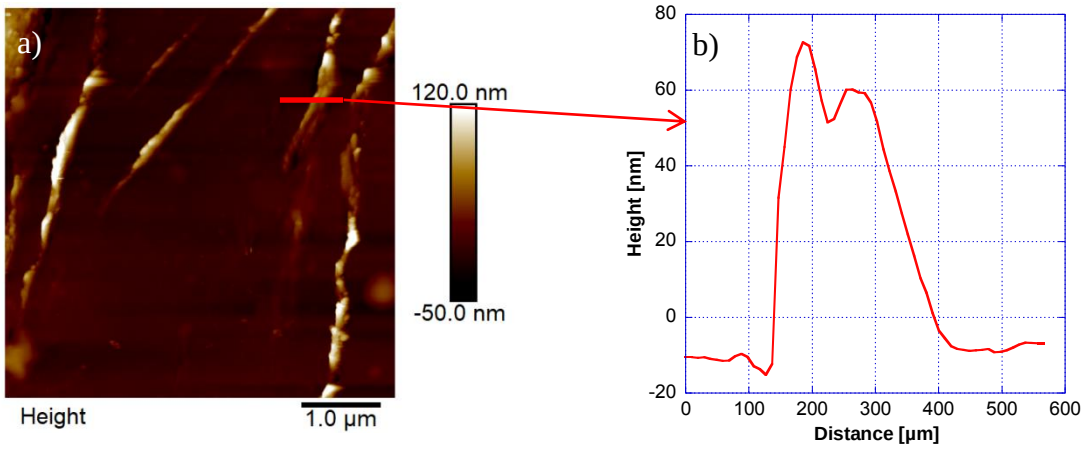

Figure 5-14 a) AFM image of the protrusion in the Figure 5-13 on the specimen surface; d) AFM profile of the protrusion

5.2.5 Some dimensions of FSM cross-sections

The TEM images of the FIB thin lamellae allow measuring the depth of intrusions, which was not possible with AFM technique. In the Figure 5-15 it is shown the method of height and depth measuring. About 35 intrusions and 35 extrusions were analyzed with a help of image processing program ImageJ. In the Figure 5-16a the comparison of extrusion heights and intrusion depths is illustrated. The majority of heights and depths are comprised between 2 and 80 nm. The average height of extrusions was 53±32 nm, and the average depth of intrusions was 53±38 nm. Thus, our results showed that the intrusion depths were equivalent to the extrusion heights after the interruption at 500 cycles. However, this is not a case for the areas of extrusions and intrusions. The areas of about 40 intrusions and 40 extrusions were measured again in the ImageJ program. In the Figure 5-16b the red points corresponding to the areas occupied by extrusions lie higher than the areas of intrusions (blue points). Moreover, about 4 different points, corresponding to the areas of protrusions and extrusion with a rare shape mentioned in the previous paragraph, are greater than 10 000 nm^2 (upper limit of y-axis).

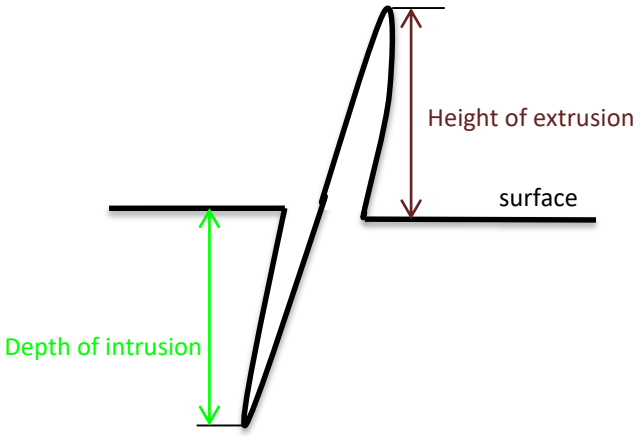

Figure 5-15 The method of the extrusion's height and intrusion's depth measurement

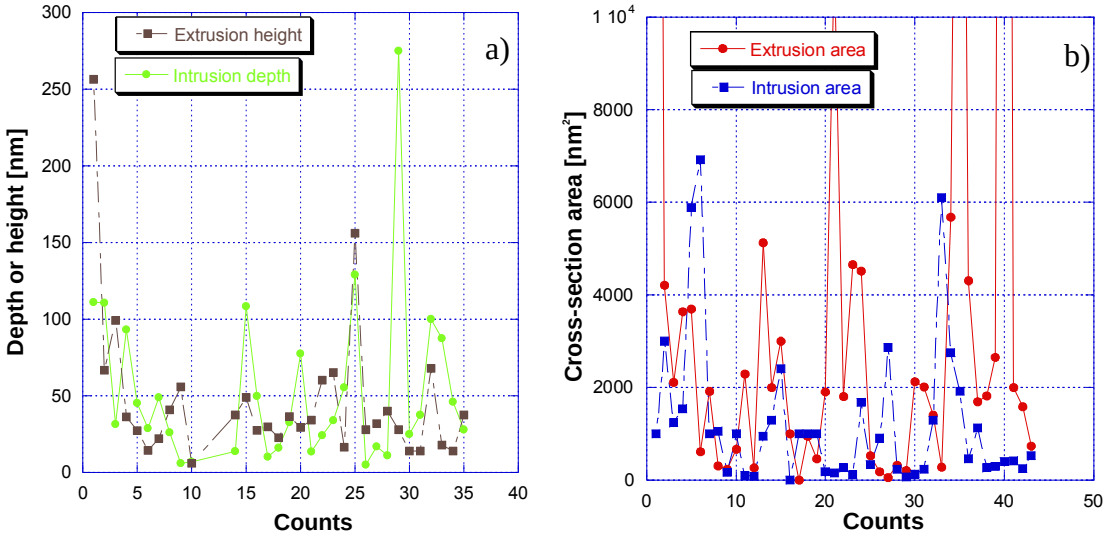

Figure 5-16 a) scatter of extrusion heights and intrusion depths; b) scatter of extrusion and intrusion areas

The integrated sum of extrusion areas was found to be 189 648 nm^2 and the sum of intrusion areas was 53 623 nm^2, i.e. the extrusion areas are 3.5 times superior to the intrusion areas at the interruption of 500 cycles. Although we cannot measure the real volume of extrusions and intrusions, it seems that the intrusions occupy less space than the extrusions. This is in a good agreement with the observations of Polak *et al.* [119]. However, the result was obtained only after 500 cycles, which is why it should be validated by the additional measurements after different steps of interrupted test.

5.2.6 Comparison with the results obtained by AFM profiling

Due to the observations, the height, width and interior angles of extrusions with a help of ImageJ image processing program were measured and compared to the results obtained by AFM profiling measurements. First of all the average height of extrusions measured on FIB lamellae after 500 cycles of loading was found to be 53±32 nm which is equivalent to the average height measured by AFM after the interruption at 500 cycles (Figure 4-17). Secondly, the heights of ten random extrusions were compared to their equivalents measured by AFM. In the Figure 5-17 the comparison graph is presented. It was revealed that the height corresponds to the one measured by AFM with a maximum difference 10%.

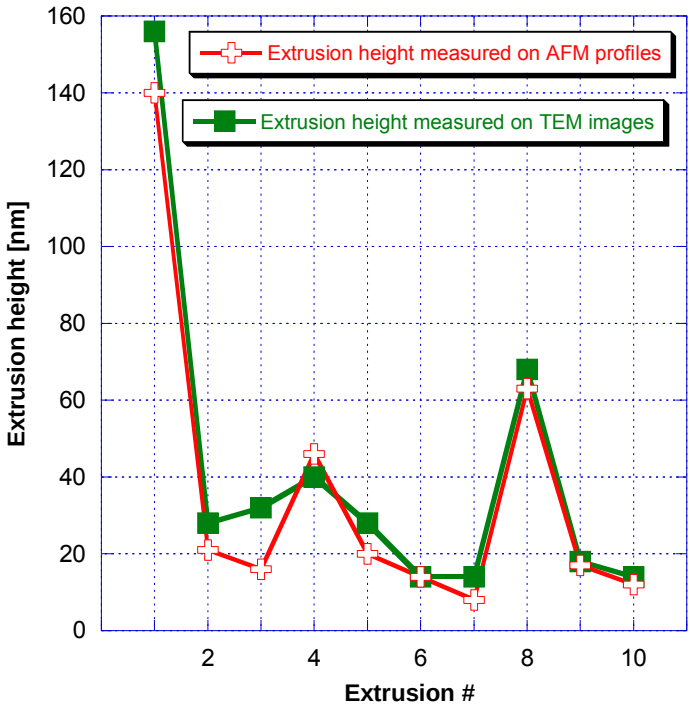

Figure 5-17 Comparison of the heights of extrusions measured on the TEM and AFM images

As for the interior angles, if they do not exceed the limit angles conditioned by the front and back angles of AFM tip and cantilever tilt, then the measurements made on TEM images correspond to the measurements of angles and width of extrusion base on the AFM images. But in the majority of cases only one of the interior angles was measured correctly by AFM. This is coherent with the observations of Polak *et al*. [95].

5.3 Coupled SEM-ECCI-EBSD-TEM study of FSM

Few experiments have been carried out with SEM-ECCI (Scanning Electron Microscope - Electron Channeling Contrast Imaging) and SEM-EBSD (Electron Backscatter Diffraction) in order to give the additional information on the observed FSM. Indeed, as TEM allows only very local observations, SEM-ECCI and SEM-EBSD give complementary data in the investigation at a large scale.

Both SEM-based techniques were performed on JEOL JSM-7800F FEG-SEM microscope fitted with an Aztec system from Oxford Instruments. EBSD data were processed using the Oxford Instruments CHANNEL5 software. The step size of EBSD acquisition was 50 nm, while the angular resolution reached 0.2°. As for the sample surface preparation it was already discussed in *3.1.3Microstructural characterization*. In the following paragraph the basics regarding the two techniques will be presented. Afterwards, the obtained results will be presented and discussed in details.

5.3.1 SEM-ECCI

The SEM principle is the scanning by the electron beam of a sample surface. The accelerating voltage is generally comprised between 5 and 30 kV. The interaction between electrons and specimen surface brings to the emission of secondary and backscattered electrons that allow surface imaging [125].

The secondary electrons (SE) are issued from the inelastic interaction between beam electrons and electrons of an analyzed material. They allow topographical imaging of samples.

The backscattered electrons (BSE), originating from the emission source, are collected after their slight quasi-elastic interaction with the sample surface atoms. They carry both the topographical information and the chemical composition variation data. Indeed, the lower the atomic number of atom, the stronger the electronic interaction and the slower the electron is. As a result, the kinetic energy differences between the backscattered electrons are used to obtain the information about the sample surface chemistry [125].

However, BSE can be used also to obtain the crystallographic contrast images between different grains of studied material or for the observation of lattice defects, for example dislocations or stacking faults, close to the sample surface. This technique is called Electron Channeling Contrast Imaging (ECCI). As shown in Figure 5-18 minimum backscattering takes place when the primary electron beam almost precisely corresponds to the Bragg angle with one of the lattice planes. The electrons then travel deep inside the crystal without intense interaction with it. This phenomenon is called electron channeling.

If a dislocation or a stacking fault is present in the crystal, then the channeling effect (coherency of channeling primary beam with the lattice) is not valid anymore and strong backscattering occurs at the position of the defect. As a consequence, the defect is illustrated as a bright feature on a dark background when the sample is observed with a backscatter electron detector.

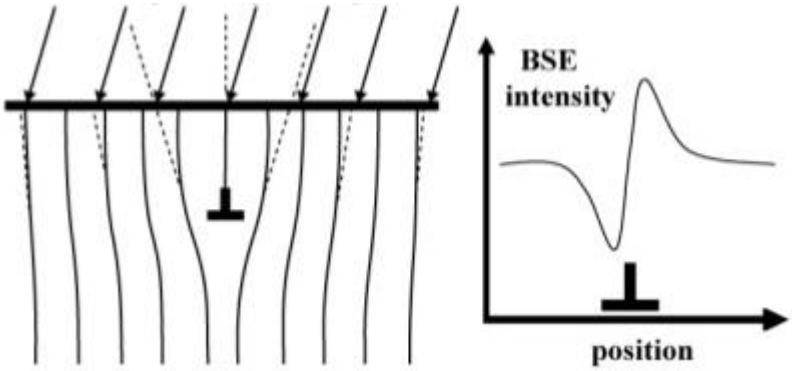

Figure 5-18 Schematics of BSE intensity variation as a function of incident beam angle [126]

5.3.2 SEM-EBSD

Electron backscatter diffraction provides the crystallographic information about the sample microstructure. This method involves interaction between an electron beam and a tilted crystalline sample. The tilting is necessary to collect the maximum of diffracted electrons.

The main idea of technique is that some of the backscatter electrons may escape the sample at the Bragg condition and diffract. The diffracted electrons give birth to a group of paired large-angle cones, which correspond to diffracting planes. Then these cones intersect the phosphor screen creating the Kikuchi bands (Figure 5-19). The created diffraction pattern is passed through the Hough transformation in order to convert the bands into the easily identifiable

points. Afterwards, they are compared to the reference database and the crystallographic orientations of diffracting planes are deduced [127].

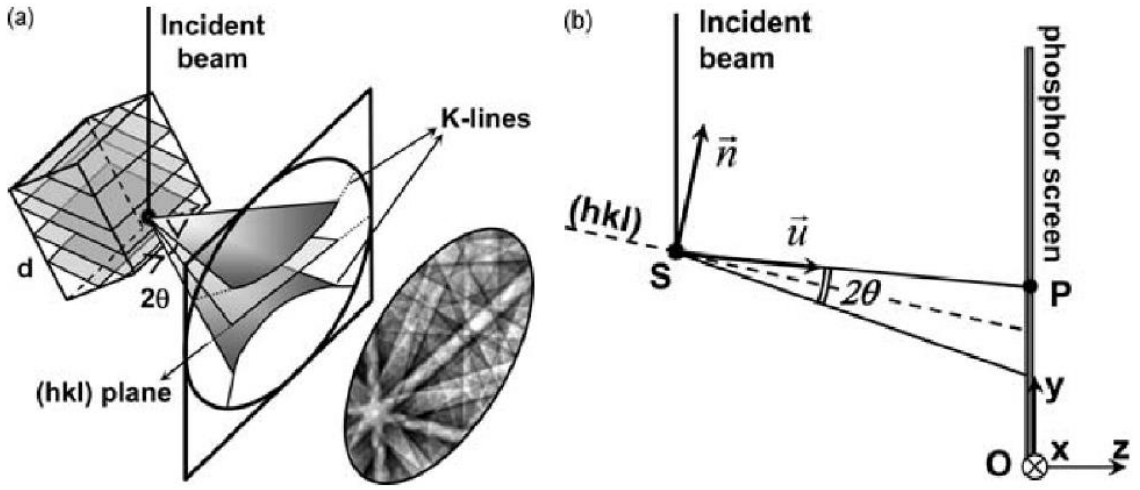

Figure 5-19 Schematics of Kikuchi bands formation during the diffraction of BSE [128]

5.3.2.1 Image quality

One of the primary applications of EBSD analyses is the Image Quality (IQ). Each pixel of IQ represents the quality of diffracting pattern. Thereby, the image quality is affected by the non-indexable areas such as defects, grain boundaries and deformation. As a consequence, the lower IQ patterns correspond to a lattice distortion that can be related to structures such as grain boundaries and dislocation sub-structures. Indeed, the deformation within the material induces the formation of two types of dislocations: the Statistically Stored Dislocations (SSD) and the Geometrically Necessary Dislocations (GND) (Figure 5-20). In the SSD regions, the global Burger's vector is close to zero on the contrary to the GND regions where there is a change in the crystallographic orientation. This can lead to the formation of subgrain boundaries. In this case, the diffraction pattern of volume is the superposition of the images of two subgrains resulting in a shift of the Kikuchi lines (Figure 5-21). GND may also come from the distortion of network induced by a phase change.

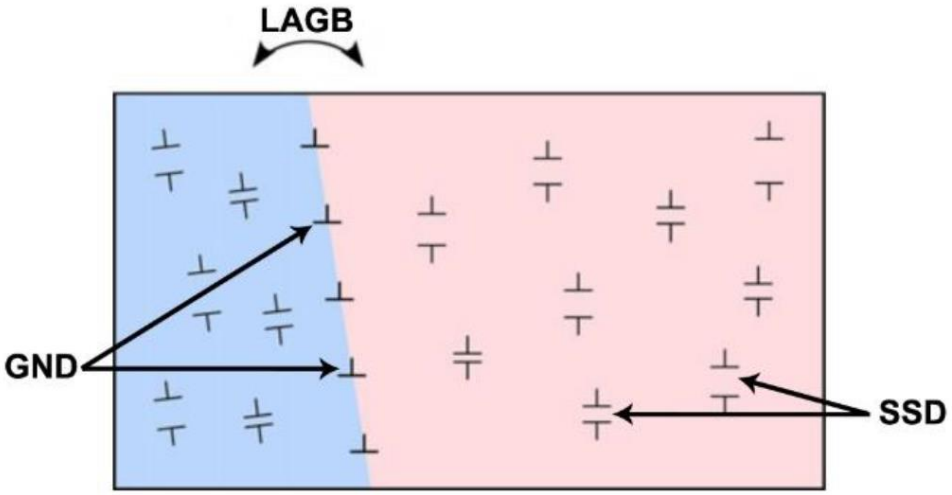

Figure 5-20 Schematics of SSD and GND [129]

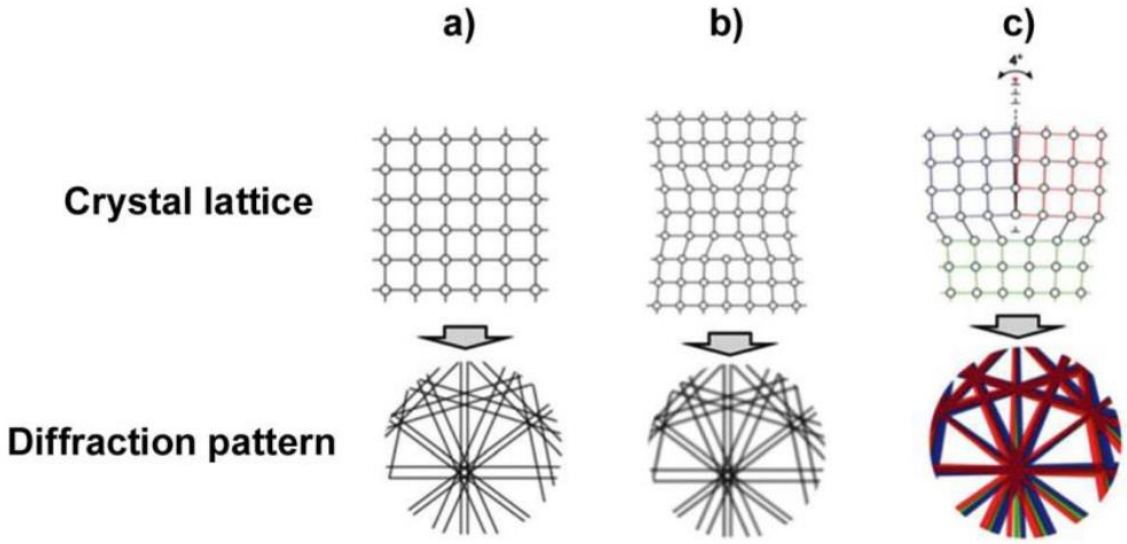

Figure 5-21 Schematic representation of crystal deformation impact on the diffraction patterns: a) non-deformed; b) SSD; c) GND [129]

5.3.2.2 Orientation Imaging Microscopy

The crystallographic orientation is deduced using the Euler angles. There are a few definitions of Euler angles, but the most common one is Bunge definition. According to it the Euler angles are the successive rotations of the sample reference around the crystal reference (Figure 5-22). These three rotations are characterized by the rotation matrices g_1, g_2, g_3. The orientation matrix

is the product of these three matrices. Three Euler angles describe a minimum set of rotations that can bring one orientation into coincidence with another [130].

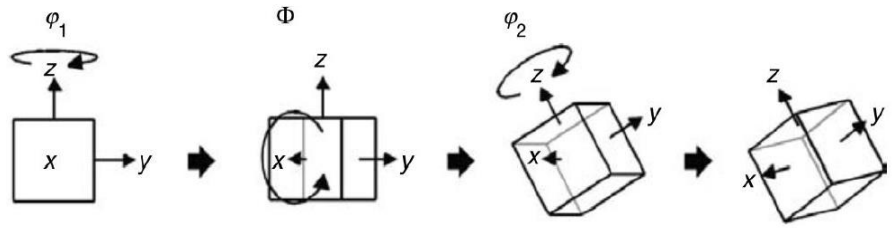

Figure 5-22 Representation of different Euler angles according to the Bunge convention [131]

5.3.2.3 Inverse Pole Figure

The crystallographic orientations are mainly illustrated by means of Inverse Pole Figure (IPF) which is a stereographic projection of the crystallographic directions of grains parallel to one of the sample directions: either the normal direction (ND), rolling direction (RD) or transverse direction (TD) (Figure 5-23). The directions of crystal planes are called poles. In the present study the plotted crystal directions are parallel to the loading direction of the sample, i.e. to the rolling direction or longitudinal direction of the sample.

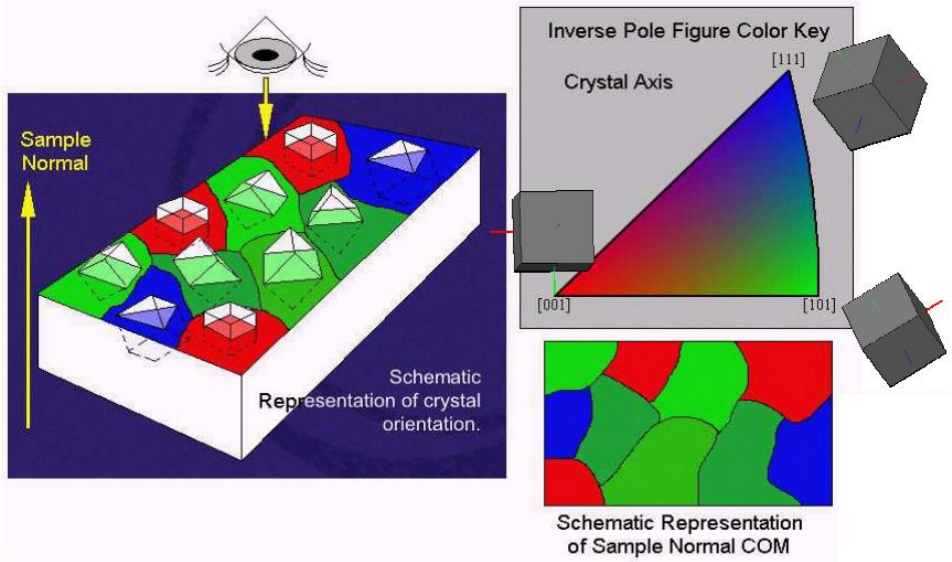

Figure 5-23 Crystallographic orientation map (COM) with IPF key: red corresponds to the (100), blue – (111), green – (110) planes parallel to the surface [132]

5.3.2.4 Line Segment Method

Line Segment Method (LSM) is a complementary EBSD approach allowing the representation of grain boundaries. As illustrated in Figure 5-24 each pixel of schematics symbolizes a resultant point of Kikuchi band indexation of scanned zone. Thus, the grain boundary traces are represented by a set of line segments separating adjacent EBSD points (pixels), the disorientation of which overpasses a limit value according to the selected criterion [133]. As a result it is possible to distinguish the High Angle Grain Boundaries (HAGB or simply HAB), with disorientations usually higher than 10°, and the Low Angle Grain Boundaries (LAGB or LAB), associated with the disorientations between 2° and 5° in the present work. It should be reminded here that PA grains, packets and blocks possess HAB, while laths and cells have LAB.

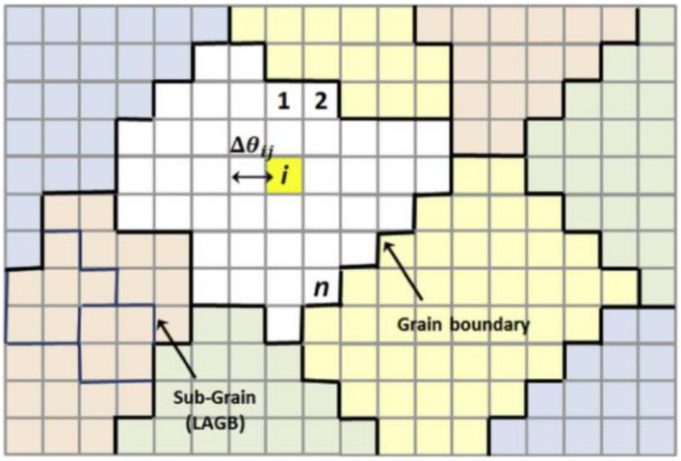

Figure 5-24 Schematics of EBSD scan with LSM approach [134]

5.3.3 Results of principal extrusion observations

In the following paragraph the observations of the zone, presented in Figure 5-25 in black box and subjected to 250 cycles at $\Delta\varepsilon$=1.2%, will be discussed in details.

The Figure 5-26 illustrates the extrusions and intrusions formed by cycling on the specimen surface. The ECCI high resolution images (Figure 5-26; Figure 5-27a) allow guessing that the two extrusions confined in a red box are in the vicinity of boundaries. Moreover, some dislocation cells are recognized on the specimen surface in Figure 5-27b. However, the type of boundaries can be identified only with a help of EBSD orientation imaging. Thus, the EBSD IPF map (Figure 5-28a) confirms the fact that both extrusions are close to the boundaries, but

still it cannot be concluded whether they are just next to the boundaries or maybe inside the boundary itself. Nevertheless, it can be summed up that both extrusions are in different blocks: extrusion ***A*** is in the (001)[120] block and the extrusion ***B*** is in the (233)[2-31] block of laths (Figure 5-28a). The extrusion ***A*** is rather close to the HAGB, and the extrusion ***B*** is in the vicinity of LAGB (Figure 5-28b).

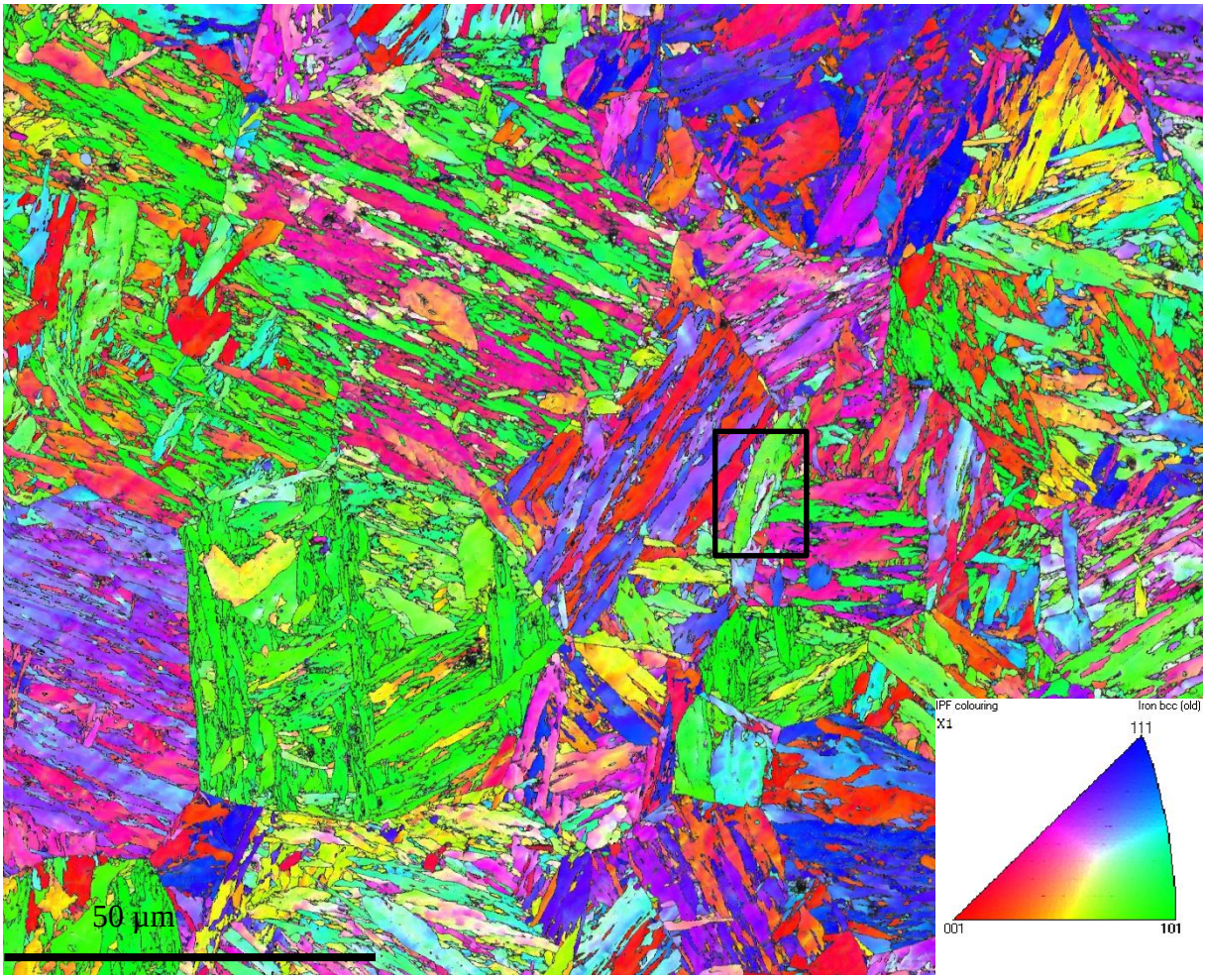

Figure 5-25 IPF map of the studied steel surface before fatigue. Black box indicates the zone that will be investigated after loading

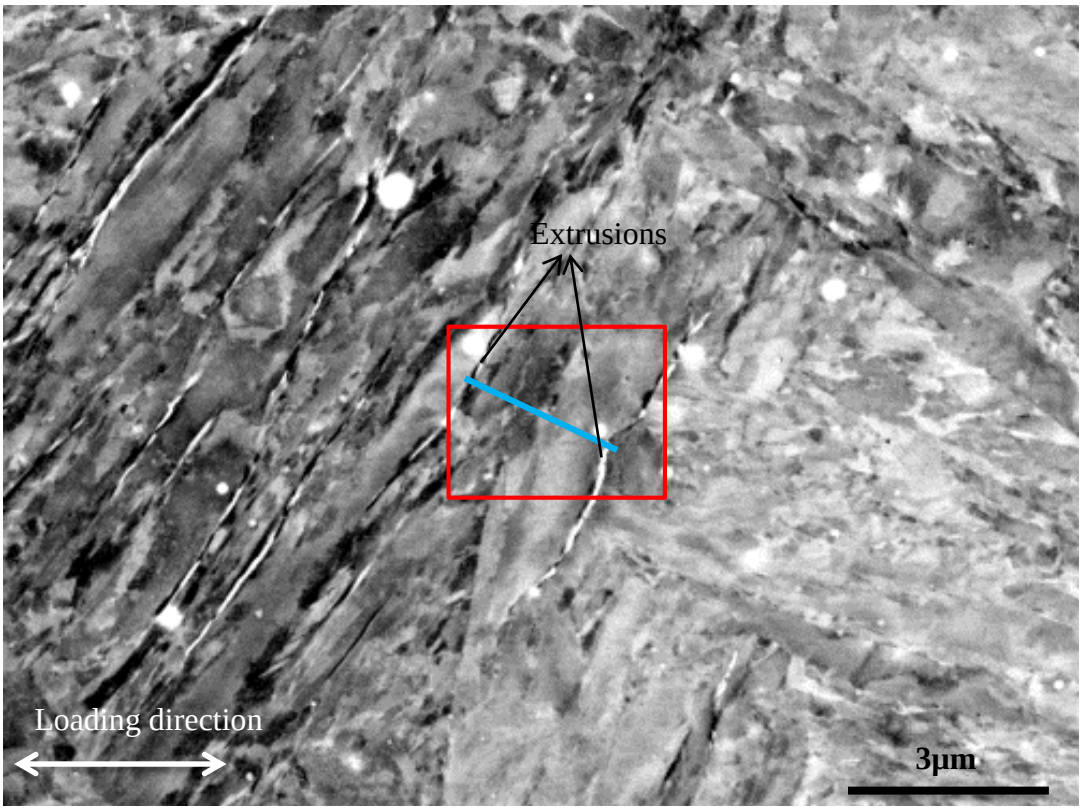

Figure 5-26 ECCI image of extrusions on the specimen surface: the contrast changes are due to the crystallographic orientations of microstructure elements; red box indicates the zone of magnified ECCI imaging and EBSD imaging presented in Figure 5-27 and Figure 5-28 respectively; blue line indicates the localization of TEM lamella extraction by FIB, the observations of which are in Figure 5-29

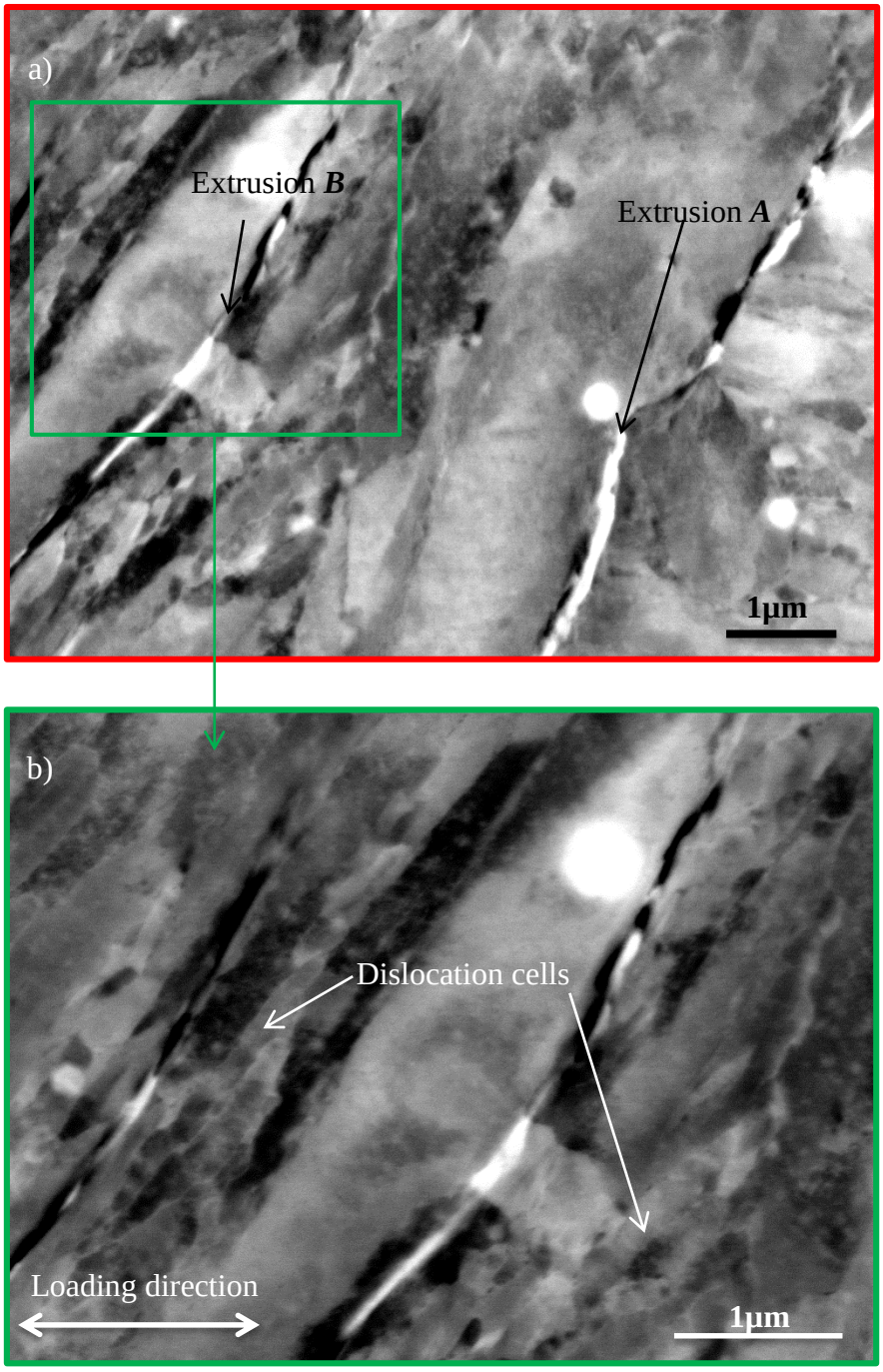

Figure 5-27 a) ECCI image of zone delimited by red in Figure 5-26 clearly revealing two extrusions with accompanying intrusions; b) magnified ECCI image of extrusion ***B*** and dislocation cells

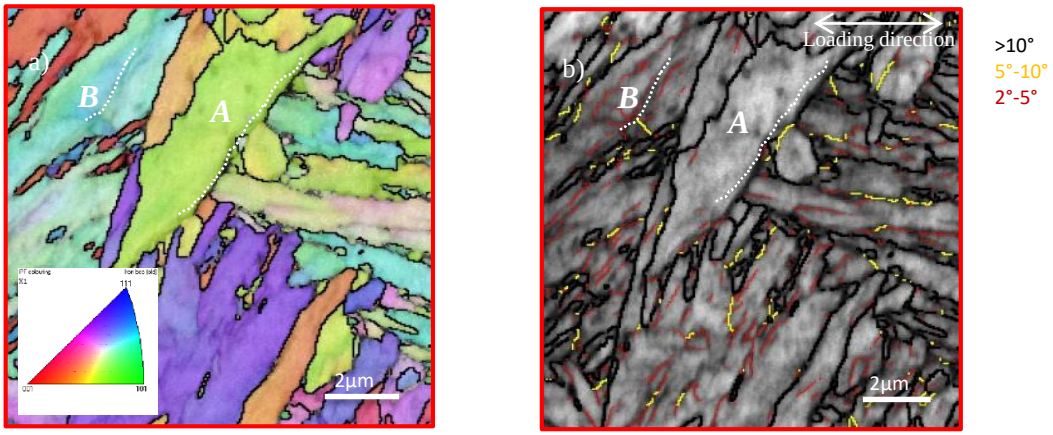

Figure 5-28 a) IPF color map of the zone with two extrusions ***A*** and ***B;*** white dashed line imitates the extrusion; c) boundary disorientations by line segment method in EBSD

The given information was accomplished by the observations of thin lamella extracted by FIB perpendicularly to the extrusions ***A*** and ***B*** as shown in Figure 5-26. The Figure 5-29a illustrates the general view of the lamella. Unfortunately, because of the non-uniform milling, only extrusion ***A***, delimited by the yellow box, could survive the FIB lamella preparation. It can be seen that the extrusion is localized inside a lath (Figure 5-29) belonging to the block (001)[120] observed in Figure 5-28a. The extrusion appeared in a lath inclined at approximately 45° to the loading axis. Some boundaries of this lath could not be observed by EBSD technique because of their low disorientation and the high density of dislocations inside the laths. Indeed, the EBSD angular resolution is 0.2°, the disorientation between two laths can be lower than 1° [46], and the very high dislocation density inside the lath induces many local low angle disorientations inside the lath. Therefore, once the minimum angle of line specification is put lower than 1.5°, the lath boundary cannot be distinguished at all among all the local disorientations between dislocation cells and single dislocations inside the lath. Only the TEM observation permitted seeing this boundary indicated by arrows in the Figure 5-29b and c. So, the extrusion ***A*** is in the lath and close to one of the boundaries of the lath. The TEM analysis also points out that this extrusion is accompanied by an intrusion. Unfortunately, any dislocations or their structures cannot be observed under the extrusion cross-section even after lamella tilting. Probably, the lamella preparation was too severe and swept out most of dislocation traces (*3.4.2.3FIB artefacts*). However, the fact that the extrusion with the intrusion are slightly aside of the boundary could be explained by the precipitate who pushed a segment of boundary inside the lath (Figure 5-29c).

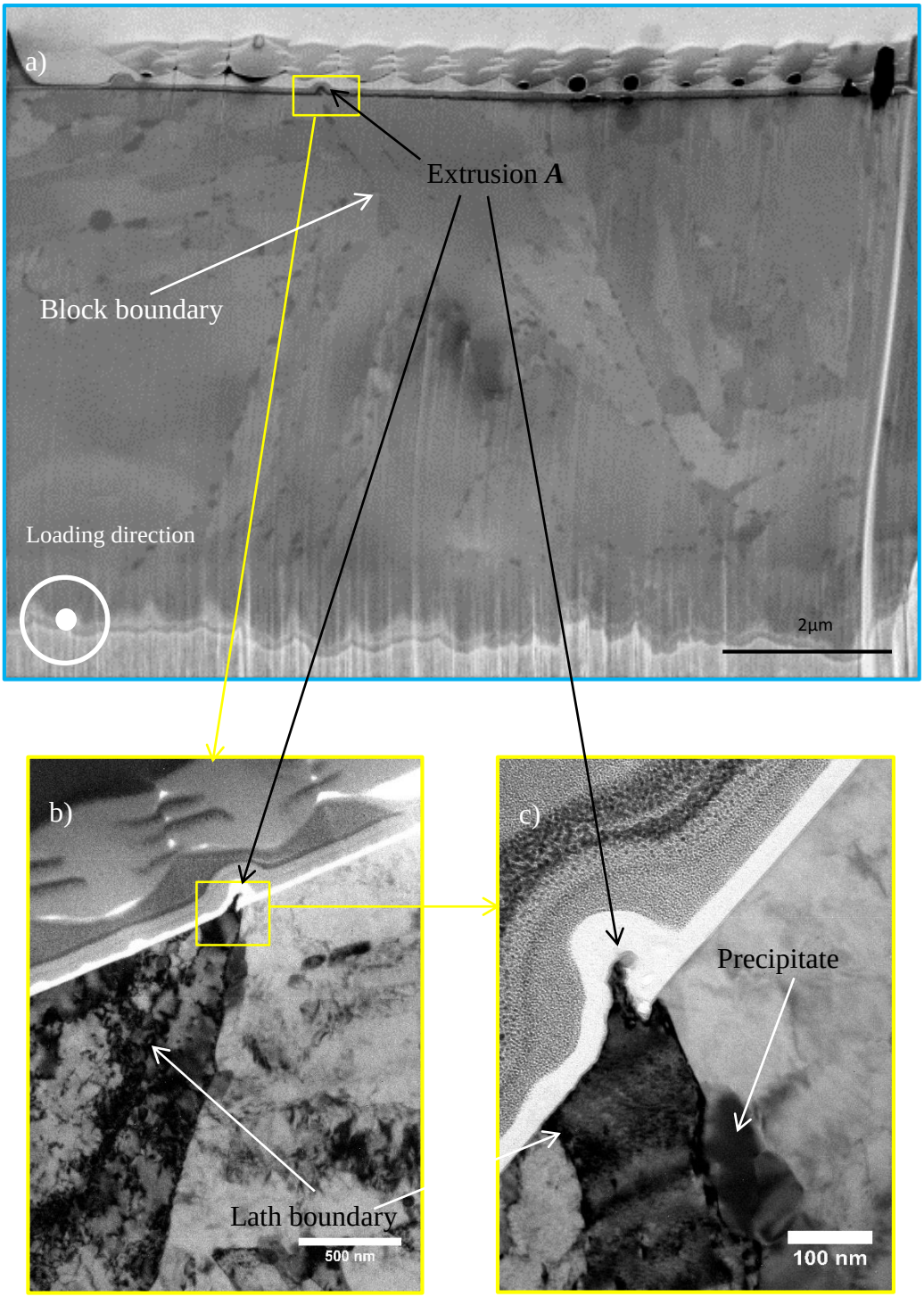

Figure 5-29 a) SEM image of lamella extracted by FIB perpendicularly to the extrusions illustrated in Figure 5-26; b) and c) extrusion ***A*** cross-section observed in TEM. The precipitate diffraction pattern and EDX analysis are in Figure 3-6

Thus, the precipitate changed the path of dislocation gliding. It means that the mobile dislocations on the whole length of the lath participate in the creation of extrusion.

EBSD Orientation Imaging Microscopy (OIM) allows identifying the slip plane traces correspondent to the particular extrusions on the surface and the Schmid factor appropriate to each block or lath. Using the Euler angles of crystal orientation and the angle between FSM trace and loading axis we could define the Schmid factor and the slip plane and direction both for extrusion ***A*** and ***B*** and for a few other principal extrusions. The results are presented in Table 5-1. The extrusion ***A*** is a consequence of gliding of dislocations on the plane (-101) with the slip direction [111] and the maximum Schmid factor 0.49. The extrusion ***B*** is the trace of slip plane (01-1) and direction [-111] with the Schmid factor of 0.47. Among 6 analyzed extrusions, 5 are the traces of the slip system {110}<111>, i.e. the close-packed planes and directions of bcc metals and the most expected slip system.

Table 5-1 Definition of slip planes, directions and Schmid factor for some principal extrusions

Extrusion #	Slip plane	Slip direction	Schmid factor
1 (***A***)	-101	111	0.49
2 (***B***)	01-1	-111	0.47
3	110	1-11	0.48
4	01-1	-111	0.41
5	121	1-11	0.46
6	01-1	-111	0.46

5.3.4 Results of secondary extrusion observations

Application of 250 cycles permitted to observe the secondary extrusions as well. Thus, AFM images in Figure 5-30ab show the sets of secondary extrusions labelled S1 and S2 accompanying the principal extrusions P1 and P2 respectively. The secondary extrusion height is of the order of 10 nm. SEM, SEM-ECCI images and IPF color map (Figure 5-30cde) show clearly that the set S1 is in the block (233)[2-21], the longitudinal direction of which is oriented at approximately 10° to the loading axis, while the secondary extrusions themselves are at approximately 60° to the loading axis.

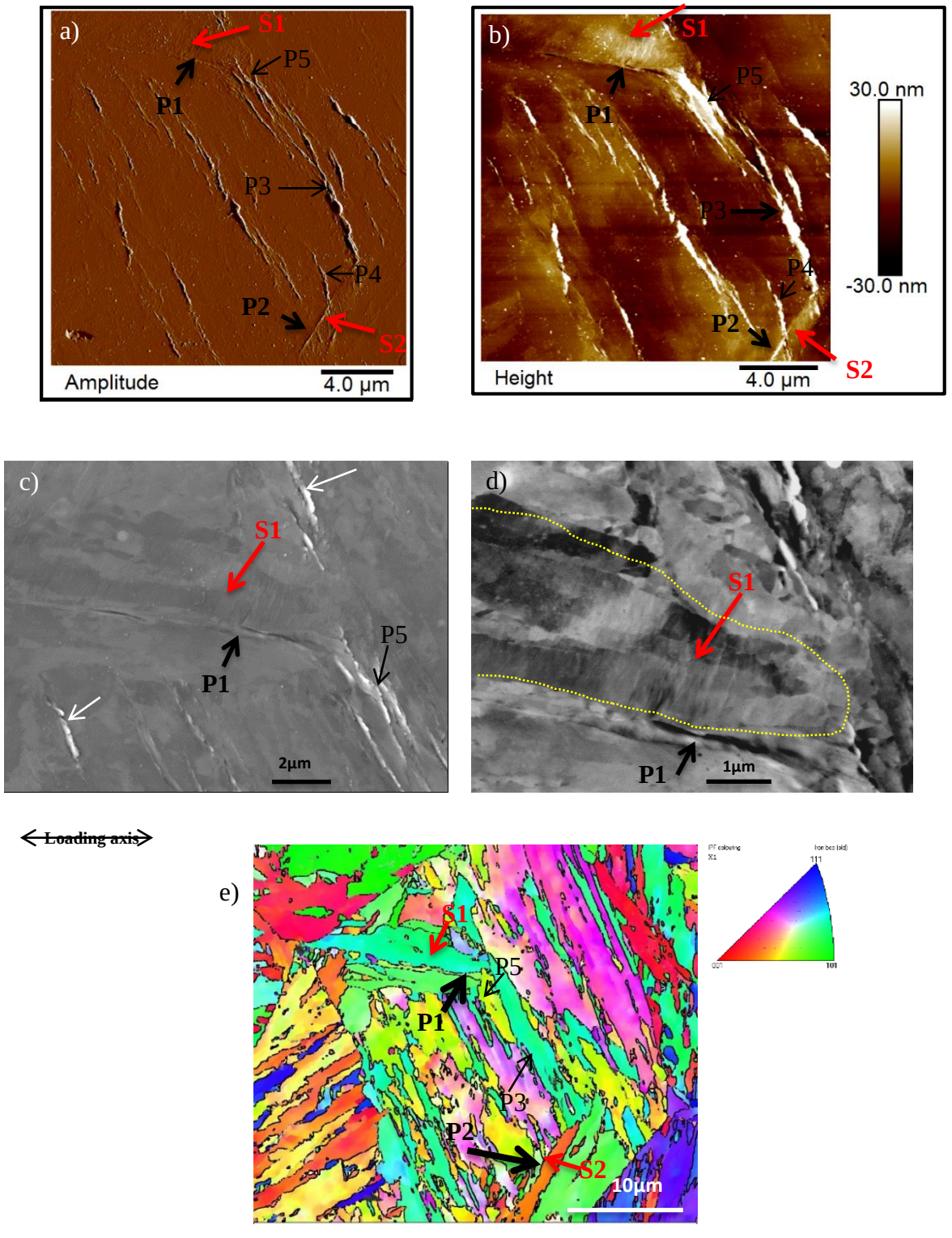

Figure 5-30 AFM amplitude signal error image (a) and topographic image (b) of specimen surface with secondary and principal extrusions; SEM image (c) and SEM-ECCI (d) images; IPF color map (e)

Moreover, the SEM-ECCI image reveals that the secondary extrusions cross over the laths and cells inside the relevant block (Figure 5-30d). Inside the block with secondary extrusions S1 there is no any principal extrusions, however, they are present in the adjacent block (201)[-351] labelled P1 and in the block (101)[-120] labelled P5.

Both P1 and P5 together with the principal extrusions P2, P3, P4, and other principal extrusions marked by white arrows result from dislocation glide in the most expected slip system {110}<111> with the highest Schmid factor as illustrated in Figure 5-31. This result is in agreement with the observations of other principal extrusions reported in the previous paragraph as well as with Batista *et al*. [46]. However, there is no any relation between Schmid factor of a given block or lath and the average height of an extrusion in the lath (Table 5-2). This result confirms the statement of Risbet *et al*. [103] about the absence of dependence between the average height and maximum height of extrusion and relative Schmid factor value in the case of nickel-based alloy.

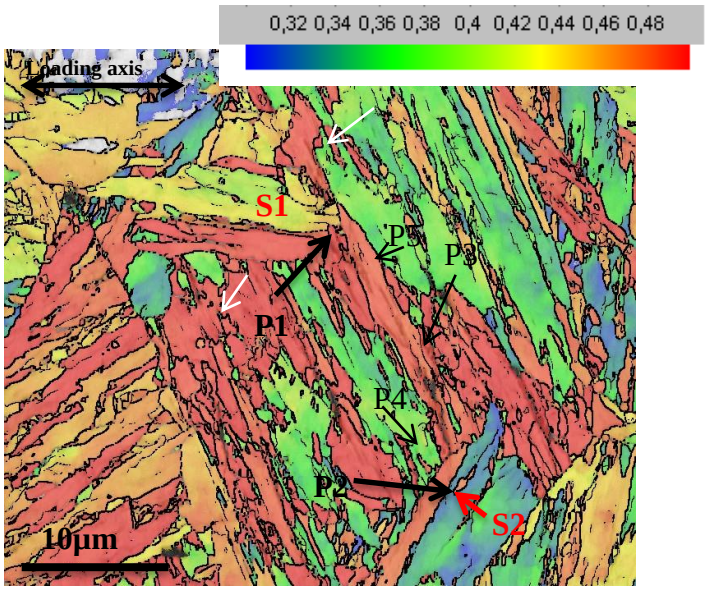

Figure 5-31 Schmid factor map for slip system {110}<111>

In the case of a set of secondary extrusions labelled S2 and a principal extrusion P2 lying in the same block oriented at approximately 60° to the loading axis, both types of extrusions glide in the same close-packed slip system {110}<111>, however the Schmid factor corresponding to the secondary extrusions S2 (0.49) is higher than the Schmid factor of principal extrusion P2 (0.39). We think that the secondary extrusions S2 with higher Schmid factor formed earlier than

the principal extrusion P2, but their growth was slower than the growth of a principal extrusion. It could be due to the fact that the principal extrusion trace is in the longitudinal direction of the lath, i.e. the gliding dislocations have long mean free path along the lath longitudinal direction. While the secondary extrusions are in the transversal direction, so the dislocation path is much shorter and as a result the dislocations are spent out faster. Moreover, the fact that the principal extrusion is really close to the block boundary has to play a role in the intensive growth of extrusion. Probably, the interactions of dislocations with the dislocations in the boundary contribute to the relatively fast development of principal extrusions. Moreover, some authors report that the local stresses next to the boundary are much higher than inside the grain, which brings to the extrusion formation close to the boundaries and not inside the grains [135], [136].

Table 5-2 Definition of slip systems, relative Schmid factor values and average height of secondary and principal extrusions depicted in Figure 5-30

Extrusion #	Slip plane	Slip direction	Schmid factor	Average height (nm)
S1	1-12	1-1-1	0.46	10
S2	-101	-11-1	0.49	10
P1	-1-10	1-1-1	0.49	20
P2	-110	-1-11	0.39	30
P3	011	-11-1	0.48	145
P4	011	-1-11	0.46	65
P5	-101	-11-1	0.49	55

To sum up the results of coupled SEM-ECCI-EBSD-TEM surface and bulk observations, the EBSD and ECCI techniques considerably clear up the development and localization of FSM. Firstly, the TEM observations of FSM cross-sections precise the localization of FSM in terms of “in the boundary” or “next to the boundary”. Secondly, the EBSD provides information on the type of boundary. In our study, the FSM were found both in the vicinity of HAB and LAB. Moreover, the technique may provide the statistical information on the slip planes and directions of extrusions. Thus, it was confirmed that the majority of principal and secondary extrusions are the result of gliding in the most probable slip system {110}<111> with the highest Schmid factor.

5.4 Conclusions

As a result of the study of microstructural evolution on the cross-sections of FSM, extracted by FIB, and coupled SEM-ECCI-EBSD-TEM study of FSM it can be concluded:

1. The fatigue loading induced the rearrangement of dislocations into the dislocation cells
2. It was certainly confirmed that the extrusions are rather inside the laths, inclined at 45° to the loading axis, or in the cells; while the intrusions are in the boundaries
3. Different morphological types of extrusions were discovered again by the observations of FSM cross-sections in TEM
4. The heights of extrusions measured on the TEM images correspond well to the heights measured on the AFM images.
5. It was found that the majority of principal and secondary extrusions are the result of gliding in the most probable slip system {110}<111> in bcc metals with the highest Schmid factor.

6. Formation of extrusion and intrusion

The present investigation shows that despite the hierarchical organization of microstructure of the investigated 12%Cr martensitic steel the relief formed at the external surface resembles that of more simple microstructural materials. Cyclic deformation is obviously accommodated by dislocation glide leading to the extrusion formation inside the laths as well as by the intrusion and incipient microcrack formation often at lath boundaries. Additionally to the manifestation of deformation on the external surface, the dislocation cells form in the bulk of material. It seems to be typical of martensitic steels as it is often reported when high precision investigation tools are employed [14], and in the present case by combining both AFM images of surface relief and TEM images of extrusion cross sections.

Furthermore, due to AFM in the present study two families of extrusions were revealed: principal and secondary extrusions. The secondary ones were observed for the first time in the martensitic steels.

The TEM imaging of FIB cross-sections confirmed that the principal extrusions are situated near the different interfaces or near the dislocation cell walls (Figure 5-4; Figure 5-5). The secondary ones, which appear often as a bundle of many small close packed extrusions or slip bands, are inside the laths or blocks, and mostly perpendicular and occasionally parallel to the principal extrusions on the free surface of material (Figure 4-13). As for the intrusions they were often localized in the interfaces (Figure 5-5; Figure 5-6).

There remains the question of how exactly the interfaces are responsible for the extrusion of material near the boundaries and the intrusion formation inside the boundaries as a result of LCF loading.

6.1 The starting point of the model

A mechanism based on interface sliding must be examined. The presence of soft layer of retained austenite at lath boundaries appears as a tempting explanation. For that, the steel has to bear the chemical composition favoring the retained austenite, i.e. has to contain gamma-stabilizing additional elements. In this way, Cretegny *et al*. and Du *et al*. [14], [45] explained the presence of extrusions at lath boundaries by the slippery property of lath boundaries due to the presence of retained austenite at the boundaries. However, Morsdorf *et al.* [44], who investigated a martensitic steel with retained austenite at lath boundaries, has shown the rapid transformation of austenite into martensite. They outlined the weak contribution of the austenite film since it transformed already after a few percents of deformation and therefore it was unable to accommodate large deformation. Another explanation for interface sliding is based on the behaviour of ultra-fine grains. Okayasu *et al.* [69] explained the intergranular fatigue fracture of a dual phase ferrite/martensite low carbon steel with a grain size of the order of a few microns by grain boundary sliding, attributed to the build-up of stress at the intersection of primary glide plane and grain boundary and the absence of relaxation of stress concentration.

However, the description of the proposed explanations for accommodation of plasticity by interfaces in our 12%Cr martensitic steel is not satisfactory. To some extent, the grain boundary sliding mechanism applied to martensitic lath boundaries would explain the occasionally observed extruded entire lath (as in Figure 5-9). For a favorable orientation relatively to the loading axis, two hard laths sandwiching a soft lath can exert a shear stress high enough to pull the whole lath out on the surface.

Therefore, we have oriented our interpretation by considering that the fatigue behaviour of the present 12%Cr martensitic steel approaches the one of fcc or bcc metals [68], [137]. The interpretation relies on the similarities between the FSM formed in our material and the FSM of copper-like materials. Polak's model [138] appears to be attractive in our case because it considers the extrusion emergence followed by intrusion nucleation which is observed in our

12%Cr martensitic steel. However, it should not be forgotten that the models of Polak and Essmann-Gösele-Mughrabi [4], [56] are known to explain the emergence of extrusions and intrusions in copper monocrystals, and copper, ferritic and austenitic polycrystals with large grains and without hierarchical microstructure. The originality of our model is to show that lath boundaries and PSB-matrix interfaces, apparently different in their origin, can be assimilated to the nucleation of intrusion. Polak's approach is based on the mass redistribution between the matrix (veins and channels) and dipolar walls and channels of PSB due to the vacancy migration caused by annihilation and multiplication of dislocations. However, such phase as "matrix and PSB" (Figure 6-1a) and therefore interface of this type, are not observed in the 12%Cr martensitic steel. We consider the lath boundary (Figure 6-1b) in the martensitic steel acting as the interface between the matrix and the PSB in copper.

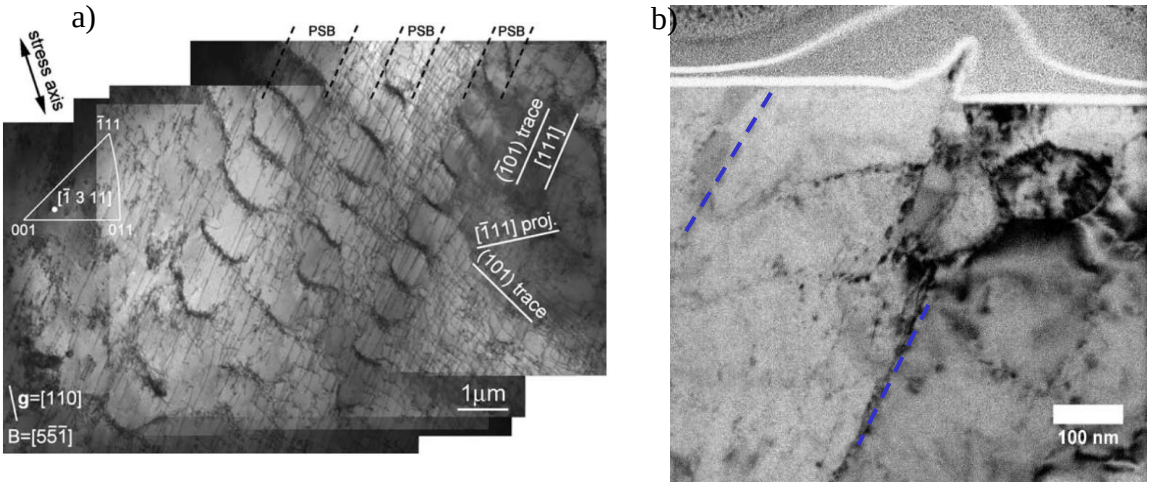

Figure 6-1 a) ladder-like structure of PSB in ferritic steel X10CrAl24 revealed by TEM after 9000 cycles at $\Delta\varepsilon_p$=0.2% [123]; b) extrusion in a lath revealed by TEM in the studied martensitic steel (X19CrMoNbVN11-1) after 500 cycles at $\Delta\varepsilon_t$=1.2% ($\Delta\varepsilon_p$=0.4%). The blue dashed lines mark the lath boundaries

6.2 The 12%Cr martensitic steel as an easy deformable material

At first, since the material has bcc structure, we confirmed that it was deformed in the high temperature regime. The measurement of internal and effective stresses determined from hysteresis loops (by using the Handfield-Dickson's method [139]) showed that the internal

stresses (about 600 MPa) are much higher than the effective stresses (around 100 MPa). In addition, the evolution of the internal stresses with the number of cycles reflected the evolution of the stress amplitude. Therefore, it can be concluded that the present 12%Cr martensitic steel is deformed in the high temperature regime.

The dislocations, distributed homogeneously in the material before loading, start to move constantly back and forward inside the laths as a result of cycling. In the majority of cases the movement happens in the longitudinal direction of lath, oriented at approximately 45° to the loading axis. The longitudinal direction of lath favors a long dislocation mean free path, while the lath inclination at about 45° to the loading axis is known to be a position of the highest shear stress. This first dislocation movement leads to the formation of steps. The steps will transform into extrusions, as it was illustrated in the paragraph *4.1Characterization of deformation relief morphology*, once the number of loading cycles will exceed ¼ cycle. Moreover, it was shown that the dislocations in the whole length of lath contribute to the FSM formation (see *5.2.2Role of precipitates in FSM localization*). But sometimes, the secondary extrusions form due to the gliding along the transversal direction of lath.

The gliding planes were determined for our material with a help of EBSD orientation mapping. Both families of extrusions were finally associated to the dislocation glide in the most probable slip systems in bcc with the highest Schmid factor. This result is an agreement with Batista *et al*. who has defined the activated slip planes participating in matter extrusion during the room temperature fatigue of EUROFER 97 [46]. He together with his coauthors found that they were the close-packed planes {110} and {112} of bcc crystal structure.

Moreover, it was noticed that the morphology of principal extrusions varied along the extrusion. The shape fluctuations may be related to the wavy slip typical of the high temperature regime of fatigue of bcc metals. The high number of slip systems (48) and the easy glide of dislocations can explain the variation in the shape of principal extrusions and also their broken line aspect. This result is in excellent agreement with the results of Man *et al.* [3], who connected the important extrusion shape fluctuations to the activity of many different slip systems in ferritic steels.

In the majority of cases the steps and then the principal extrusions appear just next to the lath boundaries because the latter slightly increase the stress in the thin band close to the boundaries [135].

6.3 Vacancy production and agglomeration

At the same time, in our material in order to minimize the energy of dislocation interactions, the dislocations arrange gradually into a cell structure (Figure 5-1), consisting of dislocation walls and cell interiors which are relatively poor in dislocations. Dislocation cells are classically observed in martensitic steels after low cycle fatigue [8], [46], [140], [141]. The average width of cells approaches that of the laths (Figure 5-2a). Sometimes, martensitic laths may coalesce under cyclic loading [64] resulting in a consequent increase of lath size. However, this was not observed in the present studied material since the width of laths did not change after loading and ranged between 200 nm and 400 nm (Figure 5-2b). The lath interfaces are therefore stable.

The alternative movement of dislocations combined with the easy cross slip makes their interaction very intensive. This brings up to annihilation or multiplication of dislocations which produces a lot of point defects. Mekhrabov *et al*. and Polak *et al*. [142], [143] concluded in their studies that both interstitials and vacancies are mobile at room temperature. Essmann *et al*. reported that copper's point defects are mobile already at -150°C [56]. Moreover, the dislocation movement may result in local temperature rise which increases the mobility of point defects. Further, the constant increase of extrusion height is a sign of mobility of point defects according to Polak *et al*. [144]. Otherwise, the static extrusion would form. The interstitials need more energy to be formed than the vacancies. Additionally, the interstitials are more mobile which means that their rate of annihilation at dislocations is higher than for vacancies. Therefore it is reasonably concluded that the vacancies' production rate is more important than the interstitials' one. But the systematic flow of interstitials cannot be neglected and it is believed to contribute to the speed of extrusion and intrusion growth and also to their shape [143]. By using positron lifetimes experiments, vacancies' agglomerations due to fatigue deformation have been highlighted in fatigued copper [67], [145] and in austenitic and martensitic steels [146]–[149]. The studies showed the increase of positron lifetimes in the fatigued samples, linked to the increase of vacancy quantity and so to the reduction of electron

number, that usually annihilate the positrons. In the case of fatigued copper single crystals, Mughrabi *et al.* [56], [150] suggested that a larger number of vacancy-type agglomerates existed in the PSBs than in the matrix as a result of their positron-lifetime measurements. Piqueras *et al*. [151] and Antonopoulos and Winter [152] detected by weak-beam TEM small unclassified defect clusters with an approximate size 4 nm whose density was higher in the walls than in the channels. Sastry *et al*. perfomed the same qualitative observations on the silver single crystals [153]. Essmann, Gosële and Mughrabi considered that the voids should be less than 10 nm if they do exist [56]. Kettunen *et al*. executed the low-angle neutron-diffraction experiments on fatigued copper crystals and concluded that the voids of about 2 nm may exist [154]. Thus, the production of vacancies in fatigued materials is discussed and believed to be true since the end of seventies.

When the vacancy encounters an edge dislocation, it annihilates itself. At the same time both the cell walls and the lath boundaries belong to LAB which consist of a few arrays of edge dislocations including debris dislocations [108], [155]. Thus, Fournier considered in his model explaining the creep mechanism of martensitic steel that the LAB of lath or subgrains of martensitic steel are tilt boundaries which are known to consist of edge dislocations. However, he outlined that it is just an assumption, while the real LAB is rather a mix of both tilt and twist boundaries [33]. Laird supposed to interpret the observed fatigue cell structures "*as perpendicular walls constructed from edge dislocation dipoles with perpendicular Burgers vectors*" [59]. It means that all the LAB interfaces are the perfect sinks for the vacancies. Moreover, Niu [156] concluded in his work on interaction between point defects and LAB in bcc tungsten that the LAB possess almost ubiquitous attraction of self-interstitials and vacancies. Indeed, the vacancies attracted by the elastic fields of edge dislocations in the cell walls and lath boundaries, tend to move there. Part of them will annihilate but another one will accumulate gradually in the interfaces partially due to the interaction of boundary dislocations with incoming dislocations. The latter reason of vacancy agglomeration is particularly true for nano-sized grains [157]. It is the case of the studied material if we suppose that a lath play a role of nano-grain.

Since it is suggested that the vacancies are supposed to concentrate at lath boundaries, a local decrease of shear and elastic modulus is expected as it has been reported in the literature [158]–[161]. The Peak Force tapping™ mode on the Dimension Icon AFM of Bruker has been used

for the measurement of local elastic modulus on the surface of fatigued studied martensitic steel. The results are shown in the Figure 6-2, where (a) is a qualitative map of Young modulus of some young extrusions (100 cycles) and (b) is an AFM topographical image of the same extrusions. The elastic modulus is higher in the light areas than in the dark ones. It should be mentioned here also that the measurements caught on the slopes of extrusions should not be taken into consideration as far as the slope modifies the measurement data; however, the measurements next to the extrusion foot can be analyzed. The image shows a decrease of elastic modulus just next to the extrusions where the future intrusions will appear later in the loading. This result is in agreement with a vacancy accumulation close to the extrusion.

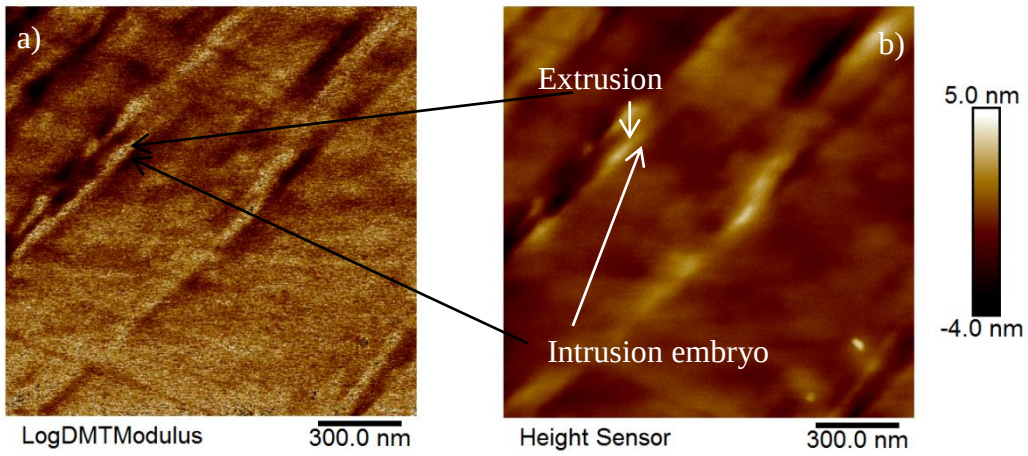

Figure 6-2 a) AFM elastic modulus image, where the contrast change indicates the local changes in elastic modulus: the elastic modulus value increases with the increase of brightness; the elastic modulus scale is absent on the image because of some technical problems however the qualitative analysis is still appropriate for this image b) AFM height image showing extrusions and intrusion embryos after 100 cycles of loading. Analysis was obtained in Peak Force tapping™ mode on the Dimension Icon AFM of Bruker

6.4 Nucleation of extrusion and intrusion

The continuous migration and annihilation of vacancies in lath boundaries or cell walls result in a motion of atoms in the opposite direction. Consequently this rearrangement of the matter (or atoms) contributes to a flow of a thin slab inside the laths right next to the boundary and a lack of the matter (or atoms) in the walls and boundaries. Both the vacancy creation and its replacement by an atom lead to the local volume increase (swelling). As a result the compressive stresses due to the volume increase within the lath or dislocation cell are

continuously relaxed by irreversible slip (i.e. dislocations do not glide in the same plane at their forward and back path) in the direction of active Burgers vector. This contributes to the matter extrusion on the specimen surface. The extrusion continues its growth. Later the tensile stresses arise too where the vacancies were attracted, i.e. in the interfaces (boundaries between laths or dislocation cells) as far as the vacancy accumulation induces some local volume increase. These microtensile stresses are released by the creation of an intrusion.

For the record, in this work an intrusion has to meet a few conditions in order to be called an intrusion. Firstly an intrusion is any crevice in the surface which does not exceed the average lath width. The lath size is considered to be an effective size because it was shown that the FSM are localized within a lath in the majority of cases. If the crevice length does exceed the average lath width, then this feature is called microcrack. Microcrack develops into crack when its length becomes visible for a “naked eye”. Secondly, according to Polak’s model the intrusion grows into metal with approximately constant rate which is driven by the vacancy generation rate. Once the rate of new surface formation due to stress concentration becomes higher than that due to vacancy generation, the surface defect can be regarded as a surface microcrack [68]. And thirdly, intrusion is a phenomenon of cyclic plasticity.

Our observations of intrusions and extrusions on 2D TEM images of FSM cross-sections as well as on the AFM images showed that the extrusions appear earlier than the intrusions and they occupy a bigger area than intrusions after 44% of lifetime. This could be due to the fact that the intrusion formation requires vacancies to reach the dislocation rich interfaces and accumulate there. This is a function of vacancy mobility which is governed by diffusion. By using classical diffusion laws, it is possible to calculate the time needed for a vacancy to reach one of the lath boundaries.

Naturally, the vacancies are produced randomly in any place of material during the fatigue loading. But if we consider a lath with an average width 300nm, then the longest path for a vacancy is for the one that is appeared in the center of this lath, i.e. the longest path is x=150nm, except that the vacancy motion is rather a random walk, i.e. each particle jump is independent of all its preceding jumps, both in length and direction. That’s why it is considered that the magnitude characteristic of a random walk at the end of the time t is the mean square displacement x^2 [162].

The mean-square displacement is a function of diffusion coefficient D:

$$x^2=D\cdot t \qquad \text{Equation 6-1}$$

At the same time for a bcc crystal structure with lattice parameter a there are 8 jump directions, each with a projected length of $\pm a/2$:

$$D=1/6\cdot v_{jump}\cdot 8\cdot a^2/4=(v_{jump}\cdot a^2)/3, \qquad \text{Equation 6-2}$$

where v_{jump} is a jump frequency towards a given site.

The jump frequency v_{jump} is given by Arrhenius equation:

$$v_{jump}=v\cdot exp(-E_{mig}/k_B\cdot T), \qquad \text{Equation 6-3}$$

where v is an attempt frequency which is a typical vibrational frequency of an atom $v_{vib}=10^{13}Hz$, E_{mig} is a potential energy barrier to diffusion or migration energy, k_B is the Boltzmann's constant and T is a temperature in Kelvin.

Finally, the mean-square displacement x^2, expressed through the lattice parameter a and the atom vibrational frequency v_{vib}, is

$$x^2=(a^2\cdot v_{vib}\cdot exp(-E_{mig}/k_B\cdot T)\cdot t)/3 \qquad \text{Equation 6-4}$$

From this equation we can deduce the time needed for a vacancy to cross a half-lath

$$t=3x^2/(a^2\cdot v_{vib}\cdot exp(-E_{mig}/k_B\cdot T)) \qquad \text{Equation 6-5}$$

The necessary physical values are known for Fe_α and presented below in the table.

Table 6-1 Values of some physical characteristics necessary for the calculation of time needed for a vacancy to cross a half-lath

x	a	v_{vib}	E_{mig}	k_B
150 nm	2.87 Å	10^{13} Hz	0.67 eV ($1.07 \cdot 10^{-19}$ J)	$1.38 \cdot 10^{-23}$ J/K

Substituting the known data in the Equation 6-5, we can calculate the time necessary for a vacancy to cross a half-lath:

$$t \approx 4.5 \textit{ hours.}$$

The fatigue tests performed in this study lasted in average for an hour. However, the obtained result does not take into account the fact that the vacancies displace under the conditions of cyclic loading, which may cause the local temperature rise due to the dislocation displacements and interactions and so can accelerate the vacancy movement. Moreover, the present result is the maximum time. The closer the vacancy is to the boundary, the less time it needs to reach the boundary.

Another reason explaining the retarded intrusion formation may be the fact that some fraction of vacancies succeed to pass through the boundaries and annihilate in the matrix far from the boundary and active lath where the strain is localized.

To sum up this chapter, the extrusions are initiated by the plane slip of dislocations and continue growing due to the vacancy production and consequent atom or matter redistribution, causing the volume change leading to the compressive stress release by the irreversible slip. The intrusions, in their turn, result from the vacancy accumulation in the interfaces [3], [68], [101], [120], [143].

6.5 Summarized mechanism

Finally, the assumption that a lath boundary in a martensitic structure could behave as an interface between the matrix and the PSB developed by plastic fatigue in simple microstructure metals such as copper sounds well to explain intrusion and extrusion formation in the multi-interfaced martensitic steel. Therefore the model of extrusion-intrusion formation is summarized in the schematics shown below in Figure 6-3.

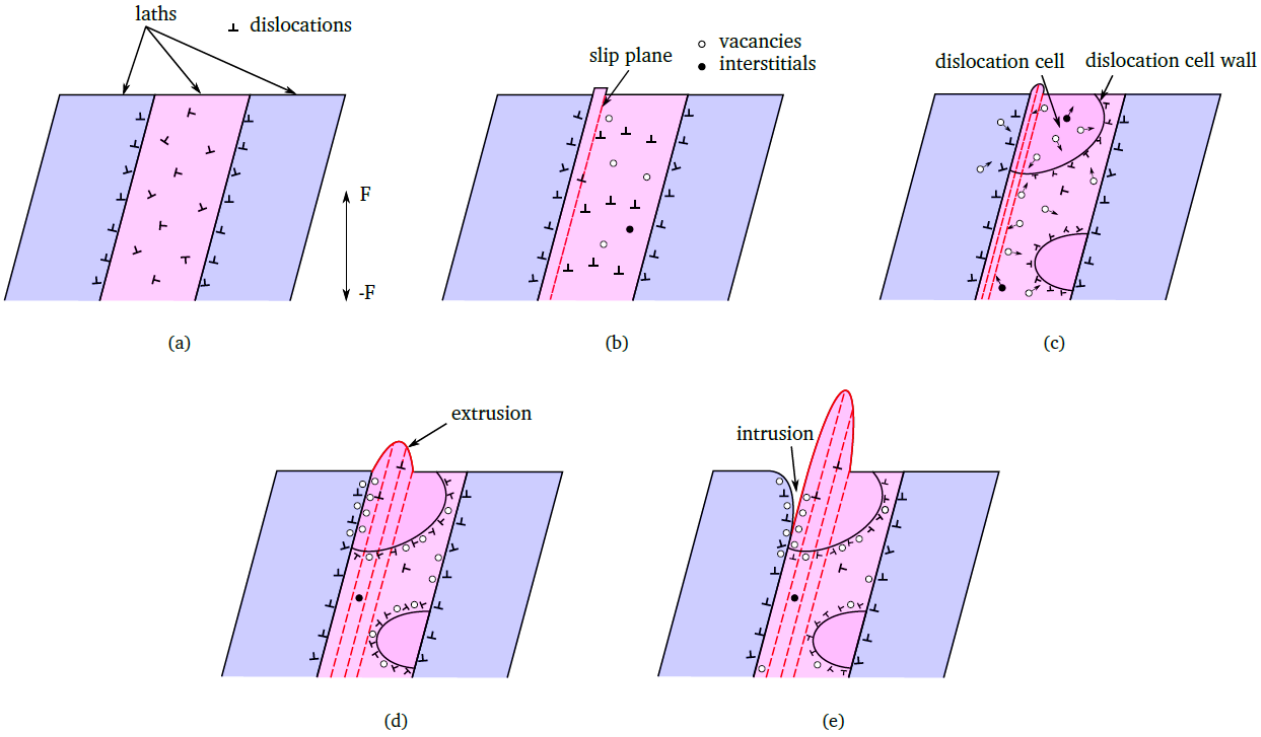

Figure 6-3 Schematics showing the main steps of deformation mechanism: a) initial state of material; b) formation of the first relief due to the plane sliding; interaction of dislocations; c) formation of cells; dislocation movement towards the interfaces; d) further growth of extrusion; e) growth of intrusion due to the vacancy concentration in the interface

7. Conclusions and perspectives

The objectives of this work were from one side to explain the mechanism of extrusion-intrusion formation in a 12%Cr martensitic steel after low cycle fatigue (LCF) loading at room temperature with a help of advanced microscopies, and from the other side to explain the contribution of the different interfaces typical of martensitic steels into the emergence of fatigue plasticity on the metallic surface. For this the LCF tests were performed on the flat specimens at $\Delta\varepsilon_t$=1.2% in air and at room temperature and with $\dot{\varepsilon}=4\cdot10^{-3}$ s^{-1} and R_ε=-1.

To achieve the purpose, first of all, the produced deformation relief was thoroughly characterized by atomic force microscope (AFM) after a few interruptions of fatigue test. After the first interruption at a quarter of cycle, steps appeared on the external metallic surface. Then these steps developed into extrusions. Two different families of extrusions were revealed. The steps developed into so-called principal extrusions that were long and high comparatively to the secondary extrusions that were observed after the interruption at 500 cycles (44%).

The fatigue slip markings (FSM) height, length and number were quantified by AFM. It was found that the number of principal extrusions increased only between ¼ cycle and 100 cycles. The change of their length was almost negligible, while the height continued to grow till the end of life. The secondary extrusions were observed after 500 cycles and grew in number and height till the end of life.

The principal extrusions and intrusions seemed to appear in the vicinity of different boundaries. The secondary extrusions were usually short and perpendicular to the principal one. This result led to the conclusion that they are rather within the laths or blocks.

The precise and unambiguous localization of extrusions has been revealed on the thin lamellae extracted by focused ion beam (FIB) and observed in transmission electron microscope (TEM). Thus, it was certainly confirmed that the extrusions are rather inside the laths or blocks, inclined often at 45° to the loading axis, or in the cells; while the intrusions are in the boundaries.

Finally, based on these experimental observations a mechanism of formation of FSM in the 12%Cr steel was proposed. The basics of this model were inspired by the Polak's model of extrusion-intrusion development. Thus, the extrusion is believed to be the direct result of slip activity of dislocations. With a help of electron backscatter diffraction microscope (EBSD) it was found that the majority of principal and secondary extrusions are the result of dislocation gliding in the most probable slip system {110}<111> in bcc metals with the highest Schmid factor. As for the intrusion, it is rather a result of vacancy accumulation due to the dislocation movement. The interfaces are considered to be a source of dislocations and at the same time the sink for vacancies.

This study allowed developing the mechanism of formation of extrusion-intrusion as a result of LCF in multi-structured martensitic steel. It appeared that the FSM are closely related to the different interfaces belonging to the studied steel. Namely, the extrusion developed often near the interface, while the intrusion was inside the interface itself due to the matter redistribution caused by vacancy accumulation. The vacancy evidence might be completed by additional observations with more sophisticated tools. For this the peak force (PF) AFM mode seems to be a reliable technique. Thus, extra images of extrusion-intrusion by PF may provide a statistical evidence of presence of vacancies estimated through the evolution of local Young's modulus. Another promising technique would be München scanning positron microscope capable of reproducing the positron lifetime maps of fatigued surfaces [147].

The tests at low temperatures seem to be very interesting to perform because the mobility of point defects reduces importantly at this condition. If the proposed model of FSM formation is right, then at low temperatures the vacancies are immobile and the intrusion would have to develop inside the lath.

The FIB is a perfect instrument to study the microstructural evolutions in direct proximity to the specimen surface and so to the FSM. In this work, we could perform the observations of FIB lamellae only after 44% of lifetime of specimen. The study of material microstructure under the FSM at different interruptions seems to be another worthy perspective. This experiment may confirm that the intrusions develop later than the extrusions and occupy less area and volume in the material.

Finally, to validate the model, other materials with similar complex microstructures may be studied. For example, the pearlitic steels with lamellar structure consisted of two phases (alpha+cementite) or ultra-fine grained steels were little investigated in the fatigue on nano-level and are interesting to study. Thus, it could be true for them too that the FSM appear in the vicinity of interfaces according to the model proposed in this study.

List of figures

Figure 1-1 One of the scenarios of fatigue crack development in a metal 16

Figure 2-1 Continuous Cooling Transformation (CCT) diagram of 1.4913 X19CrMoNbVN11-1 steel [18] 20

Figure 2-2 Bain model sketch of martensitic transformation [17] 21

Figure 2-3 The growth of lath on the habit plane [22] 22

Figure 2-4 a) sketch of the martensitic microstructure; b) optical image of a 0.2%C martensitic microstructure; c) Inverse Pole Figure (IPF) color map of the martensitic microstructure; red dashed line illustrates the PA grain boundary, yellow dashed line – packet boundary; white arrows indicate the blocks [25] 24

Figure 2-5 Microstructure of as received EUROFER 97 (9Cr-1W-0.47Mn-0.2V-0.12C) steel. Prior austenitic grains are decorated by lines of carbides. Elongated martensitic laths are not frequent. The structure is composed mainly of sub micrometric equiaxed subgrains [29]..... 25

Figure 2-6 Distribution of lath widths in Fe-0.2C martensite. Vertical dashed line shows the limit of the resolution of light microscope [17] 26

Figure 2-7 TEM images showing the microstructure of AISI 410 steel (a) [15] and of Mod.9Cr-1Mo steel (b) [33] 27

Figure 2-8 OM images of lath martensite structure in the Fe-0.2C-2Mn steel with prior austenite grain size 370 µm (a) and 28 µm (b); (c) TEM image of lath microstructure of Fe-0.2C-1.5Mn-0.15V with prior austenite grain size 2.3 µm; white solid line and dashed line indicate the prior austenite grain boundary and packet boundary respectively [36] 28

Figure 2-9 Relationship between prior austenite grain size and packet size in some low carbon steels [36] 29

Figure 2-10 Relationship between the prior austenite grain size and the block width in the quenched martensite of Fe-0.2C and Fe-0.2C-2Mn alloys [37] 30

Figure 2-11 Martensite microstructure members and its sizes for some grades of steels [39] 30

Figure 2-12 Disorientation angle distribution of lath boundaries measured by TEM Kikuchi pattern analysis in steel #2 [35] 31

Figure 2-13 IPF color map of the lath martensite structure of 0.2%C steel. The red and white lines indicate the packet and PA grain boundaries respectively. The black boundaries are drawn when the disorientation angle is greater than 10°. The symbols and numbers indicate the variant numbers [25] 32

Figure 2-14 Schematic representation of stress amplitude and plastic deformation evolution as a function of number of cycles to failure, determining the different fatigue domains [46] 35

Figure 2-15 The basic loading signal in LCF revealing the commonly used variables in the science of LCF 36

Figure 2-16 Hysteresis loop of stress versus strain 37

Figure 2-17 Evolution of stress amplitude as a function of number of cycles for 9%Cr steel EUROFER 97: red arrow points out the softening phase, green arrow – stabilization phase, black arrow - failure [45] 38

Figure 2-18 Manson-Coffin curve of modified 9Cr-1Mo steel at 600°C [48] 38

Figure 2-19 Some low energy dislocation configurations observed in a ferritic steel: a) matrix structure; b) walls; c) labyrinth; d) cells [54] 40

Figure 2-20 The ladder-like structure of PSB in copper crystal [56] 41

Figure 2-21 Microstructure of GP91 cast steel in the as received condition (a) and after LCF at strain amplitude ε_{ac}=0.25% and at 600°C (b) [60] 42

Figure 2-22 Microstructure of P91 steel in the as received condition (a) and after LCF loading at $\Delta\varepsilon_t$=0.3% and at 550°C (b) [61] 43

Figure 2-23 Microstructure of GP91 cast steel after LCF at room temperature (RT) at various levels of strain amplitude: a) ε_{ac} = 0.25%; b) ε_{ac} = 0.6%. The initial microstructure of steel is in Figure 2-21a [62] 44

Figure 2-24 Cyclic behaviour curves of EUROFER 97 steel obtained at room temperature and at three different plastic strain ranges [63] 45

Figure 2-25 Characteristic microstructure of EUROFER 97 samples fatigued at $\Delta\varepsilon_{pl}$=0.2%, at RT: a) 10 cycles, b) 500 cycles, c) 11000 cycles [9] 45

Figure 2-26 Cyclic behaviour of AISI 410 steel in comparison with EUROFER 97 steel at RT and at $\Delta\varepsilon_{p}$=0.2% [15] 46

Figure 2-27 a) initial tempered microstructure of AISI 410 steel; b) fatigued lath structure turned into equiaxed subgrain microstructure; c) fatigued lath structure with disappeared subgrain wall and saved precipitates shown in circle [15] 47

Figure 2-28 Cell structure induced by the cyclic deformation in Eurofer 97 steel, tested at room temperature, at $\Delta\varepsilon_{t}$=0.8 %, N=7261 cycles [29] 47

Figure 2-29 Schematic image of extrusion-intrusion 49

Figure 2-30 Fundamental microscopic EGM mechanism of the formation of a) extrusion formed by the annihilation of vacancy-type dipoles; b) intrusion formed by the annihilation of interstitial-type dipoles. All dislocations drawn in dipole configuration would annihilate and only the individual dislocations in A, B, A', B' would survive the annihilation [55] 51

Figure 2-31 Polak's model of surface relief formation for an individual PSB. a) section through a crystal comprising PSB and matrix in a plane and quasi-stable vacancy concentration profiles within PSB and in a plane perpendicular to PSB. Arrows indicate the vacancy fluxes within PSB and out of the PSB. b) relationship of the dislocation structure of PSB with a neighbor PSM during the point defects migration within the band. c) surface profile of a PSM when points defects move forward-and-back from the band to the matrix [3] 52

Figure 2-32 Two 9 μm-long specimens with tilted boundaries to the loading direction shown with inverse pole figure orientation map (a_1,b_1), SEM pictures before loading (a_2,b_2) and after

fracture (a_3,b_3) together with a zoom (yellow frame) of the fractured specimens (a_4,b_4). The red circles in the {110} (a_5,b_5) and {111} (a_6,b_6) pole figures indicate the favored slip system. Block and sub-block boundaries are marked with orange and black lines respectively; the fracture surface with a white dotted line. The many lath boundaries are not marked. The arrows in b_1–b_4 indicate sliding boundaries 54

Figure 2-33 Grain sliding as a result of HCF test of UFG ferrite/martensite steel: (a) SEM evidence of GBS, (b) schematic representation of GBS [68]..... 55

Figure 2-34 AFM images of extrusions on the surface of Ti-stabilized IF UFG steel after LCF test at $\dot{\varepsilon}=6\cdot10^{-3}$ s^{-1} and $\Delta\varepsilon_t=4\cdot10^{-3}$: a) extrusions with 1µm height; b) extrusions with 100 nm height [70] 56

Figure 2-35 Cross-sections of extrusions, intrusions and cracks observed in copper single crystals after approximately 300 kilocycles of loading [79] 57

Figure 2-36 SEM images showing the intergranular crack initiation in copper polycrystalline: a) $\sum\Delta\varepsilon_p=2$, arrowed regions at boundaries AD and BC indicate the presence of crack embryo; b) $\sum\Delta\varepsilon_p=4$, new crack embryos developed and others have already begun to link up; c) $\sum\Delta\varepsilon_p=8$, crack nuclei formed along boundaries AD and BC. Since the replica is of the negative type, the crack embryos show up in light contrast [82] 58

Figure 2-37 Extrusion, intrusion and crack cross-sections. The arrow points out the crack [83] 58

Figure 2-38 SEM image showing crack initiation in extrusion-intrusion pairs in T91 martensitic steel after LCF loading at room temperature and in air [12]..... 60

Figure 2-39 The SEM (a) and AFM images (b) of microcrack formation from the convergence of streaks in PH 13-8 Mo at $\Delta\varepsilon=0.4\%$; c) AFM image of a different area at slightly higher magnification than (b) illustrating a high concentration of parallel streaks, which is the precursor state before microcrack formation [14]..... 61

Figure 2-40 In situ optical images of AISI 410 steel taken during the fatigue test at: a) 0 cycle; b) 10 cycles; c) 60 cycles; d) 160 cycles [15] 62

Figure 2-41 (a) dislocation cells; (b) formation of nano-pores at the boundary; (c) crack initiation in 0.38C-13.5Cr martensitic steel subjected to VHCF loading at σ = ±650 MPa and f = 20 kHz [87] 62

Figure 3-1 X-ray diffraction pattern of the studied steel. x-axis corresponds to the 2θ angle, where θ is the angle between diffracted X-ray and surface; y-axis indicates the diffraction intensity in counts..... 66

Figure 3-2 Schaeffler's diagram (modified by Schneider) revealing the effect of equivalent Cr and Ni on the microstructure of steels. The red mark indicates the position of the studied steel [88], [89]..... 67

Figure 3-3 Microstructure of the studied material: a) optical image; b) TEM image; c) and d) SEM images 68

Figure 3-4 EBSD IPF color map, where disorientation angles higher than 10° (HAB) are marked by black line 69

Figure 3-5 Microstructure of studied material: a) ECCI image; b) TEM image..... 69

Figure 3-6 a) TEM image of a precipitate; b) STEM image of the same precipitate; c) diffraction pattern of the precipitate with the zone axis <100>; d) STEM-EDX map illustrating the chemical composition of the precipitate delimited by green rectangle in (b) 70

Figure 3-7 Dislocation density in different martensitic steels as a function of carbon content [42] 70

Figure 3-8 Distributions of each microstructural unit sizes for the studied martensitic steel .. 71

Figure 3-9 Link between the prior austenite grain size and (a) packet and (b) block size in various martensitic steels. (c) Lath width variation as a function of the carbon content in martensitic steels [42]..... 73

Figure 3-10 Stress-strain curve limited to 0.6% total deformation 74

Figure 3-11 a) specimen geometry; b) extensometer mounted on the specimen installed in the fatigue machine 75

Figure 3-12 a) stress amplitude evolution as a function of number of cycles; b) plastic strain variation as a function of number of cycles 77

Figure 3-13 AFM 78

Figure 3-14 Principle parts of AFM 78

Figure 3-15 Force-distance curve: blue arrows represent an approach, red arrows - retraction 79

Figure 3-16 Force-distance curve of the interaction of tip with a sample surface revealing the different AFM modes 80

Figure 3-17 a) tip schematics with angles defining the tip: FA – front angle; BA – back angle; SA – side angle; TSB – tip setback; h - height; b) Bruker RTESPA-300 probe (Bruker company) 84

Figure 3-18 Angle limitations in contact mode: a) scanning parallel to cantilever; b) scanning perpendicular to cantilever [93] 84

Figure 3-19 Artefact caused by the tip geometry [94] 84

Figure 3-20 Schematic surface profile at the emerging PSB consisting of an extrusion and two intrusions. The distortion of the real surface as detected by the AFM tip is shown [96]..... 85

Figure 3-21 a) One cycle of the Peak Force tapping curve: A – non-contact force, B – jump into contact, C – peak force and contact with the surface, D – tip pull off, maximum adhesion forces, E – non-contact force. This process is repeated at every XY pixel in the image, at a rate of typically 2000 Hz; b) Resulting quantitative measurements 86

Figure 3-22 The topographical map (a) and E map (b) of etched bainitic steel sample measured by PF-QNM [98] 87

Figure 3-23 Different morphologies of deformation relief in austenitic and ferritic phases of a duplex steel imaged by AFM after LCF test at $\Delta\varepsilon_t$=1.6% [100] 89

Figure 3-24 Surface relief within a grain of 316L steel fatigued at ε_{ap}=0.003 at 300 K as obtained by AFM after (a) 100 cycles and (b) 250 cycles. AFM micrographs are displayed in shadowed format [102] 89

Figure 3-25 AFM height micrograph documenting slip transmission through phase boundary between grains 5 and 8 in a duplex steel [104] 90

Figure 3-26 AFM observation of P91 steel surface with extrusions and intrusions after LCF test at 550 °C under vacuum at $\Delta\varepsilon$=0.7 % [8] 91

Figure 3-27 AFM image showing local plastic deformation, blocks and prior γ grain boundaries after monotonic plastic strain ε=0.6 %. This image was created by superimposing of two different AFM images: one reveals the prior austenite grain boundaries and another reveals the blocks. The loading axis is horizontal [105] 92

Figure 3-28 Profiles through line AB in Figure 3-27 [105] 93

Figure 3-29 The sketch representing how a diffraction pattern (a) and contrast image (b) are created in TEM [108] 96

Figure 3-30. Basic FIB instrument [109] 97

Figure 3-31 Extraction of lamella FIB (a); copper M-grid (b) 99

Figure 3-32 TEM image of FIB thin foil revealing the extrusions and intrusions with correspondent underlying ladder-like dislocation structures [119] 101

Figure 4-1 Gage section of sample with Vickers indentations and a few zones of AFM scanning 104

Figure 4-2 AFM images and profiles illustrating the evolution of deformation relief as a function of number of loading cycles 105

Figure 4-3: a) a sketch of principal extrusion consisting of small almost parallel parts and definition of principal extrusion length *l;* b) example of definition of principal extrusion length *l*; c) magnified image of the zone in black box in (b). The method for measuring of the angle α between principal extrusion and loading axis is in green in (b) 106

Figure 4-4 Different types of extrusions described in the work of Man *et al*. [3] 107

Figure 4-5 AFM height images of protrusions 108

Figure 4-6 AFM height images of tongue-like extrusions (white arrows); red arrow indicates the intrusion 108

Figure 4-7 AFM height images of cord-like extrusions 108

Figure 4-8 AFM height images of band-like extrusions 109

Figure 4-9 AFM height images of ribbon-like extrusions 109

Figure 4-10 SEM image revealing the intrusions (black arrows) accompanying the extrusions after 500 cycles of loading 110

Figure 4-11 One of the zones of observation by AFM on the surface: a) 100 cycles, extrusions but no intrusions; b) 1130 cycles, extrusions and intrusions (indicated by white arrows)..... 111

Figure 4-12 AFM amplitude signal error images. The sets of secondary extrusions are surrounded by dashed green lines and individual secondary extrusions are indicated by blue arrows. Black arrows point out the principal extrusions. Dashed white line surrounds the case when the secondary extrusions overcross the principal one 112

Figure 4-13 3D AFM representation of a set of secondary extrusions and correspondent AFM profile after 1130 cycles 113

Figure 4-14: a) evolution of the number of principal extrusions as a function of number of cycles; b) evolution of the average length of principal extrusions as a function of number of cycles 114

Figure 4-15 Method of extrusion height measurement 116

Figure 4-16 Distribution of measured heights of FSM after each interruption 117

Figure 4-17: a) evolution of average height of principal extrusions with the increase of number of cycles; b) evolution of the rate of growth of principal extrusions between interruptions . 118

Figure 4-18 AFM 3D image of surface features observed in a ferritic steel after N=2000 cycles at $\varepsilon_{pl}=2\cdot10^{-3}$[123] 119

Figure 4-19 Distribution of angles between principal extrusions and load axis 120

Figure 4-20 a) AFM signal error image showing the FSM following the packet boundary; b) SEM image of surface of polished and etched fatigued specimen revealing the microcracks at the interfaces marked by precipitates 122

Figure 4-21: a) measured width between two parallel extrusions is compared to the known ranges of sizes of microstructure units; b) comparison of length of principal extrusions to the sizes of microstructural units..... 123

Figure 4-22: a) the scatter of the distance between two parallel parts of principal extrusions; b) the scatter of the length of secondary extrusions 123

Figure 4-23 Distribution of measured grain sizes (a) and lath widths (b)..... 125

Figure 4-24 Lath microstructure of the martensitic steel austenized at 1300°C during 5 hours and imaged by TEM (a) and SEM (b) 126

Figure 4-25 a) stress amplitude evolution as a function of the number of cycles for the as received steel and for the steel austenized at 1300°C; b) plastic strain variation as a function of the number of cycles for the as received and the austenized at 1300°C steels 127

Figure 4-26 Optical image of the deformed specimen surface after 80 cycles of loading. The arrows show the extrusions and intrusions with the length of the order of PA grain and packet sizes 129

Figure 4-27 AFM height images of zones (a) and (b) after two interruptions. Dashed lines mark the boundaries 129

Figure 4-28 AFM signal error image of specimen surface after 80 cycles. Blue arrow indicates the FSM in the PA grain boundary. The dashed line comprises a packet. The black points indicate the extrusions, the distances between which are equivalent to the block widths. The green point shows a cluster of extrusions: the distances between each of them are less than 1µm 130

Figure 4-29 Evolution of average height of steps and principal extrusions with the increase of number of cycles 131

Figure 5-1 a) initial microstructure of material; b) dislocation cells after rupture at 1130 cycles 134

Figure 5-2 a) dislocation cells diameters measured at 500 cycles; b) comparison of lath width before deformation and after rupture at 1130 cycles..... 135

Figure 5-3 The FIB lamella extraction: a) the selection of area of interest; b) extracted lamella mounted on the copper grid; c) observation of lamella in TEM 136

Figure 5-4 FSM cross-sections obtained by FIB and observed in TEM after 500 cycles of loading. Green dashed lines follow the lath boundaries. White dashed lines follow the walls of dislocation cells. Extrusions are pointed out by red arrows 137

Figure 5-5 FSM cross-sections obtained by FIB and observed in TEM after 500 cycles of loading. Green dashed lines follow the lath boundaries. White dashed lines follow the walls of dislocation cells. Extrusions are pointed out by red arrows. Intrusions are pointed out by blue arrows 138

Figure 5-6 Cross-section of extrusions, intrusions and a microcrack after 500 cycles of loading 139

Figure 5-7 Role of precipitates in the extrusion-intrusion localization. Red arrows indicate the precipitates. Blue arrows indicate the lath boundaries. The dashed red line show the direction of intrusion growth. Images were captured after 500 cycles..... 140

Figure 5-8 AFM amplitude signal error image showing the secondary extrusions on the surface after 500 cycles and the place of lamella extraction by FIB (a); TEM image of the lamella FIB

of secondary extrusions located in the lath and parallel to the lath boundary indicated by the white dashed line (b) 141

Figure 5-9 FSM cross-sections presenting the lath extruded on the specimen surface are pointed out by red arrows. Images were captured after 500 cycles 142

Figure 5-10 a) AFM height image showing an extruded lath on the surface after 500 cycles; b) TEM image of FSM cross-section presenting the lath extruded on the specimen surface after 500 cycles 143

Figure 5-11 Protrusion cross-section. AFM image shows the same protrusion from the top. The dashed lines indicate the slight boundaries of cells defining the intrusions of protrusion. The images were captured after 500 cycles 144

Figure 5-12 Cross-sections of protrusions after 500 cycles. The white dashed line indicates the cell wall; the arrows show the lath boundaries 145

Figure 5-13 a) TEM image of protrusion cross-section after 500 cycles; the white dashed lines indicate the cell walls; the red dashed lines inside the cell indicate the slight LAB which define the route of intrusion; b) magnified TEM image of protrusion in (a) 145

Figure 5-14 a) AFM image of the protrusion in the Figure 5-13 on the specimen surface; d) AFM profile of the protrusion 146

Figure 5-15 The method of the extrusion's height and intrusion's depth measurement 147

Figure 5-16 a) scatter of extrusion heights and intrusion depths; b) scatter of extrusion and intrusion areas 147

Figure 5-17 Comparison of the heights of extrusions measured on the TEM and AFM images 148

Figure 5-18 Schematics of BSE intensity variation as a function of incident beam angle [126] 150

Figure 5-19 Schematics of Kikuchi bands formation during the diffraction of BSE [128] ... 151

Figure 5-20 Schematics of SSD and GND [129] 152

Figure 5-21 Schematic representation of crystal deformation impact on the diffraction patterns: a) non-deformed; b) SSD; c) GND [129] 152

Figure 5-22 Representation of different Euler angles according to the Bunge convention [131] 153

Figure 5-23 Crystallographic orientation map (COM) with IPF key: red corresponds to the (100), blue – (111), green – (110) planes parallel to the surface [132] 153

Figure 5-24 Schematics of EBSD scan with LSM approach [134] 154

Figure 5-25 IPF map of the studied steel surface before fatigue. Black box indicates the zone that will be investigated after loading 155

Figure 5-26 ECCI image of extrusions on the specimen surface: the contrast changes are due to the crystallographic orientations of microstructure elements; red box indicates the zone of magnified ECCI imaging and EBSD imaging presented in Figure 5-27 and Figure 5-28 respectively; blue line indicates the localization of TEM lamella extraction by FIB, the observations of which are in Figure 5-29 156

Figure 5-27 a) ECCI image of zone delimited by red in Figure 5-26 clearly revealing two extrusions with accompanying intrusions; b) magnified ECCI image of extrusion ***B*** and dislocation cells 157

Figure 5-28 a) IPF color map of the zone with two extrusions ***A*** and ***B;*** white dashed line imitates the extrusion; c) boundary disorientations by line segment method in EBSD 158

Figure 5-29 a) SEM image of lamella extracted by FIB perpendicularly to the extrusions illustrated in Figure 5-26; b) and c) extrusion ***A*** cross-section observed in TEM. The precipitate diffraction pattern and EDX analysis are in Figure 3-6 159

Figure 5-30 AFM amplitude signal error image (a) and topographic image (b) of specimen surface with secondary and principal extrusions; SEM image (c) and SEM-ECCI (d) images; IPF color map (e) 161

Figure 5-31 Schmid factor map for slip system {110}<111> 162

Figure 6-1 a) ladder-like structure of PSB in ferritic steel X10CrAl24 revealed by TEM after 9000 cycles at $\Delta\varepsilon_p$=0.2% [123]; b) extrusion in a lath revealed by TEM in the studied martensitic steel (X19CrMoNbVN11-1) after 500 cycles at $\Delta\varepsilon_t$=1.2% ($\Delta\varepsilon_p$=0.4%). The blue dashed lines mark the lath boundaries 167

Figure 6-2 a) AFM elastic modulus image, where the contrast change indicates the local changes in elastic modulus: the elastic modulus value increases with the increase of brightness; b) AFM height image showing extrusions and intrusion embryos after 100 cycles of loading. Analysis was obtained in Peak Force tapping™ mode on the Dimension Icon AFM of Bruker 171

Figure 6-3 Schematics showing the main steps of deformation mechanism: a) initial state of material; b) formation of the first relief due to the plane sliding; interaction of dislocations; c) formation of cells; dislocation movement towards the interfaces; d) further growth of extrusion; e) growth of intrusion due to the vacancy concentration in the interface 175

List of tables

Table 3-1 Chemical composition of studied material 65

Table 3-2 Microstructural unit sizes and disorientation angle types of the studied material ... 74

Table 3-3 Mechanical properties of material 75

Table 3-4 Summary of some works on fatigue and tension of metallic alloys by AFM 94

Table 5-1 Definition of slip planes, directions and Schmid factor for some principal extrusions 160

Table 5-2 Definition of slip systems, relative Schmid factor values and average height of secondary and principal extrusions depicted in Figure 5-30 163

Table 6-1 Values of some physical characteristics necessary for the calculation of time needed for a vacancy to cross a half-lath 174

References

[1] H. Mughrabi, "Cyclic slip irreversibility and fatigue life: A microstructure-based analysis," *Acta Mater.*, vol. 61, no. 4, pp. 1197–1203, 2013.

[2] H. Mughrabi, "Microstructural fatigue mechanisms: Cyclic slip irreversibility, crack initiation, non-linear elastic damage analysis," *Int. J. Fatigue*, vol. 57, pp. 2–8, 2013.

[3] J. Man, K. Obrtlík, and J. Polák, "Extrusions and intrusions in fatigued metals. Part 1. State of the art and history," vol. 1, pp. 1–13, 2011.

[4] J. Polák and J. Man, "Mechanisms of extrusion and intrusion formation in fatigued crystalline materials," *Mater. Sci. Eng. A*, vol. 596, pp. 15–24, Feb. 2014.

[5] J.-B. Vogt, G. Degallaix, and J. Foct, "CYCLIC MECHANICAL BEHAVIOR A N D MICROSTRUCTURE OF A 12Cr-Mo-V MARTENSITIC STAINLESS STEEL," *Fatigue Fract. Engng. Mater. Struct.*, vol. 11, no. 6, pp. 435–446, 1988.

[6] Z. S. Basinski and S. J. Basinski, "Formation and growth of subcritical fatigue cracks," *Scr. Metall.*, vol. 18, no. 8, pp. 851–856, Aug. 1984.

[7] U. Essmann and H. Mughrabi, "Annihilation of dislocations during tensile and cyclic deformation and limits of dislocation densities," *Philos. Mag.*, vol. 40, no. 6, pp. 731–756, 1979.

[8] B. Fournier, "Fatigue-fluage des aciers martensitiques à 9-12% Cr," École des Mines de Paris, 2007.

[9] M. F. Giordana, I. Alvarez-Armas, and a. Armas, "Microstructural characterization of EUROFER 97 during low-cycle fatigue," *J. Nucl. Mater.*, vol. 424, no. 1–3, pp. 247–251, 2012.

[10] R. Mishnev, N. Dudova, and R. Kaibyshev, "Low cycle fatigue behavior of a 10Cr–2W–Mo–3Co–NbV steel," *Int. J. Fatigue*, vol. 83, pp. 344–355, Nov. 2015.

[11] J.-B. Vogt, A. Verleene, I. Serre, and A. Legris, "Mechanical behaviour of the T91 martensitic steel under monotonic and cyclic loadings in liquid metals," *J. Nucl. Mater.*, vol. 335, no. 2, pp. 222–226, 2004.

[12] A. Verleene, J.-B. Vogt, I. Serre, and A. Legris, "Low cycle fatigue behaviour of T91 martensitic steel at 300°Cin air and in liquid lead bismuth eutectic," *Int. J. Fatigue*, vol. 28, no. 8, pp. 843–851, 2006.

[13] M. L. Martin, T. Auger, D. D. Johnson, and I. M. Robertson, "Liquid–metal-induced fracture mode of martensitic T91 steels," *J. Nucl. Mater.*, vol. 426, no. 1–3, pp. 71–77, Jul. 2012.

[14] L. Cretegny and A. Saxena, "Evolution of surface deformation during fatigue of PH 13-8 Mo stainless steel using atomic force microscopy," *Fatigue Fract. Eng. Mater. Struct.*, vol. 25, no. 3, pp. 305–314, 2002.

[15] M. N. Batista, S. Hereñú, and I. Alvarez- Armas, "The role of microstructure in fatigue crack initiation and propagation in 9-12Cr ferritic-martensitic steels," *Procedia Eng.*, vol. 74, pp. 228–231, 2014.

[16] J. W. Christian, "Twinning and Martensitic Transformation," *Le J. Phys. Colloq.*, vol. 35, no. C7, pp. C7-65-C7-76, 1974.

[17] G. Krauss, *Steels: Processing, Structure, and Performance*. Ohio: ASM International, 2005.

[18] Steel Data, "1.4913." [Online]. Available: http://www.steeldata.info/std/cct/html/4440.html.

[19] O. Bletton, "Les aciers inoxydables martensitiques," in *Les aciers inoxidables*, P. Lacombe, B. Baroux, and G. Beranger, Eds. Paris: Les editions de physique, 1990, pp. 491–518.

[20] H. K. D. H. Bhadeshia and R. Honeycombe, *Steels: Microstructure and properties*, Third. Elsevier Ltd., 2006.

[21] "Martensite," *The Great Soviet Encyclopedia*. The Gale Group.

[22] J. Brachet, "Alliages martensitiques 9Cr-1Mo : effets de l'addition de l'azote, du niobium et du vanadium sur la microstructure, les transformations de phase et les propriétés mécanique," Commissariat à l'énergie atomique, Centre d'études de Saclay, 1991.

[23] D. Porter and K. Easterling, *Phase transformations in metals and alloys*. 1992.

[24] Z. Nishiyama, "X-ray investigation of the mechanism of the transformation from face centered cubic lattice to body centered cubic," *Sci. Rep. Tohoku Univ.*, vol. 23, p. 637, 1934.

[25] A. B. Greninger and A. R. Troiano, "Orientation Habit of Martensite," *Nature*, vol. 141, p. 38, 1938.

[26] H. Kitahara, R. Ueji, N. Tsuji, and Y. Minamino, "Crystallographic features of lath martensite in low-carbon steel," *Acta Mater.*, vol. 54, no. 5, pp. 1279–1288, 2006.

[27] R. A. Barrett, P. E. O'Donoghue, and S. B. Leen, "A dislocation-based model for high temperature cyclic viscoplasticity of 9-12Cr steels," *Comput. Mater. Sci.*, vol. 92, pp. 286–297, 2014.

[28] G. Krauss and a. R. Marder, "The morphology of martensite in iron alloys," *Metall. Trans.*, vol. 2, no. 9, pp. 2343–2357, 1971.

[29] M. Sauzay, B. Fournier, M. Mottot, A. Pineau, and I. Monnet, "Cyclic softening of martensitic steels at high temperature-Experiments and physically based modelling," *Mater. Sci. Eng. A*, vol. 483–484, no. 1–2 C, pp. 410–414, 2008.

[30] P. Marmy and T. Kruml, "Low cycle fatigue of Eurofer 97," *J. Nucl. Mater.*, vol. 377, pp. 52–58, 2008.

[31] G. Krauss, "Martensite in steel: strength and structure," *Mater. Sci. Eng. A*, vol. 273–275, pp. 40–57, 1999.

[32] C. Zhang *et al.*, "Effect of martensitic morphology on mechanical properties of an as-quenched and tempered 25CrMo48V steel," *Mater. Sci. Eng. A*, vol. 534, pp. 339–346, 2012.

[33] B. Fournier, M. Sauzay, and A. Pineau, "Micromechanical model of the high temperature

cyclic behavior of 9-12%Cr martensitic steels," *Int. J. Plast.*, vol. 27, no. 11, pp. 1803–1816, 2011.

[34] T. Endo, F. Masuyama, and K.-S. Park, "Change in Vickers Hardness and Substructure during Creep of a Mod.9Cr-1Mo Steel," *Mater. Trans.*, vol. 44, no. 2, pp. 239–246, 2003.

[35] S. Morito, H. Tanaka, R. Konishi, T. Furuhara, and T. Maki, "The morphology and crystallography of lath martensite in Fe-C alloys," *Acta Mater.*, vol. 51, no. 6, pp. 1789–1799, Apr. 2003.

[36] S. Morito, X. Huang, T. Furuhara, T. Maki, and N. Hansen, "The morphology and crystallography of lath martensite in alloy steels," *Acta Mater.*, vol. 54, no. 19, pp. 5323–5331, Nov. 2006.

[37] S. Morito, H. Saito, T. Ogawa, T. Furuhara, and T. Maki, "Effect of Austenite Grain Size on the Morphology and Crystallography of Lath Martensite in Low Carbon Steels," *ISIJ Int.*, vol. 45, no. 1, pp. 91–94, 2005.

[38] S. Morito, H. Yoshida, T. Maki, and X. Huang, "Effect of block size on the strength of lath martensite in low carbon steels," *Mater. Sci. Eng. A*, vol. 438–440, no. SPEC. ISS., pp. 237–240, 2006.

[39] T. Maki, K. Tsuzaki, and I. Tamura, "The morphology of microstructure composed of lath martensite in steels," *Trans. Iron Steel Inst. Jpn.*, vol. 20, pp. 207–214, 1980.

[40] T. M. Hatem and M. a. Zikry, "Dynamic shear-strain localization and inclusion effects in lath martensitic steels subjected to high pressure loads," *J. Mech. Phys. Solids*, vol. 58, no. 8, pp. 1057–1072, 2010.

[41] S. Morito, X. Huang, T. Furuhara, T. Maki, and N. Hansen, "The morphology and crystallography of lath martensite in alloy steels," *Acta Mater.*, vol. 54, no. 19, pp. 5323–5331, 2006.

[42] S. Morito, Y. Adachi, and T. Ohba, "Morphology and Crystallography of Sub-Blocks in Ultra-Low Carbon Lath Martensite Steel," *Mater. Trans.*, vol. 50, no. 8, pp. 1919–1923, 2009.

[43] E. I. Galindo-Nava and P. E. J. Rivera-Díaz-del-Castillo, "A model for the microstructure behaviour and strength evolution in lath martensite," *Acta Mater.*, vol. 98, pp. 81–93, Oct. 2015.

[44] L. Morsdorf, O. Jeannin, D. Barbier, M. Mitsuhara, D. Raabe, and C. C. Tasan, "Multiple mechanisms of lath martensite plasticity," *Acta Mater.*, vol. 121, pp. 202–214, 2016.

[45] C. Du, J. P. M. Hoefnagels, R. Vaes, and M. G. D. Geers, "Plasticity of lath martensite by sliding of substructure boundaries," *Scr. Mater.*, vol. 120, pp. 37–40, 2016.

[46] M. N. Batista, M. C. Marinelli, S. Hereñú, and I. Alvarez-Armas, "The role of microstructure in fatigue crack initiation of 9–12%Cr reduced activation ferritic–martensitic steel," *Int. J. Fatigue*, vol. 72, pp. 75–79, Mar. 2015.

[47] H. Mughrabi, "Dual role of deformation-induced geometrically necessary dislocations with respect to lattice plane misorientations and/or long-range internal stresses," *Acta Mater.*, vol. 54, no. 13, pp. 3417–3427, Aug. 2006.

[48] F. Léaux, "THESE DE DOCTORAT Présentée à L ' UNIVERSITE DE SCIENCES ET

TECHNOLOGIES USTL LILLE 1 Floriane LÉAUX Relation entre microstructure et fatigue d ' un acier ferritique utilisé dans l ' industrie automobile : élaboratio n d ' indicateurs d ' endommagement," 2012.

[49] P. Verma, J. Basu, N. C. Santhi Srinivas, and V. Singh, "Deformation behavior of modified 9Cr–1Mo steel under low cycle fatigue at 600 °C," *Mater. Charact.*, vol. 131, pp. 244–252, Sep. 2017.

[50] J. Ewing and J. Humfrey, "The Fracture of Metals under Repeated Alternations of Stress," *Philos T R Soc L.*, vol. 200, pp. 241–50, 1903.

[51] P. J. E. Forsyth, "Some Further observations on the Fatigue Process in Pure Aluminium," *J. Inst. Met.*, vol. 82, pp. 449–455, 1953.

[52] P. J. E. Forsyth and C. A. Stubbington, "The Slip-band Extrusion Effect Observed in Some Aluminium Alloys Subjected to Cyclic Stresses," *J. Inst. Met.*, vol. 83, pp. 395–399, 1954.

[53] D. Hull, "Surface Structure of Slip Bands on Copper Fatigued at 293, 90, 20, and 42 K," *J. Inst. Met.*, vol. 86, pp. 425–430, 1957.

[54] A. E. King and D. G. Teer, "Crack Initiation in Polycrystalline Aluminium Fatigued at Low Strain," *Met. Sci. J.*, vol. 3, pp. 121–126, 1969.

[55] H. J. Roven and E. Nes, "Cyclic deformation of ferritic steel-II. Stage II crack propagation," *Acta Metall. Mater.*, vol. 39, no. 8, pp. 1735–1754, 1991.

[56] U. Essmann, U. Gosele, and H. Mughrabi, "A Model of Extrusions and Intrusions in Fatigued Metals l. Point-defect Production and the Growth of Extrusions," *Philos. Mag. A*, vol. 44, no. 2, pp. 405–426, 1981.

[57] H. Mughrabi, O. Brulin, and R. K. T. Hsieh, "Continuum models of discrete systems," in *Proceedings of the Fourth International Conference on Continuum Models of Discrete Systems*, 1981, pp. 241–257.

[58] R. J. Amodeo and N. M. Ghoniem, "A Review of Experimental Observations and Theoretical Models of Dislocation Cells and Subgrains," *Res Mech.*, vol. 23, pp. 137–160, 1988.

[59] C. Laird, P. Charsley, and H. Mughrabi, "Low Energy Dislocation Structures Produced by Cyclic Deformation," *Mater. Sci. Eng.*, vol. 81, pp. 433–450, 1986.

[60] A. Nagesha *et al.*, "Isothermal and thermomechanical fatigue studies on a modified 9Cr–1Mo ferritic martensitic steel," *Mater. Sci. Eng. A*, vol. 554, pp. 95–104, Sep. 2012.

[61] G. Golański and J. Kepa, "Evolution of Microstructure in Martensitic GX12CrMoVNbN9 – 1 Cast Steel after Low Cycle Fatigue," in *Mechatronic Systems and Materials V*, 2013, vol. 199, pp. 418–423.

[62] F. Benjamin, S. Maxime, R. Alexandra, B. Françoise, and P. André, "Microstructural evolutions and cyclic softening of 9%Cr martensitic steels," *J. Nucl. Mater.*, vol. 386–388, pp. 71–74, 2009.

[63] G. Golański and S. Mroziński, "Low cycle fatigue and cyclic softening behaviour of martensitic cast steel," *Eng. Fail. Anal.*, vol. 35, pp. 692–702, 2013.

[64] M. F. Giordana, P. F. Giroux, I. Alvarez-Armas, M. Sauzay, a. Armas, and T. Kruml, "Microstructure evolution during cyclic tests on EUROFER 97 at room temperature. TEM observation and modelling," *Mater. Sci. Eng. A*, vol. 550, pp. 103–111, 2012.

[65] J. C. Earthman, G. Eggeler, and B. Ilschner, "Deformation and Damage Processes in a 12%Cr-Mo-V Steel under High Temperature Low Cycle Fatigue Conditions in Air and Vacuum," *Mater. Sci. Eng.*, vol. A110, pp. 103–114, 1989.

[66] J. I. Dickson and J. B. Vogt, "The Formation of Ribbon-like Extrusions and Intrusions during the Cyclic Deformation of Copper," in *Proceedings of the ll Conference of Fatigue Damage*, 1987.

[67] T. Lepisto, J. Yli-Kauppila, P. Kettunen, and P. Hautojarvi, "Voids in Fatigued Copper Single Crystals," *phys. stat. sol.*, 1981.

[68] J. Polák, "On the role of point defects in fatigue crack initiation," *Mater. Sci. Eng.*, vol. 92, pp. 71–80, 1987.

[69] M. Okayasu, K. Sato, M. Mizuno, D. Y. Hwang, and D. H. Shin, "Fatigue properties of ultra-fine grained dual phase ferrite/martensite low carbon steel," *Int. J. Fatigue*, vol. 30, no. 8, pp. 1358–1365, 2008.

[70] S. Onaka, S. Soeta, M. Kato, and R. Tanaka, "High-temperature deformation and fracture behaviour of Cu-Si02 bicrystals," *J. Mater. Sci.*, vol. 23, pp. 577–582, 1988.

[71] T. Niendorf, D. Canadinc, H. J. Maier, and I. Karaman, "On the microstructural stability of ultrafine-grained interstitial-free steel under cyclic loading," *Metall. Mater. Trans. A Phys. Metall. Mater. Sci.*, vol. 38 A, no. 9, pp. 1946–1955, 2007.

[72] J. C. Grosskreutz, "Fundamental knowledge of fatigue fracture," in *Proceedings of Third International Conference on Fracture*, 1973, pp. 1–26.

[73] C. Laird, "Fatigue," *Mater. Sci. Eng.*, vol. 25, pp. 187–191, 1973.

[74] L. M. Brown, "Dislocation substructures and the initiation of cracks by fatigue," in *Conference Fatigue 1977 in Cambridge*, 1977, pp. 315–320.

[75] J. M. Finney and C. Laird, "The Development of Slip Offsets within Persistent Slip Bands during a Single Fatigue Cycle," *Mater. Sci. Eng.*, vol. 54, pp. 137–141, 1982.

[76] A. Hunsche and P. Neumann, "Quantitative measurement of persistent slip band profiles and crack initiation," *Acta Metall.*, vol. 34, no. 2, pp. 207–217, 1986.

[77] Z. S. Basinski and S. J. Basinski, "Copper Single Crystal PSB Morphology between 4.2 and 350 K," *Acta Met.*, vol. 37, no. 12, pp. 3263–3273, 1989.

[78] Z. S. Basinski, R. Pascual, and S. J. Basinski, "Low Amplitude Fatigue of Copper Single Crystals-l. The Role of the Surface in Fatigue Failure," *Acta Met.*, vol. 31, no. 4, pp. 591–602, 1983.

[79] Z. S. Basinski and S. J. Basinski, "Low Amplitude Fatigue of Copper Single Crystals-ll. Surface Observations," *Acta Met.*, vol. 33, no. 7, pp. 1307–1317, 1985.

[80] Z. S. Basinski and S. J. Basinski, "Low Amplitude Fatigue of Copper Single Crystals-lll. PSB Sections," *Acta Met.*, vol. 33, no. 7, pp. 1319–1327, 1985.

[81] P. Neumann and A. Tonnessen, "Cyclic Deformation and Crack Initiation," in

Conference Fatigue 87 in Virginia, 1987, pp. 3–22.

[82] A. S. Cheng and C. Laird, "Fatigue Life Behavior of Copper Single Crystals. Part ll : Model for Crack Nucleation in Persistent Slip Bands," *Fatigue Eng. Mater. Struct.*, vol. 4, no. 4, pp. 343–353, 1981.

[83] J. C. Figueroa and C. Laird, "Crack Initiation Mechanisms in Copper Polycrystals Cycled under Constant strain Amplitudes and in Step Tests," *Mater. Sci. Eng.*, vol. 60, pp. 45–48, 1983.

[84] B. T. Ma and C. Laird, "Overview of fatigue behavior in copper single crystals- II. Population, size distribution and growth kinetics of stage I cracks for tests at constant strain amplitude," *Acta Met.*, vol. 37, no. 2, pp. 337–348, 1989.

[85] F. Guiu, R. Dulniak, and B. C. Edwards, "On the Nucleation of Fatigue Cracks in Pure Polycrystalline alfa-Iron," *Fatigue Eng. Mater. Struct.*, vol. 5, no. 4, pp. 311–321, 1982.

[86] K. Pohl, P. Mayr, and E. Macherauch, "Shape and Structure of Persitent Slip Bands in Iron Carbon Alloys," in *Defects, Fracture and Fatigue*, G. C. Sih and J. W. Provan, Eds. The Hague: Martinus Nijhoff Publisher, 1983, pp. 147–159.

[87] J. B. Vogt, G. Degallaix, J. C. Tissier, and J. Foct, "The nature of fatigue extrusions in a 12 Cr steel," *J. Mater. Sci. Lett.*, vol. 7, no. 7, pp. 700–702, 1988.

[88] G. Chai, T. Forsman, and F. Gustavsson, "Microscopic and nanoscopic study on subsurface damage and fatigue crack initiation during very high cycle fatigue," *Int. J. Fatigue*, vol. 83, pp. 288–292, 2016.

[89] J. Z. Briggs and T. D. Parker, *The Super 12% Cr Steels*, 1st ed. New York: Climax Molybdenum Company, 1965.

[90] G. B. Olson and M. Cohen, "Kinetics of strain-induced martensitic nucleation," *Met. Trans. A*, vol. 6, no. 4, pp. 791–795, 1975.

[91] G. Junak and M. Cieśla, "Low-cycle fatigue of P91 and P92 steels used in the power engineering industry," *Arch. Mater. Sci. Eng.*, vol. 48, no. 1, pp. 19–24, 2011.

[92] I. Kuběna, J. Polák, P. Marmy, and T. Kruml, "A comparison of microstructure evolution due to fatigue loading in eurofer 97 and ODS eurofer steels," *Procedia Eng.*, vol. 74, pp. 401–404, 2014.

[93] C. Odin, J. P. Aime, Z. El Kaakour, and T. Bouhacina, "Tip's finite size effects on atomic force microscopy in the contact mode: Simple geometrical considerations for rapid estimation of apex radius and tip angle based on the study of polystyrene latex balls," *Surf. Sci.*, p. 317,321, 1994.

[94] L. Aigouy, Y. De Wilde, and C. Frétigny, *Les nouvelles microscopies, à la decouverte du nanomode*. Paris: Belin, 2006.

[95] J. Polák, I. Kuběna, and J. Man, "The shape of early persistent slip markings in fatigued 316L steel," *Mater. Sci. Eng. A*, vol. 564, pp. 8–12, Mar. 2013.

[96] J. Man, K. Obrtlik, and J. Polak, "Study of surface relief evolution in fatigued 316L austenitic stainless steel by AFM," *Mater. Sci. Eng. A*, vol. 351, no. 1–2, pp. 123–132, 2003.

[97] B. Pittenger, N. Erina, and C. Su, "Quantitative Mechanical Property Mapping at the Nanoscale with Peak Force QNM," *Bruker Corporation Application Note AN128*, 2010. .

[98] L. Morales-Rivas, A. González-Orive, C. Garcia-Mateo, A. Hernández-Creus, F. G. Caballero, and L. Vázquez, "Nanomechanical characterization of nanostructured bainitic steel: Peak Force Microscopy and Nanoindentation with AFM," *Sci. Rep.*, vol. 5, pp. 1–16, 2015.

[99] I. Serre, D. Salazar, and J.-B. Vogt, "Atomic force microscopy investigation of surface relief in individual phases of deformed duplex stainless steel," *Mater. Sci. Eng. A*, vol. 492, no. 1–2, pp. 428–433, Sep. 2008.

[100] D. Salazar, "Etude du partage de la plasticité cyclique d'un acier duplex par microscopie à force atomique," p. 171, 2008.

[101] J. Man *et al.*, "Study of cyclic strain localization and fatigue crack initiation using FIB technique," *Int. J. Fatigue*, vol. 39, pp. 44–53, Jun. 2012.

[102] J. Man *et al.*, "AFM and SEM-FEG study on fundamental mechanisms leading to fatigue crack initiation," *Int. J. Fatigue*, 2014.

[103] M. Risbet, X. Feaugas, C. Guillemer-Neel, and M. Clavel, "Damage in nickel base superalloy: Influence of local parameters measured by electron backscattered diffraction and atomic force microscopy," *Scr. Mater.*, vol. 60, no. 5, pp. 269–272, 2009.

[104] S. Fréchard, F. Martin, C. Clément, and J. Cousty, "AFM and EBSD combined studies of plastic deformation in a duplex stainless steel," *Mater. Sci. Eng. A*, vol. 418, pp. 312–319, 2006.

[105] M. Hayakawa, S. Matsuoka, and Y. Furuya, "Nanoscopic measurement of local plastic deformation for a tempered martensitic steel by atomic force microscopy," *Mater. Lett.*, vol. 57, no. 20, pp. 3037–3042, 2003.

[106] A. Hayakawa, S. Matsuoka, K. Tsuzaki, H. Hanada, M. Sugisaki, and M. Hayakawa, "Atomic force microscopy of induction- and furnace-heating-tempered prestressed steels with different delayed fracture properties (vol 47, pg 655, 2002)," *Scr. Mater.*, vol. 47, p. 467, 2002.

[107] M. Hayakawa, S. Matsuoka, and Y. Furuya, "Atomic force microscopy of local plastic deformation for tempered martensite in a medium-carbon steel," *Nippon Kinzoku Gakkaishi/Journal Japan Inst. Met.*, vol. 67, pp. 354–361, 2003.

[108] D. Hull and D. J. Bacon, *Introduction to Disclocations*, 4th ed. Oxford: Butterworth-Heinemann, 2001.

[109] L. A. Giannuzzi and F. A. Stevie, "Introduction To Focused Ion," *Springer*, 2005.

[110] J. Orloff, L. W. Swanson, and M. W. Utlaut, *High Resolution Focused Ion Beams: Fib and Its Applications : The Physics of Liquid Metal Ion Sources and Ion Optics and Their Application to Focused Ion Beam Technology*. 2003.

[111] N. Yao, *Focused ion beam systems: basics and applications*. 2007.

[112] The Engineering ToolBox, "Thermal conductivity of some common Materials and Gases." [Online]. Available: http://www.engineeringtoolbox.com/thermal-conductivity-

d_429.html.

[113] C. A. Volkert and A. M. Minor, "Focused Ion Beam Microscopy and Micromachining," *MRS Bull.*, vol. 32, no. 5, pp. 389–399, 2007.

[114] J. P. McCaffrey, M. W. Phaneuf, and L. D. Madsen, "Surface damage formation during ion-beam thinning of samples for transmission electron microscopy," *Ultramicroscopy*, vol. 87, no. 3, pp. 97–104, Apr. 2001.

[115] N. I. Kato, "Reducing focused ion beam damage to transmission electron microscopy samples," *J. Electron Microsc. (Tokyo).*, vol. 53, no. 5, p. 451, 2004.

[116] M. Andrzejczuk, T. Płociński, W. Zieliński, and K. J. Kurzydłowski, "TEM characterization of the artefacts induced by FIB in austenitic stainless steel," *J. Microsc.*, vol. 237, no. 3, pp. 439–442, 2010.

[117] J. Mayer, L. a Giannuzzi, T. Kamino, and J. Michael, "TEM Sample Preparation and FIB-Induced Damage," *MRS Bull.*, vol. 32, no. 5, pp. 400–407, 2007.

[118] S. Hémery, T. Auger, J. L. Courouau, and F. Balbaud-Célérier, "Effect of oxygen on liquid sodium embrittlement of T91 martensitic steel," *Corros. Sci.*, vol. 76, pp. 441–452, Nov. 2013.

[119] J. Polák, V. Mazánová, M. Heczko, I. Kuběna, and J. Man, "Profiles of persistent slip markings and internal structure of underlying persistent slip bands," *Fatigue Fract. Eng. Mater. Struct.*, 2017.

[120] J. Polák, J. Man, T. Vystavěl, and M. Petrenec, "The shape of extrusions and intrusions and initiation of stage I fatigue cracks," *Mater. Sci. Eng. A*, vol. 517, no. 1–2, pp. 204–211, Aug. 2009.

[121] J. Man, M. Petrenec, K. Obrtlík, and J. Polák, "AFM and TEM study of cyclic slip localization in fatigued ferritic X10CrAl24 stainless steel," *Acta Mater.*, vol. 52, no. 19, pp. 5551–5561, 2004.

[122] J.-B. Vogt, D. Salazar, and I. Proriol Serre, "Partition of Cyclic Plasticity in the 25Cr-7Ni-0.25N duplex Stainless Steel Investigated by Atomic Force Microscopy," *Duplex Stainl. Steel*, pp. 275–302, 2009.

[123] J. Man, M. Petrenec, K. Obrtlík, and J. Polák, "AFM and TEM study of cyclic slip localization in fatigued ferritic X10CrAl24 stainless steel," *Acta Mater.*, vol. 52, no. 19, pp. 5551–5561, Nov. 2004.

[124] J. Man, P. Klapetek, O. Man, A. Weidner, K. Obrtlík, and J. Polák, "Extrusions and intrusions in fatigued metals. Part 2. AFM and EBSD study of the early growth of extrusions and intrusions in 316L steel fatigued at room temperature," *Philos. Mag.*, vol. 89, no. 16, pp. 1337–1372, 2009.

[125] J. Ruste, "Microscopie électronique à balayage - Principe et équipement," *Techniques de l'Ingénieur*, 2013. .

[126] A. J. Wilkinson and P. B. Hirsch, "Electron diffraction based techniques in scanning electron microscopy of bulk materials," *Micron*, vol. 28, no. 4, pp. 279–308, Aug. 1997.

[127] A. J. Wilkinson and T. Ben Britton, "Strains, planes, and EBSD in materials science," *Mater. Today*, vol. 15, no. 9, pp. 366–376, 2012.

[128] C. Maurice and R. Fortunier, "A 3D Hough transform for indexing EBSD and Kossel patterns," *J. Microsc.*, vol. 230, no. 3, pp. 520–529, 2008.

[129] S. I. Wright, M. M. Nowell, and D. P. Field, "A Review of Strain Analysis Using Electron Backscatter Diffraction," *Microsc. Microanal.*, vol. 17, no. 3, pp. 316–329, 2011.

[130] J.-L. Pouchou, "Introduction à l'analyse EBSD : principes généraux et mise en oeuvre dans un MEB," in *L'analyse EBSD. Principes et applications*, J.-L. Pouchou, Ed. Paris: EDP Sciences, 2004, pp. 1–24.

[131] T. Maitland and S. Sitzman, "EBSD technique and materials characterization examples," in *Scanning Microscopy for Nanotechnology. Techniques and Applications*, W. Zhou and Z. L. Wang, Eds. Springer, 2007, pp. 41–76.

[132] T. Ben Britton, "Presentation at Oxford Instruments: Introduction to EBSD," High Wycombe, 2013.

[133] M. Jedrychowski, J. Tarasiuk, B. Bacroix, and S. Wronski, "Electron backscatter diffraction investigation of local misorientations and orientation gradients in connection with evolution of grain boundary structures in deformed and annealed zirconium. A new approach in grain boundary analysis," *J. Appl. Crystallogr.*, vol. 46, no. 2, pp. 483–492, 2013.

[134] J. Bouquerel, B. Diawara, A. Dubois, M. Dubar, J.-B. Vogt, and D. Najjar, "Investigations of the microstructural response to a cold forging process of the 6082-T6 alloy," *Mater. Des.*, vol. 68, pp. 245–258, Mar. 2015.

[135] C. Schayes, J.-B. Vogt, J. Bouquerel, F. Palleschi, and S. Zaefferer, "Cyclic plasticity mechanism of the M330-35A steel," *Int. J. Fatigue*, vol. 82, pp. 530–539, 2016.

[136] C. Schayes, "PhD thesis UNIVERSITE DE LILLE 1 - SCIENCES ET TECHNOLOGIES Low cycle fatigue of the Fe-3Si steel : damage mechanisms and strain localisation by EBSD PhD supervisor," 2016.

[137] H. Mughrabi, "Microstructural mechanisms of cyclic deformation, fatigue crack initiation and early crack growth," *Philos. Trans. R. Soc. A*, vol. 373, no. 2038, p. 20140132, 2015.

[138] J. Polák and J. Man, "Fatigue crack initiation - The role of point defects," *Int. J. Fatigue*, vol. 65, pp. 18–27, 2014.

[139] J. I. Dickson, J. Boutin, and L. Handfield, "A comparison of two simple methods for measuring cyclic internal and effective stresses," *Mater. Sci. Eng.*, vol. 64, pp. 7–11, 1984.

[140] J. B. Vogt, C. Biegeon, and J. Foct, "Combined effect of nitrogen and silicon on LCF of a 12Cr martensitic stainless steel," *Z. Met. 85*, pp. 92–99, 1994.

[141] A. F. Armas, C. Petersen, R. Schmitt, M. Avalos, and I. Alvarez, "Cyclic instability of martensite laths in reduced activation ferritic/martensitic steels," *J. Nucl. Mater.*, vol. 329–333, pp. 252–256, 2004.

[142] A. O. O. Mekhrabov, E. Sato, M. Shimotomai, and M. Doyama, "Damage Recovery in Electron-Irradiated Fe-Ni-Cr Alloys," *J. Nucl. Mater.*, vol. 134, pp. 549–552, 1985.

[143] J. Polák and J. Man, "Fatigue crack initiation – The role of point defects," *Int. J. Fatigue*, vol. 65, pp. 18–27, Aug. 2014.

[144] J. Polak and J. Man, "Experimental evidence and physical models of fatigue crack initiation," *Int. J. Fatigue*, vol. 91, pp. 294–303, 2016.

[145] P. Alexopoulos and J. G. Byrne, "Positron Lifetime Changes During the Fatigue of Cu," *Metall. Trans.*, vol. 9A, pp. 1829–1833, 1978.

[146] A. Barbieri, S. Hansen-Ilzhofer, A. Ilzhofer, and U. Holzwarth, "Nondestructive positron-lifetime measurements during fatigue of austenitic stainless steel using a mobile positron beam," *Appl. Phys. Lett.*, vol. 77, no. 12, pp. 1911–1913, 2000.

[147] W. Egger *et al.*, "Vacancy clusters close to a fatigue crack observed with the München scanning positron microscope," *Appl. Surf. Sci.*, vol. 194, no. 1–4, pp. 214–217, 2002.

[148] P. Schaaff and U. Holzwarth, "Nondestructive detection of fatigue damage in austenitic stainless steel by positron annihilation," *J. Mater. Sci.*, vol. 40, no. 23, pp. 6157–6168, 2005.

[149] K. Sugita, Y. Mutou, and Y. Shirai, "Vacancy clustering behavior in hydrogen-charged martensitic steel AISI 410 under tensile deformation," *Int. Work. Positron Stud. Defects 2014/Journal Phys. Conf. Ser. 674 012006*, 2016.

[150] H. Mughrabi, R. Myllylä, and K. Maier, "Paper presented at Hauptversammlung der Deutschen Gesellschaft für Metallkunde," den Haag, 1979.

[151] J. Piqueras, J. C. Grosskreutz, and W. Frank, "The influence of point defect clusters on fatigue hardening of copper single crystals," *Phys. Status Solidi*, vol. 11, pp. 567–580, 1972.

[152] J. G. Antonopoulos and A. T. Winter, "Weak-beam study of dislocation structures in fatigued copper," *Philos. Mag.*, vol. 33, no. 1, pp. 87–95, 1976.

[153] S. M. L. Sastry, B. Ramaswami, and F. Goetz, "Fatigue deformation of silver single crystals," *Metall. Trans. A*, vol. 7, no. 2, pp. 243–248, 1976.

[154] P. O. Kettunen, T. Lepistö, G. Kostorz, and G. Göltz, "Voids produced by fatigue in copper single crystals of <111>-orientation," *Acta Metall.*, vol. 29, no. 6, pp. 969–972, Jun. 1981.

[155] J. W. Morris, "Dislocation Plasticity : Overview," *Introduction to Materials Science*, 2007. [Online]. Available: http://www.mse.berkeley.edu/groups/morris/.

[156] L.-L. Niu *et al.*, "Interplay between intrinsic point defects and low-angle grain boundary in bcc tungsten: effects of local stress field," *J. Phys. Condens. Matter*, vol. 27, p. 255007, 2015.

[157] Z. Fan, "Simulation atomistique de la fatigue dans les métaux cubiques à faces centrées," Université Paris-Saclay, 2016.

[158] A. S. Fedorov, D. A. Fedorov, Z. I. Popov, Y. E. Anan'eva, N. S. Eliseeva, and A. A. Kuzubov, "Mobility of vacancies under deformation and their effect on the elastic properties of graphene," *J. Exp. Theor. Phys.*, vol. 112, no. 5, pp. 820–824, 2011.

[159] A. Tapia, R. Peón-Escalante, C. Villanueva, and F. Avilés, "Influence of vacancies on

the elastic properties of a graphene sheet," *Comput. Mater. Sci.*, vol. 55, pp. 255–262, 2012.

[160] R. a. Konchakov and V. a. Khonik, "Effect of vacancies and interstitials in the dumbbell configuration on the shear modulus and vibrational density of states of copper," *Phys. Solid State*, vol. 56, no. 7, pp. 1368–1373, 2014.

[161] J. Xi, P. Zhang, C. He, H. Zang, D. Guo, and T. Li, "The role of point defects in the swelling and elastic modulus of irradiated cubic silicon carbide," *Nucl. Instruments Methods Phys. Res. Sect. B Beam Interact. with Mater. Atoms*, vol. 356–357, pp. 62–68, 2015.

[162] J. Philibert, *Atom movements. Diffusion and mass transport in solids*. 1991.

Abstract. The particularity of martensitic steels is their complex hierarchical microstructure consisting of prior austenite grains, packets, blocks and laths, the influence of which on the early-stage fatigue deformation at nano-scale is little studied. As a result the objective of this work is to explain the mechanism of extrusion-intrusion pair formation in a 12%Cr martensitic steel during low cycle fatigue at room temperature in regards to the different interfaces creating the material complexity. **To** achieve the purpose, the fatigue slip markings were thoroughly investigated at the fatigued metal surface with a help of atomic force microscope and then the microstructural evolution was studied directly under fatigue slip markings on the transmission electron microscope thin lamellae extracted by focused ion beam. **The** atomic force microscope analysis of the specimen surface after each interruption step of low cycle fatigue test revealed two different morphological types of extrusions that were named principal and secondary extrusions. For the latter there was not found any scientific equivalence in the case of martensitic steels in the reviewed literature bank. Additionally, this technique gave an idea about the localization of principal extrusions in the vicinity of different boundaries making the complex martensitic microstructure. **The** transmission electron microscope investigation of microstructural evolutions under the fatigue slip markings demonstrated the localization of principal extrusions in the vicinity of different martensitic boundaries as well as of fatigue dislocation cell walls, and the localization of intrusions in the boundaries or walls themselves. As for the secondary ones, their localization inside the laths was validated too. **The** ensemble of results together with the Polak's model helped to propose the mechanism of formation of fatigue slip markings in the hierarchically organized martensitic steel. Thus, the existing different boundaries and the formed dislocation cells were found to play a definitive role in the creation of intrusions. The extrusion is believed to be the direct result of slip activity of dislocations close to the boundary as well as the result of volume swelling caused by vacancy generation and migration directed by the boundary dislocations. The intrusion is rather a result of vacancy accumulation in the boundaries or walls due to the dislocation movement. As follows, the martensitic hierarchical interfaces and dislocation cell walls are considered to be a source of dislocations and at the same time a sink for vacancies.

Keywords: Low Cycle Fatigue, plastic deformation, microcrack initiation, martensitic microstructure, boundary, 12%Cr steel, Persistent Slip Markings, Atomic Force Microscope, Transmission Electron Microscope analysis

---

Résumé. La spécificité des aciers martensitiques est leur microstructure hiérarchisée complexe constituée d'anciens grains austénitiques, de paquets, de blocs et de lattes. L'influence de chaque élément de cette microstructure sur les premières étapes de l'amorçage des microfissures de fatigue est cependant peu étudiée. En conséquence, l'objectif de ce travail est, d'une part, d'expliquer le mécanisme de formation d'extrusion-intrusion par fatigue oligocyclique à température ambiante à la surface d'un acier martensitique à 12% de chrome et, d'autre part, de définir le rôle des différentes interfaces de la microstructure sur la formation des extrusions et des intrusions. **Pour** atteindre cet objectif, les marques de glissement observées à la surface après sollicitation cyclique ont été étudiées en détail à l'aide de la microscopie à force atomique. L'évolution de la microstructure en dessous des marques de glissement a été ensuite analysée à partir d'observations en microscopie électronique en transmission des sections transverses obtenues par extraction de lames par faisceau d'ions focalisé. **L'analyse** en microscope à force atomique de la surface de l'échantillon après chaque interruption de l'essai de fatigue oligocyclique a révélé deux morphologies d'extrusions qui ont été appelées extrusions principales et extrusions secondaires. Pour ces dernières, aucune équivalence scientifique dans le cas des aciers martensitiques n'a été mentionnée auparavant dans la littérature. De plus, ces analyses, ont montré que les extrusions principales étaient localisées à proximité des différents joints – des éléments constituant la microstructure martensitique. **L'étude** des évolutions microstructurales sous les marques de glissement à l'aide de la microscopie électronique à transmission a confirmé la localisation des extrusions principales à proximité des différentes interfaces de la structure martensitique ou des murs des cellules de dislocations, et prouvé la localisation des intrusions dans les interfaces elles-mêmes. Quant aux extrusions secondaires, leur localisation à l'intérieur des lattes a également été validée. **L'ensemble** des résultats confrontés au modèle de Polak a conduit à proposer un mécanisme de formation des extrusions et intrusions à la surface de l'acier martensitique hiérarchiquement organisé. Ainsi, les différents joints inhérents à la structure martensitique et les cellules de dislocation formées par fatigue jouent un rôle primordial dans la création des intrusions. Nous pensons que l'extrusion serait le résultat direct du glissement des dislocations au sein même de la latte et proches d'un joint, ainsi que le résultat d'un gonflement de volume causé par la génération des lacunes et leur migration vers les dislocations aux interfaces. L'intrusion résulterait plutôt de l'accumulation de lacunes dans les joints ou les parois des cellules de dislocation en raison du mouvement des dislocations. Ainsi, les interfaces de la structure martensitique hiérarchisée et les parois des cellules de dislocations sont à la fois considérées comme source de dislocations et puits de lacunes.

Mots clés : fatigue oligocyclique, déformation plastique, nucléation de microfissure, microstructure martensitique, joint microstructural, acier 12%Cr, marque de glissement, microscopie à force atomique, microscopie électronique à transmission